Analytical Modelling and Upscaling of Multicomponent Suspension-Colloidal Transport in Porous Media

---

Gabriel de Veiga Cabral Malgaresi, B.Sc.(Hons), M.Sc.

A thesis submitted for the degree of

Doctor of Philosophy (Ph.D.)

Australian School of Petroleum

Faculty of Engineering, Computer & Mathematical Sciences

The University of Adelaide



November 2019

To

my sister, Marina

who has always been my inspiration and encouragement during all periods of my academic life.

and my mother and my father, who have always loved me unconditionally and gave me all the support that I needed to face any challenge in my life.

Table of Contents

Abstract ..... **iii**

Declaration ..... **vi**

Acknowledgement ..... **vii**

Thesis by Publication ..... **x**

1 Contextual Statement **1**

1.1 Thesis Structure 4

1.2 How the Publications are related to the Thesis 6

1.3 References 9

2 Literature Review **11**

2.1 Introduction 11

2.2 Multiple mechanisms of particle retention in porous media 12

2.3 Cotransport of colloids with multiple capture mechanisms 19

2.4 Mathematical modelling of multi-component suspension-colloidal transport in porous media 23

2.5 Hyper-exponential retention profiles – explanation and mathematical model 27

2.6 Non-monotonic retention profiles – explanation and mathematical model 31

2.7 Application – Validation, and prediction of non-monotonic retention profiles in axisymmetric colloidal flows 38

2.8 Summary 39

2.9 References 40

3 Exact Solutions for Multiple Capture Mechanisms **48**

3.1 Exact Solutions for Suspension-Colloidal Transport with Multiple Capture Mechanisms 49

3.2 Cotransport of Suspended Colloids and Nanoparticles in Porous Media 67

4 Exact Upscaling for Transport of Size- Distributed Colloids **95**

5 Model to match hyper-exponential retention profiles.....126

5.1 A modified model for colloidal transport to match hyper-exponential particle retention……..127

5.2 A Transport of high-concentration colloids with two particle-capture mechanisms.....170

6 Explaining non-monotonic retention profiles during flow of size-distributed colloids.....201

7 Non-monotonic retention profiles during axi-symmetric colloidal flows 216

8 Conclusions.....232

Abstract

Hereby I present a PhD thesis by publications. The thesis includes seven journal papers, from which five have already been published, one has been submitted for publication and is presently under review, and another one is under final preparation to be submitted. The journal publications include high-impact-factor academic journals, e.g., Chemical Engineering Journal, Water Resources Research, Journal of Hydrology, and Transport in Porous Media, which are the major academic journals in transport in porous media. Besides that, during the PhD candidature, I have published an extended abstract in the International Journal of Chemical and Molecular Engineering, and a shared conference paper at The APPEA Journal.

The thesis presents *new mathematical models for transport and cotransport of colloidal and nano-particles flow in porous media*. The novelties in this thesis are the development of new systems of equations, able to model phenomena that differ from the classical deep bed filtration theory, as breakthrough curves that asymptotically increase until stabilising at a lower limit than the injected concentration; prediction of non-exponential retention profiles (hyper-exponential and non-monotonic retention profiles); and the development of a new uspcaled procedure able to predict the behaviour of micro-scale particle populations.

The application of colloids, engineered nano-particles, and suspension, in general, has been rapidly growing in the last two decades. The demand for these particles in several industries and processes has increased the disposal of these particles in subterranean aquifers and reservoirs. Therefore, understanding and modelling of the phenomena of particles flow through porous media have gained a lot of attention recently. In order to explain, model and predict the behaviour of the colloidal

suspension and nano-particles disposal into porous structures, this thesis presents mathematical models and new physical-explanation for different phenomena that occur in porous media.

Firstly, the thesis explain the transport of a single particle population that shows breakthrough curves that increase asymptotically and tends to a stabilization at a value lower than the injected concentration by two-particle capture mechanisms, where one mechanism is attachment-based on Langmuir's blocking function, and the other mechanism is straining or size-exclusion based on constant filtration function. Secondly, the thesis proposes a new mathematical model for cotransport of a binary colloidal-species that accounts for the same two capture mechanisms previously mentioned; however, these mechanisms are applied for each particle population. The thesis also presents a new exact averaging (upscaling) procedure that results in a large-scale system of equations, which significantly differs from the traditional deep bed filtration model. The proposed upscaled model is based on the average concentrations of suspended and retained particles and also includes a new site-occupation kinetic equation. Sequentially, the thesis introduces a new and simple mathematical model based on mass activity law accounting separately for single and two particles capture mechanisms, able to predict hyper-exponential retention profiles. Finally, the thesis proposes an original explanation for non-monotonic retention profiles based on a mathematical model that accounts for binary colloidal populations. This mathematical model is upscaled in radial coordinates and the behaviour non-monotonic retention profiles are predicted in reservoir-scale along with formation damage prediction.

All mathematical models developed in this thesis are applicable for different areas and industrial processes and they are useful for successfully close matching of several laboratory data available in the contemporaneous literature.

Declaration

I certify that this work contains no material which has been accepted for the award of any other degree or diploma in my name, in any university or other tertiary institution and, to the best of my knowledge and belief, contains no material previously published or written by another person, except where due reference has been made in the text. In addition, I certify that no part of this work will, in the future, be used in a submission in my name, for any other degree or diploma in any university or other tertiary institution without the prior approval of the University of Adelaide and where applicable, any partner institution responsible for the joint-award of this degree. I give consent to this copy of my thesis when deposited in the University Library, being made available for loan and photocopying, subject to the provisions of the Copyright Act 1968. The author acknowledges that the copyright of published works contained within this thesis resides with the copyright holder(s) of those works.

I also give permission for the digital version of my thesis to be made available on the web, via the University's digital research repository, the Library Search and also through web search engines, unless permission has been granted by the University to restrict access for a period of time.

I acknowledge the support I have received for my research through the provision of CNPq (Brazilian Scientific Fund) and an Australian Government Research Training Program Scholarship.

Gabriel de Veiga Cabral Malgaresi 22/11/2019

Acknowledgement

I would have never been able to complete this journey without the patience and support of many people. Therefore, I would like to take the opportunity to express my gratitude to whatever person who somehow had contributed to the preparation and development of my thesis and my personal life.

Firstly, I would like to express my sincere gratitude to my supervisor, Prof. Pavel Bedrikovetsky, for his support even before I started my PhD candidature, for his hard work, constant support, motivation, and patience, without his guidance and expertise I would not be able to conclude my PhD thesis.

I would also like to thank my co-supervisors, Dr. Abbas Zeinijahromi and Dr. Sara Borazjani for providing all support during my PhD candidature. Dr. Sara Borazjani thank you for all your kind and supportive words.

A very special thank you to all people that, although not being my supervisors, made an enormous contribution to my work, motivating me, being patient, sharing their knowledge with me, and giving me technical assistance. Dr. Themis Carageorgos, what would be my PhD candidature without your support, patience, and help in writing papers, and performing experiments – *Muito obrigado*! Dr. Alex Badalyan, thank you very much for all your lessons in the laboratory work-place and for making my days funnier and relaxed. Dr. Zhenjiang You, thank you for always being so patient and helpful. Dr. Hadi Madani, thank you very much indeed for all your help, fruitful discussions, and support. I would also like to thank Dr. Alexandre Sérvulo, who was one of the persons responsible for bringing me to Australia – *Muito obrigado*!

During this PhD candidature, I also had the opportunity to meet amazing people, that were very helpful and made this journey easier, much more fun and less stressful.

A sincere THANK YOU to my all friends in the Australian School of Petroleum, Abdullah, Abolfaz, Ben, Hao, Mike, Monica, Paul, Reza, Roozbeh, Saurabh, Shahdad, Shuyan, Tammy, Thomas, Yazan and Yulong. Thanks for all your support during this journey, thank you for your availability to have technical discussions, for your help with my work, and your criticism. Thank you for all the pleasant and funny moments at coffee and lunch time. Thank you, guys, for being patient, supportive and for listening to my complaints when I was in a bad mood, when the day was not a very good one.

During this journey, I also had the opportunity to build up friendships that I will keep for life. A very special thank you to my close friend Abdullah Sarihi, you have helped me even before I arrived in Australia, you were always kind and patient, and one of the persons who have listened to my everyday complaints. Thank you for being such a good friend, for teaching me so much, and for your support and encouragement to endure the hardship of this PhD. A very special thank you to my close friend Mohammadreza Zare, thank you for listening to me, for being patient, supportive, a friend on any occasion, and for teaching me so much. You are a true friend.

Very special thank you to my Brazilian fellow, Larissa Chequer. My friend, thank you for all your support and kindness during this journey, you became part of my family, it was a pleasure to live, discuss, and share all good and bad moments with you in these three and a half years, without your friendship and support, I do not know if I would be able to complete this work.

Last but not least, I would like to express my enormous gratitude to my family. Firstly, I would like to thank my girlfriend, Pollyana, for her support, love, and encouragement. Thank you for making my mornings funnier and relaxing, even when

I was in a very bad mood. Pollyana, thank you for listening to my complaints and for your wonderful support. Without you, I would not be able to finish this journey. You have no idea how you helped me. Now, I am coming home baby!!!! Secondly, I would like to thank my aunt Carmem, my cousin Gabiru and my godson Vicente. They made me forget for while how hard this time was. All Saturdays and Sundays calls were just great, you have no idea how these phone/video calls have helped me during this time far from you guys. Thirdly, I would like to thank my sister, Marina. Marina, I already told this several times, but you are one of the reasons that I kept going in my academic life until now. Thank you for all your support, love, encouragement and for listening to complaints, for the long calls/video calls discussing our academic life, without you, I would not even imagine come so far in the academic life. Finally, I would like to thank the most important persons in my life, my mom and my day. *Obrigado*! I hope you are proud of me wherever you are. You were the base of everything. Thank you for your support in my studies, thank you for helping me to build my personality, thank you for everything – I would not be able to achieve everything that I have achieved without your support – *Eu amo vocês*!

Thesis by Publication

Published Peer-Reviewed Journal Papers

Malgaresi, G., Khazali, N., Bedrikovetsky, P., 2020. Non-monotonic retention profiles during axi-symmetric colloidal flows. J. Hydrology, 580: 124235. DOI:https://doi.org/10.1016/j.jhydrol.2019.124235

Malgaresi, G., Collins, B., Alvaro, P. and Bedrikovetsky, P., 2019. Explaining non-monotonic retention profiles during flow of size-distributed colloids. Chemical Engineering Journal, p.121984.

Bedrikovetsky, P., Osipov, Y., Kuzmina, L. and **Malgaresi, G.,** 2019. Exact Upscaling for Transport of Size- Distributed Colloids. Water Resources Research, 55(2), pp.1011-1039.

Malgaresi, G.V.C., Zhang, H., Chrysikopoulos, C.V. and Bedrikovetsky, P., 2019. Cotransport of Suspended Colloids and Nanoparticles in Porous Media. Transport in Porous Media, 128(1), pp.153-177.

Zhang, H., **Malgaresi, G.V.C.** and Bedrikovetsky, P., 2018. Exact solutions for suspension-colloidal transport with multiple capture mechanisms. International Journal of Non-Linear Mechanics, 105, pp.27-42.

Submitted Journal Papers

Xu, C., **Malgaresi, G.**, Osipov, Y., Kuzmina, L. and**,** Bedrikovetsky, P., 2019. A modified model for colloidal transport to match hyper-exponential particle retention. Chemical Engineering Journal.

Malgaresi, G., Osipov, Y., Kuzmina, L. and**,** Bedrikovetsky, P., 2019. Transport of high-concentration colloids with two particle-capture mechanisms. (To be submitted).

International conference papers and presentations

Naik, S., **Malgaresi, G.,** You, Z. and Bedrikovetsky, P., 2018. Well productivity enhancement by applying nanofluids for wettability alteration. The APPEA Journal, 58(1), pp.121-129.

Malgaresi, G., Borazjani, S., Madani, H., and Bedrikovetsky, P., 2018. Evaluation of nanoparticle application to control formation damage in porous media. International Journal of Chemical and Molecular Engineering, 12(2). (Extended abstract)

1 Contextual Statement

Significance of the project The significance of the project is defined by its theoretical impact and industrial application. The project aims to develop a novel mathematical model for the transport of multi-components colloids in porous media. This theoretical work encompasses derivation of micro-scale population balance equations, upscaling and analytical solution for one-dimensional colloidal transport. The proposed analytical model is capable of promoting the formulation of inverse problems for treatment of the laboratory data. The theoretical results are applicable in various areas of suspension, colloidal, and ionic transport in porous rocks and materials.

The industrial impact includes the development of practical mathematical models for cotransport of colloids and nanoparticles. The model can be applied in various technologies where nano-particles affect and control natural colloidal and suspensions flows. Another significant industrial application includes well injectivity during the injection of poor quality water.

The above mentioned theoretical and practical developments are recommended for applications in diverse industrial processes e.g., in chemical and environmental engineering for physical and chemical treatments and filtration processes (Fogler, 2016; Harter et al., 2000), evaluation of viruses and bacteria propagation in sub-terrain reservoirs (Albinger et al., 1994; Asraf-Snir and Gitis, 2011; Bolster et al., 1999; Gitis, 2013); in petroleum engineering for water injection to maintain the reservoir pressure (Bedrikovetsky et al., 2012; Guedes et al., 2006), fines detachment and migration (Chequer et al., 2019; Oliveira et al., 2014), fixation of clays (Yuan and Moghanloo, 2018; Yuan and Wang, 2018); among others.

State of the art During the last three decades, theory of colloidal and suspension transport in porous media has been significantly transformed and extended if compared with the traditional fluid mechanics of multi-components hydrodynamics in porous media (Bedrikovetsky, 2008; Bedrikovetsky et al., 2017; Shapiro and Yuan, 2012b; Shapiro, 2007; Yuan and Shapiro, 2011). This development has been stimulated by growing environmental restrictions posed upon numerous chemical, environmental, civil, petroleum, and agriculture engineering technologies (Chrysikopoulos et al., 2009; Chrysikopoulos and Syngouna, 2014; Kim et al., 2009). The above-mentioned developments include mathematical models of suspension and colloidal transport on the pore scale, created in the framework of computation of fluid mechanics and statistical physics, multi-scale flow equations, formulations of laboratory tests, their interpretation, and laboratory-based three-dimensional simulation for field-scale predictions.

However, several mathematical models for significant processes have not been developed and are unavailable in the contemporaneous literature. Regarding the current thesis, the list of theoretical problems that have not been solved in the contemporaneous literature is detailed as follow:

1. The suspension transport equations that capture stabilization of breakthrough curves at the concentration which is below the injected value have not been derived;

2. The equations for cotransport of two species, like colloids and nano-particles, or colloids and surfactants, or a general form of binary flow account for two capture mechanisms for each population with a few empirical constants allowing for effective matching of the laboratory data are not available;

3. Transport of colloids with distributed particle properties includes as many equations as many digital points that approximate the distribution histogram, which makes the model

extremely cumbersome, computed time consuming, and not suited to history matching. An upscaled model for multi-properties colloids flows in porous media that allows for an exact solution is not available in the literature;

4. A simple extension of the traditional model for deep bed filtration that reproduces hyper-exponential retention profiles is not available;

5. A simple generalization of the traditional deep bed filtration model that capture non-monotonic behaviour of the retention profiles is not available;

6. A robust and reliable mathematical method to predict injection well behaviour during injection of low-quality water, with distributed particle properties, is not available.

The above mentioned scientific and research problems, which have not been solved currently, have been highlighted in numerous publications. The current thesis proposes a novelty and scientific explanation, besides the mathematical model for each problem listed above.

Scope of the work The main achievements of the thesis are listed below:

1. Suspension transport equations that capture stabilization of breakthrough curves, at the concentration below the injected value have been derived and used to tune several laboratory data that shows this trend;

2. The equations for cotransport of two particle-species, like colloids and nano-particles, or colloids and surfactants, or a general form for binary flow accounting for two capture mechanisms, for each particle population, have been derived and several laboratory data have been successfully tuned;

3. The equations for transport of colloids with distributed particles properties have been derived and upscaled from fundamental physics and deep bed filtration theory and, they also have been used to match numerous laboratory data that show particles properties variation;

4. An extension of the traditional deep bed filtration model that reproduces hyper-exponential retention profiles has been proposed and analytically derived and, it has also been used to tune various coreflood experiments that show hyper-exponential retention profiles;

5. A generalization of the traditional model for deep bed filtration that exhibits non-monotonic behaviour of retention profiles has been analytically derived and, a novel explanation for the non-monotonicity has been proposed;

6. A robust and reliable mathematical method to predict well injection behaviour during injection of low-quality water with distributed particle properties has been developed and, it has been used to predict well injectivity and formation damage zone.

1.1 Thesis Structure

This is a PhD thesis by publication. Seven journal papers are included in the thesis, of which five papers have been published in peer-reviewed journals and one has been submitted to an academic journal and is currently under review, and another one is in the final stage to be submitted to a peer-reviewed journal.

The thesis body is organized in eight Chapters. The *first chapter* presents an introduction of the importance of the work for environmental, chemical, civil and petroleum engineering processes. The *second chapter* contains a critical literature review on modelling and experimental procedures of transport and cotransport of nano- and colloidal suspension particles in porous media. *Chapters three*, *four*, *five*, *six* and *seven* are the novelty and original parts of this thesis. The thesis summary and the main conclusion during the research period are presented in *Chapter eight*.

The third chapter discusses the exact analytical solution for the non-linear 1D problem system of suspension-colloidal flow in porous media with two particle-capture mechanisms. It also presents a mathematical proof that any quantity of capture mechanisms can be aggregated

into one mechanism. Based on the same principle this chapter also develops a model for cotransport of colloids and nanoparticles in porous media under two-particle capture mechanisms for each particle population.

The fourth chapter derives the exact solutions for continuous injection of colloidal suspension distributed by properties, for migration of reservoir fines induced by high-flow-rates. This chapter also discusses colloidal-nano flow with particle attachment probability, where the filtration coefficients and area occupied by a particle on the grain surface are stochastically distributed.

The fifth chapter presents an extension of the traditional deep bed filtration model for suspended particle transport to match hyper-exponential retention profiles, assuming a single-particle capture mechanism. Moreover, this chapter discusses a different approach for deep bed filtration model to fit hyper-exponential retention profiles considering two-capture mechanisms and high-colloidal injection concentration.

The sixth chapter provides a new phenomenological explanation for non-monotonic retention profiles and the derivation of an exact analytical model to predict non-monotonic retention profiles based on the heterogeneity of colloidal particle properties.

Subsequently, the seventh chapter presents the upscaled procedure for axi-symmetric transport of suspension-colloidal-nano with size-distributed colloids in porous reservoirs and validates the proposed one-dimensional mathematical model with different experimental corefloods data that shows non-monotonic post-mortem retention profiles. The tuned parameters of the linear model are used to predict non-monotonic behaviour of the particle retention profiles in radial coordinates, followed by a prediction of damaged zone and well injectivity decline during suspension injection, which is important for well stimulation design.

Chapter	Paper	Title	Status
Chapter 3	1	Exact solutions for suspension-colloidal transport with multiple capture mechanisms	Published
	2	Cotransport of Suspended Colloids and Nanoparticles in Porous Media	Published
Chapter 4	3	Exact Upscaling for Transport of Size- Distributed Colloids	Published
Chapter 5	4	A modified model for colloidal transport to match hyper-exponential particle retention	Submitted for publication
	5	Transport of high-concentration colloids with two particle-capture mechanisms	To be submitted
Chapter 6	6	Explaining non-monotonic retention profiles during flow of size-distributed colloids	Published
Chapter 7	7	Non-monotonic retention profiles during axi-symmetric colloidal flows	Published

1.2 How the Publications are related to the Thesis

The paper "Exact solutions for suspension-colloidal transport with multiple capture mechanisms" derives a new non-linear mathematical model for colloidal transport in porous media. The paper considers two-particle retention mechanisms for one-dimensional problem and shows mathematically that, any number of capture mechanisms can be aggregated into a single capture retention. The two mechanisms used in this paper were Langmuir's blocking and constant filtration functions. The results of the exact analytical model exhibit breakthrough curves that asymptotically grow after the breakthrough and, stabilizes to a value lower than the injected concentration. The model successfully matches several experimental data.

The previously derived two-capture mechanisms model, in the first paper, is used in the paper "Cotransport of Suspended Colloids and Nanoparticles in Porous Media", to match the

transport of colloids and nano-particles, separately. In addition, the paper presents a novel model for cotransport of colloids and nano-particles where the new filtration function incorporates two simultaneous retention mechanisms (Langmuir's blocking and constant function) for each particle population. The cotransport model successfully matches two breakthrough curves for each particle population, simultaneously. The proposed cotransport model shows good agreement with the laboratory data available in the literature, by fitting only two model parameters, which validates the model.

In order to study the transport of particles distributed by properties accounting for particle capture by the porous media, the paper "Exact Upscaling for Transport of Size- Distributed Colloids" develops an upscaled procedure to convert micro-scale system in an averaged-system. The micro-scale system contains two governing equations for particle conservation law and kinetics of particle attachment, while the averaged system consists of three equations for particle conservation law and kinetics of particle attachment and vacancies occupation. The upscaled particle kinetics is proportional to $f(c)$ which is the suspension function. The suspension function – $f(c)$ is derived from individual suspension functions of each particle population at the micro-scale. The upscaled model presents 3×3 system of equations, while the traditional deep bed filtration model presents 2×2 system of equations; however, the upscaled model degenerates into the traditional deep bed filtration model, for the case where different attached particles occupy the same vacancy area into the porous media. The upscaled 3×3 system allows for exact solutions for the case where it is assumed Langmuir (blocking) filtration function. The paper also presents the upscaled equations for binary colloidal-suspension system, which is used to math several laboratory data on colloidal and nanoparticle injections into porous columns, while the traditional deep bed filtration model exhibits significant deviation.

Sequentially, in the paper "A modified model for colloidal transport to match hyper-exponential particle retention" a new and simple model that allows for an exact solution is proposed to fit several colloidal transport experiments that exhibit hyper-exponential retention profiles. The paper proposes a modification of the traditional deep bed filtration model analogous to active mass law for chemical reactions. The proposed model uses a one-parametric exponential-quadratic suspended function, which successfully matches, simultaneously, breakthrough curves and retention profiles that present hyper-exponential behaviour. The validation of the model is claimed due to the closely matching and prediction of several laboratory data, where the number of degrees of freedom of the experimental data array exceeds the number of model coefficients. However, the "A modified model for colloidal transport to match hyper-exponential particle retention" accounts just for a single capture mechanism. In order to fit experiments that present two-particle capture mechanisms for high suspension-colloidal injection concentration, the paper "Transport of high-concentration colloids with two particle-capture mechanisms" derives a semi-analytical model for the same one-parametric exponential-quadratic suspension function. The two-capture mechanisms used in this paper are Langmuir's blocking and constant filtration functions. The proposed model shows excellent agreement with numerous experimental data that shows breakthrough curves that asymptotically grow until they stabilise at a value that is below the injected concentration and hyper-exponential retention profiles.

In the paper, "Explaining non-monotonic retention profiles during flow of size-distributed colloids", it is discussed multi-component colloidal transport in porous media that considers pore accessibility and consequent flux reduction, slow particle motion, adsorption, and detachment-free. The kinetic of particle-capture is a function of the vacant area for attachment to the grain surface (Langmuir's blocking). The upscaled procedure is developed based on the

micro-scale population-balance equations resulting in the mass balance and kinetics equations for averaged concentrations. The proposed model allows for analytical solution and exhibits non-monotonic retention profile. The upscaled binary-colloid model successfully fits numerous sets of experiments. Furthermore, the dimension of the measured data array exceeds the number of tuned parameters, which validates the model. The tuned model coefficients are used to perform downscaling and determine the individual properties for each particle population. Following the same topic, the paper "Non-monotonic retention profiles during axi-symmetric colloidal flows" derives the upscaled 1D model for radial flows allowing prediction of the well injectivity decline using the tuned laboratory-based model parameters. This paper predicts non-monotonic retention profiles in reservoir scale and formation damage zone for this scenario.

Finally, the above mentioned seven journal papers present the mathematical modelling and the analytical solution for multi-component one-phase flow in porous media, accounting for the distribution of properties of particles, high concentration of colloidal suspensions and new physics explanation for colloidal and suspension-nano flow in porous material.

1.3 References

Albinger, O., Biesemeyer, B.K., Arnold, R.G., Logan, B.E., 1994. Effect of bacterial heterogeneity on adhesion to uniform collectors by monoclonal populations. FEMS Microbiol. Lett., 124(3): 321-326.

Asraf-Snir, M., Gitis, V., 2011. Tracer studies with fluorescent-dyed microorganisms—A new method for determination of residence time in chlorination reactors. Chem. Eng. J., 166(2): 579-585. DOI:https://doi.org/10.1016/j.cej.2010.11.027

Bedrikovetsky, P., 2008. Upscaling of stochastic micro model for suspension transport in porous media. Transp. Porous Med., 75(3): 335-369.

Bedrikovetsky, P., You, Z., Badalyan, A., Osipov, Y., Kuzmina, L., 2017. Analytical model for straining-dominant large-retention depth filtration. Chem. Eng. J., 330: 1148-1159.

Bedrikovetsky, P., Zeinijahromi, A., Siqueira, F.D., Furtado, C.A., de Souza, A.L.S., 2012. Particle detachment under velocity alternation during suspension transport in porous media. Transp. Porous Med., 91(1): 173-197.

Bolster, C.H., Mills, A.L., Hornberger, G.M., Herman, J.S., 1999. Spatial distribution of deposited bacteria following Miscible Displacement Experiments in intact cores. Water Resour. Res., 35(6): 1797-1807. DOI:10.1029/1999wr900031

Chequer, L., Bedrikovetsky, P., Carageorgos, T., Badalyan, A., Gitis, V., 2019. Mobilization of Attached Clustered Colloids in Porous Media. Water Resour. Res., 55(7): 5696-5714. DOI:10.1029/2018wr024504

Chrysikopoulos, C.V., Masciopinto, C., La Mantia, R., Manariotis, I.D., 2009. Removal of biocolloids suspended in reclaimed wastewater by injection into a fractured aquifer model. Environ. Sci. Technol., 44(3): 971-977.

Chrysikopoulos, C.V., Syngouna, V.I., 2014. Effect of gravity on colloid transport through water-saturated columns packed with glass beads: Modeling and experiments. Environ. Sci. Technol., 48(12): 6805-6813.

Fogler, S.H., 2016. Elements of chemical reaction engineering. Prentice Hall.

Gitis, V., 2013. Dyed viruses and metal particles for advanced separation studies. Journal of Water Supply: Research and Technology-Aqua, 63(5): 325-331. DOI:10.2166/aqua.2013.204

Guedes, R.G., Al-Abduwani, F.A., Bedrikovetsky, P.G., Currie, P.K., 2006. Injectivity decline under multiple particle capture mechanisms, SPE international symposium and exhibition on formation damage control. Society of Petroleum Engineers.

Harter, T., Wagner, S., Atwill, E.R., 2000. Colloid Transport and Filtration of Cryptosporidium parvum in Sandy Soils and Aquifer Sediments. Environ. Sci. Technol., 34(1): 62-70. DOI:10.1021/es990132w

Kim, H.N., Bradford, S.A., Walker, S.L., 2009. Escherichia coli O157: H7 transport in saturated porous media: Role of solution chemistry and surface macromolecules. Environ. Sci. Technol., 43(12): 4340-4347.

Oliveira, M.A. et al., 2014. Slow migration of mobilised fines during flow in reservoir rocks: laboratory study. Journal of Petroleum Science and Engineering, 122: 534-541.

Shapiro, A., Yuan, H., 2012. Application of stochastic approaches to modelling suspension flow in porous media, Statistical Mechanics and Random Walks: Principles, Processes and Applications. Nova Science Publishers.

Shapiro, A.A., 2007. Elliptic equation for random walks. Application to transport in microporous media. Physica A: Statistical Mech. its Applic., 375(1): 81-96.

Yuan, B., Moghanloo, R.G., 2018. Nanofluid pre-treatment, an effective strategy to improve the performance of low-salinity waterflooding. Journal of Petroleum Science and Engineering, 165: 978-991. DOI:https://doi.org/10.1016/j.petrol.2017.11.032

Yuan, B., Wang, W., 2018. Using nanofluids to control fines migration for oil recovery: Nanofluids co-injection or nanofluids pre-flush?-A comprehensive answer. Fuel, 215: 474-483.

Yuan, H., Shapiro, A.A., 2011. A mathematical model for non-monotonic deposition profiles in deep bed filtration systems. Chem. Eng. J., 166(1): 105-115.

2 Literature Review

2.1 Introduction

The prediction of colloidal suspension and nanoparticles transport and deposition in porous media has become very relevant for different applications ranging from optimization of natural granular filter for water treatment (Gitis et al., 2011), remediation of natural reservoir clays detachment (Arab and Pourafshary, 2013; Yuan et al., 2016), colloidal-facilitated contaminant transport (Chrysikopoulos et al., 2009), to petroleum production and well injectivity (Bedrikovetsky, 2013; Guedes et al., 2006). The understanding of fate and transport of nano- and micro-particles that have unique structure and, incomparable physical and chemical properties have been aimed by many research groups (Bradford et al.; Johnson et al.; Shapiro; Tufenkji and Elimelech) in order to propose mathematical models able to predict and evaluate the behaviour of these particles, that differ from the conventional (traditional) deep bed filtration theory.

This chapter introduces the critical contemporaneous literature review for mathematical models of colloidal and suspension-nano flow in porous media. Section 2.2.1 presents a brief literature review for multiple particle capture mechanisms in porous media for a single particle population, while Section 2.2.2 shows a cotransport of the binary colloidal mixture. In section 2.2.3, it is presented an extensive literature review for mathematical models of multi-component suspension-colloidal transport in porous media. Following this structure, section 2.2.4 presents the available models to match hyper-exponential retention profiles, and finally, section 2.2.5 finalizes this chapter showing mathematical models and physical explanation for non-monotonic retention profiles available in the contemporaneous literature.

2.2 Multiple mechanisms of particle retention in porous media

Transport of nanoparticles and colloidal-suspension in porous media occur in numerous important natural and engineering processes, including disposal of industrial waste in aquifers, injection of cold water in geothermal reservoirs, plant irrigation, groundwater contamination, management of potable water, and water injection in oil filed for pressure maintenance (Bradford et al., 2013; Bradford et al., 2002; Chrysikopoulos et al., 2017; Katzourakis and Chrysikopoulos, 2015; Mikhailov et al., 2018; Sotirelis and Chrysikopoulos, 2017). The development of mathematical modelling is of great importance to design and plan several of the technological processes previously mentioned.

During suspension-colloidal flows, the interaction between particles and rock can occur by several capture mechanisms, as attachment, straining, size exclusion, segregation, diffusion into dead-end pores, bridging etc., as shown in Fig.1 (Bedrikovetsky, 2008; Bradford et al., 2013; Bradford et al., 2002; Chen and Bai, 2015; Chequer et al., 2017; Elimelech et al., 2013; Guedes et al., 2006; Katzourakis and Chrysikopoulos, 2014). The particle retention via any of the mechanisms cited above decreases suspension concentration and can cause severe permeability declining. The prediction and understanding of retention of suspension concentration are important for industrial waste disposal, propagation of virus and bacteria into aquifers (Bekhit et al., 2009; Gitis, 2013; Li and Johnson, 2005), while the formation damage due to permeability decline is important for production and injection wells (Alvarez et al., 2007; Chequer et al., 2017; Mikhailov et al., 2018).

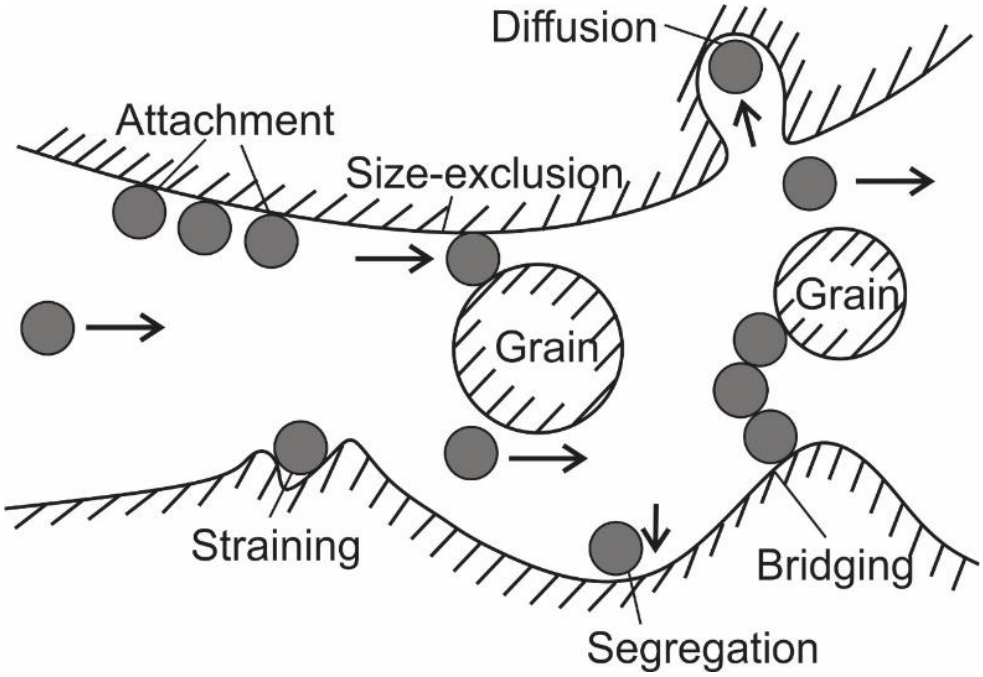


Figure 1 Multiple capture-mechanisms in a single pore (Zhang et al., 2018)

The mathematical model for deep bed filtration (DBF) in porous media is composed by mass balance for suspended and retained particles, and particle capture rate that is proportional to the particle advective flux, and Darcy's law accounting for permeability decline due to particle retention (Bai et al., (2017); Bedrikovetsky, 2008; Bedrikovetsky, 2013; Polyanin and Zaitsev, 2012; Polyanin and Manzhirov, 2006):

$$\frac{\partial}{\partial t}\left(\phi c + s\right) + U\frac{\partial c}{\partial x} = \frac{\partial}{\partial x}\left(D\frac{\partial c}{\partial x}\right) \tag{2.1}$$

$$\frac{\partial s}{\partial t} = h\left(s\right)cU \tag{2.2}$$

$$U = -\frac{k\left(s\right)}{\mu\left(c\right)}\frac{\partial P}{\partial x} \tag{2.3}$$

where t [T] is the time, x [L] is the Cartesian coordinate in the flow direction, c [NL^{-3}] is the suspended concentration, s [NL^{-3}] is the attached concentrations, ϕ is the porosity, U [LT^{-1}] is the fluid velocity, D [L^2T^{-1}] is the dispersion (diffusion) coefficient, h [L^{-1}] is the filtration

function, k [L] is the permeability, μ [$ML^{-1}T^{-1}$] is the viscosity, and p [$MT^{-2}L$] is the pressure across the core. Here, the suspension concentration c is defined as the number of suspended particles in a unitary volume of carrier fluid, while the retained concentration s is determined as the number of attached particles in a unitary volume of the rock.

Injection of constant particles concentration into clean porous media corresponds to the following initial and boundary conditions:

$$t = 0: \; c = s = 0 \tag{2.4}$$

$$x = 0: \; c = c^0 \tag{2.5}$$

The initial condition defined by Eq. (2.4) holds as the length of the porous media/reservoir tends to infinity.

In general, the retention rate equation for particle capture is proportional only to Darcy's velocity, however, depending on the suspension properties and flow velocity, the retention rate is proportional to the total particle flux q, which accounts for the total flux (summing of diffusive and advective fluxes) (Bai et al., (2017); Bedrikovetsky et al., 2006; Chen and Bai, 2015):

$$\frac{\partial s}{\partial t} = h(s)q, \quad q = cU - D\frac{\partial c}{\partial x} \tag{2.6}$$

In this scenario, dispersivity has an important role in particle capture. The difference between capture scenarios described by Eq. (2.2) and Eq. (2.6) is shown in Fig. 2. The vertical line represents a sieve-screen where particle capture can be captured. Eq. (2.2) represents the scenario where the particle is retained during the advective process (Fig. 2a), while Eq. (2.6) corresponds to the diffusive process (Fig. 2b) (Bedrikovetsky et al., 2006). In order to evaluate if the particle capture needs to account for diffusive flux, the ratio between the advective and

dispersive fluxes, defined as Peclet number, is an important evaluation condition. In large-scale approximation, where the typical reservoir length exceeds 100m, Peclet number considerably exceeds one, $UL/D>>1$, and the diffusion terms are neglected in both Eqs. (2.1) and (2.6).

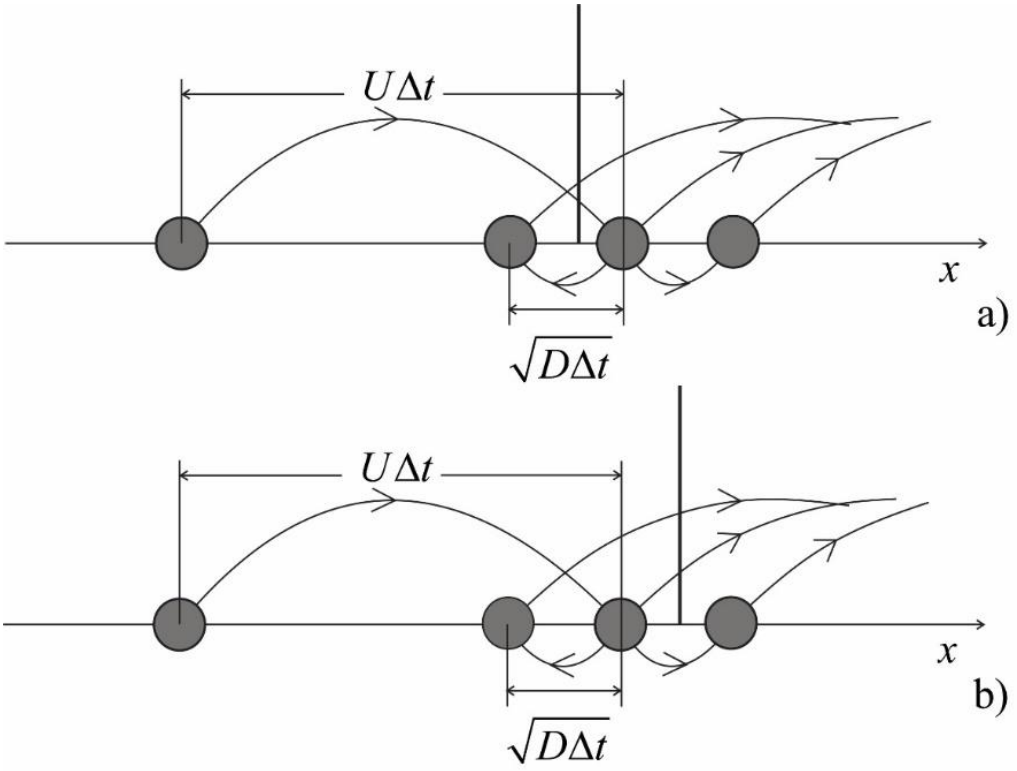


Figure 2 Classical and modified models for particle capture by the porous media, where the vertical bar corresponds to the capture site: (a) particle capture from the advective flux; (b) particle capture from the overall advective and diffusive flux (Zhang et al., 2018).

However, during laboratory experiments, where the typical core length is 0.1m, Peclet number can approximate to unity or even be lower than one, therefore, in this scenario, the diffusive flux becomes important, and Eq. (2.6) needs to be used (Bai et al., (2017); Bedrikovetsky et al., 2006; Chen and Bai, 2015).

The retention rate also accounts for suspension function *h(s)* that depends on particle retention and, it can assume different forms according to the particle capture mechanisms (Bedrikovetsky, 2013; Bedrikovetsky et al., 2006). One of the most common suspension functions used in the literature is Langmuir's blocking function, where it assumes monolayer

attachment, where one attached particle occupies one vacancy, and vice versa. This assumption can easily be compared with the "active-mass" law for the particle-vacancy "reaction" (Herzig et al., 1970; Khilar and Fogler, 1998; Polyanin and Zhurov, 2014):

$$h(s)=\begin{cases}\lambda_0\left(1-\dfrac{s}{s_m}\right), & s<s_m\\ 0, & s>s_m\end{cases} \tag{2.7}$$

where s_m is defined as the maximum number of retention vacancies per unitary volume that a particle can occupy by the attachment process.

The process described by Langmuir blocking filtration function, given by Eq. (2.7), is usually referred to as a monolayer of electrostatically attached particles on the rock surface. However, this function can also be applied for straining and size exclusion, where the pore throats are the vacancy spaces (Elimelech et al., 2013; Herzig et al., 1970; Khilar and Fogler, 1998). The shape of the Langmuir filtration function is presented in curve 2 in Fig. 3a. Curve 2 in Fig. 3b shows the breakthrough of the analytical solution of the 1D flow problem given by Eqs. (2.1-2.5), considering free diffusive processes. As shown in Fig. 3b, the particle suspension concentration at the outlet of the core is zero before the breakthrough, and then jumps up to some value at the moment when one pore volume is injected, and then tends asymptotically to the injected concentration when the injection time tends to infinity (Herzig et al., 1970).

When the maximum number of retention vacancies is much larger than the retained concentration ($s<<s_m$), the filtration function is assumed as a constant filtration coefficient, $h(s)=\lambda_1$, represented by the straight line, curve 1, in Fig. 3a. For this particular case, the problem given by Eqs (1-5) also presents an exact solution. Fig. 3b, curve 1 shows that after the breakthrough (at one pore volume injected) the suspension concentration jumps up to some

value and remains constant during the overall injection period (Herzig et al., 1970). These types of breakthrough behaviour have been observed for several capture mechanisms and, discussed in various laboratory experiments (Bradford et al., 2013; Bradford et al., 2002; Chrysikopoulos et al., 2017; Katzourakis and Chrysikopoulos, 2014; Katzourakis and Chrysikopoulos, 2015; Mirabolghasemi et al., 2015).

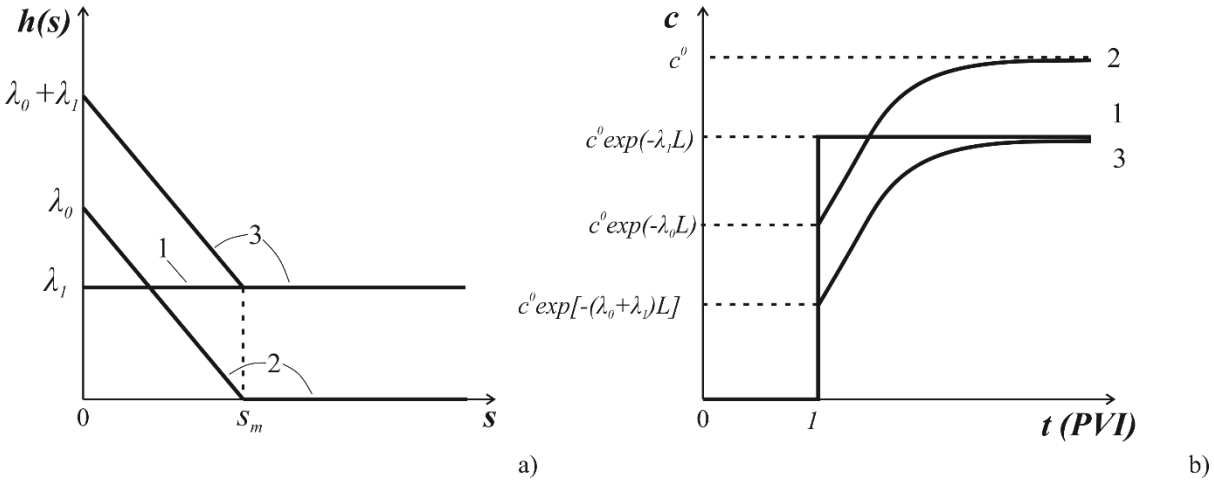


Figure 3 Forms of breakthrough curves for different forms of filtration function: a) filtration functions; b) breakthrough curves. Here 1 – constant filtration function, 2 – Langmuir (blocking) filtration function, and 3 is the binary filtration function (Zhang et al., 2018).

Moreover, numerous laboratory observations show a breakthrough curve that is equal to zero before the breakthrough moment, jumps up to some value and then, tends to a limit lower than the injected concentration as time tends to infinity (Araújo and Santos, 2013; Bai et al., (2017); Bradford et al., 2013; Chen and Bai, 2015; Chequer et al., 2017; Chrysikopoulos et al., 2017; Elimelech et al., 2013; Khilar and Fogler, 1998; Kuzmina and Osipov, 2014). However, this particular behaviour of breakthrough curves has not been analysed by different capture kinetics or in terms of an exact analytical mathematical model. Besides, a filtration function that produces the behaviour described by Fig. 3 is not available.

As mentioned before, the particles present in the suspension-colloidal flow in porous media can be captured by different mechanisms (Fig. 1). Each capture-mechanism depends on

porous media and particle properties like pore throat, surface charge, roughness, tortuosity, particle sizes, etc, and all these parameters are stochastically distributed. The stochastic models for transport of particles in porous media contain random-walk equations (Shapiro, 2007; Yuan and Shapiro, 2012), Boltzmann's model (Shapiro and Wesselingh, 2008; Yuan and Shapiro, 2012), randomly distributed filtration coefficients (Elimelech et al., 2013; Yuan and Shapiro, 2012; Yuan and Shapiro, 2010), network and 3D computational fluid dynamics (CFD) models (Mirabolghasemi et al., 2015).

The population balance models take in account particle distribution in size, shape, surface charge, etc (Sharma and Yortsos, 1987a; Sharma and Yortsos, 1987b). These models also account for accessibility and inaccessibility of different pores due to geometric restrictions and the corresponding reduction of the overall particle (Bedrikovetsky, 2008; Santos and Bedrikovetsky, 2006). If the suspension is considered homogeneous, the population balance equations permit for exact averaging; the averaged equations coincide with the classical DBF system that contains accessibility and flux-reduction functions (Bedrikovetsky, 2008).

The inverse problems are well-posed by the exact solution of the DBF Eqs. (2.1-2.3). The breakthrough curve determines the filtration function given by Eq. (2.2), and the pressure drop history across the core is used to calculate the formation damage function given by Eq. (2.3) (Alvarez et al., 2007). It is also possible to determine the filtration function from retention profiles, and this method significantly decreases data scattering, if compared with breakthrough data (Alvarez et al., 2007).

Laboratory experiments can be qualitatively evaluated by exact analytical solutions of models, together with the interpretation of the model parameters. A comparison of the concentration waves calculated by the analytical models, with those measured during injection

of particles experiments or, even with field tests, yields a deeper understanding of the transport processes in porous media.

Several studies on suspension-colloidal flow have been used two-capture mechanisms models that accounted for attachment and straining to describe the retention of particle in porous media (Bradford et al., 2013; Bradford et al., 2002; Kuzmina and Osipov, 2015; Yuan and Shapiro, 2011). There are some models available in the literature that consider BDF of a mixture of two distinct particle populations, where each particle population is captured by its own separate capture mechanism. These models allow for an exact solution and they present high-quality match using both, constant and Langmuir's filtration functions (Araújo and Santos, 2013). Models that account for two-particle-population and two-capture-mechanism have also been obtained (Kuzmina et al., 2017; Kuzmina et al., 2018). However, exact analytical solutions for homogeneous particles and, for two simultaneous capture mechanisms, are not available.

In the current thesis, the non-linear 1D problem for suspension-colloidal transport in porous media with, two simultaneous particle capture mechanisms, is presented in Chapter 3.

2.3 Cotransport of colloids with multiple capture mechanisms

The detachment and transport of natural fines in reservoirs have been widely studied (Civan, 2015). However, the increasing disposal of engineered particles in aquifers and in the environment, in general, has become a challenge in the last decade (Chrysikopoulos et al., 2017; Liang et al., 2013a; Tufenkji and Elimelech, 2005a). Several types of clay colloids are frequently present in various occasions of groundwater contamination, filtration invasion into reservoir formation due to well drilling, cold-water injection in geothermal formations, low-salinity water injection into oil- and gas- fields, etc. (Bai et al., 2017; Farajzadeh et al., 2017;

Mikhailov et al., 2018; You et al., 2015). Usually, clays are adhered to the rock surface by the mechanical equilibrium of forces acting on the body of the clay. The mechanical equilibrium is described by the torque balance of the most relevant forces acting on the particle as shown in Fig. 4 (Bedrikovetsky et al., 2011; Chequer et al., 2017; Muecke, 1979; Russell et al., 2018).

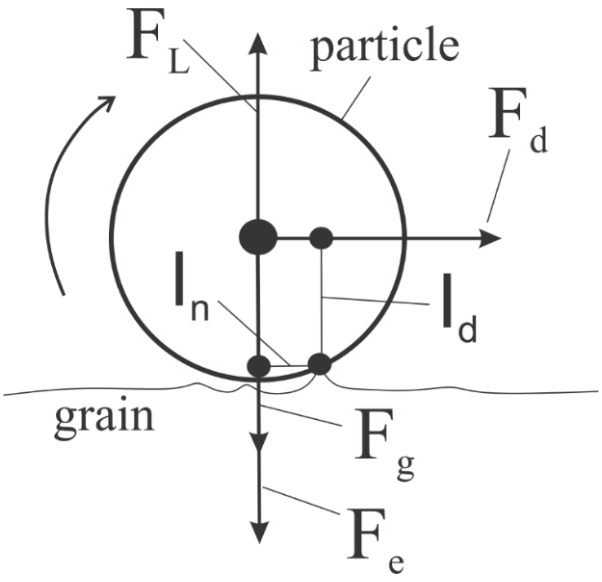


Figure 4: Mechanical Equilibrium of attached and detached forces acting on a single particle. The forces acting on the particles are electrostatic, gravity, lift and drag forces (F_e, F_g, F_L, and F_d) and lever arms l_n and l_d for the attached particle (Russell et al., 2018).

Different engineered nanoparticles have been used in several applications including the water purification, biochemical processes, fixing movable fines in oilfields for formation damage inhibition (Arab et al., 2014; Chrysikopoulos et al., 2017; Yuan and Moghanloo, 2017; Yuan et al., 2016), and enhanced oil recovery by injection of nanofluids (Arab and Pourafshary, 2013). The transport of nanoparticles in porous media is relatively complex, because it can be affected by several external factors including temperature, flow velocity, the presence of organic matters, solution chemistry, and the presence of different suspended colloids (Klaine et al., 2008; Rottman et al., 2013; Syngouna et al., 2017).

There are numerous deterministic and stochastic mathematical models to describe particle transport, capture and the alteration of rock structure. Shapiro and Yuan (2012a) and

Yuan et al. (2012) have provided a reasonably review of the available stochastic models, described by population balance equations (Bedrikovetsky et al., 2017; Santos and Bedrikovetsky, 2006; Sharma and Yortsos, 1987b), random walk models (Shapiro, 2007; Yuan et al., 2012), DBF equation with stochastically distributed filtration coefficient (Elimelech et al., 2013; Yuan and Shapiro, 2010), and Boltzmann's equation (Shapiro and Wesselingh, 2008). Mathematical models that account for population balance, with a probabilistic distribution of particles and pore properties, allow for exact analytical upscaling for suspensions of uniform size, and the system of equations coincides with the traditional filtration theory for the averaged values (Bedrikovetsky, 2008; Hammadi et al., 2017).

Numerous mathematical models for deep bed filtration of homogenous colloids (transport) and particle mixtures (cotransport) are available in the literature (Abdel-Salam and Chrysikopoulos, 1995; Bekhit et al., 2009; Katzourakis and Chrysikopoulos, 2014; Katzourakis and Chrysikopoulos, 2015). The general assumptions of the available models are proportionality between the particle capture rate and the advective particle flux.

Araújo and Santos (2013) developed an analytical model for deep bed filtration of a binary colloidal mixture, where each particle is captured by its separate capture mechanism. The model assumes either constant or Langmuir's filtration functions. However, recent studies have demonstrated that for clay-particle and some engineered NP cotransport, the attachment capture can be simultaneous for both suspended colloids as shown in Fig. 5 (Chrysikopoulos et al., 2017; Sotirelis and Chrysikopoulos, 2017).

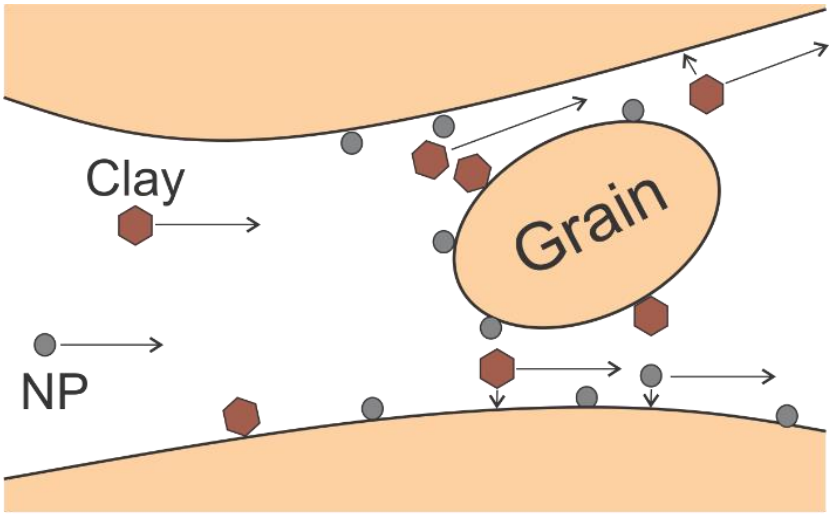


Figure 5: Attachment and straining capture mechanisms for cotransport of nano- and clay particles.

Several authors have proposed mathematical models that divide the particle population depending on particle velocities (Bradford et al., 2009b; Kuzmina et al., 2017; Yuan and Shapiro, 2010). It is claimed that suspended colloids near rough rock surface travel with significantly smaller velocity than the mean interstitial flow velocity (Sefrioui et al., 2013). On the other hand, Yuan et al. (2016), Yuan and Moghanloo (2017) and Yuan and Wang (2018) have developed mathematical models for clays and nanoparticles cotransport accounting for adsorption of nanoparticles on clays surface as well as on rocks surface, as the main capture mechanism. However, a mathematical model that describes colloids and nanoparticles cotransport, with simultaneous attachment and straining/size exclusion of both particles-species population, is not available. In this thesis, Chapter 3 presents a new mathematical model for cotransport of a binary colloid mixture with two-capture mechanisms, where the novel filtration function incorporates two simultaneous capture mechanisms: Langmuir (blocking) and constant (low-retention) filtration of each particle-population.

2.4 Mathematical modelling of multi-component suspension-colloidal transport in porous media

The properties of suspension, colloids, and nanofluids during flow in porous media can vary by orders of magnitude depending on different factors (Arab and Pourafshary, 2013; Liang et al., 2013b). The development of stochastic models to account for all different populations and their properties are very complex and cumbersome (Bedrikovetsky et al., 2019). Therefore, the main aim is on solving non-steady-state one-dimensional (1D) problems of either injection of dirty water (with heterogeneous particle population) in groundwater, or detaching, mobilization and migration of natural clays originally from the reservoir. The mathematical solution is applicable in numerous areas as propagation of bacteria and viruses in subterranean waters, exploitation of geothermal wells, re-injection of water produced from oilfields, migration of natural reservoir clays, and others (Bradford et al., 2011a; Bradford et al., 2011b; Chrysikopoulos and Syngouna, 2012; Chrysikopoulos et al., 2012; Elimelech et al., 2013; Rosenbrand et al., 2015).

Each particle population presents its own properties, and it may directly affect the physical particle capture mechanisms (Bradford et al., 2009a; Bradford et al., 2003; Mirabolghasemi et al., 2015; Yuan and Shapiro, 2012). During suspension-colloidal flows in porous media, the most common particle capture mechanisms are size exclusion, straining, attachment, segregation, adsorption, diffusion into dead-end pores, bridging, incomplete plugging and consequently internal cake, etc. Nonetheless, these mechanisms may boost as the suspension becomes more heterogeneous as shown in Fig. 6 (Bradford and Torkzaban, 2015; Bradford et al., 2015; Chrysikopoulos et al., 2017; Chrysikopoulos and Syngouna, 2012; Civan, 2015; Winter and Tartakovsky, 2002).

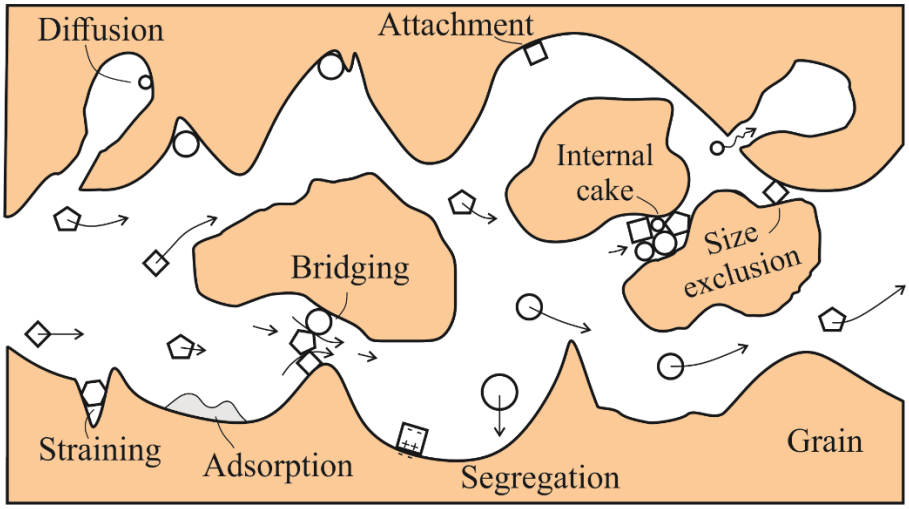


Figure 6: Conceptual schematic for multi-colloidal population transport with different particle capture mechanisms in pore space.

Frequently, the assumption of filtration function *h(s)* in Eq. (2.2) is monolayer Langmuir's blocking attachment (Eq. (2.7)), where one attached particle occupies one available free space on the rock surface. This assumption is analogous to the "active-mass" law where the particles and the rock-vacancy are seen as "reactants" (Elimelech et al., 2013). Other common assumptions are small suspended and attached concentrations. These assumptions lead to the retention rate to be proportional to the suspended concentration *c* (Eq. (2.2)) (Elimelech et al., 2013). However, for large suspended and vacancy concentrations, the monolayer Langmuir's blocking attachment assumption and suspended concentration *c* in Eq. (2.2) are substituted by their non-linear functions, similar to the large concentrations of reacting species are replaced by their activities coefficients in the active mass law

$$\frac{\partial s}{\partial t} = h(s)\, f(c) U \qquad (2.8)$$

The derivation of extended equation (2.8) was not developed from either first principles or micro-scale mechanics, however, it has been used just for matching purposes of the laboratory data (Bradford et al., 2015; Civan, 2015).

One-dimensional problem for linear suspension function - $f(c)=\lambda c$ and for any arbitrary filtration function *h(s)* allow for exact analytical solutions (Goldberg et al., 2014; Polyanin and Zaitsev, 2012; Polyanin and Manzhirov, 2006). Considering diffusion free, the 2×2 system (1, 2.8) determines suspended and retained concentrations *c* and *s*, and then the pressure *p(x,t)* is calculated from Eq. (2.3). It is possible the determination of the filtration function *h(s)* from inverse problems through analyses of breakthrough concentration *c(L,t)*, and formation damage function *k(s)* – from analyses of the pressure drop across the core $\Delta p = p(0,t)-p(L,t)$, where *L* is the core length (see Fig. 7). The inverse problems of both functions *h(s)* and *k(s)* are regularized by the exact analytical solutions (Alvarez et al., 2007). Well-posed inverse solutions combined with the exact analytical solutions permit designing laboratory tests for prediction of *h(s)* and *k(s)* from the experimental data (Vaz et al., 2017; Vaz et al., 2016). Both function *h(s)* and *k(s)* are affected by different parameters like particle size and shape, pore size distribution, z-potential of both grain and colloid surfaces, mineral composition of the rock, ionic composition of carrier fluid, etc. In an environmental- or even in some industrial-processes, the previously mentioned parameters can differ considerably by orders of magnitude and are randomly distributed at the micro-scale (Bradford et al., 2013; Brady et al., 2015; Elimelech et al., 2013; Yu et al., 2018).

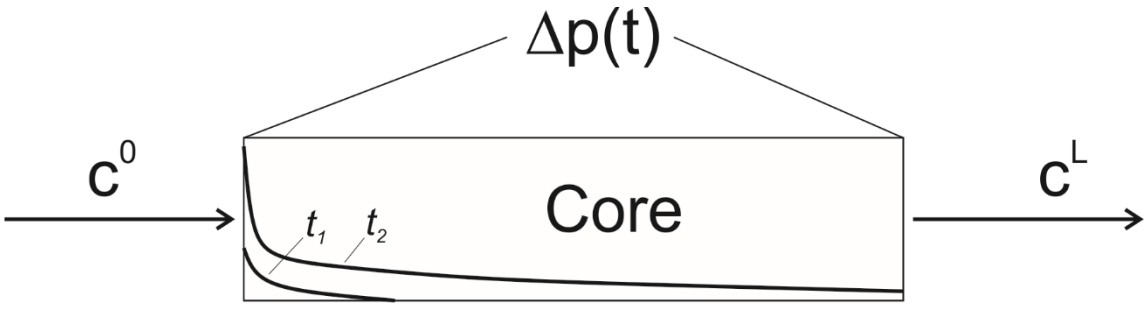


Figure 7: Schematic of the laboratory test on suspension-colloidal-nano flow in porous media where the pressure drop across the core and the retention profiles are monitored over time.

The micro-scale variation on suspension-colloidal transport in porous media can only be modelled by complex mathematical models that use pore-scale parameters. These models consider trajectory analysis (Payatakes et al., 1974), Navier-Stokes equations at the pore-scale and prediction of the filtration coefficient λ as a function of micro-scale factors (Bradford et al., 2011b; Tufenkji and Elimelech, 2004a), random-walk modelling applying the Master-equation (Shapiro and Yuan, 2012a; Shapiro, 2007; Yuan and Shapiro, 2012), Boltzmann's equation (Shapiro and Wesselingh, 2008) and population-balance modelling.

Several authors have proposed population-balance models that account for multiple capture mechanisms (attachment and straining), pore- and colloid-size distribution, pore network, permeability decline, inaccessibility of fractional pore and flow of particles, percolation due to size exclusion and incomplete pore-blocking/plugging. (Bedrikovetsky, 2008; Sharma and Yortsos, 1987a; Sharma and Yortsos, 1987b; Yuan et al., 2012).

The development of upscaling models that account for micro-heterogeneity during transport in porous media has significantly increased in the last two decades providing a better understanding and knowledge accumulation (Dagan et al., 2013; Tartakovsky et al., 2017).

For the particular case of diffusion free, the upscaling of population balance equations for homogeneous particles-size and size-exclusion retained mechanism generates the system of equations (2.1, 2.2) for deep bed filtration (Bedrikovetsky, 2008). Furthermore, as a result of the exact upscaling procedure, the exact analytical solution of the one-dimensional upper-scale system allows for downscaling (Bedrikovetsky et al., 2017). However, up to now, the upscaled equations that account for particles-size-distribution flow with attachment capture mechanism are not available in the literature. Chapter 4 presents the derivation of multiple-sized particles associated with particle retention by the rock. Therefore, this thesis fills the mentioned gap.

2.5 Hyper-exponential retention profiles – explanation and mathematical model

In the last twenty years, several laboratory experiments in transport of suspensions, colloids and nanoparticles have exhibit hyper-exponential retention profiles (Albinger et al., 1994; Jiang et al., 2012; Kasel et al., 2013; Li and Johnson, 2005; Li et al., 2004; Tong and Johnson, 2007; Tufenkji and Elimelech, 2005a; Tufenkji and Elimelech, 2005b; Wang et al., 2011; Wang et al., 2013). These profiles significantly differ from the traditional exponential retention profiles due to high particle retention near the core inlet followed by abrupt decreasing of particle retention after a small distance from the core inlet (Tong and Johnson, 2007; Yuan and Shapiro, 2010). The classical deep bed filtration model is not able to fit hyper-exponential profiles (Goldberg et al., 2014; Tufenkji and Elimelech, 2005a). Some authors have shown that the classical model (2.2), for $h(s)=\lambda_1$ highly disagrees with the retention concentrations measured in numerous experiments (Tufenkji and Elimelech, 2004b; Tufenkji and Elimelech, 2005a; Tufenkji and Elimelech, 2005b). In order to match hyper-exponential retention profiles, Tufenkji and Elimelech (2005b) considered the probabilistic distribution of the filtration coefficient. The proposed model accounts for bimodal distribution, where the particle population is divided into slow and fast captured rates due to unfavourable and favourable colloid-grain interaction. This model has successfully fitted several retention profiles using a total of five model parameters.

Schijven et al. (2002) proposed a two-kinetics site model to evaluate the different behaviour of breakthrough curves. The two-kinetics site model presents different rates of attachment and detachment that are explained by the surface charge heterogeneity of the porous media. Despite, Schijven et al. (2002) have successfully used two-kinetics model to tune and predict only breakthrough curves, Goldberg et al. (2014), in a critical review of mathematical models,

demonstrated that two-kinetics model can also predict hyper-exponential retention profile, however, does not match simultaneously breakthrough curves and retention profile. The governing equations for the two-kinetics model include advection-dispersion equation, reversible attachment/adoption for two types of kinetics sites, and inactivation of free and attached particle/virus/bacteria are presented below:

$$\frac{\partial c}{\partial t}+\frac{\rho_b}{\phi}\frac{\partial s_1}{\partial t}+\frac{\rho_b}{\phi}\frac{\partial s_2}{\partial t}=\alpha_L v\frac{\partial^2 c}{\partial x^2}-v\frac{\partial c}{\partial x}-\mu_1 c-\mu_{s1}\frac{\rho_b}{\phi}s_1-\mu_{s2}\frac{\rho_b}{\phi}s_2\ , \tag{2.9}$$

$$\frac{\rho_b}{\phi}\frac{\partial s_1}{\partial t}=k_{att1}c-k_{\det 1}\frac{\rho_b}{\phi}s_1-\mu_{s1}\frac{\rho_b}{\phi}s_1\,, \tag{2.10}$$

$$\frac{\rho_b}{\phi}\frac{\partial s_2}{\partial t}=k_{att2}c-k_{\det 2}\frac{\rho_b}{\phi}s_2-\mu_{s2}\frac{\rho_b}{\phi}s_2\ , \tag{2.11}$$

where c is concentration of free bacteria/colloids [L^{-3}]; s is concentration of attached particle/bacteria/virus [L^{-3}]; α_L is dispersivity [L]; v is average interstitial water velocity [LT^{-1}]; ρ_b is dry bulk density [ML]; ϕ is porosity [−]; k_{att} and k_{det} are the attachment and detachment date coefficients, respectively [T^{-1}]; μ_1 and μ_s are inactivation rate coefficients of free and attached phage, respectively [T^{-1}]. The subscripts 1 and 2 refer to the two different kinetics sites.

After several laboratory observations of hyper-exponential retention profiles in Bradford research group (Bradford et al., 2002), Bradford et al. (2003) developed a conceptual model where it accounts for two different mechanisms, attachment, and straining. In order to model attachment, Bradford et al. (2003) have considered the traditional reversible attachment/detachment theory, whereas, the straining model was described by irreversible first-order straining and depth dependency, i.e. $h=h(s,x)$. The following system of equations

describe colloidal-suspension mass balance, the kinetics of attachment and staining, respectively:

$$\frac{\partial(\phi c)}{\partial t} = -U\frac{\partial c}{\partial x} - \frac{\partial(\rho_b s_{att})}{\partial t} - \frac{\partial(\rho_b s_{str})}{\partial t} \ , \tag{2.12}$$

$$\frac{\partial(\rho_b s_{att})}{\partial t} = \phi k_{att}\psi_{att} c - \rho_b k_{\det} s_{att} \ , \tag{2.13}$$

$$\frac{\partial(\rho_b s_{str})}{\partial t} = \phi k_{str}\psi_{srt} c \ , \tag{2.14}$$

where ψ_{att} is a dimensionless colloid attachment function [−]; k_{str} is the straining coefficient [T^{-1}], and ψ_{str} is a dimensionless colloid straining function [−].

The dimensionless colloid attachment function (ψ_{att}) can gain different forms. Bradford et al. (2003) assume ψ_{att}=1, however, it can account for Langmuir blocking, ripening, and other forms (Ives, 1970; Johnson and Elimelech, 1995). For dimensionless colloid straining function (ψ_{str}), Bradford et al. (2003) proposed a depth dependency power-law function:

$$\psi_{srt} = \left(\frac{d_{50} + x}{d_{50}}\right)^{-\beta_{str}} \ , \tag{2.15}$$

where β_{str} is a fitting parameter responsible to control the shape of the spatial distribution of the RP [−]; d_{50} is the average pore length [L]. The combination of these two mechanisms, attachment, and straining, together with the depth dependency function demonstrated to be a good mathematical model to predict simultaneously breakthrough curve and hyper-exponential retention profile. Although depth dependency function hypothesis is not clear (Goldberg et al., 2014), due to the high agreement between the laboratory and model data, several studies have been using the depth dependency function to tune and interpret numerous experimental data on colloidal transport (Bai et al., 2018; Bradford and Bettahar, 2006; Bradford et al., 2004; Wang

et al., 2013). In order to study transport and retention of colloids in heterogeneous porous media, Bradford et al. (2004) developed a model constituted by the system of equations (2.12, 2.13, and 2.14), however, the depth dependency function gained a different form:

$$\psi_{srt} = H\left(x - x_0\right)\left(\frac{d_{50} + x - x_0}{d_{50}}\right)^{-\beta_{str}} , \qquad (2.16)$$

where $H(x\text{-}x_0)$ is the Heaviside function, and x_0 [L] is the depth from the column inlet that accounts for changes in porous media. For this particular case, the Heaviside function sets $\psi_{str}=0$ from intel until certain depth in the porous media (x_0) where the configuration of the porous media drastic changes it becomes less permeable.

The hyper-exponential retention profiles have been also explained due to the properties distribution of colloidal particles (Li et al., 2004; Tong and Johnson, 2007; Tufenkji and Elimelech, 2004b; Tufenkji and Elimelech, 2005a). Yuan and Shapiro (2010) explain hyper-exponential retention profiles by multi-colloid populations extending the random walk model with stochastically distributed lengths and durations of jumps (Shapiro, 2007), in order to match simultaneously retention profile and breakthrough curve. Averaging of the Master equation with distributed jump lengths and flight times results in elliptic transport equation. The filtration coefficient is assumed to be dependent on a particle property, like size, shape, surface charge, etc. Introduction of probabilistic distributions of the filtration coefficient and of the particle flight time into Master equation yields system of elliptic transport equations, where each equation corresponds to a particle population. The derived "integral" system successfully matches hyper-exponential retention profiles and breakthrough curves, simultaneously. However, the exact averaging of a stochastic system results in the representation of a distributed parameter by a number (function). For example, jump length distribution in random walks and consequent averaging result in the diffusion coefficient

(Einstein, 1905). Averaging of stochastically distributed lengths and durations of jumps leads to diffusion and timely-diffusion coefficients (Shapiro, 2007). The discretisation of wide filtration-coefficient distribution in the system with distributed lengths and durations of jumps requires several values for the filtration coefficient and leads to solution of the system containing the same number of elliptic equations. This results in cumbersome and computer time consuming calculations for direct runs and for iterative data-matching procedures. Averaging of this system would significantly simplify solutions of forward and inverse problems.

Tong and Johnson (2007) also discussed hyper-exponential retention profiles by multiple populations in the colloidal fluids. The same size particles can have different surface charges and zeta-potentials, so the particles with high filtration coefficients retain near to the inlet, while those with lower filtration coefficient move further in the core. The total of two exponential RPs with highly different decrements is non-exponential.

In the current thesis, Chapter 5 presents two simple different approaches based on the transformation of deep bed filtration model to match hyper-exponential-retention profiles and breakthrough curves, simultaneously.

2.6 Non-monotonic retention profiles – explanation and mathematical model

The complexity of transport of colloids, nanoparticles and general suspension in porous media has been observed experimentally by numerous research groups (Bradford et al., 2006; Choy et al., 2008; Elimelech et al., 2013; Gitis et al., 2011; Johnson et al., 2007; Johnson et al., 2018; Li and Johnson, 2005; Li et al., 2008; Liang et al., 2013b; Liu et al., 2007; Redman et al., 2001; Tong et al., 2005; Tufenkji and Elimelech, 2004a; Wang et al., 2014a; Wang et al.,

2010; Yuan et al., 2012; Yuan and Shapiro, 2011). There are several models that account for different mechanisms and factors trying to predict the behaviour of colloidal-suspension in complex structured porous media. One of the most complete mathematical models that allow for analytical solution and considers mass balance of suspended, retained and adsorbed colloids concentrations, and particle capture kinetics (Bianco et al., 2016; Chrysikopoulos and Syngouna, 2014; Elimelech et al., 2013; Santos and Bedrikovetsky, 2006; Vecchia et al., 2009) is given below:

$$\frac{\partial}{\partial t}\left(\phi s_0 c + s + \Gamma c\right) + U\frac{\partial\left(f_0 c\right)}{\partial x} = 0 \ , \tag{2.17}$$

$$\frac{\partial s}{\partial t} = h\left(s\right) c f_0 U \ . \tag{2.18}$$

Here s_0 is the accessibility factor, f_0 is the fraction of the overall flux moving the accessible pores, Γ is Henry's adsorption coefficient, and $h(s)$ is the filtration function, where, $h(s)$ function can assume any different forms. Fig. 8 shows different scenarios of colloidal transport in porous media account for accessibility factor and fraction of the accessible pore volume. Fig. 8b shows that each particle travels in a porous media distributed by size and the particle size exceeds some of the capillary size $(1-s_0)$-fraction (Bedrikovetsky, 2008).

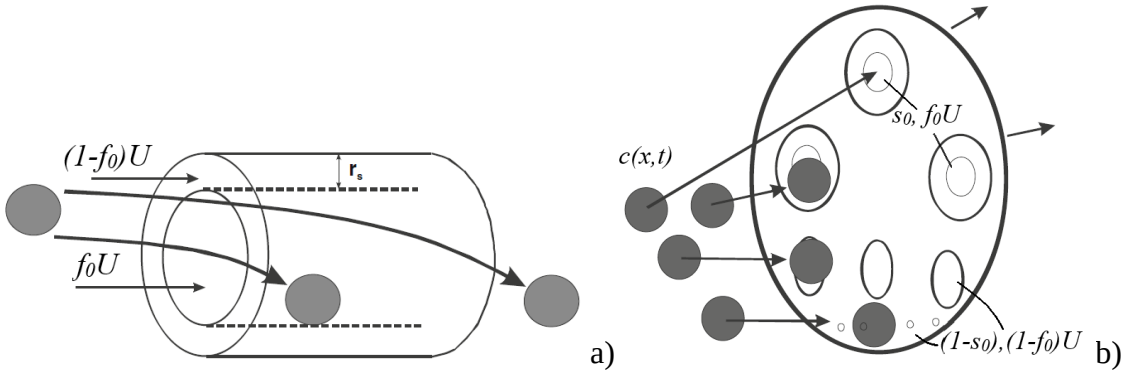


Figure 8: Schematic for a) particle retention due to attachment in situ the pore wall and size-exclusion/straining at the capillary entrance (Bedrikovetsky, 2008).

Despite, the mathematical model (2.17, 2.18) is very cumbersome and capture diverse mechanisms and features due to the structure of porous media, this model exhibits only monotonic decreasing retention profiles. In fact, all available deep bed filtration models that allow for exact solution exhibit only retention profiles that monotonically decrease over the time until reach stabilization (Gitis et al., 2010; Guerrero et al., 2009; Guerrero et al., 2013; Polyanin and Lychev, 2016; Shapiro and Yuan, 2012a; Shapiro, 2007; You et al., 2014; Yuan and Shapiro, 2010; Yuan and Sin, 2011; Ziskind et al., 2011). However, there are several laboratory experiments of colloidal-suspension flows into porous media that exhibit non-monotonic retention profiles. These unexpected behaviour have been observed for microorganisms (Bolster et al., 1999; Harter et al., 2000; Li et al., 2006; Tong and Johnson, 2007), engineered nano-particles (Choy et al., 2008; Liang et al., 2013a; Wang et al., 2014a), and latex microspheres (Li and Johnson, 2005; Tong and Johnson, 2007) and others.

Some mathematical models have been developed to reproduce non-monotonic retention profiles. Bradford et al. (2006) assumed two different colloid-species flowing through porous media (monodispersed and aggregated species), also introduced a depth dependency filtration function $h(x,s)$ (similar to Eqs. (2.14, 2.15)), where this dependency is assumed as a power-law form, in order to tune bacteria flow in engineered porous media. The proposed model closed match breakthrough curves and retention profiles, however, the authors claim non-uniqueness of parameters estimation. Moreover, Goldberg et al. (2014) recommended more physics explanations for the depth-dependency of the filtration function. Despite all limitations, this model has been widely used for prediction, analyses, and interpretation of experimental data on colloids and nano transport (Bianco et al., 2016; Goldberg et al., 2014).

Another approach to explain non-monotonic retention profiles is given by a mathematical model that considers two-velocities of particles in porous media. Yuan and Shapiro (2011)

developed a mathematical model where particles with slow speed are assumed to travel along the rock surfaces with possibility of being captured into stagnant zones, while particles with fast speed flow in the bulk of the carrier fluid, as shown in Fig. 9.

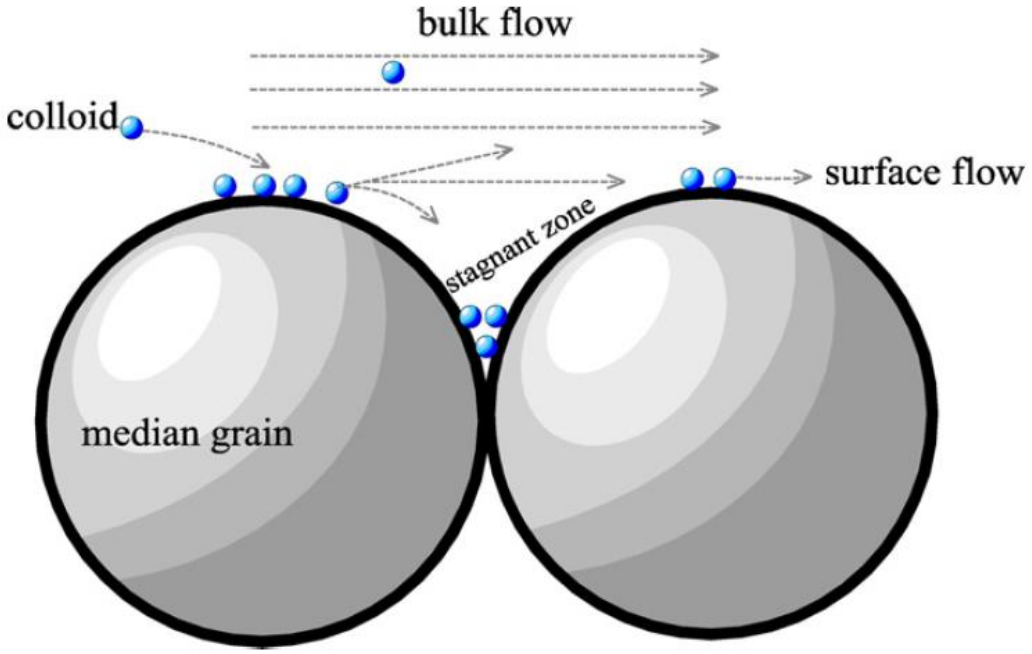


Figure 9: Schematic of two-velocities particle flow near the grain surface and at the bulk aqueous phase, and capture mechanisms at the grain surface and into stagnant zones (Yuan and Shapiro, 2011).

Yuan and Shapiro (2011) model's also considers attachment and detachment of colloids. As shown by the system of Eqs. (2.19-2.21), the model contains seven empirical parameters, which are tuned from the laboratory data.

$$\frac{\partial c}{\partial t}+\frac{U}{\phi}\frac{\partial c}{\partial x}=D\frac{\partial^2 c}{\partial x^2}+\left(\lambda_r s+\lambda_{mgr}s_{mg}\right)-\left(\lambda_s+\lambda_d\right)c\ , \tag{2.19}$$

$$\frac{\partial s_{mg}}{\partial t}+v_{mg}\frac{\partial s_{mg}}{\partial x}=D_{mg}\frac{\partial^2 s_{mg}}{\partial x^2}+\lambda_s c-\left(\lambda_{mg}+\lambda_{mgr}\right)s_{mg}\,, \tag{2.20}$$

$$\frac{\partial s}{\partial t}=\lambda_{mg}s_{mg}+\lambda_d c-\lambda_r s\,, \tag{2.21}$$

Where the subscript "*mg*" corresponds to the "*migration surface-associated phase*" (MSA), therefore, s_{mg} is the number of particles in the MSA per unit of pore volume, D_{mg} is the diffusion coefficient in the MSA, λ_{mg}, λ_s, λ_d, λ_r, and λ_{mgr} are the filtration coefficient for MSA, immobilized particles, for transport from the bulk phase to MSA, for releasing of immobilized particles, and for releasing of MSA to bulk phase.

The model (2.19-2.21) presents a high match of both breakthrough curves and retention profiles. However, the proposed model does not present an analytical solution, and understanding of the micro-level of filtration mechanisms is essential to differentiate between the model populations.

Bradford et al. (2011a) also present a different model based on two-speed to explain the non-monotonic retention profiles. The conceptual model accounts for two regions in porous media.

The first region represents the bulk fluid, where particles flow with fast velocity, while the second region considers the fraction of the pore-space near to the grain surface, where particles travel with slow velocity. This explanation is similar to Yuan and Shapiro (2011), however, Bradford et al. (2011a) assumed mass exchange between the two regions, and just attachment/detachment mechanisms, as shown in Fig. 10. The model contains in general six model coefficients, and successfully fits several experimental data; however, the authors discuss non-uniqueness of the tuning parameters, where the same experimental data can be matched by different sets of the model coefficients.

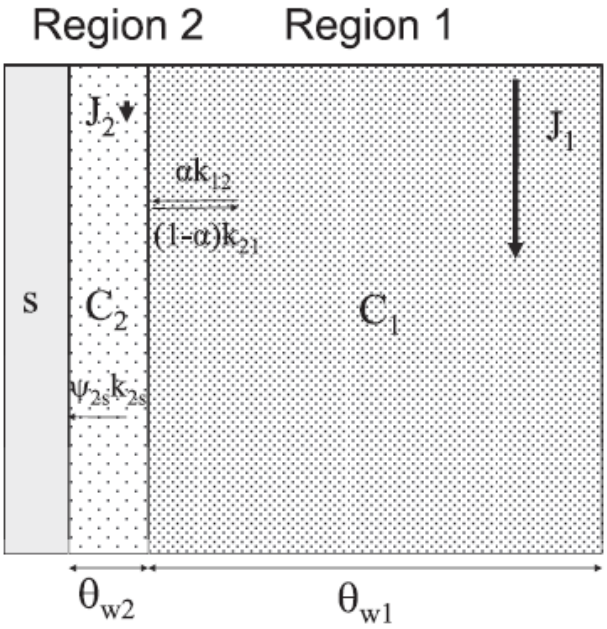


Figure 10: Schematic picture of colloidal-suspension flow processes that consider two different colloidal velocities. The colloid flowing in region 1 (bulk phase) presents a fast velocity, while the particles flowing in region 2 (near to the grain surface) have slow speed (Bradford et al., 2011a).

Usually, the two-velocities effects are noticeable in non-homogeneous porous media with high discrepancy size of micro-heterogeneity, as fractured-media formations, or even formation of cake in the rock surface (Kuzmina et al., 2017). For the case where the distances between the lower-and higher-conductivity channels have a similar order of magnitude of the pore length-scale, the Peclet's number varies from 10^{-3}-10^{-5}, meaning instantaneous equalization of both populations (fast and slow particles) (Polyanin and Dil′man, 1994). Therefore, the two populations segregated by velocities yield in one effective single-population flow with an average "low" velocity (Oliveira et al., 2014; Yang et al., 2016).

Another completely different way to explain the non-monotonic retention profiles is given by Wang et al. (2014b). The authors performed laboratory experiments of quantum dots coated with a synthetic polymer. These experiments have presented non-monotonic retention profiles. In order to explain this phenomenon, Wang et al. (2014b) stated that residual polymers, surfactants or even organic matters present in the colloidal-suspension could be responsible for

non-monotonic retention profiles due to adsorption of free polymer/surfactant onto the grain surface near the column inlet as shown in Fig. 11. This explanation has been modelled and used by others authors (Becker et al., 2015; Liang et al., 2013b), however, there are several experiments that have shown non-monotonic retention profiles even in the absence of polymer/surfactants/organic matters (Beryani et al., 2020; Chen et al., 2011; Li and Johnson, 2005; Redman et al., 2001).

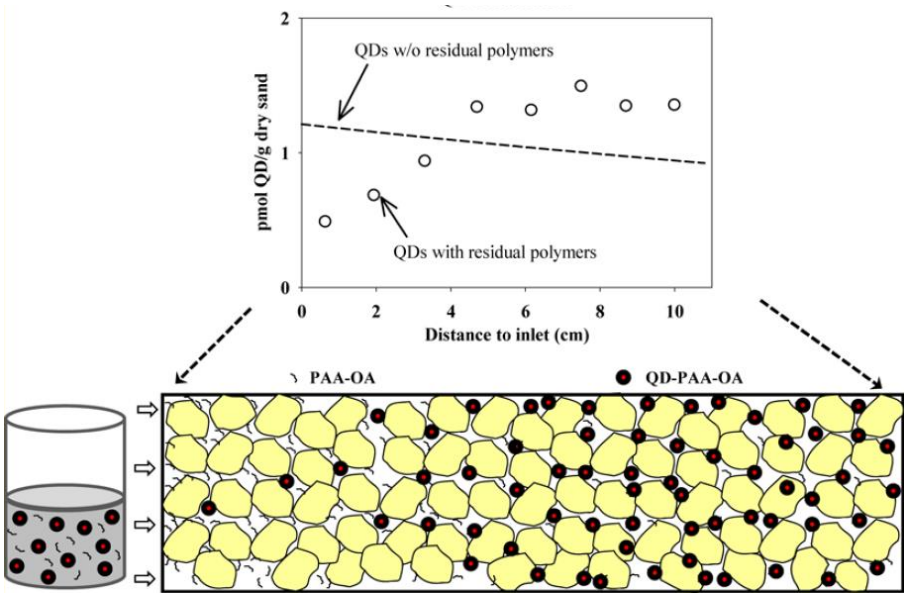


Figure 11: Schematic picture of the influence of residual polymer on the deposition of nanoparticles in porous media (Wang et al., 2014b)

Non-monotonic retention profiles have become an important subject in transport in porous media and they have been targeted frequently in debates (Bradford et al., 2006; Choy et al., 2008; Johnson et al., 2007; Johnson et al., 2018; Li and Johnson, 2005; Li et al., 2008; Liang et al., 2013b; Liu et al., 2007; Redman et al., 2001; Tong et al., 2005; Wang et al., 2014a; Wang et al., 2010; Yuan and Shapiro, 2011). Currently, there is no agreement on the physics phenomena responsible for non-monotonic retention profiles.

The current thesis explains and presents a mathematical model for non-monotonic retention behaviour based on colloid heterogeneity and the basic physics of colloidal-attachment (Chapter 6).

2.7 Application – Validation, and prediction of non-monotonic retention profiles in axisymmetric colloidal flows

Particle retention and detachment have been widely investigated as a significant cause of permeability alteration during well production and injection, which may lead to subsequent damage in the reservoir (Civan, 2015; Sarkar and Sharma, 1990; Vaz et al., 2010). As mentioned in the previous sections (2.2-2.5), the permeability decline is attributed to a different capture mechanism (Bradford et al., 2013; Bradford et al., 2011a; Cheng et al., 2019; Chrysikopoulos et al., 2017; Farajzadeh, 2019; Farajzadeh et al., 2019; Hilpert and Johnson, 2018; Hilpert et al., 2017; Rabinovich, 2019; Rosenbrand et al., 2014; Sahai and Moghanloo, 2019; Yakirevich et al., 2013; Yu et al., 2012; Yuan and Moghanloo, 2017; Yuan and Moghanloo, 2018; Zhang et al., 2015; Zhang et al., 2016). Therefore, the decision-making on injection of water into reservoirs, physical-chemical treatment, and storage or even on discard of dirty water is based on laboratory-based mathematical modelling. The prediction of well behaviour is estimated via experimental data from corefloods tests, followed by tuning the laboratory data using the adequate linear (x,t)-flow model, and finally, using the model parameters in axi-symmetric *(r,t)*-flow model (Chequer et al., 2017; Civan, 2015; Zhang et al., 2015; Zhang et al., 2016).

Recently, non-monotonic retention profiles have been studied and successfully matched by different models for suspension-colloidal transport (Bradford et al., 2006; Bradford et al., 2011a; Yuan and Shapiro, 2011). However, none of the mentioned models was upscaled or

even implemented to predict the behaviour of non-monotonic retention profiles in axi-symmetric coordinates. In the current thesis, more specifically in Chapter 7, the linear model for prediction of non-monotonic retention profiles is validated, and an upscaled governing equation for radial flows is derived to investigate the propagation of different populations of particles during water injection.

2.8 Summary

The critical analysis of the contemporaneous literature on suspension and colloidal transport in porous media and natural reservoirs allows concluding the following theoretical and practical engineering problems:

1) Breakthrough curves that exhibit monotonically grow after the breakthrough and tend to the limit that is lower than the injected concentration cannot be reproduced by the traditional deep-bed filtration model;

2) A mathematical model for cotransport of colloids and nano-particles with simultaneous attachment and straining (size exclusion) mechanisms of both species with minimum empirical constants has not been derived;

3) Upscaled equations for multi-sized particle transport with attachment has not been developed;

4) A simple mathematical model with an analytical solution is not available to predict hyper-exponential retention profiles; and

5) A physical explanation for non-monotonic retention profiles based on the distribution of properties of particles (size, surface charge, form) has not been provided.

The current thesis fills entirely the gaps previously mentioned. The above-mentioned problems have been solved and published in the following papers:

"Exact solutions for suspension-colloidal transport with multiple capture mechanisms", "Cotransport of Suspended Colloids and Nanoparticles in Porous Media", "Exact Upscaling

for Transport of Size- Distributed Colloids", "A modified model for colloidal transport to match hyper-exponential particle retention", "Transport of high-concentration colloids with two particle-capture mechanisms", "Explaining non-monotonic retention profiles during flow of size-distributed colloids", and "Non-monotonic retention profiles during axi-symmetric colloidal flows".

2.9 References

Abdel-Salam, A., Chrysikopoulos, C.V., 1995. Modeling of colloid and colloid-facilitated contaminant transport in a two-dimensional fracture with spatially variable aperture. Transp. Porous Med., 20(3): 197-221.

Albinger, O., Biesemeyer, B.K., Arnold, R.G., Logan, B.E., 1994. Effect of bacterial heterogeneity on adhesion to uniform collectors by monoclonal populations. FEMS Microbiol. Lett., 124(3): 321-326.

Alvarez, A.C., Hime, G., Marchesin, D., Bedrikovetsky, P.G., 2007. The inverse problem of determining the filtration function and permeability reduction in flow of water with particles in porous media. Transp. Porous Med., 70(1): 43-62.

Arab, D., Pourafshary, P., 2013. Nanoparticles-assisted surface charge modification of the porous medium to treat colloidal particles migration induced by low salinity water flooding. Colloids and Surfaces A: Physicochemical Eng. Aspects, 436: 803-814.

Arab, D., Pourafshary, P., Ayatollahi, S., 2014. Mathematical modeling of colloidal particles transport in the medium treated by nanofluids: deep bed filtration approach. Transp. Porous Med., 103(3): 401-419.

Araújo, J.A., Santos, A., 2013. Analytic model for DBF under multiple particle retention mechanisms. Transp. Porous Med., 97(2): 135-145.

Asraf-Snir, M., Gitis, V., 2011. Tracer studies with fluorescent-dyed microorganisms—A new method for determination of residence time in chlorination reactors. Chem. Eng. J., 166(2): 579-585. DOI:https://doi.org/10.1016/j.cej.2010.11.027

Bai, B., Wang, J., Zhai, Z., Xu, T., 2017. The Penetration Processes of Red Mud Filtrate in a Porous Medium by Seepage. Transp. Porous Med., 117(2): 207-227.

Bai, B., Xu, T., Li, H., (2017). The semi-analytical solution of particle transport in porous media induced by seepage. Feb-Fresenius Environmental Bulletin: 6286.

Bai, H., Lassabatere, L., Lamy, E., 2018. Colloid Transport in Aggregated Porous Media with Intra-and Interaggregate Porosities. Industrial & Engineering Chemistry Research, 57(18): 6553-6567.

Becker, M.D., Wang, Y., Pennell, K.D., Abriola, L.M., 2015. A multi-constituent site blocking model for nanoparticle and stabilizing agent transport in porous media. Environmental Science: Nano, 2(2): 155-166.

Bedrikovetsky, P., 2008. Upscaling of stochastic micro model for suspension transport in porous media. Transp. Porous Med., 75(3): 335-369.

Bedrikovetsky, P., 2013. Mathematical theory of oil and gas recovery: with applications to ex-USSR oil and gas fields, 4. Springer Science & Business Media.

Bedrikovetsky, P., Osipov, Y., Kuzmina, L., Malgaresi, G., 2019. Exact Upscaling for Transport of Size-Distributed Colloids. Water Resour. Res., 55(2): 1011-1039. DOI:10.1029/2018wr024261

Bedrikovetsky, P., Siqueira, A., de Souza, A., Shecaira, F., 2006. Correction of basic equations for deep bed filtration with dispersion. Journal of Petroleum Science and Engineering, 51(1-2): 68-84.

Bedrikovetsky, P., Siqueira, F.D., Furtado, C.A., Souza, A.L.S., 2011. Modified particle detachment model for colloidal transport in porous media. Transp. Porous Med., 86(2): 353-383.
Bedrikovetsky, P., You, Z., Badalyan, A., Osipov, Y., Kuzmina, L., 2017. Analytical model for straining-dominant large-retention depth filtration. Chem. Eng. J., 330: 1148-1159.
Bedrikovetsky, P., Zeinijahromi, A., Siqueira, F.D., Furtado, C.A., de Souza, A.L.S., 2012. Particle detachment under velocity alternation during suspension transport in porous media. Transp. Porous Med., 91(1): 173-197.
Bekhit, H.M., El-Kordy, M.A., Hassan, A.E., 2009. Contaminant transport in groundwater in the presence of colloids and bacteria: Model development and verification. J. Contam. Hydrol., 108(3-4): 152-167.
Beryani, A. et al., 2020. Key factors affecting graphene oxide transport in saturated porous media. Sci. Total Environ., 698: 134224.
Bianco, C., Tosco, T., Sethi, R., 2016. A 3-dimensional micro-and nanoparticle transport and filtration model (MNM3D) applied to the migration of carbon-based nanomaterials in porous media. J. Contam. Hydrol., 193: 10-20.
Bolster, C.H., Mills, A.L., Hornberger, G.M., Herman, J.S., 1999. Spatial distribution of deposited bacteria following Miscible Displacement Experiments in intact cores. Water Resour. Res., 35(6): 1797-1807. DOI:10.1029/1999wr900031
Bradford, S.A., Bettahar, M., 2006. Concentration dependent transport of colloids in saturated porous media. J. Contam. Hydrol., 82(1-2): 99-117.
Bradford, S.A., Bettahar, M., Simunek, J., Van Genuchten, M.T., 2004. Straining and attachment of colloids in physically heterogeneous porous media. Vadose Zone Journal, 3(2): 384-394.
Bradford, S.A., Kim, H.N., Haznedaroglu, B.Z., Torkzaban, S., Walker, S.L., 2009a. Coupled factors influencing concentration-dependent colloid transport and retention in saturated porous media. Environ. Sci. Technol., 43(18): 6996-7002.
Bradford, S.A., Simunek, J., Bettahar, M., van Genuchten, M.T., Yates, S.R., 2003. Modeling colloid attachment, straining, and exclusion in saturated porous media. Environ. Sci. Technol., 37(10): 2242-2250.
Bradford, S.A., Simunek, J., Walker, S.L., 2006. Transport and straining of E. coli O157:H7 in saturated porous media. Water Resour. Res., 42(12). DOI:10.1029/2005wr004805
Bradford, S.A., Torkzaban, S., 2015. Determining parameters and mechanisms of colloid retention and release in porous media. Langmuir, 31(44): 12096-12105.
Bradford, S.A., Torkzaban, S., Leij, F., Simunek, J., 2015. Equilibrium and kinetic models for colloid release under transient solution chemistry conditions. J. Contam. Hydrol., 181: 141-152.
Bradford, S.A., Torkzaban, S., Leij, F., Šimůnek, J., van Genuchten, M.T., 2009b. Modeling the coupled effects of pore space geometry and velocity on colloid transport and retention. Water Resour. Res., 45(2).
Bradford, S.A., Torkzaban, S., Shapiro, A., 2013. A theoretical analysis of colloid attachment and straining in chemically heterogeneous porous media. Langmuir, 29(23): 6944-6952.
Bradford, S.A., Torkzaban, S., Simunek, J., 2011a. Modeling colloid transport and retention in saturated porous media under unfavorable attachment conditions. Water Resour. Res., 47(10).
Bradford, S.A., Torkzaban, S., Wiegmann, A., 2011b. Pore-scale simulations to determine the applied hydrodynamic torque and colloid immobilization. Vadose Zone Journal, 10(1): 252-261.
Bradford, S.A., Yates, S.R., Bettahar, M., Simunek, J., 2002. Physical factors affecting the transport and fate of colloids in saturated porous media. Water Resour. Res., 38(12).
Brady, P.V., Morrow, N.R., Fogden, A., Deniz, V., Loahardjo, N., 2015. Electrostatics and the low salinity effect in sandstone reservoirs. Energy & Fuels, 29(2): 666-677.
Chen, G., Liu, X., Su, C., 2011. Transport and retention of TiO2 rutile nanoparticles in saturated porous media under low-ionic-strength conditions: measurements and mechanisms. Langmuir, 27(9): 5393-5402.
Chen, X., Bai, B., 2015. Experimental investigation and modeling of particulate transportation and deposition in vertical and horizontal flows. Hydrogeology Journal, 23(2): 365-375.

Cheng, K.B., Rabinovich, A., Dagan, G., 2019. Stochastic modeling of oscillatory pumping in heterogeneous aquifers with application to Boise aquifer test. J. Hydrology, 569: 278-290.
Chequer, L., Bedrikovetsky, P., Carageorgos, T., Badalyan, A., Gitis, V., 2019. Mobilization of Attached Clustered Colloids in Porous Media. Water Resour. Res., 55(7): 5696-5714. DOI:10.1029/2018wr024504
Chequer, L. et al., 2017. Non-monotonic permeability variation during colloidal transport: governing equations and analytical model. J. Hydrology.
Choy, C.C., Wazne, M., Meng, X., 2008. Application of an empirical transport model to simulate retention of nanocrystalline titanium dioxide in sand columns. Chemosphere, 71(9): 1794-1801.
Chrysikopoulos, C.V., Masciopinto, C., La Mantia, R., Manariotis, I.D., 2009. Removal of biocolloids suspended in reclaimed wastewater by injection into a fractured aquifer model. Environ. Sci. Technol., 44(3): 971-977.
Chrysikopoulos, C.V., Sotirelis, N.P., Kallithrakas-Kontos, N.G., 2017. Cotransport of Graphene Oxide Nanoparticles and Kaolinite Colloids in Porous Media. Transp. Porous Med., 119(1): 181-204.
Chrysikopoulos, C.V., Syngouna, V.I., 2012. Attachment of bacteriophages MS2 and ΦX174 onto kaolinite and montmorillonite: Extended-DLVO interactions. Colloids and Surfaces B: Biointerfaces, 92: 74-83.
Chrysikopoulos, C.V., Syngouna, V.I., 2014. Effect of gravity on colloid transport through water-saturated columns packed with glass beads: Modeling and experiments. Environ. Sci. Technol., 48(12): 6805-6813.
Chrysikopoulos, C.V., Syngouna, V.I., Vasiliadou, I.A., Katzourakis, V.E., 2012. Transport of Pseudomonas putida in a 3-D bench scale experimental aquifer. Transp. Porous Med., 94(3): 617-642.
Civan, F., 2015. Reservoir formation damage. Gulf Professional Publishing.
Dagan, G., Fiori, A., Jankovic, I., 2013. Upscaling of flow in heterogeneous porous formations: Critical examination and issues of principle. Adv. Water Resour., 51: 67-85.
Einstein, A., 1905. Investigations on the theory of Brownian motion. Translated by AD Cowper.
Elimelech, M., Gregory, J., Jia, X., 2013. Particle deposition and aggregation: measurement, modelling and simulation. Butterworth-Heinemann.
Farajzadeh, R., 2019. Sustainable production of hydrocarbon fields guided by full-cycle exergy analysis. Journal of Petroleum Science and Engineering: 106204.
Farajzadeh, R., Guo, H., van Winden, J., Bruining, J., 2017. Cation exchange in the presence of oil in porous media. ACS Earth Space Chem., 1(2): 101-112.
Farajzadeh, R., Zaal, C., van den Hoek, P., Bruining, J., 2019. Life-cycle assessment of water injection into hydrocarbon reservoirs using exergy concept. Journal of Cleaner Production, 235: 812-821.
Fogler, S.H., 2016. Elements of chemical reaction engineering. Prentice Hall.
Gitis, V., 2013. Dyed viruses and metal particles for advanced separation studies. Journal of Water Supply: Research and Technology-Aqua, 63(5): 325-331. DOI:10.2166/aqua.2013.204
Gitis, V., Dlugy, C., Gun, J., Lev, O., 2011. Studies of inactivation, retardation and accumulation of viruses in porous media by a combination of dye labeled and native bacteriophage probes. J. Contam. Hydrol., 124(1): 43-49. DOI:https://doi.org/10.1016/j.jconhyd.2011.02.001
Gitis, V., Rubinstein, I., Livshits, M., Ziskind, G., 2010. Deep-bed filtration model with multistage deposition kinetics. Chem. Eng. J., 163(1-2): 78-85.
Goldberg, E., Scheringer, M., Bucheli, T.D., Hungerbühler, K., 2014. Critical assessment of models for transport of engineered nanoparticles in saturated porous media. Environ. Sci. Technol., 48(21): 12732-12741.
Guedes, R.G., Al-Abduwani, F.A., Bedrikovetsky, P.G., Currie, P.K., 2006. Injectivity decline under multiple particle capture mechanisms, SPE international symposium and exhibition on formation damage control. Society of Petroleum Engineers.

Guerrero, J.P., Pimentel, L., Skaggs, T., Van Genuchten, M.T., 2009. Analytical solution of the advection–diffusion transport equation using a change-of-variable and integral transform technique. Int. J. Heat Mass Transfer, 52(13): 3297.

Guerrero, J.P., Pontedeiro, E., van Genuchten, M.T., Skaggs, T., 2013. Analytical solutions of the one-dimensional advection–dispersion solute transport equation subject to time-dependent boundary conditions. Chem. Eng. J., 221: 487-491.

Hammadi, A., Ahfir, N.-D., Alem, A., Wang, H., 2017. Effects of particle size non-uniformity on transport and retention in saturated porous media. Transp. Porous Med., 118(1): 85-98.

Harter, T., Wagner, S., Atwill, E.R., 2000. Colloid Transport and Filtration of Cryptosporidium parvum in Sandy Soils and Aquifer Sediments. Environ. Sci. Technol., 34(1): 62-70. DOI:10.1021/es990132w

Herzig, J., Leclerc, D., Goff, P.L., 1970. Flow of suspensions through porous media—application to deep filtration. Ind. Eng. Chem., 62(5): 8-35.

Hilpert, M., Johnson, W.P., 2018. A binomial modeling approach for upscaling colloid transport under unfavorable attachment conditions: Emergent prediction of nonmonotonic retention profiles. Water Resour. Res., 54(1): 46-60.

Hilpert, M., Rasmuson, A., Johnson, W.P., 2017. A binomial modeling approach for upscaling colloid transport under unfavorable conditions: Emergent prediction of extended tailing. Water Resour. Res., 53(7): 5626-5644.

Ives, K., 1970. Rapid filtration. Water Res., 4(3): 201-223.

Jiang, X., Tong, M., Lu, R., Kim, H., 2012. Transport and deposition of ZnO nanoparticles in saturated porous media. Colloids and Surfaces A: Physicochemical Eng. Aspects, 401: 29-37.

Johnson, P.R., Elimelech, M., 1995. Dynamics of Colloid Deposition in Porous Media: Blocking Based on Random Sequential Adsorption. Langmuir, 11(3): 801-812. DOI:10.1021/la00003a023

Johnson, W.P., Li, X., Yal, G., 2007. Colloid Retention in Porous Media: Mechanistic Confirmation of Wedging and Retention in Zones of Flow Stagnation. Environ. Sci. Technol., 41(4): 1279-1287. DOI:10.1021/es061301x

Johnson, W.P., Rasmuson, A., Pazmiño, E., Hilpert, M., 2018. Why Variant Colloid Transport Behaviors Emerge among Identical Individuals in Porous Media When Colloid–Surface Repulsion Exists. Environ. Sci. Technol., 52(13): 7230-7239. DOI:10.1021/acs.est.8b00811

Kasel, D. et al., 2013. Transport and retention of multi-walled carbon nanotubes in saturated porous media: Effects of input concentration and grain size. Water Res., 47(2): 933-944.

Katzourakis, V.E., Chrysikopoulos, C.V., 2014. Mathematical modeling of colloid and virus cotransport in porous media: Application to experimental data. Adv. Water Resour., 68: 62-73.

Katzourakis, V.E., Chrysikopoulos, C.V., 2015. Modeling dense-colloid and virus cotransport in three-dimensional porous media. J. Contam. Hydrol., 181: 102-113.

Khilar, K.C., Fogler, H.S., 1998. Migrations of fines in porous media, 12. Springer Science & Business Media.

Kim, H.N., Bradford, S.A., Walker, S.L., 2009. Escherichia coli O157: H7 transport in saturated porous media: Role of solution chemistry and surface macromolecules. Environ. Sci. Technol., 43(12): 4340-4347.

Klaine, S.J. et al., 2008. Nanomaterials in the environment: behavior, fate, bioavailability, and effects. Environ. Toxicol. Chem., 27(9): 1825-1851.

Kuzmina, L.I., Osipov, Y.V., 2014. Particle transportation at the filter inlet. International Journal for Computational Civil and Structural Engineering, 10(3): 17-22.

Kuzmina, L.I., Osipov, Y.V., 2015. Asymptotic solution for deep bed filtration with small deposit. Procedia Engineering, 111: 491-494.

Kuzmina, L.I., Osipov, Y.V., Galaguz, Y.P., 2017. A model of two-velocity particles transport in a porous medium. Int J. Non-linear Mech., 93: 1-6.

Kuzmina, L.I., Osipov, Y.V., Zheglova, Y.G., 2018. Analytical model for deep bed filtration with multiple mechanisms of particle capture. Int J. Non-linear Mech.

Li, X., Johnson, W.P., 2005. Nonmonotonic Variations in Deposition Rate Coefficients of Microspheres in Porous Media under Unfavorable Deposition Conditions. Environ. Sci. Technol., 39(6): 1658-1665. DOI:10.1021/es048963b

Li, X., Lin, C.-L., Miller, J.D., Johnson, W.P., 2006. Role of Grain-to-Grain Contacts on Profiles of Retained Colloids in Porous Media in the Presence of an Energy Barrier to Deposition. Environ. Sci. Technol., 40(12): 3769-3774. DOI:10.1021/es052501w

Li, X., Scheibe, T.D., Johnson, W.P., 2004. Apparent Decreases in Colloid Deposition Rate Coefficients with Distance of Transport under Unfavorable Deposition Conditions: A General Phenomenon. Environ. Sci. Technol., 38(21): 5616-5625. DOI:10.1021/es049154v

Li, Y., Wang, Y., Pennell, K.D., Abriola, L.M., 2008. Investigation of the Transport and Deposition of Fullerene (C60) Nanoparticles in Quartz Sands under Varying Flow Conditions. Environ. Sci. Technol., 42(19): 7174-7180. DOI:10.1021/es801305y

Liang, Y. et al., 2013a. Retention and remobilization of stabilized silver nanoparticles in an undisturbed loamy sand soil. Environ. Sci. Technol., 47(21): 12229-12237.

Liang, Y., Bradford, S.A., Simunek, J., Vereecken, H., Klumpp, E., 2013b. Sensitivity of the transport and retention of stabilized silver nanoparticles to physicochemical factors. Water Res., 47(7): 2572-2582. DOI:https://doi.org/10.1016/j.watres.2013.02.025

Liu, Y., Yang, C.-H., Li, J., 2007. Influence of Extracellular Polymeric Substances on Pseudomonas aeruginosa Transport and Deposition Profiles in Porous Media. Environ. Sci. Technol., 41(1): 198-205. DOI:10.1021/es061731n

Mikhailov, D., Zhvick, V., Ryzhikov, N., Shako, V., 2018. Modeling of Rock Permeability Damage and Repairing Dynamics Due to Invasion and Removal of Particulate from Drilling Fluids. Transp. Porous Med., 121(1): 37-67.

Mirabolghasemi, M., Prodanović, M., DiCarlo, D., Ji, H., 2015. Prediction of empirical properties using direct pore-scale simulation of straining through 3D microtomography images of porous media. J. Hydrology, 529: 768-778.

Muecke, T.W., 1979. Formation fines and factors controlling their movement in porous media. Journal of petroleum technology, 31(02): 144-150.

Oliveira, M.A. et al., 2014. Slow migration of mobilised fines during flow in reservoir rocks: laboratory study. Journal of Petroleum Science and Engineering, 122: 534-541.

Payatakes, A.C., Rajagopalan, R., Tien, C., 1974. Application of porous media models to the study of deep bed filtration. The canadian journal of chemical engineering, 52(6): 722-731.

Polyanin, A., Dil′man, V.V., 1994. Methods of modeling equations and analogies in chemical engineering. CRC Press, Boca Raton.

Polyanin, A., Zaitsev, V., 2012. Handbook of nonlinear partial differential equations. Chapman & Hall/CRC Press, Boca Raton.

Polyanin, A.D., Lychev, S.A., 2016. Decomposition methods for coupled 3D equations of applied mathematics and continuum mechanics: Partial survey, classification, new results, and generalizations. Applied Mathematical Modelling, 40(4): 3298-3324. DOI:https://doi.org/10.1016/j.apm.2015.10.016

Polyanin, A.D., Manzhirov, A.V., 2006. Handbook of mathematics for engineers and scientists. CRC Press, Boca Raton.

Polyanin, A.D., Zhurov, A.I., 2014. Non-linear instability and exact solutions to some delay reaction–diffusion systems. Int J. Non-linear Mech., 62: 33-40.

Rabinovich, A., 2019. An analytical solution for cyclic flow of two immiscible phases. J. Hydrology, 570: 682-691.

Redman, J.A., Grant, S.B., Olson, T.M., Estes, M.K., 2001. Pathogen Filtration, Heterogeneity, and the Potable Reuse of Wastewater. Environ. Sci. Technol., 35(9): 1798-1805. DOI:10.1021/es0010960

Rosenbrand, E., Haugwitz, C., Jacobsen, P.S.M., Kjøller, C., Fabricius, I.L., 2014. The effect of hot water injection on sandstone permeability. Geothermics, 50: 155-166.

Rosenbrand, E., Kjøller, C., Riis, J.F., Kets, F., Fabricius, I.L., 2015. Different effects of temperature and salinity on permeability reduction by fines migration in Berea sandstone. Geothermics, 53: 225-235.

Rottman, J., Sierra-Alvarez, R., Shadman, F., 2013. Real-time monitoring of nanoparticle retention in porous media. Environ. Chem. Lett., 11(1): 71-76.

Russell, T. et al., 2018. Chapter Three - Formation Damage by Fines Migration: Mathematical and Laboratory Modeling, Field Cases. In: Yuan, B., Wood, D.A. (Eds.), Formation Damage During Improved Oil Recovery. Gulf Professional Publishing, pp. 69-175. DOI:https://doi.org/10.1016/B978-0-12-813782-6.00003-8

Sahai, R., Moghanloo, R.G., 2019. Proppant transport in complex fracture networks – A review. Journal of Petroleum Science and Engineering, 182: 106199. DOI:https://doi.org/10.1016/j.petrol.2019.106199

Santos, A., Bedrikovetsky, P., 2006. A stochastic model for particulate suspension flow in porous media. Transp. Porous Med., 62(1): 23-53.

Sarkar, A.K., Sharma, M.M., 1990. Fines migration in two-phase flow. Journal of petroleum technology, 42(05): 646-652.

Schijven, J.F., Hassanizadeh, S.M., de Bruin, R.H., 2002. Two-site kinetic modeling of bacteriophages transport through columns of saturated dune sand. J. Contam. Hydrol., 57(3-4): 259-279.

Sefrioui, N., Ahmadi, A., Omari, A., Bertin, H., 2013. Numerical simulation of retention and release of colloids in porous media at the pore scale. Colloids and Surfaces A: Physicochemical Eng. Aspects, 427: 33-40.

Shapiro, A., Wesselingh, J., 2008. Gas transport in tight porous media: gas kinetic approach. Chem. Eng. J., 142(1): 14-22.

Shapiro, A., Yuan, H., 2012a. Application of stochastic approaches to modelling suspension flow in porous media, Statistical Mechanics and Random Walks: Principles, Processes and Applications. Nova Science Publishers, Incorporated, pp. 1-36.

Shapiro, A., Yuan, H., 2012b. Application of stochastic approaches to modelling suspension flow in porous media, Statistical Mechanics and Random Walks: Principles, Processes and Applications. Nova Science Publishers.

Shapiro, A.A., 2007. Elliptic equation for random walks. Application to transport in microporous media. Physica A: Statistical Mech. its Applic., 375(1): 81-96.

Sharma, M., Yortsos, Y., 1987a. Fines migration in porous media. AlChE J., 33(10): 1654-1662.

Sharma, M., Yortsos, Y., 1987b. Transport of particulate suspensions in porous media: model formulation. AlChE J., 33(10): 1636-1643.

Sotirelis, N.P., Chrysikopoulos, C.V., 2017. Heteroaggregation of graphene oxide nanoparticles and kaolinite colloids. Sci. Total Environ., 579: 736-744.

Syngouna, V.I., Chrysikopoulos, C.V., Kokkinos, P., Tselepi, M.A., Vantarakis, A., 2017. Cotransport of human adenoviruses with clay colloids and TiO2 nanoparticles in saturated porous media: Effect of flow velocity. Sci. Total Environ., 598: 160-167.

Tartakovsky, A.M., Panzeri, M., Tartakovsky, G.D., Guadagnini, A., 2017. Uncertainty Quantification in Scale- Dependent Models of Flow in Porous Media. Water Resour. Res., 53(11): 9392-9401.

Tong, M., Johnson, W.P., 2007. Colloid Population Heterogeneity Drives Hyperexponential Deviation from Classic Filtration Theory. Environ. Sci. Technol., 41(2): 493-499. DOI:10.1021/es061202j

Tong, M., Li, X., Brow, C.N., Johnson, W.P., 2005. Detachment-Influenced Transport of an Adhesion-Deficient Bacterial Strain within Water-Reactive Porous Media. Environ. Sci. Technol., 39(8): 2500-2508. DOI:10.1021/es049013t

Tufenkji, N., Elimelech, M., 2004a. Correlation equation for predicting single-collector efficiency in physicochemical filtration in saturated porous media. Environ. Sci. Technol., 38(2): 529-536.

Tufenkji, N., Elimelech, M., 2004b. Deviation from the classical colloid filtration theory in the presence of repulsive DLVO interactions. Langmuir, 20(25): 10818-10828.

Tufenkji, N., Elimelech, M., 2005a. Breakdown of colloid filtration theory: Role of the secondary energy minimum and surface charge heterogeneities. Langmuir, 21(3): 841-852.
Tufenkji, N., Elimelech, M., 2005b. Spatial distributions of Cryptosporidium oocysts in porous media: Evidence for dual mode deposition. Environ. Sci. Technol., 39(10): 3620-3629.
Vaz, A., Bedrikovetsky, P., Fernandes, P.D., Badalyan, A., Carageorgos, T., 2017. Determining model parameters for non-linear deep-bed filtration using laboratory pressure measurements. Journal of Petroleum Science and Engineering, 151: 421-433. DOI:10.1016/j.petrol.2017.01.001
Vaz, A., Bedrikovetsky, P., Furtado, C., de Souza, A., 2010. Well Injectivity Decline for Nonlinear Filtration of Injected Suspension: Semi-Analytical Model. Journal of Energy Resources Technology, 132(3): 033301.
Vaz, A., Maffra, D., Carageorgos, T., Bedrikovetsky, P., 2016. Characterisation of formation damage during reactive flows in porous media. J. Natural Gas Sci. Eng., 34: 1422-1433. DOI:10.1016/j.jngse.2016.08.016
Vecchia, E.D., Luna, M., Sethi, R., 2009. Transport in Porous Media of Highly Concentrated Iron Micro- and Nanoparticles in the Presence of Xanthan Gum. Environ. Sci. Technol., 43(23): 8942-8947. DOI:10.1021/es901897d
Wang, D. et al., 2014a. Hyperexponential and nonmonotonic retention of polyvinylpyrrolidone-coated silver nanoparticles in an Ultisol. J. Contam. Hydrol., 164: 35-48. DOI:https://doi.org/10.1016/j.jconhyd.2014.05.007
Wang, D. et al., 2011. Facilitated transport of Cu with hydroxyapatite nanoparticles in saturated sand: effects of solution ionic strength and composition. Water Res., 45(18): 5905-5915.
Wang, D., Zhang, W., Hao, X., Zhou, D., 2013. Transport of biochar particles in saturated granular media: effects of pyrolysis temperature and particle size. Environ. Sci. Technol., 47(2): 821-828.
Wang, Y., Becker, M.D., Colvin, V.L., Abriola, L.M., Pennell, K.D., 2014b. Influence of residual polymer on nanoparticle deposition in porous media. Environ. Sci. Technol., 48(18): 10664-10671.
Wang, Y. et al., 2010. Transport and Retention of Fullerene Nanoparticles in Natural Soils. Journal of Environmental Quality, 39: 1925-1933. DOI:10.2134/jeq2009.0411
Winter, C.L., Tartakovsky, D.M., 2002. Groundwater flow in heterogeneous composite aquifers. Water Resour. Res., 38(8).
Yakirevich, A. et al., 2013. Modeling the impact of solute recycling on groundwater salinization under irrigated lands: A study of the Alto Piura aquifer, Peru. J. Hydrology, 482: 25-39.
Yang, Y., Siqueira, F.D., Vaz, A.S., You, Z., Bedrikovetsky, P., 2016. Slow migration of detached fine particles over rock surface in porous media. J. Natural Gas Sci. Eng., 34: 1159-1173.
You, Z., Bedrikovetsky, P., Badalyan, A., Hand, M., 2015. Particle mobilization in porous media: temperature effects on competing electrostatic and drag forces. Geophysical Res. Lett., 42(8): 2852-2860.
You, Z., Osipov, Y., Bedrikovetsky, P., Kuzmina, L., 2014. Asymptotic model for deep bed filtration, Chemical Engineering Journal, vol. 258, p.
Yu, C., Gao, B., Muñoz-Carpena, R., 2012. Effect of dense vegetation on colloid transport and removal in surface runoff. J. Hydrology, 434: 1-6.
Yu, M. et al., 2018. Imaging analysis of fines migration during water flow with salinity alteration. Adv. Water Resour., 121: 150-161. DOI:10.1016/j.advwatres.2018.08.006
Yuan, B., Moghanloo, R.G., 2017. Analytical model of well injectivity improvement using nanofluid preflush. Fuel, 202: 380-394. DOI:https://doi.org/10.1016/j.fuel.2017.04.004
Yuan, B., Moghanloo, R.G., 2018. Nanofluid pre-treatment, an effective strategy to improve the performance of low-salinity waterflooding. Journal of Petroleum Science and Engineering, 165: 978-991. DOI:https://doi.org/10.1016/j.petrol.2017.11.032
Yuan, B., Moghanloo, R.G., Zheng, D., 2016. Analytical evaluation of nanoparticle application to mitigate fines migration in porous media. SPE Journal, 21(06): 2,317-2,332.

Yuan, B., Wang, W., 2018. Using nanofluids to control fines migration for oil recovery: Nanofluids co-injection or nanofluids pre-flush?-A comprehensive answer. Fuel, 215: 474-483.
Yuan, H., Shapiro, A., 2012. Colloid transport and retention: recent advances in colloids filtration theory, Colloids: Classification, Properties and Applications. Nova Science Publishers, Incorporated.
Yuan, H., Shapiro, A., You, Z., Badalyan, A., 2012. Estimating filtration coefficients for straining from percolation and random walk theories. Chem. Eng. J., 210: 63-73.
Yuan, H., Shapiro, A.A., 2010. Modeling non-Fickian transport and hyperexponential deposition for deep bed filtration. Chem. Eng. J., 162(3): 974-988.
Yuan, H., Shapiro, A.A., 2011. A mathematical model for non-monotonic deposition profiles in deep bed filtration systems. Chem. Eng. J., 166(1): 105-115.
Yuan, H., Sin, G., 2011. Uncertainty and sensitivity analysis of filtration models for non-Fickian transport and hyperexponential deposition. Chem. Eng. J., 168(2): 635-648.
Zhang, H., Malgaresi, G., Bedrikovetsky, P., 2018. Exact solutions for suspension-colloidal transport with multiple capture mechanisms. Int J. Non-linear Mech., 105: 27-42.
Zhang, W., Tang, X.-Y., Weisbrod, N., Zhao, P., Reid, B.J., 2015. A coupled field study of subsurface fracture flow and colloid transport. J. Hydrology, 524: 476-488.
Zhang, W. et al., 2016. A field study of colloid transport in surface and subsurface flows. J. Hydrology, 542: 101-114.
Ziskind, G., Shmueli, H., Gitis, V., 2011. An analytical solution of the convection–dispersion–reaction equation for a finite region with a pulse boundary condition. Chem. Eng. J., 167(1): 403-408.

3 Exact Solutions for Multiple Capture Mechanisms

3.1 Exact Solutions for Suspension-Colloidal Transport with Multiple Capture Mechanisms

H. Zhang, **G. Malgaresi**, P. Bedrikovetsky

International Journal of Non-Linear Mechanics.

Statement of Authorship

Title of Paper	Exact solutions for suspension-colloidal transport with multiple capture mechanisms
Publication Status	☑ Published ☐ Accepted for Publication ☐ Submitted for Publication ☐ Unpublished and Unsubmitted w ork w ritten in manuscript style
Publication Details	Zhang, H., Malgaresi, G.V.C. and Bedrikovetsky, P., 2018. Exact solutions for suspension-colloidal transport with multiple capture mechanisms. International Journal of Non-Linear Mechanics, 105, pp.27-42.

Principal Author

Name of Principal Author	Hao Zhang		
Contribution to the Paper	Derived the mathematical model, analysed and matched the laboratory data, and, interpreted the results.		
Signature		Date	25/10/2019

Co-Author Contributions

By signing the Statement of Authorship, each author certifies that:

i. the candidate's stated contribution to the publication is accurate (as detailed above);

ii. permission is granted for the candidate in include the publication in the thesis; and

iii. the sum of all co-author contributions is equal to 100% less the candidate's stated contribution.

Name of Co-Author	Gabriel Malgaresi		
Contribution to the Paper	Helped with the derivation of analytical solution and numerical solution. Helped in laboratory data interpretation, and developed the DLVO calculation.		
Overall percentage (%)	40%		
Certification:	This paper reports on original research I conducted during the period of my Higher Degree by Research candidature and is not subject to any obligations or contractual agreements with a third party that would constrain its inclusion in this thesis.		
Signature		Date	25/10/2019

Name of Co-Author	Pavel Bedrikovetsky		
Contribution to the Paper	Problem formulation and supervision of the development of the whole work.		
Signature		Date	23/10/2019

International Journal of Non-Linear Mechanics 105 (2018) 27–42

Contents lists available at ScienceDirect

International Journal of Non-Linear Mechanics

journal homepage: www.elsevier.com/locate/nlm

Exact solutions for suspension-colloidal transport with multiple capture mechanisms

H. Zhang, G.V.C. Malgaresi, P. Bedrikovetsky *

Australian School of Petroleum, University of Adelaide, Australia

A B S T R A C T

We discuss one-dimensional (1D) non-linear problems of suspension-colloidal transport in porous media with two simultaneous particle capture mechanisms. The first mechanism corresponds to low retention concentration and constant filtration function. The second mechanism corresponds to large retention concentration with blocking (Langmuir) filtration function. The 1D flow problems are non-linear; however, they allow for exact solutions. The exact solutions are obtained for the general two-capture case, and also for piecewise-linear approximation of the filtration function. The proposed filtration function describes the breakthrough curves (BTCs) that monotonically increase with time and stabilise at some value lower than the injected concentration; those BTCs are observed for numerous suspension-colloidal flows. The tuning method for determining the model coefficients is developed. Close agreement between the laboratory and modelling data validates the proposed form of filtration function.

1. Introduction

Colloidal-suspension flows in porous media occur in different processes of environmental, chemical, civil and petroleum engineering, and also in energy sector and geology [1–3]. Mathematical modelling is an essential part of design and planning of various technological processes in those areas, like industrial waste management in aquifers, injection of cold water and hot water/steam production from geothermal reservoirs, industrial filtering, management of potable water resources, water injection in oil fields for pressure maintenance, etc. [3–6].

Particle capture by the rock during suspension-colloidal flows occurs by size exclusion, straining, attachment, segregation, diffusion into dead-end pores, etc. [1,4,7–12], (Fig. 1). The effects of particle retention are decreasing suspension concentration and permeability. The suspension concentration decline due to retention is important for industrial waste disposal and aquifer contamination, while the permeability decline yields production and injection well impairment.

Governing equations for deep bed filtration (DBF) in porous media contain mass balance for suspended and retained particles, particle capture rate that is proportional to the particle advective flux, and Darcy's law accounting for permeability decline due to particle retention [7,13–16]:

$$\frac{\partial}{\partial t}(\phi c+\sigma)+U\frac{\partial c}{\partial x}=\frac{\partial}{\partial x}\left(D\frac{\partial c}{\partial x}\right) \tag{1}$$

$$\frac{\partial \sigma}{\partial t}=\lambda(\sigma)\,cU \tag{2}$$

$$U=-\frac{k(\sigma)}{\mu(c)}\frac{\partial p}{\partial x} \tag{3}$$

where x is the linear coordinate in the flow direction, t is the time, c and σ are the suspended and attached concentrations, ϕ is the porosity, U is the fluid velocity, D is the dispersion (diffusion) coefficient, λ is the filtration coefficient, k is the permeability, μ is the viscosity, and p is the pressure. The suspension concentration c is determined as the number of suspended particles in unitary volume of carrier fluid, while the retained concentration σ is defined as the number of attached particles in unitary volume of the rock.

Constant-concentration injection into clean bed corresponds to the following initial and boundary conditions:

$$t=0:\ c=\sigma=0 \tag{4}$$

$$x=0:\ c=c^0 \tag{5}$$

The initial condition (4) for concentration c holds as x tends to infinity.

Another form of the retention rate equation is its proportionality of the rate to overall particle flux q, which is the total of advective and diffusive fluxes [8,13,17]:

$$\frac{\partial \sigma}{\partial t}=\lambda(\sigma)\,q,\quad q=cU-D\frac{\partial c}{\partial x} \tag{6}$$

Fig. 2 shows the difference in capture scenarios by models given by Eqs. (2) and (6). The capture occurs at a site shown as a sieve-screen. The overall particle displacement by the flux q is decomposed into those by the advective and diffusive fluxes. Eq. (2) corresponds to the case where the capture occurs during the advective move (Fig. 2a). Eq. (6) corresponds to diffusive move (Fig. 2b).

* Corresponding author.
E-mail address: pavel@asp.adelaide.edu.au (P. Bedrikovetsky).

https://doi.org/10.1016/j.ijnonlinmec.2018.07.007
Received 3 June 2018; Received in revised form 10 July 2018; Accepted 15 July 2018
Available online 27 July 2018
0020-7462/© 2018 Elsevier Ltd. All rights reserved.

Index

c	Suspended particle concentration [L^{-3}]
c^0	Injected particle concentration [L^{-3}]
C	Dimensionless suspended particle concentration [-]
D	Dispersion (diffusion) coefficient [$L^2\ T^{-1}$]
j	Jamming ratio [-]
L	Length of the core [L]
p	Pressure [$M\ L^{-1}\ T^{-2}$]
q	Total flux [$L^{-2}\ T^{-1}$]
r	Radius [L]
r_p	Mean pore radius [L]
r_s	Particle radius [L]
S	Dimensionless total retained particle concentration [-]
S_1	Dimensionless attached particle concentration for 1st mechanism [-]
S_2	Dimensionless strained particle concentration for 2nd mechanism [-]
S_m	Dimensionless maximum retained particle concentration [-]
t	Time [T]
T	Dimensionless time [PVI]
T_{inj}	Dimensionless injection time [PVI]
T_m	Dimensionless stabilisation time at the inlet [PVI]
U	Flow velocity [$L\ T^{-1}$]
x	Axial coordinate [L]
X	Dimensionless axial coordinate [-]

Greek letters

γ	Salinity [mM]
ε	Small filtration coefficient variable [-]
σ	Retained particle concentration [L^{-3}]
σ_1	Attached particle concentration [L^{-3}]
σ_2	Strained particle concentration [L^{-3}]
σ_m	Maximum attached particle concentration [L^{-3}]
ϕ	Porosity [-]
λ	Filtration coefficient [L^{-1}]
λ_0	Attachment filtration coefficient at no retention [L^{-1}]
λ_1	Straining filtration coefficient [L^{-1}]
Λ	Dimensionless filtration [-]
Λ_0	Dimensionless initial attachment filtration coefficient [-]
Λ_1	Dimensionless straining filtration coefficient [-]
ρ	Density [$M\ L^{-3}$]
μ	Viscosity [$M\ L^{-1}\ T^{-1}$]

Superscripts

0	Initial value

Subscripts

inj	Injection
m	Maximum (for retained concentration and time)
p	Pore
s	Suspension

Abbreviations

BTC	Breakthrough curve
DBF	Deep bed filtration
ODE	Ordinary differential equation
PDE	Partial differential equation
CFD	Computational fluid dynamics

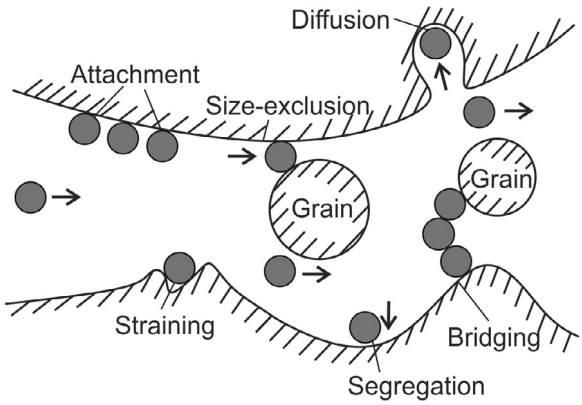


Fig. 1. Various particle capture mechanisms in a single pore.

The Peclet number is the ratio between the advective and dispersive fluxes. In large scale (reservoir) approximation, where the typical boundary size exceeds 100m, Peclet number significantly exceeds one, $UL/D >> 1$, and the dispersive/diffusion terms are neglected in both Eqs. (2) and (6). During laboratory corefloods, where the typical core length is 0.1 m, Peclet number can be lower than one, and the diffusion is important.

The assumptions of monolayer Langmuir's attachment where one attached particle occupies one vacancy, and vice versa, yield the "active-mass" law for the particle–vacancy "reaction" [18–20]:

$$\lambda(\sigma) = \begin{cases} \lambda_0 \left(1 - \dfrac{\sigma}{\sigma_m}\right), & \sigma < \sigma_m \\ 0, & \sigma > \sigma_m \end{cases} \tag{7}$$

where σ_m is the maximum number of retention vacancies per unitary volume occupied by the attached particles. The Langmuir blocking filtration function, given by Eq. (7) is usually used for monolayer electrostatic attachment of particles on the rock surface, but is also applicable for straining and size exclusion [10,18,19]. Plot of the Langmuir filtration function corresponds to curve 2 in Fig. 3a. The exact solution of the 1D flow problem (1)–(5) corresponds to breakthrough curve 2 in Fig. 3b, which is zero before the breakthrough at the moment of injection of one pore volume, then jumps up to some value and tends to injected concentration when time tends to infinity [18].

For small retained concentration, where $\sigma << \sigma_m$, the filtration coefficient is assumed to be constant, $\lambda(\sigma) = \lambda_1$ (straight line 1 in Fig. 3a). For this case, the breakthrough concentration is equal zero before the breakthrough moment, then jumps up to some value and remains constant during the overall flow period (curve 1 in Fig. 3b) [18]. This type of the breakthrough behaviour was observed for various capture mechanisms [1,4–6,11,21]. To be specific, further in the text the term attachment corresponds to the Langmuir's blocking capture, while the low-retention mechanism is called size exclusion, or straining.

BTCs that equal zero before the breakthrough moment, jumping up to some value and then tending to a limit that is lower than the injected concentration as time tends to infinity, have been observed in numerous laboratory tests (curve 3 in Fig. 3b) [4,5,8–10,13,19,22,23]. However, this specific type of BTCs has not been interpreted by capture kinetics neither in terms of an analytical model; the filtration functions that yield this type of breakthrough curves, are not available.

Suspended-colloidal particles are subject to different capture mechanisms (Fig. 1). Each capture process depends on parameters that are stochastically distributed over the porous space, like surface charge, pore throat and particle sizes, roughness, tortuosity, etc. The stochastic models for suspension-colloidal-nano transport include random-walk equations [24,25], Boltzmann's model [25,26], network and 3D computational fluid dynamics (CFD) models [21], and randomly distributed filtration coefficients [10,25,27].

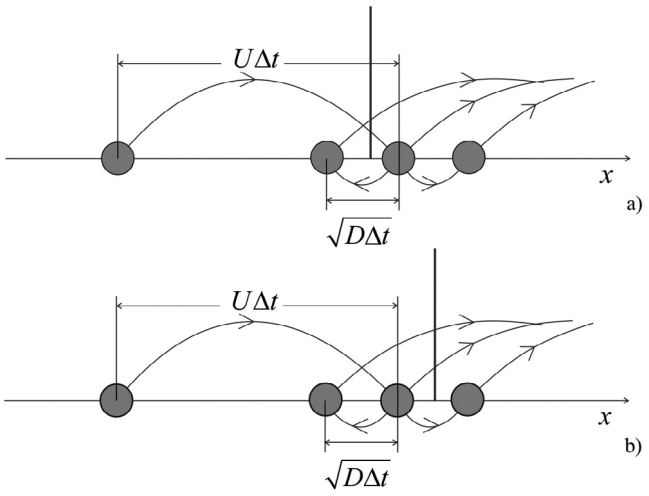


Fig. 2. Traditional and modified models for particle capture by the porous media, where the vertical bar corresponds to the capture site: (a) particle capture from the advective flux; (b) particle capture from the overall advective and diffusive flux.

The population balance models account for fine particle distribution in size, surface charge, shape, etc. [28,29] and for accessibility of different pores by different size particles due to geometric restrictions and the corresponding reduction of the overall particle flux [7,30]. For transport of homogeneous suspension, the population balance equations allow for exact averaging; the upscaled equations coincide with the traditional DBF system that accounts for accessibility and flux-reduction functions [7].

Exact solutions for DBF Eqs. (1)–(3) yield well-posed inverse problems. The filtration function in Eq. (2) is determined from BTC, and formation damage function in Eq. (3) is calculated from the pressure drop history across the core [31]. The filtration function can also be determined from the retention profile, claiming significantly lower data scattering than after BTC treatment [31].

Exact analytical solutions are also used for qualitative interpretation of the results of laboratory coreflooding and calculation of the model coefficients. The comparison of the concentration waves provided by the analytical models with those measured during corefloods or field tests yields a more profound understanding of the transport processes. The analytical models are also widely used in three-dimensional reservoir simulations using stream-line and front-tracking techniques. The above applications have motivated numerous studies on the exact solutions for 1D colloidal-suspended and reactive transport problems [15,16,20,23,32–37].

Two-capture mechanism models with size exclusion and attachment are widely used in suspension-colloidal studies [1,4,38,39]. An analytical model for deep bed filtration of a binary mixture of two distinct particle populations, where each specie is captured by its own separate capture mechanism is derived; high quality match using constant and Langmuir's filtration functions is achieved [22]. The asymptotic solutions for two-population and two-capture models have been obtained [40,41]. However, exact solutions for two simultaneous capture mechanisms of uniform particles are not available.

In the current paper, we discuss non-linear 1D problem for suspension-colloidal transport in porous media with two simultaneous particle capture mechanisms. We prove that any number of capture mechanisms can be aggregated into one mechanism following either of scenarios given by Eqs. (2) or (6). For dispersion-free case with two simultaneous particle capture mechanisms given by constant and blocking (Langmuir) filtration functions, we derive an exact solution. The solution exhibits BTC that monotonically grows after the breakthrough and tends to the limit that is lower than the injected concentration. The analytical model closely matches numerous laboratory tests, validating the interpretation of BTCs that stabilise below the injected concentration, by the two-capture model.

The structure of the paper is as follows. Section 2 and Appendices A and B present mathematical model for suspension-colloidal flows with multiple capture mechanisms, and show that it is equivalent to a single-capture system. Section 3 discusses two capture mechanisms with constant (straining) and Langmuir (attachment) filtration functions, including derivation of exact solution for 1D flow, and the exact and approximate formulae for aggregation. Section 4 derives the exact solution for binary (piecewise linear) filtration function with explicit formulae for BTCs. Section 5 presents sensitivity study of filtration functions and BTCs with respect to three model parameters. Section 6 compares the exact and numerical solutions. Section 7 matches two series of laboratory tests and exhibits the results of matching by the analytical model. Section 8 derives the aggregation procedure and exact solution for reactive flows with multiple chemical reactions. Section 9 discusses the results, the limitations of the model and some practical applications. Section 10 draws the conclusions and finalises the paper.

2. Suspension-colloidal flow system with multiple capture mechanisms

System of equations for DBF of particles with n capture mechanisms accounting for dispersion (diffusion) of particles, given by Eqs. (A.1)–(A.3) is presented in Appendix A. Here any combination of different particle capture mechanisms, presented in Fig. 1, is discussed. All capture rates are proportional to the particle advective flux [12,18].

Lemma 1. *System (A.1)– (A.3) for suspension-colloidal flow with n particle capture mechanisms $\lambda_i(\sigma_1, \sigma_2 \ldots \sigma_n)$ is equivalent to that with a single capture*

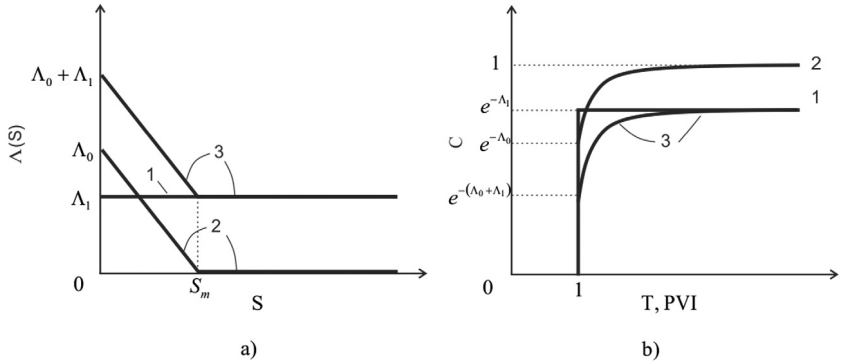


Fig. 3. Various forms of breakthrough curves for different forms of filtration function: (a) filtration functions; (b) breakthrough curves. Here 1 – constant filtration function, 2 – Langmuir (blocking) filtration function, and 3 is the binary filtration function.

mechanism (2), where the aggregated filtration function $\lambda(\sigma)$ is determined by Cauchy's problem for system of ordinary differential equations (ODE) (A.9).

The proof is presented in Appendix A.

Appendix B discusses the modified DBF system with dispersion, where the capture rate is proportional to the overall particle flux that includes advective and diffusive fluxes, given by Eqs. (1), (6) ([8,13,17]). Lemma 1 is also valid for system (A.1), (A.2), (B.1). The proof is presented in Appendix B.

Further we discuss the large-scale flows, where the dispersion is negligible.

Introduce the following dimensionless parameters and variables into dispersion-free systems (1), (2) and (4), (5):

$$T=\frac{Ut}{\phi L};\ X=\frac{x}{L};\ C=\frac{c}{c^0};\ \Lambda_0=\lambda_0 L;\ S_m=\frac{\sigma_m}{\phi c^0};\ S=\frac{\sigma}{\phi c^0};\ \Lambda_1=\lambda_1 L;$$
$$S_1=\frac{\sigma_1}{\phi c^0};\ S_2=\frac{\sigma_2}{\phi c^0} \tag{8}$$

The dimensionless system becomes:

$$\frac{\partial(C+S)}{\partial T}+\frac{\partial C}{\partial X}=0 \tag{9}$$

$$\frac{\partial S}{\partial T}=\Lambda(S)C \tag{10}$$

Initial and boundary conditions (4), (5) for dimensionless variables become

$$T=0:\ C=S=0 \tag{11}$$

$$X=0:\ C=1 \tag{12}$$

The exact solution for system (9), (10) subject to initial and boundary conditions (11), (12) is derived in the next section.

3. Suspension-colloidal flow system with two capture mechanisms

In the current section we derive the expression for filtration function that corresponds to two fines capture mechanisms (Section 3.1), develop the exact solution for the general case of aggregated filtration function (Section 3.2) and its particular case for two capture mechanisms (Section 3.3). Then, properties of the filtration function, which is the aggregation of Langmuir and constant filtration functions, are described (Section 3.4). The explicit asymptotic formulae for aggregated two-mechanism filtration functions with small rate by either mechanism are derived (Section 3.5)

3.1. Aggregation formula for overall filtration function

Consider the case $n=2$ of two capture mechanisms. One mechanism with low retention has constant filtration function. Another one has the Langmuir blocking filtration function, given by Eq. (7).

Changing T to S_2 as a free variable in ODE that corresponds to the capture rate for the first capture mechanism (A.3) at $X=$ const yields

$$\frac{dS_1}{dS_2}=\frac{dS_1}{dT}\Big/\frac{dS_2}{dT}=\frac{\Lambda_0}{\Lambda_1}\left(1-\frac{S_1}{S_m}\right) \tag{13}$$

Accounting for initial conditions (11), (12) and integrating Eq. (13) by separation of variables results in

$$S_2=-\frac{S_m\Lambda_1}{\Lambda_0}\ln\left(1-\frac{S_1}{S_m}\right) \tag{14}$$

The total retained concentration and overall filtration function become

$$S(S_1)=S_1+S_2=S_1-\frac{S_m\Lambda_1}{\Lambda_0}\ln\left(1-\frac{S_1}{S_m}\right) \tag{15}$$

$$\Lambda(S)=\Lambda_0\left(1-\frac{S_1(S)}{S_m}\right)+\Lambda_1 \tag{16}$$

respectively, where $S_1=S_1(S)$ is the inverse function to Eq. (15). So, the formula for the aggregated filtration function (16) contains transcendental Eq. (15).

Fig. 4a presents the continuous curve for the aggregated filtration function.

3.2. Exact solution for any aggregated filtration function $\Lambda(S)$

Following works [15–17], here we present the general schema for solution of Eqs. (9), (10) for any arbitrary filtration function. Introducing the potential $\Phi(S)$ from Eq. (10)

$$\Phi(S)=\int_0^S\frac{du}{\Lambda(u)} \tag{17}$$

transforms Eq. (10) into

$$C=\frac{\partial\Phi(S)}{\partial T} \tag{18}$$

Substituting expression (18) into Eq. (9) and changing order of differentiation in the third term yields:

$$\frac{\partial}{\partial T}\left(\frac{\partial\Phi(S)}{\partial T}+S\right)+\frac{\partial}{\partial T}\left(\frac{\partial\Phi(S)}{\partial X}\right)=0 \tag{19}$$

Integration of Eq. (19) in T accounting for initial conditions (11), (12) results in:

$$\frac{\partial\Phi(S)}{\partial T}+S+\frac{\partial\Phi(S)}{\partial X}=0 \tag{20}$$

Performing differentiation in (20) yields

$$\frac{\partial S}{\partial T}+\frac{\partial S}{\partial X}=-\Lambda(S)S \tag{21}$$

Representing Eq. (21) in characteristic form with T as a parameter along characteristics shows that $S=0$ at $T<X$ (Fig. 5a). Ahead of the concentration front $X=T$, $S=0$. Breakthrough in Fig. 5b occurs after the moment t_1, so the S-value in profile in Fig. 5c is zero.
The characteristic form at $T>X$ is:

$$\frac{dS}{dX}=-\Lambda(S)S,\ \frac{dT}{dX}=1 \tag{22}$$

Ordinate axes is a characteristic for quasi-linear hyperbolic system (9), (10), i.e. (11), (12) is a Goursat problem [12]. It allows determining $S(0, T)$ from Eq. (10) and boundary condition (12). Accounting for boundary condition (12) in Eq. (10) and integrating it by separation of variables yields

$$\int_0^{S(0,T)}\frac{du}{\Lambda(u)}=T \tag{23}$$

Integration of ODE (22) with initial condition (11) yields

$$\int_{S(0,T-X)}^{S(X,T)}\frac{du}{\Lambda(u)u}=-X \tag{24}$$

Here $S(0, T\text{-}X)$ is determined from transcendental Eq. (23). Then $S(X, T)$ is determined from transcendental Eq. (24).

The Riemann invariant for system (9), (10) that corresponds to unity eigen-value is C/S [15–17,42]:

$$\frac{C(X,T)}{S(X,T)}=\frac{1}{S(0,T-X)} \tag{25}$$

yielding the explicit expression for suspended concentration $C(X, T)$ versus $S(X, T)$.

3.3. Exact solution for 1D transport with two mechanism capture

In this section we derive the exact solution for aggregated function of two capture mechanisms, given by Eqs. (15) and (16).

The system for two-mechanism capture with Langmuir and constant filtration functions is:

$$\frac{\partial(C+S_1+S_2)}{\partial T}+\frac{\partial C}{\partial X}=0 \tag{26}$$

$$\frac{\partial S_1}{\partial T}=\Lambda^1(S_1)C,\quad \Lambda^1(S_1)=\begin{cases}\Lambda_0\left(1-\dfrac{S_1}{S_m}\right), & S_1<S_m\\ 0, & S_1>S_m\end{cases} \tag{27}$$

$$\frac{\partial S_2}{\partial T}=\Lambda_1 C \tag{28}$$

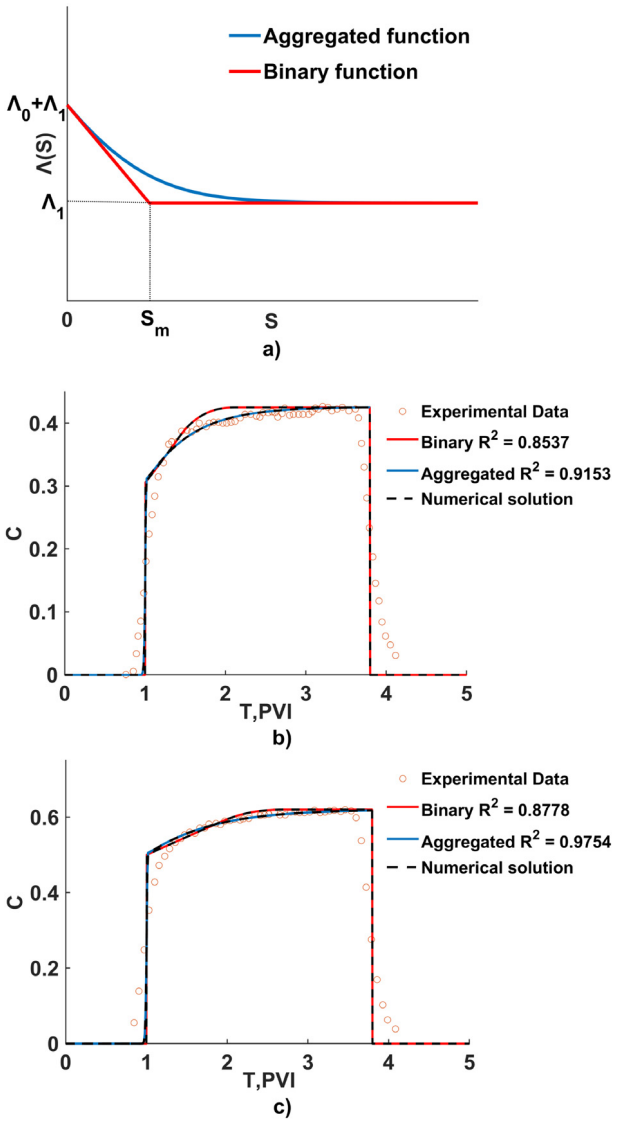


Fig. 4. Comparison between analytical and numerical solutions: (a) aggregated and binary filtration functions (blue and red curves, respectively); (b,c) breakthrough concentrations calculated by analytical models for aggregated and binary filtration functions (blue and red curves). Dashed black curves are obtained by numerical modelling. (For interpretation of the references to colour in this figure legend, the reader is referred to the web version of this article.)

Introducing potential from Eq. (27)

$$\Phi\left(S_1\right)=\int_0^{S_1}\frac{du}{\Lambda^1\left(u\right)} \tag{29}$$

transforms Eq. (27) into

$$C=\frac{\partial\Phi\left(S_1\right)}{\partial T} \tag{30}$$

Substituting Eqs. (14) and (30) into Eq. (26) yields

$$\frac{\partial}{\partial T}\left(\frac{\partial\Phi\left(S_1\right)}{\partial T}+S_1+S_2\left(S_1\right)\right)+\frac{\partial}{\partial X}\left(\frac{\partial\Phi\left(S_1\right)}{\partial T}\right)=0 \tag{31}$$

Changing order of derivatives in second differential term in Eq. (31), integrating the result in T accounting for initial condition (11), (12) yields

$$\frac{1}{\Lambda^1\left(S_1\right)}\frac{\partial S_1}{\partial T}+\frac{1}{\Lambda^1\left(S_1\right)}\frac{\partial S_1}{\partial X}=-S_1+\frac{S_m\Lambda_1}{\Lambda_0}\ln\left(1-\frac{S_1}{S_m}\right) \tag{32}$$

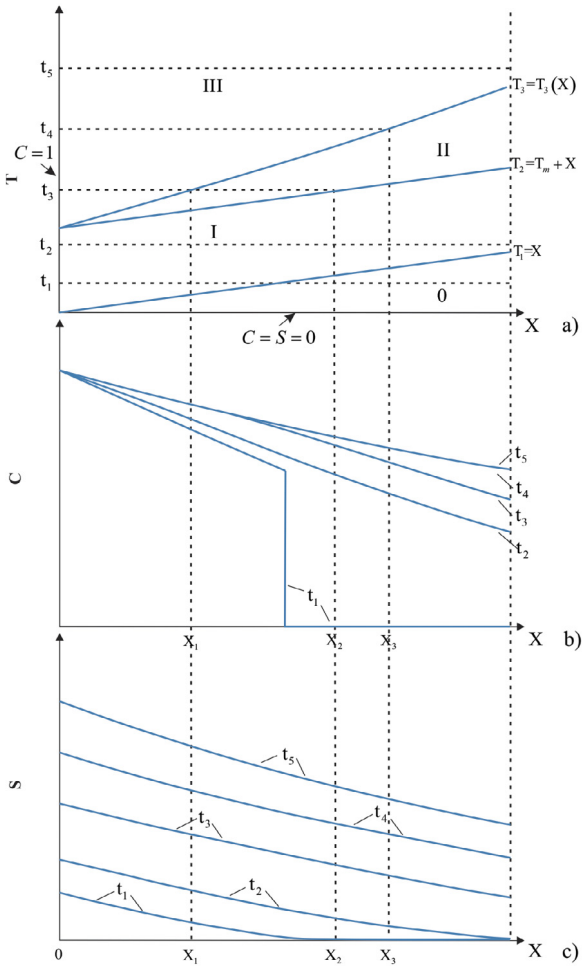


Fig. 5. Exact solution for 1D suspension-colloidal flow with piecewise-linear filtration function: (a) movement of concentration fronts (x, t)-plane; (b) suspended concentration profiles; (c) retained concentration profiles.

Representing Eq. (32) in characteristic form with T as a parameter along characteristics shows that $S_1=S_2=0$ at $T<X$ (Fig. 5a).

Characteristic form of Eq. (32) at $T>X$ is

$$\frac{dS_1}{dX}=\Lambda^1\left(S_1\right)\left[-S_1+\frac{S_m\Lambda_1}{\Lambda_0}\ln\left(1-\frac{S_1}{S_m}\right)\right],\ \frac{dT}{dX}=1 \tag{33}$$

At $T=0$, where $C=1$, separation of variables in Eq. (27) results in

$$S_1(0,T)=S_m\left[1-\exp(-\frac{\Lambda_0}{S_m}T)\right] \tag{34}$$

Integration of ODE (33) along the characteristic line results in

$$\int_{S_1(0,T-X)}^{S_1(X,T)}\frac{dS_1}{\Lambda_0(1-\frac{S_1}{S_m})\left[S_1-\frac{S_m\Lambda_1}{\Lambda_0}\ln(1-\frac{S_1}{S_m})\right]}=-X \tag{35}$$

Substitution of expression (34) into Eq. (35) determines S_1 in implicit form:

$$\int_{S_m\left[1-\exp\left[-\frac{\Lambda_0}{S_m}(T-X)\right]\right]}^{S_1(X,T)}\frac{dS_1}{\Lambda_0(1-\frac{S_1}{S_m})\left[S_1-\frac{S_m\Lambda_1}{\Lambda_0}\ln(1-\frac{S_1}{S_m})\right]}=-X \tag{36}$$

$S_2(0,T)$ is calculated from Eq. (28) with $C=1$:

$$S_2(0,T)=\Lambda_1 T \tag{37}$$

Using Riemann invariant C/S (25) of system (26)–(28) and Eqs. (14), (36) allows calculating suspended concentration $C(X, T)$:

$$\frac{C(X,T)}{S_1(X,T) - \frac{S_m \Lambda_1}{\Lambda_0} \ln\left[1 - \frac{S_1(X,T)}{S_m}\right]} = \frac{1}{S_m\left[1 - \exp\left[-\frac{\Lambda_0}{S_m}(T-X)\right]\right] + \Lambda_1 (T-X)} \tag{38}$$

Both retained concentrations are zero along the concentration front $T_1(X) = X$. The suspended concentration behind the front $C^-(T, T)$ is calculated from Eq. (26):

$$C^-(T,T) = \exp\left[-\left(\Lambda_0 + \Lambda_1\right) T\right] \tag{39}$$

The solution shows that initial data are held ahead of the concentration front $T_1(X) = X$ (Fig. 5a). Behind the concentration front, the exact solution for $S_1(X, T)$ is expressed implicitly by transcendental Eq. (36), allowing for explicit calculation of S_2 using formula (14) and explicit calculation of $C(X, T)$ using formula (38).

Fig. 4a shows forms of aggregated filtration function (blue curve) and binary filtration function (red curve). Fig. 4b shows breakthrough concentrations $C(1, T)$ as obtained from the least square fit [43] by using the binary model (red curve), which is obtained for $\Lambda_0 = 0.2151$, $\Lambda_1 = 0.4780$ and $S_m = 0.5614$. The tuning data for this laboratory test and the coefficient of determination are presented in eighth row of Table 2. The blue curve corresponds to aggregated model with $S_m = 0.1164$. BTCs at $T = 1$ and their stabilised values are the same, so the filtration coefficients Λ_0 and Λ_1 are the same for both models.

Fig. 4c also shows the comparison between matching the laboratory data by the binary and aggregated models. The filtration coefficients for both models are $\Lambda_0 = 0.3318$ and $\Lambda_1 = 0.8557$. Maximum retained concentrations are $S_m = 0.4331$ and $S_m = 0.1005$ for binary and aggregated models, respectively. The tuning data for this laboratory test and the coefficient of determination are presented in fifth row of Table 2.

3.4. Properties of aggregated function for two capture mechanisms

Eq. (39) shows that suspended concentration at the breakthrough time $T = 1$ is equal to

$$C(1,1) = \exp\left(-\Lambda_0 - \Lambda_1\right) \tag{40}$$

Eq. (38) shows that at $T \to \infty$, suspended concentration tends to

$$C(1,\infty) = \exp\left(-\Lambda_1\right) \tag{41}$$

Formulae (40) and (41) allow determining both filtration coefficients from the breakthrough curve

$$\Lambda_1 = -\ln\left[C(1,\infty)\right] \tag{42}$$

$$\Lambda_0 = \ln\left[\frac{C(1,\infty)}{C(1,1)}\right] \tag{43}$$

The parameter S_m is determined by matching the BTC at intermediate times $[1,\infty)$.

Now let us describe some properties of the aggregated filtration function.

At $S = 0$, as it follows from Eqs. (27), (28),

$$\Lambda(0) = \Lambda_0 + \Lambda_1 \tag{44}$$

For large retention concentrations,

$$\lim_{S\to\infty} \Lambda(S) = \Lambda_1 \tag{45}$$

Lemma 2. *The aggregated filtration function is convex, i.e. $\Lambda''(S)>0$.*

The derivative of $\Lambda = \Lambda(S)$ is calculated from Eq. (16)

$$\frac{d\Lambda(S)}{dS} = -\frac{\Lambda_0}{S_m}\frac{dS_1(S)}{dS} \tag{46}$$

where

$$\frac{dS_1(S)}{dS} = \left(1 - \frac{S_m \Lambda_1}{\Lambda_0 S_m - \Lambda_0 S_1 + S_m \Lambda_1}\right) \tag{47}$$

Substituting Eq. (47) into Eq. (46) yields

$$\frac{d\Lambda(S)}{dS} = -\frac{\Lambda_0}{S_m}\left(1 - \frac{S_m \Lambda_1}{\Lambda_0 S_m - \Lambda_0 S_1 + S_m \Lambda_1}\right) \tag{48}$$

The second derivative can be calculated from Eq.(48)

$$\frac{d^2\Lambda(S)}{dS^2} = \frac{\Lambda_1 \Lambda_0^2}{\left(\Lambda_0 S_m - \Lambda_0 S_1 + \Lambda_1 S_m\right)^2}\frac{dS_1(S)}{dS} > 0 \tag{49}$$

Taking derivative of Eq. (15) shows that $dS/dS_1>0$, which proves the lemma.

Now we introduce the binary filtration function as a total of linear and constant filtration coefficient, as given in Eq. below:

$$\Lambda(S) = \begin{cases} \Lambda_0\left(1 - \frac{S}{S_m}\right) + \Lambda_1 & , S \le S_m \\ \Lambda_1 & , S > S_m \end{cases} \tag{50}$$

Lemma 3. *Let the aggregated and binary filtration functions have the same values of coefficients Λ_0, S_m and Λ_1. The aggregated filtration function is higher than the corresponding binary filtration function.*

Derivative of the aggregated function (16) is obtained from Eq. (48)

$$\left.\frac{d\Lambda(S)}{dS}\right|_{S=0} = -\frac{{\Lambda_0}^2}{S_m\left(\Lambda_0 + \Lambda_1\right)} \tag{51}$$

Derivative of the binary function (50) is:

$$\left.\frac{d\Lambda(S)}{dS}\right|_{S=0} = -\frac{\Lambda_0}{S_m} \tag{52}$$

Slope (52) is lower than slope (51). Therefore, the curve is located above the straight line at some neighbourhood of $S = 0$. The curve $\Lambda(S)$ is convex, so for all $S > 0$, curve is located above the straight line. The curve is located above horizontal straight line, $\Lambda(S) = \Lambda_1$, which proves the lemma.

Blue curve in Fig. 4a possesses the above mentioned properties.

3.5. Asymptotic formulae for aggregated filtration function

Consider the case of small filtration coefficient of Langmuir blocking function. Substituting $\varepsilon\Lambda_0$ instead of Λ_0 in Eqs. (50) and keeping zero and first terms in Taylor series yields the explicit formula

$$\Lambda(S) = \Lambda_1 + \varepsilon\Lambda_0 \tag{53}$$

Green and black curves in Fig. 8a correspond to $\varepsilon = 0.1$ and $\varepsilon = 0.3$. The forms of both filtration curves correspond to dominant straining. The corresponding BTC curves in Fig. 8b exhibit variation that has order of magnitude ε. The higher is the filtration coefficient Λ_0, the lower is the BTC.

Now consider the case of small constant filtration coefficient Λ_1. Substituting $\varepsilon\Lambda_1$ instead of Λ_1 in Eqs. (50) and keeping zero and first terms in Taylor series yields the explicit formula

$$\Lambda(S) = \Lambda_0\left(1 - \frac{S}{S_m}\right) + \varepsilon\Lambda_1\left[1 - \ln\left(1 - \frac{S}{S_m}\right)\right] \tag{54}$$

Red and blue curves in Fig. 8a correspond to $\varepsilon = 0.1$ and $\varepsilon = 0.3$. The declined intervals of the filtration curves correspond to attachment, while the stabilised intervals correspond to straining. The forms of both filtration curves show that attachment capture mechanism dominates.

4. Exact solutions for binary filtration function

In this section we derive the explicit formulae for solution for the case of binary filtration function (50).

Ahead of concentration front $X > T$ in zone 0, $C = S = 0$ (Fig. 5a).

Table 1
Fitted parameters from binary analytical model.

Porous media	r_p (μm)	r_s (μm)	C^0 (L^{-1})	Λ_1	Λ_0	S_m	T_m	T_{inj}	T_3	R^2
Glass beads	20	0.225	4.24×10^{11}	0.4155	0.0788	0.4531	0.9986	2.8186	2.5603	0.9168
		0.5	3.86×10^{10}	1.6869	0.2793	1.6987	0.9319	3.2511	6.3653	0.9506
		1	4.85×10^{9}	1.8209	0.7048	2.5257	1.1725	3.4887	9.3540	0.9492
Sand 70110	11.5	0.225	4.24×10^{11}	0.3696	0.4744	0.5376	0.9357	1.9538	2.5862	0.9657
		0.5	3.86×10^{10}	0.5108	0.5390	1.5146	2.0242	1.8827	5.0008	0.9950
		1	4.85×10^{9}	2.8276	–	–	–	1.8467	–	–
Sand 3550	27.5	0.225	4.24×10^{11}	0.1863	0.1162	0.2719	1.1343	1.7662	2.4332	0.9510
		0.5	3.86×10^{10}	0.1393	0.0839	0.1851	1.0401	1.7767	2.2387	0.8757
		1	4.85×10^{9}	1.5344	–	–	–	1.7873	–	–
Sand 2030	54.5	0.225	4.24×10^{11}	0.1508	0.0849	0.1879	0.9883	1.5921	2.1911	0.9572
		0.5	3.86×10^{10}	0.1924	–	–	–	1.5241	–	–
		1	4.85×10^{9}	0.6349	0.3327	0.7675	0.9720	1.7583	3.0440	0.8542

Table 2
Fitted parameters from binary analytical model — Injection time: $T_{inj} = 2.8$ PVI.

Porous media	r_p (μm)	r_s (μm)	C^0 (L^{-1})	γ (mM)	Λ_1	Λ_0	S_m	T_m	T_3	R^2
Glass beads	25.4	0.0315	3.6×10^{12}	20	0.1221	0.1263	0.2695	1.5146	2.8012	0.8725
			2.2×10^{12}	30	0.6636	0.2039	0.6212	0.8164	2.6980	0.9579
			5.8×10^{11}	33	2.0402	0.3677	2.4572	1.1073	10.167	0.8624
		0.16	6.6×10^{10}	20	0.0513	0.1844	0.0963	0.7964	1.8953	0.9190
			2.8×10^{10}	30	0.4780	0.2151	0.5614	0.9697	2.6895	0.8778
			1.7×10^{10}	40	1.2040	0.2231	1.4718	1.1215	4.9739	0.9003
			1×10^{10}	30	0.4080	0.3260	0.1931	0.3561	1.6001	0.8440
		1.5	5×10^{9}	100	0.8557	0.3318	0.4331	0.4277	2.1125	0.8537
			5.1×10^{9}	300	1.8326	0.3747	0.4407	0.2188	2.4819	0.7542

The potential Φ is calculated explicitly:

$$\Phi(S) = \frac{\Lambda_0}{S_m} \ln\left[\frac{\Lambda_0 + \Lambda_1}{\Lambda_0\left(1 - \frac{S}{S_m}\right) + \Lambda_1}\right] \tag{55}$$

It allows calculating retention concentration at the inlet:

$$S(0,T) = \begin{cases} \dfrac{\Lambda_0 + \Lambda_1}{\Lambda_0} S_m \\ \quad \times\left(1 - \exp\left(-\frac{\Lambda_0}{S_m} T\right)\right), & T < T_m = -\dfrac{S_m}{\Lambda_0} \ln\left(\dfrac{\Lambda_1}{\Lambda_0 + \Lambda_1}\right) \\ \Lambda_1 (T - T_m) + S_m & T < T_m \end{cases} \tag{56}$$

where T_m is a moment when retained concentration at the inlet reaches the value S_m.

The explicit solution in zone I is calculated by formulae (24), (56):

$$S(X,T) = \frac{S_m \frac{(\Lambda_0 + \Lambda_1)}{\Lambda_0}\left(1 - \exp\left[-\frac{\Lambda_0}{S_m}(T - X)\right]\right)}{\left[1 - \exp\left[-\frac{\Lambda_0}{S_m}(T - X)\right]\right] + \exp\left[\left(\Lambda_0 + \Lambda_1\right) X - \frac{\Lambda_0}{S_m}(T - X)\right]\Big]} \tag{57}$$

Suspended concentration is calculated from Riemann invariant (38) as:

$$C(X,T) = \left[1 - \exp\left[-\frac{\Lambda_0}{S_m}(T - X)\right] + \exp\left[\left(\Lambda_0 + \Lambda_1\right) X - \frac{\Lambda_0}{S_m}(T - X)\right]\right]^{-1} \tag{58}$$

In zone III where $S > S_m$, the filtration function is constant and equal to Λ_1. The solution is determined from Eqs. (24), (38), (56):

$$C(X,T) = \exp\left(-\Lambda_1 X\right) \tag{59}$$

$$S(X,T) = \left[\Lambda_1\left(T - X - T_m\right) + S_m\right] \exp\left(-\Lambda_1 X\right) \tag{60}$$

The front boundary of zone III, where $S = S_m$, is calculated from Eq. (60):

$$T = \frac{S_m}{\Lambda_1}\left[\exp\left(\Lambda_1 X\right) - 1\right] + X + T_m \tag{61}$$

The solution in zone II is determined by Eqs. (24), (38) along the characteristic straight lines with boundary condition $S = S_m$ at the moving boundary (61): Eqs. (62) and (63) are given in Box I. Fig. 5b and c show suspended and retained concentration profiles at five different moments. Profile at the moment t_1 before the breakthrough encompasses zones 0 and I. At the moment t_2 after the breakthrough, the profile corresponds to zone I. Moment t_3 represents zones III, II and I. Moment t_4 represents zones III and II, at the moment t_5 only zone III remains in the profile. Fig. 5c shows monotonic increase of retained concentration during accumulation according to retention rate (10). Monotonically decreasing filtration function (50) yields monotonic increase of suspended concentration (Fig. 5b).

5. Sensitivity study

Fig. 6a shows the sensitivity of the aggregated and binary filtration functions for two commingled capture mechanisms with respect to Λ_0 and Λ_1. Fig. 6b shows the corresponding BTCs. Continuous curves correspond to aggregated filtration function, while the results for binary filtration function are shown by dashed curves. Increase in Λ_1 yields increase of both filtration functions. Points $S = 0$ and $S \to \infty$ in Fig. 6a shift up by the values of Λ_1. Increase in Λ_0 also yields the increase in filtration functions, but the asymptotic values remain the same. The higher is the filtration function, the lower is the breakthrough concentration, so BTCs move down with increase of either Λ_0 or Λ_1.

Fig. 7a shows the behaviour of both filtration functions given for different S_m. Points $S = 0$ and $S \to \infty$ with changing S_m in Fig. 7a and points $T = 0$ and $T \to \infty$ *in Fig. 7b remain the same. The larger is the* S_m *the slower is the stabilisation of the filtration function at the value* $\Lambda(S) = \Lambda_1$ (Fig. 7b).

Fig. 8a presents sensitivity study of aggregated filtration function with small blocking (green and black curves) and small straining (red and blue curves) as calculated by formulae (53) and (54). Fig. 8b shows the corresponding BTCs. The higher is the filtration function, the lower is the BTC.

6. Comparison between exact and numerical solutions

Fig. 4b and c show the comparison between the exact and numerical solutions. The black dashed curves correspond to numerical solutions for the same values of the model coefficients that are obtained in

$$S(X,T) = \frac{S_m(\Lambda_0+\Lambda_1)}{\Lambda_1 \exp\left[(\Lambda_0+\Lambda_1)\left(X - \frac{1}{\Lambda_1}\ln\left[\frac{\Lambda_1}{S_m}(T-X-T_m)+1\right]\right)\right]+\Lambda_0} \tag{62}$$

$$C(X,T) = \frac{S_m(\Lambda_0+\Lambda_1)}{\left[\Lambda_1(T-X-T_m)+S_m\right]\left\{\Lambda_1 \exp\left[(\Lambda_0+\Lambda_1)\left(X - \frac{1}{\Lambda_1}\ln\left[\frac{\Lambda_1}{S_m}(T-X-T_m)+1\right]\right)\right]+\Lambda_0\right\}} \tag{63}$$

Box I.

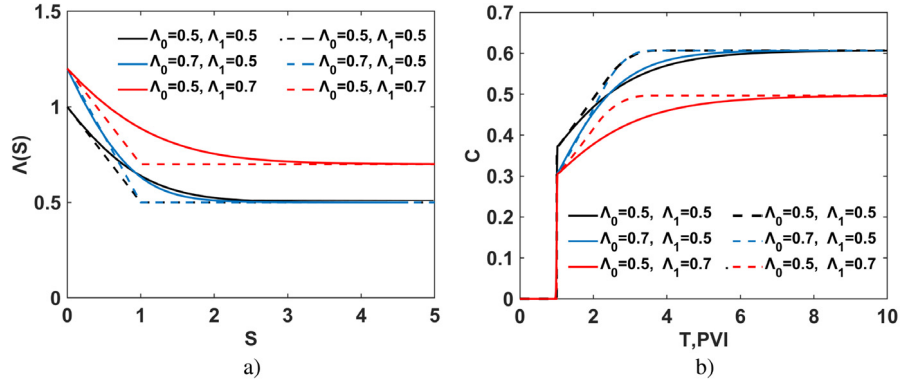


Fig. 6. Exact and approximate forms of filtration function for two simultaneous capture mechanisms and sensitivity analysis with respect to Λ_0, and Λ_1 where $S_m = 0.5$: (a) filtration functions; (b) breakthrough curves.

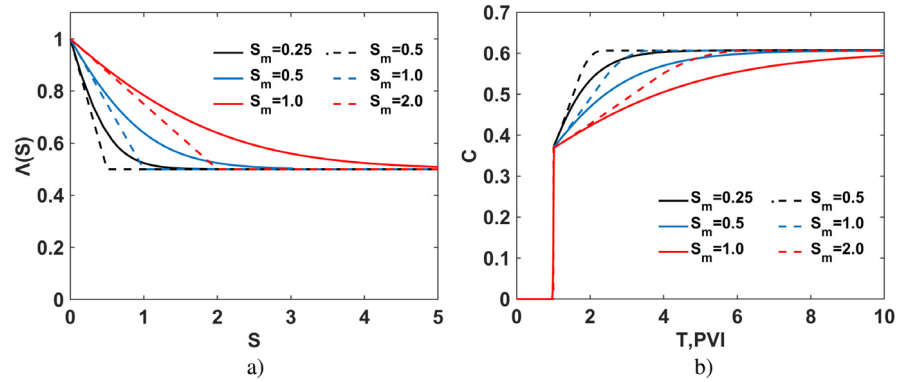


Fig. 7. Exact and approximate forms of filtration function for two simultaneous capture mechanisms and sensitivity analysis with respect to S_m where $\Lambda_0 = \Lambda_1 = 0.5$: (a) filtration functions; (b) breakthrough curves.

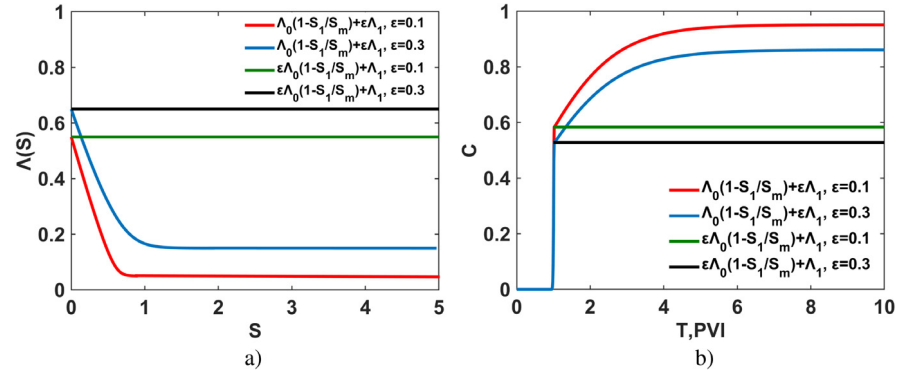


Fig. 8. Aggregated filtration function with small straining $\varepsilon\Lambda_1$ (red and blue curves for $\varepsilon = 0.1$ and $\varepsilon = 0.3$, respectively) and small attachment $\varepsilon\Lambda_0$ (green and black curves for $\varepsilon = 0.1$ and $\varepsilon = 0.3$, respectively) using asymptotic formulae for aggregation: (a) forms of filtration functions; (b) breakthrough curves. (For interpretation of the references to colour in this figure legend, the reader is referred to the web version of this article.)

Section 3.3 by matching the laboratory data using the binary and aggregated filtration functions.

The governing equations (26)–(28) subject to initial and boundary conditions (11), (12) were solved numerically using the Shampine's

software package [44,45]. The algorithm implements a two-step Lax–Friedrichs finite-difference method [45]. The Matlab computer program, and pertinent supporting information are available from http://faculty.smu.edu/shampine/current.html. The space and time steps employed in the finite-difference method are $\Delta X = 0.0001$, $\Delta T = 0.00009$. Numerical solutions for aggregated and binary filtration functions are given by black dashed curves.

The numerically and analytically calculated curves coincide.

7. Analysis of the results of laboratory data tuning

This section treats the laboratory data using the analytical model (57)–(63) for binary retention function. Calculations of electrostatic forces (using the DLVO theory, [10,19]) show that the particles are attracted to the rock surface.

The results of injection of particles with radii $r_s = 0.225$, 0.5, and 1.0 μm into porous media with pore radii $r_p = 20$, 11.5, 27.5, and 54.5 μm are shown in Fig. 9 [1]. Fig. 9a, d, g, and j present the results of injection of particles with radius $r_s = 0.225$ μm. Fig. 9b, e, h, and k present the results of injection of particles with radius $r_s = 0.5$ μm. Fig. 9c, f, i, and l present the results into pores with radius $r_s = 1$ μm. Table 1 presents the injected concentrations and the matching results using the analytical model for binary filtration function.

Fig. 10 shows the dependencies of three model parameters of jamming ratio

$$j = \frac{r_s}{r_p} \tag{64}$$

where r_s and r_p are the particle and pore radii, respectively.

Assume that Langmuir blocking function corresponds to monolayer attachment of particles, and the filtration coefficient Λ_1 is for straining. Fig. 10a, b, c, and d corresponds to four series of tests with different porous media. The larger are the particles, the stronger is the electrostatic particle–rock attachment, and the higher is the filtration coefficient Λ_0 [1,4,10]. The larger are the particles, the higher is the surface occupied by one particle, and the lower is the total concentration of attached particles that cover the overall rock surface. The larger are the particles, the higher is the jamming ratio, and the higher is the straining filtration coefficient Λ_1 [2,18,21].

Fig. 11 shows 9 tests with injection of particles with three different radii $r_s = 0.0315$ μm, $r_s = 0.16$ μm, and $r_s = 1.5$ μm in the same porous media with $r_p = 25.4$ μm [46]. Different salinities 20, 30, 33, 40, 100 and 300 are used. Fig. 12a, b and c corresponds to $r_s = 0.0315$ μm, $r_s = 0.16$ μm, and $r_s = 1.5$ μm, respectively.

The higher is the salinity the higher is the electrostatic grain-particle attraction, the higher is filtration coefficient Λ_1. The higher is the attraction, the more compact occupation of the rock surface occurs, and the higher is the S_m [1,4,46]. The same dependency of straining coefficient Λ_1 versus salinity takes place. It is explained by increasing attachment to pore throats with salinity increase, so the throats become thinner, jamming ratio decreases, and the filtration coefficient for straining increases [1,4,10,46].

The cases for $r_s = 0.16$ μm and $\gamma = 30$ mM, and $r_s = 1.5$ μm and $\gamma = 100$ mM have been treated by the aggregated model. Fig. 4b and c show the binary model by red curves, and blue curves correspond to aggregated model. The aggregated model presents more precise match than the binary model. The coefficient of determination R^2 is higher for the aggregated model for all the cases which have been calculated.

8. Chemical reactive flow with multiple reactions: aggregation, exact solution

The aggregation technique (Appendices A and B) and introduction of potential yielding an exact solution (Section 3.2) can be extended for the case of chemical reactive flow with multiple reactions between the fluid and multicomponent rock.

Mass balance for reacting fluid flowing through the multicomponent rock is

$$\phi \frac{\partial c}{\partial t} + U \frac{\partial c}{\partial x} = -\sum_k \frac{1}{n_k} \frac{\partial y_k}{\partial t} \tag{65}$$

where ϕ is the porosity, c is the molar concentration of reagent dissolved in the fluid, U is Darcy velocity, y_k is the molar concentration of kth component in the rock, n_k is the number of moles reacting with one molar of the fluid component (stoichiometric coefficient).

The reaction rate for kth component is

$$\frac{\partial y_k}{\partial t} = -K_{ak} c y_k^{n_k} \tag{66}$$

where K_{ak} is the kinetic coefficient.

Initial and boundary conditions corresponding to reacting fluid injection into porous media are:

$$t = 0 : y_k = y_{k0}, \quad c = 0 \tag{67}$$

$$x = 0 : c = c^0 \tag{68}$$

Adding Eq. (66) we obtain the expression for the total reaction rate

$$\frac{\partial y}{\partial t} = -c \sum_k K_{ak} y_k^{n_k} \tag{69}$$

For fixed x, Eq. (69) form system of n ODE for unknowns $y_k = y_k(t)$. Changing independent variable from t to y and performing chain differentiation in Eq. (69) yields a system of n ODE for unknowns $y_k = y_k(y)$

$$\frac{dy_k}{dy} = \frac{K_{ak} y_k^{n_k}}{\sum_k K_{ak} y_k^{n_k}} \tag{70}$$

As it follows from Eq. (67), initial conditions for system (70) are:

$$t = 0 : y_{k0}, \; y_0 = \sum_k y_{k0} \tag{71}$$

The solution of system (70) subject to initial conditions (71) is

$$y_k = y_k(y) \tag{72}$$

Calculations of mass balance follow from Eq. (65):

$$\phi \frac{\partial c}{\partial t} + U \frac{\partial c}{\partial x} = -\frac{\partial}{\partial t} \sum_k \frac{y_k(y)}{n_k} = -\frac{\partial G(y)}{\partial t}, \quad G(y) = \sum_k \frac{y_k(y)}{n_k} \tag{73}$$

Calculations of the total reactive rate follow from Eq. (69):

$$\frac{\partial y}{\partial t} = -c \sum_k K_{ak} y_k^{n_k}(y) = -c F(y), \quad F(y) = \sum_k K_{ak} y_k^{n_k}(y) \tag{74}$$

Finally, we obtain system of 2×2 partial differential equations

$$\phi \frac{\partial c}{\partial t} + U \frac{\partial c}{\partial x} = -\frac{\partial G(y)}{\partial t}, \frac{\partial y}{\partial t} = -c F(y) \tag{75}$$

with the following initial and boundary conditions

$$t = 0 : y_0 = \sum_k y_{k0}, \; c = 0$$
$$x = 1 : c = c^0 \tag{76}$$

The exact solution of the problem (75), (76) is obtained using the method of potential, presented in Section 3.2. Introduction of potential from Eq. (17), its substitution into Eq. (75) and integration in t reduces the system to one scalar hyperbolic equation. This equation is solved by method of characteristics, like in Section 3.2.

9. Summary and discussion

Nonlinear methods of aggregation and potential We derived exact solutions for several non-linear initial–boundary value problems corre-

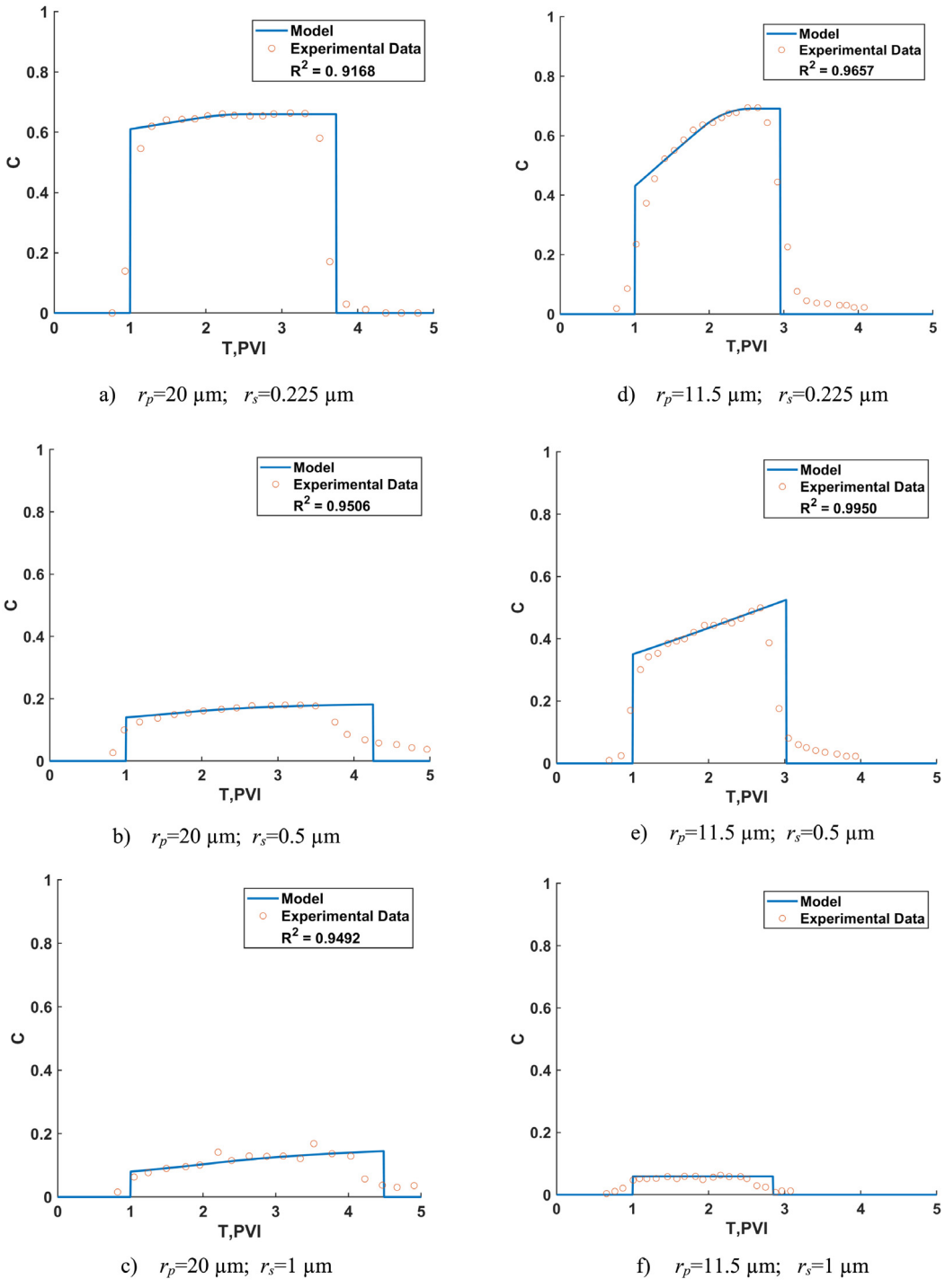


Fig. 9. Matching the breakthrough curves by the analytical model; the laboratory data are taken from paper [1].

sponding to two-capture deep be filtration. The solution process includes two developments:

1 – Introduction of a free variable, which is equal to the total retained concentration, instead of time, in n ODEs for capture kinetics (A.3) that yields the reduction of $(n+1) \times (n+1)$ classical advection–diffusion system (A.1)–(A.3) to 2×2 system (1), (2);

2 – Introduction of potential (17) that reduces 2×2 aggregated diffusion-free system (9), (10) to a scalar first order hyperbolic equation, where method of characteristics yields implicit solution (36) and explicit solution (57)–(63).

The first aggregation procedure is applied for a modified advection–diffusion system (1), (6), yielding its reduction to 2×2 system (1), (6).

The so-called aggregated procedure reduces system with n different particle capture mechanisms to a single-capture system. The binary filtration function is the approximation of the aggregated function, which is obtained for two capture mechanisms with constant and blocking (Langmuir) filtration functions.

In the case where of small retained concentrations and constant filtration functions, non-linear systems (A.1)–(A.3) and (A.1), (A.2), (B.1) degenerate into linear systems. The aggregation procedure degenerates

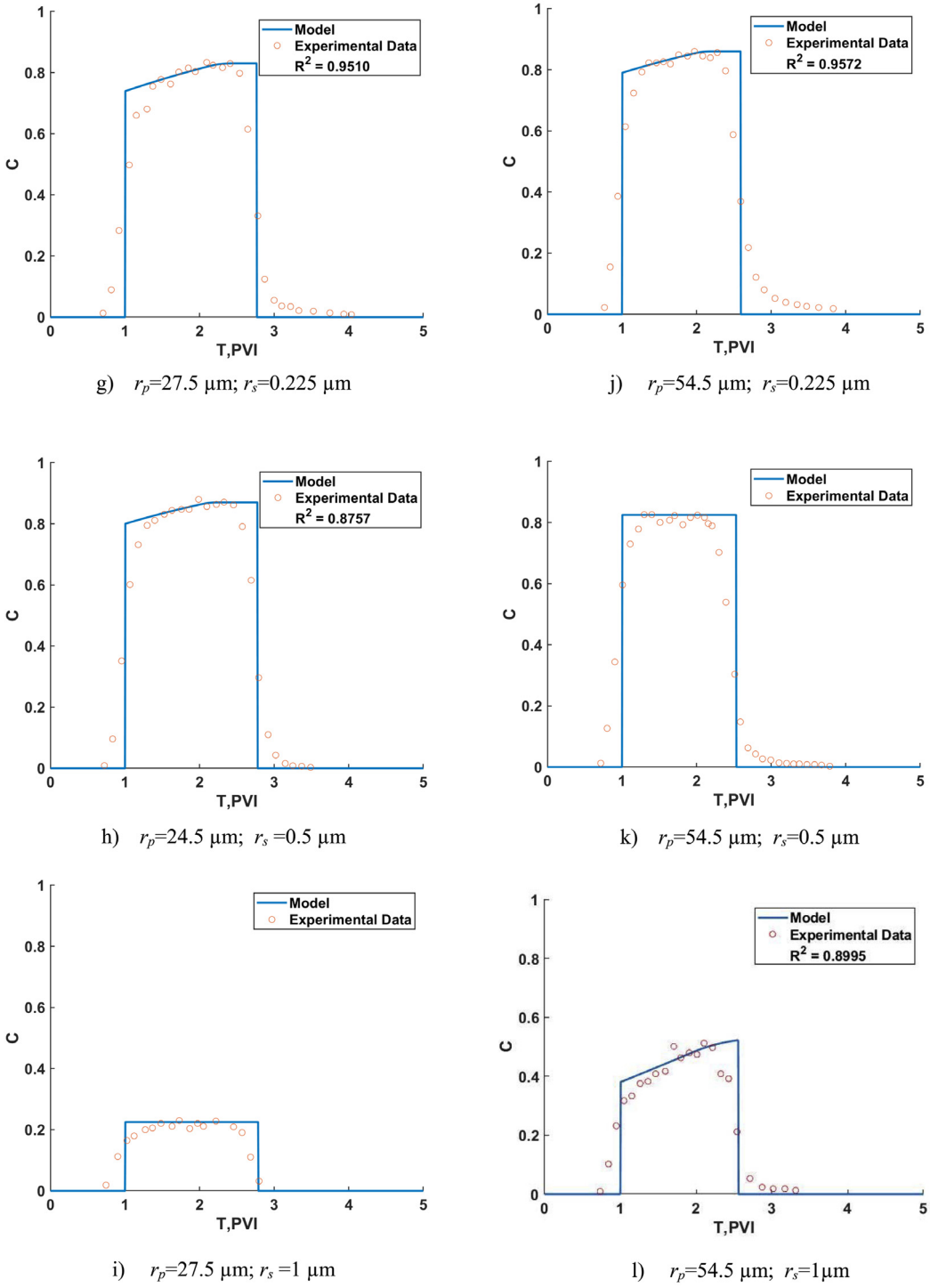


Fig. 9. (*continued*)

into the sum of individual filtration constants. The exact solutions of linear systems (1), (2), (A.1)–(A.3) and (A.1), (A.2), (B.1) exhibit steady state suspension concentration behind the front $T_1(X) = X$, and retained concentrations accumulating linearly with time. Even for two-capture system $n = 2$ with one varying filtration function, the system becomes non-linear, and the solution is significantly more complex.

Matching of BTCs with constant concentration by constant filtration function, and BTCs with concentration monotonically increasing up to the injected concentration, is widely applied in suspension-colloidal studies [1,4,10,46]. The exact solutions derived show that both aggregated and binary filtration functions exhibit BTCs where concentration monotonically increases up to the value that is lower than the injected concentrations; this type of BTCs is also widely spread for suspension-colloidal systems [1,13,22,46].

The exact solution for binary filtration function (Eqs. (57)–(63)) contains explicit formulae only, which is an advantage for tuning the

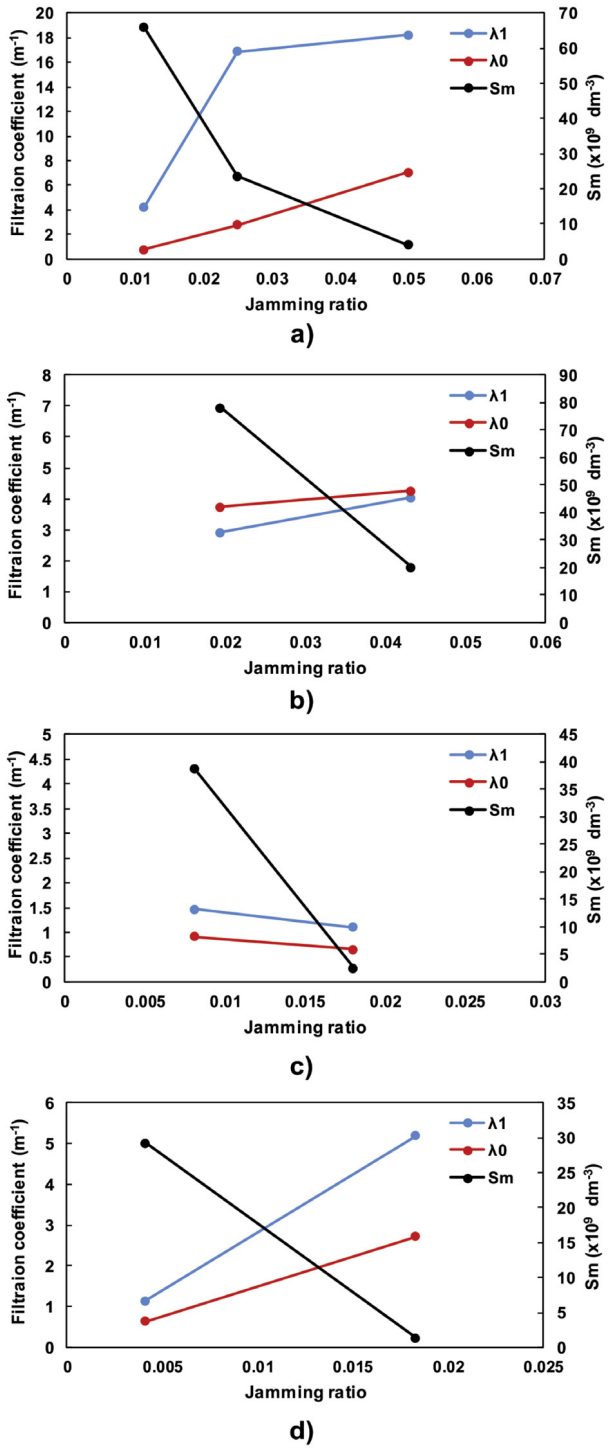


Fig. 10. Jamming-ratio dependency for the dimensional filtration coefficients and maximum retained particle concentration: (a) Glass breads (r_p = 20 μm); (b) Sand 70 110 (r_p = 11.5 μm); (c) Sand 3550 (r_p = 27.5 μm); (d) Sand 2030 (r_p = 54.5 μm) [1].

laboratory data, and also for 3D modelling using streamline simulators. The exact solution for aggregated filtration function contains implicit integral expressions.

Both binary and aggregated filtrations functions are fully determined by three constants: the initial attachment filtration coefficient Λ_0, maximum concentration for attachment vacancies S_m, and the filtration coefficient for size exclusion Λ_1. The total of Λ_0 and Λ_1 can be determined directly from the breakthrough concentration at the arrival time of 1PVI. The filtration coefficient for size exclusion Λ_1 can be determined directly from the stabilised breakthrough concentration with time tending to infinity. The maximum concentration for attachment vacancies must is determined by matching of the intermediate values of breakthrough concentrations.

The values Λ_0, Λ_1 and S_m as obtained from tuning the binary filtration function, can be used as initial value for tuning the exact aggregation function using minimisation least square iterative algorithm [43]. The overall calculations with minimisation using the exact aggregated function and software Shampaine is about 2 h, while the procedure using the piecewise-linear binary function takes about 1 min only. Moreover, sometimes the minimisation procedure after matching by the binary filtration function is not necessary. In the cases of r_s = 0.16 μm and γ = 30 mM, and r_s = 1.5 μm and γ = 100 mM, the minimisation provides only 7%–10% improvement, respectively, reducing coefficient of determination from R^2 = 0.9754 to R^2 = 0.8778, and R^2 = 0.9153 to R^2 = 0.8537.

The model validity Main purposes of matching the experimental results are prediction of the laboratory data for planning of the new tests, and the laboratory-based prediction of 3D reservoir behaviour. For both purposes, both aggregated and binary models match the laboratory data with high accuracy.

However, the aggregated model is derived from first principles, while the binary model is its approximation. The laboratory tests have been treated by both aggregated and binary models. The coefficient of determination R^2 is always higher for the aggregated model (Fig. 4b, c). This fact supports the validity of the aggregated model.

Applications The aggregation method (Lemma 1 in Section 2) and introduction of potential (18) yield exact solutions for numerous 1D suspension-colloidal transport processes in porous media.

Initial and boundary conditions (11), (12) correspond to injection of suspensions and colloids into clean bed. In exact solutions for non-zero initial retained concentration S_I, the value S_I adds to the clean-bed solution given by Eqs. (36) and (62).

Migration of natural reservoir fines corresponds to initial and boundary conditions

$$t = 0 : c_i = c_i^0,\ \sigma = 0, x = 0 : c_i = 0 \tag{77}$$

The aggregated Lemma 1 is fulfilled for the problem (1)–(3) and (77); the solution method is the same as that developed in Sections 3.3 and 4.

For the sake of simplicity, the Langmuir blocking function is attributed to attachment, and constant filtration function to straining. However, upscaling the transport of mono-sized suspensions in porous media with bimodal pore size distribution with straining yields the blocking Langmuir filtration function. Any of capture mechanisms with small retention corresponds to constant retention function [12] (Fig. 1).

Multiplying the flux U by the drift delay factor α in Eqs. (1), (2) and (A.1), (A.2) allows reflecting the phenomena of slow fines drift and rolling along the rock surface [39,47,48]. The translation $t \to \alpha t$ and rearranging dimensionless parameters reduces the problems to the original forms.

The aggregation method and introduction of the potential can be applied to suspension-colloidal flows of large particles with non-linear terms of changing porosity and flux in Eqs. (1), (2) and (A.1), (A.2) [7,22].

10. Conclusions

Derivation of exact solutions for non-linear 1D problems of suspension-colloidal transport in porous media with multiple capture

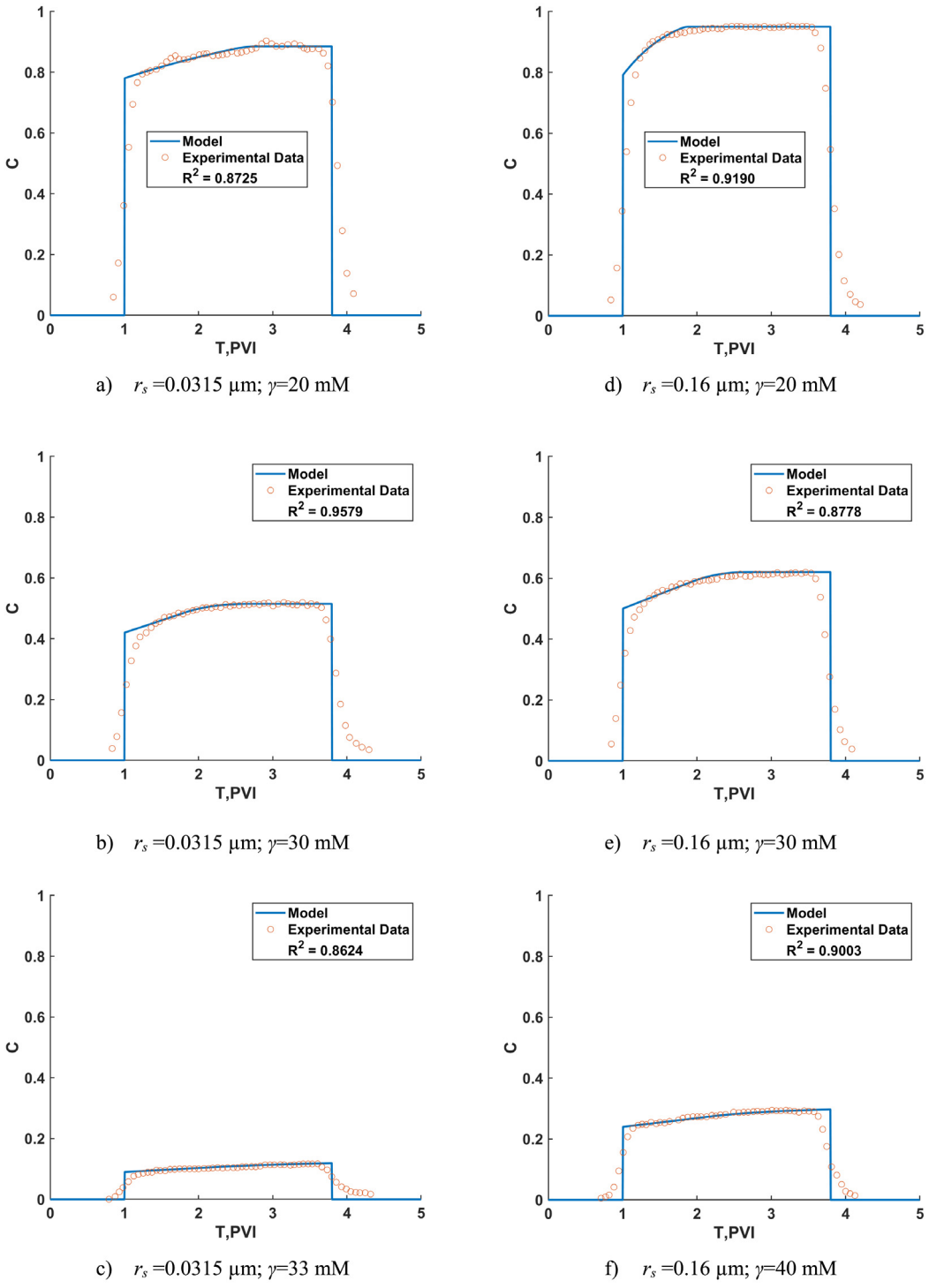


Fig. 11. Matching the breakthrough curves by the analytical model; the laboratory data are taken from paper [46].

mechanisms and development of the aggregation technique to reduce the multi-capture to single capture mechanism allow drawing the following conclusions:

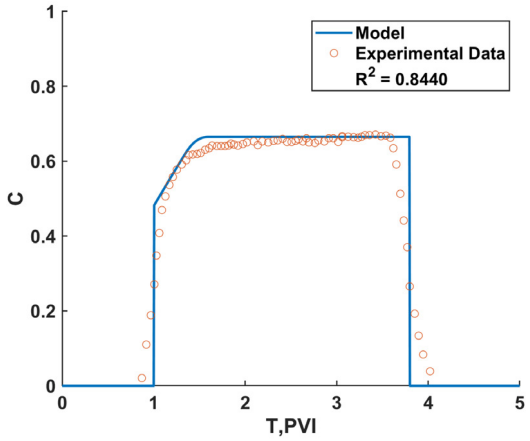
System of $n+1$ PDEs for colloidal-suspension advective–diffusive transport with n particle capture mechanisms is equivalent to the 2×2 system with single capture. The aggregated filtration function is obtained by solution of n non-linear ODEs.

The exact solutions are obtained for both aggregated model and its piecewise-linear approximation (so-called binary model).

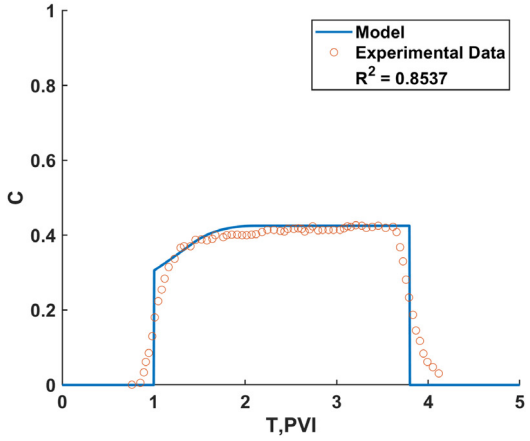
The solution for binary model is expressed by explicit formulae for suspended and retained concentrations, while that for aggregated model contains one transcendental equation with integral terms.

Both exact solutions exhibit BTCs with monotonic growth during several PVIs with further stabilisation at concentration that is lower than the injected concentration.

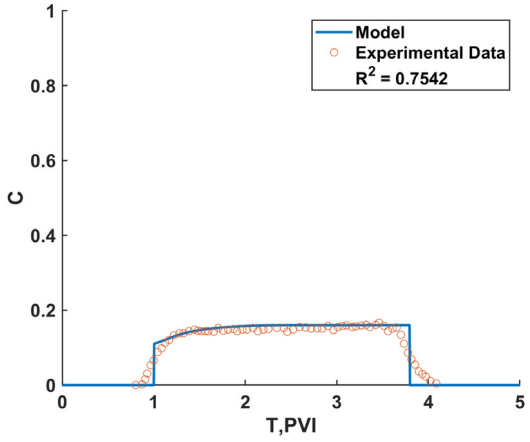
Both aggregated and binary models are determined by three constants – filtration coefficients Λ_0 and Λ_1, and maximum attachment



g) r_s =1.5 μm; γ=30 mM



h) r_s =1.5 μm; γ=100 mM



i) r_s =1.5 μm; γ=300 mM

Fig. 11. (*continued*)

capacity S_m. The filtration functions for both models take the same values at $S = 0$ and S tending to infinity. The corresponding BTCs also take the same values at the breakthrough moment $T = 1$ and at T tending to infinity. The aggregated function always exceeds the binary function, so BTC for aggregated function always lays below than that for the binary function.

The filtration coefficients Λ_0 and Λ_1 for both filtration functions are determined from stabilised BT concentration, and from the BT

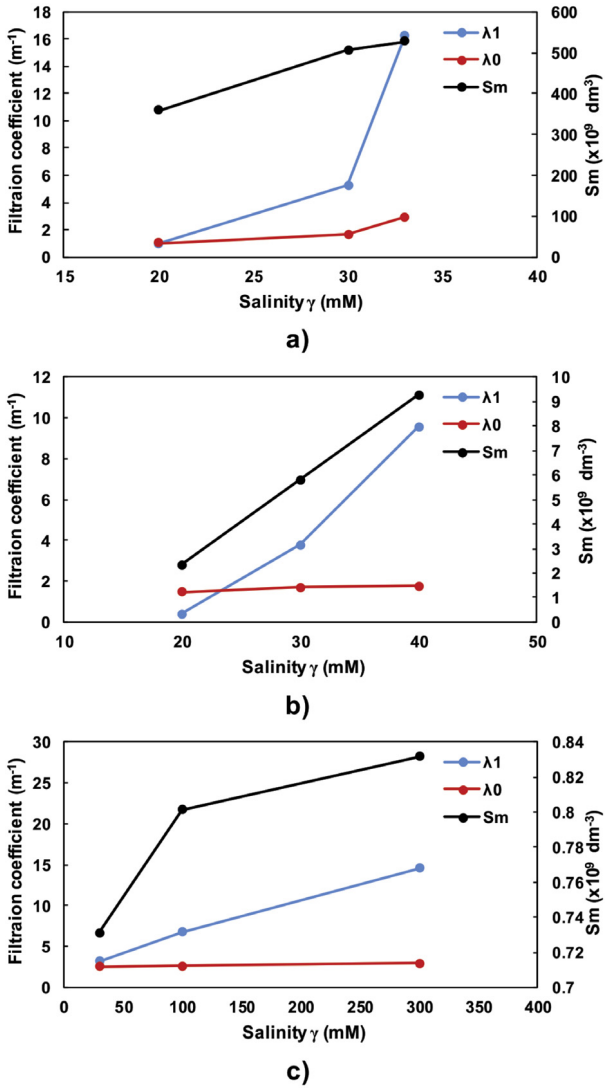


Fig. 12. Salinity dependency for the dimensional filtration coefficients and maximum retained particle concentration: (a) 0.0315 μm; (b) 0.16 μm; (c) 1.5 μm for Salinity vs. parameters [46].

concentration at the moment $T = 1$, leaving just one parameter S_m to be adjusted from the intermediate values of the BTC.

High accuracy of matching allows validating the interpretation of BTCs stabilising at lower value than injected concentration, by the model with binary filtration function.

Matching of numerous laboratory tests yields higher accuracy by the aggregated model than by the binary model.

The tuned model coefficients for different jamming ratios and salinities exhibit the same behaviour as that predicted by the theory of suspension-colloidal transport in porous media.

Appendix A. Proof of the aggregation lemma for multi-capture filtration with particle dispersion

This Appendix shows that colloidal-suspended system (1)–(3) of multiple-capture $(n+1) \times (n+1)$ can be reduced into the 2×2 system by a by the aggregation of n filtration coefficients into a single coefficient. The aggregated filtration coefficient can be expressed in term of the total retained concentration.

The $(n+1) \times (n+1)$ system of governing equation with advection and dispersion transport mechanisms consists of mass balance for suspended and retained particles [10,18,19]:

$$\frac{\partial}{\partial t}(c\phi + \sum_{i=1}^{n} \sigma_i) + \frac{\partial q}{\partial x} = 0 \tag{A.1}$$

$$q = cU - D\frac{\partial c}{\partial x} \tag{A.2}$$

and rate equations for n particle capture mechanisms

$$\frac{\partial \sigma_i}{\partial t} = \lambda_i\left(\sigma_1, \sigma_2 \cdots \sigma_n\right) cU, i = 1, 2 \cdots n \tag{A.3}$$

The sum of n kinetics (A.3) leads to the total particle capture rate,

$$\frac{\partial \sigma}{\partial t} = \sum_{i=1}^{n} \frac{\partial \sigma_i}{\partial t} = \left(\sum_{i=1}^{n} \lambda_i(\sigma_1, \sigma_2 \cdots \sigma_n)\right) cU \tag{A.4}$$

The total filtration coefficient is an algebraic sum of all filtration coefficients, which depends on all retained particle concentrations

$$\lambda(\sigma_1, \sigma_2 \cdots \sigma_n) = \sum_{i=1}^{n} \lambda_i(\sigma_1, \sigma_2 \cdots \sigma_n) \tag{A.5}$$

The total retained concentration is

$$\sigma = \sum_{i=1}^{n} \sigma_i \tag{A.6}$$

Fixing $x = x_0$ and assuming that $c\,(x, t)$ is already knows, yields a system of ordinary differential equations for retained concentrations

$$\frac{d\sigma_i}{dt} = \lambda_i(\sigma_1, \sigma_2 \cdots \sigma_n) cU \tag{A.7}$$

Time derivative of total retained concentration becomes

$$\frac{d\sigma}{dt} = \sum_{i=1}^{n} \frac{d\sigma_i}{dt} = \left(\sum_{i=1}^{n} \lambda_i(\sigma_1, \sigma_2 \cdots \sigma_n)\right) cU \tag{A.8}$$

Change independent variable in system (A.8) from t to σ:

$$\frac{d\sigma_i}{d\sigma} = \frac{d\sigma_i}{dt}\frac{dt}{d\sigma} = \frac{d\sigma_i}{dt} \Big/ \frac{d\sigma}{dt} = \frac{\lambda_i(\sigma_1, \sigma_2 \cdots \sigma_n)}{\left[\sum_{i=1}^{n} \lambda_i(\sigma_1, \sigma_2 \cdots \sigma_n)\right]} \tag{A.9}$$

Initial condition for system (A.9) follows from initial conditions (11) for each retained concentration:

$$\sigma = 0 : \sigma_i = 0, i = 1, 2 \ldots n \tag{A.10}$$

Substituting the solution of ODEs (A.9) subject to initial condition (A.10) into Eq. (A.5) allows expressing the aggregated filtration coefficient versus total retained concentration,

$$\lambda(\sigma) = \sum_{i=1}^{n} \lambda_i(\sigma_1(\sigma), \sigma_2(\sigma) \cdots \sigma_n(\sigma)) \tag{A.11}$$

Substituting Eq. (A.11) into (A.8) reduces system with n capture mechanisms (A.3) to a single capture system (1)–(3).

Appendix B. Proof of the aggregation lemma for multi-capture filtration in the modified dispersion model

This Appendix proves that the colloidal-suspension flow with n capture mechanisms can be reduced to a single-capture system (1), (3), (4) for the case of so-called modified system of DBF, where the capture rate is proportional to the overall particle flux [8,13,17]:

$$\frac{\partial \sigma_i}{\partial t} = \lambda_i\left(\sigma_1, \sigma_2 \cdots \sigma_n\right) q, i = 1, 2 \cdots n \tag{B.1}$$

Mass balance equation (A.1) and the total flux expression (A.2) close system for $n+1$ unknowns c, σ_1, $\sigma_2 \ldots \sigma_n$.

Eqs. (A.5), (A.6) hold for modified system (A.1), (A.2), (B.1).

Fixing $x = x_0$ and assuming that flux $q\,(x, t)$ is already knows, yields a system of ordinary differential equations for retained concentrations

$$\frac{d\sigma_i}{dt} = \lambda_i(\sigma_1, \sigma_2 \cdots \sigma_n) q \tag{B.2}$$

Time derivative of total retained concentration becomes

$$\frac{d\sigma}{dt} = \sum_{i=1}^{n} \frac{d\sigma_i}{dt} = \left(\sum_{i=1}^{n} \lambda_i(\sigma_1, \sigma_2 \cdots \sigma_n) \right) q \tag{B.3}$$

Change independent variable in system (B.3) from t to σ yields the same aggregated Eqs. (A.9) and (A.11).

Substituting Eqs. (A.6), (A.11) into system with n capture mechanisms (A.1), (A.2), (B.1) reduces this system to a single capture system (1), (4), (3).

References

[1] S.A. Bradford, S.R. Yates, M. Bettahar, J. Simunek, Physical factors affecting the transport and fate of colloids in saturated porous media, Water Resour. Res. 38 (2002).

[2] D. Mikhailov, V. Zhvick, N. Ryzhikov, V. Shako, Modeling of Rock Permeability Damage and Repairing Dynamics Due to Invasion and Removal of Particulate from Drilling Fluids, Transp. Porous Media 121 (2018) 37–67.

[3] N.P. Sotirelis, C.V. Chrysikopoulos, Heteroaggregation of graphene oxide nanoparticles and kaolinite colloids, Sci. Total Environ. 579 (2017) 736–744.

[4] S.A. Bradford, S. Torkzaban, A. Shapiro, A theoretical analysis of colloid attachment and straining in chemically heterogeneous porous media, Langmuir 29 (2013) 6944–6952.

[5] C.V. Chrysikopoulos, N.P. Sotirelis, N.G. Kallithrakas-Kontos, Cotransport of graphene oxide nanoparticles and kaolinite colloids in porous media, Transp. Porous Media 119 (2017) 181–204.

[6] V.E. Katzourakis, C.V. Chrysikopoulos, Modeling dense-colloid and virus cotransport in three-dimensional porous media, J. Contam. Hydrol. 181 (2015) 102–113.

[7] P. Bedrikovetsky, Upscaling of stochastic micro model for suspension transport in porous media, Transp. Porous Media 75 (2008) 335–369.

[8] X. Chen, B. Bai, Experimental investigation and modeling of particulate transportation and deposition in vertical and horizontal flows, Hydrogeol. J. 23 (2015) 365–375.

[9] L. Chequer, T. Russell, A. Behr, L. Genolet, P. Kowollik, A. Badalyan, A. Zeinijahromi, P. Bedrikovetsky, Non-monotonic permeability variation during colloidal transport: governing equations and analytical model, J. Hydrol. (2017).

[10] M. Elimelech, J. Gregory, X. Jia, Particle Deposition and Aggregation: Measurement, Modelling and Simulation, Butterworth-Heinemann, 2013.

[11] V.E. Katzourakis, C.V. Chrysikopoulos, Mathematical modeling of colloid and virus cotransport in porous media: Application to experimental data, Adv. Water Resour. 68 (2014) 62–73.

[12] R.G. Guedes, F.A. Al-Abduwani, P.G. Bedrikovetsky, P.K. Currie, Injectivity decline under multiple particle capture mechanisms, in: SPE International Symposium and Exhibition on Formation Damage Control, Society of Petroleum Engineers, 2006.

[13] B. Bai, T. Xu, H. Li, The semi-analytical solution of particle transport in porous media induced by seepage, Feb-Fresenius Environ. Bull. (2017) 6286.

[14] P. Bedrikovetsky, Mathematical Theory of Oil and Gas Recovery: With Applications to Ex-USSR Oil and Gas Fields, Springer Science & Business Media, 2013.

[15] A.D. Polyanin, A.V. Manzhirov, HandBook of Mathematics for Engineers and Scientists, CRC Press, 2006.

[16] A. Polyanin, V. Zaitsev, HandBook of Nonlinear Partial Differential Equations, Chapman & Hall/CRC Press, Boca Raton, 2012.

[17] P. Bedrikovetsky, A. Siqueira, A. de Souza, F. Shecaira, Correction of basic equations for deep bed filtration with dispersion, J. Pet. Sci. Eng. 51 (2006) 68–84.

[18] J. Herzig, D. Leclerc, P.L. Goff, Flow of suspensions through porous media—application to deep filtration, Ind. Eng. Chem. 62 (1970) 8–35.

[19] K.C. Khilar, H.S. Fogler, Migrations of Fines in Porous Media, Springer Science & Business Media, 1998.

[20] A.D. Polyanin, A.I. Zhurov, Non-linear instability and exact solutions to some delay reaction–diffusion systems, Int. J. Non-Linear Mech. 62 (2014) 33–40.

[21] M. Mirabolghasemi, M. Prodanović, D. DiCarlo, H. Ji, Prediction of empirical properties using direct pore-scale simulation of straining through 3D microtomography images of porous media, J. Hydrol. 529 (2015) 768–778.

[22] J.A. Araújo, A. Santos, Analytic model for DBF under multiple particle retention mechanisms, Transp. Porous Media 97 (2013) 135–145.

[23] L.I. Kuzmina, Y.V. Osipov, Particle transportation at the filter inlet, Int. J. Comput. Civil Struct. Eng. 10 (2014) 17–22.

[24] A.A. Shapiro, Elliptic equation for random walks. Application to transport in microporous media, Physica A 375 (2007) 81–96.

[25] H. Yuan, A. Shapiro, Colloid transport and retention: recent advances in colloids filtration theory, in: Colloids: Classification, Properties and Applications, Nova Science Publishers, Incorporated, 2012.

[26] A. Shapiro, J. Wesselingh, Gas transport in tight porous media: gas kinetic approach, Chem. Eng. J. 142 (2008) 14–22.

[27] H. Yuan, A.A. Shapiro, Modeling non-Fickian transport and hyperexponential deposition for deep bed filtration, Chem. Eng. J. 162 (2010) 974–988.

[28] M. Sharma, Y. Yortsos, Transport of particulate suspensions in porous media: model formulation, AIChE J. 33 (1987) 1636–1643.

[29] M. Sharma, Y. Yortsos, Fines migration in porous media, AIChE J. 33 (1987) 1654–1662.

[30] A. Santos, P. Bedrikovetsky, A stochastic model for particulate suspension flow in porous media, Transp. Porous Media 62 (2006) 23–53.

[31] A.C. Alvarez, G. Hime, D. Marchesin, P.G. Bedrikovetsky, The inverse problem of determining the filtration function and permeability reduction in flow of water with particles in porous media, Transp. Porous Media 70 (2007) 43–62.

[32] M. Hayek, G. Kosakowski, A. Jakob, S.V. Churakov, A class of analytical solutions for multidimensional multispecies diffusive transport coupled with precipitation-dissolution reactions and porosity changes, Water Resour. Res. 48 (2012).

[33] M. Hayek, Exact solutions for one-dimensional transient gas flow in porous media with gravity and Klinkenberg effects, Transp. Porous Media 107 (2015) 403–417.

[34] A.D. Polyanin, A.I. Zhurov, Exact solutions of linear and non-linear differential-difference heat and diffusion equations with finite relaxation time, Int. J. Non-Linear Mech. 54 (2013) 115–126.

[35] K. Sorbie, A. Stamatiou, Analytical solutions of a one-dimensional linear model describing scale inhibitor precipitation treatments, Transp. Porous Media (2018) 1–17.

[36] B. Yuan, R.G. Moghanloo, Analytical model of well injectivity improvement using nanofluid preflush, Fuel 202 (2017) 380–394.

[37] B. Yuan, W. Wang, Using nanofluids to control fines migration for oil recovery: Nanofluids co-injection or nanofluids pre-flush?-A comprehensive answer, Fuel 215 (2018) 474–483.

[38] L.I. Kuzmina, Y.V. Osipov, Asymptotic solution for deep bed filtration with small deposit, Procedia Eng. 111 (2015) 491–494.

[39] H. Yuan, A.A. Shapiro, A mathematical model for non-monotonic deposition profiles in deep bed filtration systems, Chem. Eng. J. 166 (2011) 105–115.

[40] L.I. Kuzmina, Y.V. Osipov, Y.P. Galaguz, A model of two-velocity particles transport in a porous medium, Internat. J. Non-Linear Mech. 93 (2017) 1–6.

[41] L.I. Kuzmina, Y.V. Osipov, Y.G. Zheglova, Analytical model for deep bed filtration with multiple mechanisms of particle capture, Int. J. Non-Linear Mech. (2018).

[42] A. Alvarez, P. Bedrikovetsky, G. Hime, A. Marchesin, D. Marchesin, J. Rodrigues, A fast inverse solver for the filtration function for flow of water with particles in porous media, Inverse Problems 22 (2005) 69.

[43] T.F. Coleman, Y. Li, An interior trust region approach for nonlinear minimization subject to bounds, SIAM J. Optim. 6 (1996) 418–445.

[44] L. Shampine, Solving hyperbolic PDEs in MATLAB, Appl. Numer. Anal. Comput. Math. 2 (2005) 346–358.

[45] L.F. Shampine, Two-step Lax–Friedrichs method, Appl. Math. Lett. 18 (2005) 1134–1136.

[46] N. Tufenkji, M. Elimelech, Breakdown of colloid filtration theory: Role of the secondary energy minimum and surface charge heterogeneities, Langmuir 21 (2005) 841–852.

[47] N. Sefrioui, A. Ahmadi, A. Omari, H. Bertin, Numerical simulation of retention and release of colloids in porous media at the pore scale, Colloids Surf. A 427 (2013) 33–40.

[48] Y. Yang, F.D. Siqueira, A.S. Vaz, Z. You, P. Bedrikovetsky, Slow migration of detached fine particles over rock surface in porous media, J. Nat. Gas Sci. Eng. 34 (2016) 1159–1173.

3.2 Cotransport of Suspended Colloids and Nanoparticles in Porous Media

G. Malgaresi, H. Zhang, C.V. Chrysikopoulos, and P. Bedrikovetsky

Journal of Transport in Porous Media

Statement of Authorship

Title of Paper	Cotransport of suspended colloids and nanoparticles in porous media
Publication Status	☑ Published ☐ Accepted for Publication ☐ Submitted for Publication ☐ Unpublished and Unsubmitted w ork w ritten in manuscript style
Publication Details	G. V. C. Malgaresi, H. Zhang, C.V. Chrysikopoulos, and P. Bedrikovetsky. Cotransport of suspended colloids and nanoparticles in porous media. Submitted to Transport in Porous Media.

Principal Author

Name of Principal Author (Candidate)	Gabriel Malgaresi
Contribution to the Paper	Derivation of the mathematical model for transport and cotransport of nano- and colloids particles, tuned the laboratory data, performed the DLVO calculations for interaction between nanoparticle-nanoparticle, nanoparticle-colloid, nanoparticle-grain surface, colloid-colloid and colloid-grain surface, and provided an explanation for experiment result and parameters trends.
Overall percentage (%)	70%
Certification:	This paper reports on original research I conducted during the period of my Higher Degree by Research candidature and is not subject to any obligations or contractual agreements with a third party that would constrain its inclusion in this thesis. I am the primary author of this paper.
Signature	Date 25/10/2019

Co-Author Contributions

By signing the Statement of Authorship, each author certifies that:

i. the candidate's stated contribution to the publication is accurate (as detailed above);

ii. permission is granted for the candidate in include the publication in the thesis; and

iii. the sum of all co-author contributions is equal to 100% less the candidate's stated contribution.

Name of Co-Author	Hao Zhang
Contribution to the Paper	Derivation of the mathematical model for single population transport, and helped in the interpretation of the model results
Signature	Date 25/10/2019

Name of Co-Author	Constantinos Chrysikopoulos
Contribution to the Paper	Helped with the explanations of laboratory tests and manuscript evaluation.
Signature	Date 29/10/2019

Name of Co-Author	Pavel Bedrikovetsky		
Contribution to the Paper	Problem formulation and supervision of the development of the whole work.		
Signature		Date	23/10/2019

Transport in Porous Media
https://doi.org/10.1007/s11242-019-01239-5

Cotransport of Suspended Colloids and Nanoparticles in Porous Media

G. V. C. Malgaresi[1] · H. Zhang[1] · C. V. Chrysikopoulos[2] · P. Bedrikovetsky[1]

Received: 3 July 2018 / Accepted: 17 January 2019
© Springer Nature B.V. 2019

Abstract
The objective of this study is to develop a model for cotransport of colloids and nanoparticles (NPs) in porous media under two particle capture mechanisms. The particle capture rate is proportional to the capture probability, which is a function of retained concentration, called the filtration function. Laboratory bench-scale experiments of individual transport of NPs and colloidal-size kaolinite clay particles through packed columns produced breakthrough curves (BTCs) that monotonically increased with time and stabilised at some value lower than the injected concentration. We discuss the filtration function that corresponds to BTCs stabilising at the concentration lower than the injected value. This so-called binary filtration function incorporates two particle capture mechanisms. The analytical transport model with a binary filtration function was capable to fit successfully BTCs obtained from individual transport experiments using kaolinite and NPs conducted by Chrysikopoulos et al. (Transp Porous Med 119(1):181–204, 2017). Assuming that the electrostatic particle–solid matrix interaction and the fraction of the solid matrix surface area occupied by a single attached particle (kaolinite or NP) are the same for individual transport of either kaolinite particles or NPs and for simultaneous cotransport of kaolinite particles and NPs, the proposed binary filtration function was extended for the cotransport case. Although the breakthrough data from cotransport experiments with kaolinite particles and NPs have six degrees of freedom, the developed cotransport model successfully matches the BTCs by tuning two constants only. This validates the developed model for cotransport of two colloidal populations with different attachments and straining rates.

Keywords Colloidal transport · Nanoparticles · Cotransport · Analytical model · Attachment and straining

List of Symbols
c Suspended concentration [ML^{-3}]
C Normalised suspended concentration [–]
k Permeability [L^2]
S Retained concentration [ML^{-3}]

✉ P. Bedrikovetsky
pavel.russia@gmail.com

[1] Australian School of Petroleum, University of Adelaide, Adelaide, Australia

[2] School of Environmental Engineering, Technical University of Crete, Chania, Greece

Published online: 05 February 2019

s_m Maximum attached concentration [ML^{-3}]
S Normalised retained concentration [–]
t Time [T]
T Dimensionless time [PVI]
U Flow velocity [LT^{-1}]
x Axial coordinate [L]
X Dimensionless axial coordinate [–]

Greek Letters

ϕ Porosity [–]
λ_0 Initial attachment filtration coefficient [L^{-1}]
Λ_0 Dimensionless initial filtration coefficient [–]
λ_1 Size exclusion (straining) filtration coefficient [L^{-1}]
Λ_1 Dimensionless size exclusion filtration coefficient [–]
λ Filtration coefficient [L^2M^{-1}]
μ Viscosity [$ML^{-1}T^{-1}$]

Subscripts

K Kaolinite
m Maximum value
N Nanoparticle

1 Introduction

Migration of suspended colloids predominately occurs in subsurface formations. However, flow of suspended colloids in porous media has also been observed in various processes of environmental, chemical, civil, and petroleum engineering (Civan 2015). Kaolinite clay particles are often present in numerous occasions of subterranean water contamination, plant irrigation, cold water injection into geothermal reservoirs, artificial recharge of aquifers, well drilling with filtrate invasion into formations, seawater intrusion into coastal aquifers, and low-salinity water injection into oilfields (You et al. 2015; Farajzadeh et al. 2017; Mirabolghasemi et al. 2015; Mikhailov et al. 2018). Kaolinite fines are detached from surfaces of sandstone rocks, yielding water contamination and permeability decline (Russell et al. 2017; Chequer et al. 2017).

Engineered nanoparticles have received considerable attention in a very large number of applications including the treatment of contaminated aquifers, fixing movable fines in oil and gas reservoirs for formation damage prevention (Arab et al. 2014; Yuan et al. 2016a; Yuan and Moghanloo 2017; Mansouri et al. 2019), and enhanced oil recovery by water flooding (Arab and Pourafshary 2013). The transport of NPs in porous media is relatively complicated, because it is affected by several factors including: interstitial velocity, solution chemistry, temperature, and the presence of other suspended particles (Rottman et al. 2013; Syngouna et al. 2017; Yuan et al. 2016b).

Numerous stochastic and deterministic mathematical models are developed to describe particle transport, capture, and the consequent rock alteration (Arab et al. 2014; Mirabolghasemi et al. 2015; Hammadi et al. 2017; Bashtani et al. 2018). The reviews by Shapiro and Yuan (2012) and Yuan et al. (2012) give a reasonably complete account of the available stochastic models. The stochastic models are described

by population balance equations (Sharma and Yortsos 1987; Santos and Bedrikovetsky 2006; Bedrikovetsky et al. 2017; Hayek et al. 2012), random walk models (Shapiro and Bedrikovetsky 2008, 2010; Yuan et al. 2012), deep bed filtration equation with stochastically distributed filtration coefficient (Yuan and Shapiro 2010; Elimelech et al. 2013), and Boltzmann's equation (Shapiro and Wesselingh 2008). Shapiro et al. 2007 derived deep bed filtration equations with incomplete pore plugging and derived exact solutions for 1D flows.

Averaging (aggregation and upscaling) of stochastic models with size-distributed particles and pores and multiple capture mechanisms is necessary to reduce the numerical burden. Guedes et al. (2009) proposed the mathematical procedure allowing aggregating multiple kinetic rate equations for particle retention into a single equation for the capture rate for dispersion-free transport. This method has been recently extended for advective-capture flow with dispersion (Zhang et al. 2018). Population balance equations with probabilistic distribution of pore and particle sizes allow for exact upscaling for suspensions of uniform size, and the resulting system coincides with the classical filtration equations for the averaged values (Bedrikovetsky 2008).

Several mathematical models for deep bed filtration of individual (transport) as well as binary mixtures (cotransport) are available in the literature (Abdel-Salam and Chrysikopoulos 1995; Bekhit et al. 2009; Katzourakis and Chrysikopoulos 2014, 2015). The common assumption is proportionality between the particle capture rate and the advective particle flux; their ratio is called the filtration function. The nonlinear deterministic deep bed filtration model allows for an exact solution (Polyanin and Manzhirov 2006; Polyanin and Zaitsev 2012). Furthermore, exact solutions for direct problem yield regularisation of the corresponding inverse problems, which allow for determination of the associated model functions from the laboratory tests (Alvarez et al. 2005, 2007; Hayek 2015; Hayek et al. 2012). An analytical model for deep bed filtration of a binary mixture, where each species is captured by a separate capture mechanism, using constant and Langmuir's filtration functions, is proposed in Araújo and Santos (2013). However, recent studies have shown that for kaolinite and graphene oxide (GO) NP cotransport, the attachment processes can be simultaneous for both suspended particles (Chrysikopoulos et al. 2017; Sotirelis and Chrysikopoulos 2017). Because suspended particles near rough pore walls migrate with significantly smaller velocity than the mean interstitial velocity (Sefrioui et al. 2013), several investigators proposed mathematical models for two populations of particles with two different velocities (Yuan and Shapiro 2010; Bradford et al. 2009b; Kuzmina et al. 2017). Yuan and Moghanloo (2017) and Yuan et al. (2016a) proposed mathematical models for kaolinite and NPs cotransport with adsorption as a major capture mechanism. However, a mathematical model for cotransport of colloids and NPs with simultaneous attachment and straining (size exclusion) of both species is not available.

The objective of the present work is to develop a mathematical model for cotransport of colloids and NPs in porous media using a novel filtration function capable of matching closely the experimental data collected by Chrysikopoulos et al. (2017) for kaolinite and NPs transport. The proposed novel filtration function incorporates two simultaneous capture mechanisms: Langmuir (blocking) and constant (low-retention) filtration. The cotransport model successfully matches six-dimensional set of the laboratory data on commingled injection of kaolinite and nanoparticles by tuning two model coefficients only, which validates the model.

2 Theoretical Developments

This section proposes the so-called binary filtration function that yields the BTCs with stabilised concentration lower than the injected concentration (Sect. 2.1), derives the exact solution for 1D transport of single colloidal population (Sect. 2.2, Table 1) and performs its qualitative analysis (Sect. 2.3). Then, we extend the binary filtration function for two-population transport, and develop the cotransport equations (Sect. 2.4), which are solved numerically (Sect. 2.5).

2.1 Transport Models for a Single-Particle Population

Assuming that the interstitial fluid is incompressible (water), the suspended particles are uniformly sized, particle concentration is low so that the carrier fluid density is not altered, particle dispersion (diffusion) is negligible compared to the interstitial velocity, particle capture by the solid matrix follows linear kinetics with capture rate proportional to the particle advective flux and occurs by size exclusion, straining, attachment, segregation, diffusion into dead-end pores, etc. (see Fig. 1a), permeability decline due to particle retention is adequately described Darcy's law, and the governing equations for transport in porous media are as follows (Herzig et al. 1970; Alvarez et al. 2005, 2007):

$$\frac{\partial}{\partial t}(\phi c + s) + U\frac{\partial c}{\partial x} = 0, \tag{1}$$

$$\frac{\partial s}{\partial t} = \lambda(s) c U, \tag{2}$$

$$U = -\frac{k(s)}{\mu(c)}\frac{\partial P}{\partial x}, \tag{3}$$

where x is the linear coordinate in the flow direction, t is time, c and s are the suspended and attached concentrations, ϕ is the porosity, U is the fluid velocity, λ is the filtration coefficient, k is the permeability, μ is the viscosity, and P is the pressure. The suspended particle concentration c is determined as the number of suspended particles in a unit volume of carrier fluid, while the retained particle concentration s is equal to the number of attached particles in a unit volume of the solid matrix. It should be noted that the effects of particle retention are in decreasing the suspended particle concentration and permeability. The suspended particle concentration decline due to retention is important for industrial waste disposal and aquifer contamination, while the permeability decline yields the impairment of production and injection wells.

For constant particle concentration injection in a typical bench-scale core or packed column, initially free of particles, the appropriate initial and boundary conditions are (Fig. 2):

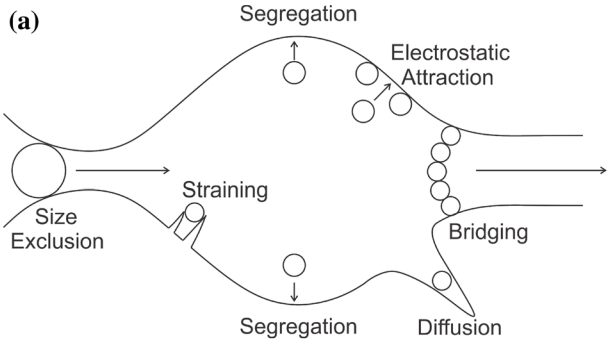
$$c(x, 0) = s(x, 0) = 0, \tag{4}$$

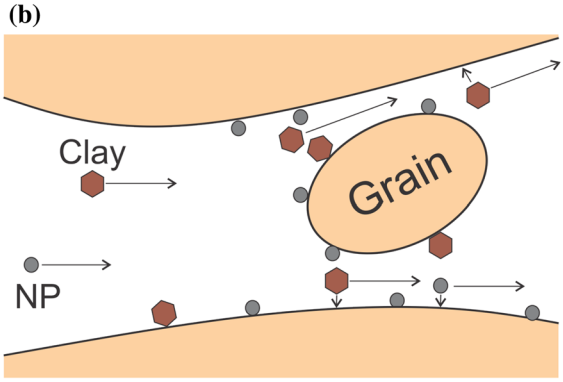
$$c(0, t) = c^0, \tag{5}$$

where c^0 is the injected suspended particle concentration. The assumptions of a monolayer particle attachment (Langmuir type), where one attached particle occupies one vacancy,

Table 1 Explicit dimensionless expressions for suspended and attached particle concentrations

Zone	Domains	$C(X,T)$	$S(X,T)$
0	$T(X) \le X$	0	0
I	$X < T(X) \le X + T_{\mathrm{m}}$	$\frac{1}{\left[1-\exp\left[-\frac{\Lambda_0}{S_{\mathrm{m}}}(T-X)\right]+\exp\left[\left(\Lambda_0+\Lambda_1\right)X-\frac{\Lambda_0}{S_{\mathrm{m}}}(T-X)\right]\right]}$	$\frac{S_{\mathrm{m}}\frac{\left(\Lambda_0+\Lambda_1\right)}{\Lambda_0}\left(1-\exp\left[-\frac{\Lambda_0}{S_{\mathrm{m}}}(T-X)\right]\right)}{\left[1-\exp\left[-\frac{\Lambda_0}{S_{\mathrm{m}}}(T-X)\right]+\exp\left[\left(\Lambda_0+\Lambda_1\right)X-\frac{\Lambda_0}{S_{\mathrm{m}}}(T-X)\right]\right]}$
II	$X + T_{\mathrm{m}} < T(X) < \frac{S_{\mathrm{m}}}{\Lambda_1}\left(\exp\left(\Lambda_1 X\right)-1\right) + X + T_{\mathrm{m}}$	$\frac{S_{\mathrm{m}}\left(\frac{\Lambda_0+\Lambda_1}{\Lambda_0}\right)}{\left[\Lambda_1(T-X-T_{\mathrm{cr}})+S_{\mathrm{m}}\right]\left\{\frac{\Lambda_1}{\Lambda_0}\exp\left[\left(\Lambda_0+\Lambda_1\right)\left(X-\frac{1}{\Lambda_1}\ln\left[\frac{\Lambda_1}{S_{\mathrm{m}}}(T-X-T_{\mathrm{cr}})+1\right]\right)\right]+1\right\}}$	$\frac{S_{\mathrm{m}}\left(\frac{\Lambda_0+\Lambda_1}{\Lambda_0}\right)}{\frac{\Lambda_1}{\Lambda_0}\exp\left[\left(\Lambda_0+\Lambda_1\right)\left(X-\frac{1}{\Lambda_1}\ln\left[\frac{\Lambda_1}{S_{\mathrm{m}}}(T-X-T_{\mathrm{m}})+1\right]\right)\right]+1}$
III	$T(X) \ge \frac{S_{\mathrm{m}}}{\Lambda_1}\left(\exp\left(\Lambda_1 X\right)-1\right) + X + T_{\mathrm{m}}$	$\exp\left(-\Lambda_1 X\right)$	$\left[\Lambda_1\left(T-X-T_{\mathrm{m}}\right)+S_{\mathrm{m}}\right]\exp\left(-\Lambda_1 X\right)$





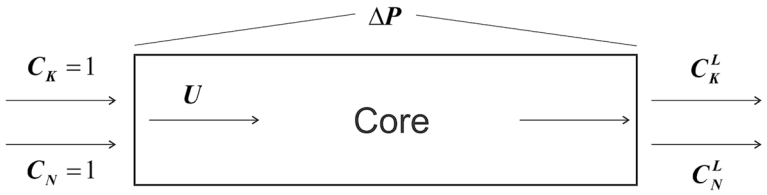


Fig. 1 Multiple particle capture mechanisms: **a** various capture mechanisms at the pore scale; **b** attachment and straining of nanoparticles and clay particles

Fig. 2 Schematic illustration of a bench-scale porous medium. Kaolinite clay particles (C_K) and nanoparticles (C_N) are injected simultaneously. The dimensionless inlet concentrations are equal to one ($C_K = C_N = 1$)

and of the small suspended and attached particle concentrations, yield the following "active-mass" law for the particle–vacancy "reaction" (Elimelech et al. 2013).

$$\lambda(s) = \begin{cases} \lambda_0\left(1 - \frac{s}{s_m}\right), & s < s_m \\ 0, & s > s_m \end{cases}, \tag{6}$$

where λ_0 is the initial filtration coefficient as determined by the solid matrix–particle attraction and s_m is the maximum concentration of attached particles (Bedrikovetsky 2008). Langmuir's filtration function is given by curve 2 in Fig. 3b. The maximum value s_m corresponds to complete occupation of the solid matrix surfaces by the attached particles, and $1/s_m$ relates to the solid matrix fraction occupied by a single particle. After the retained

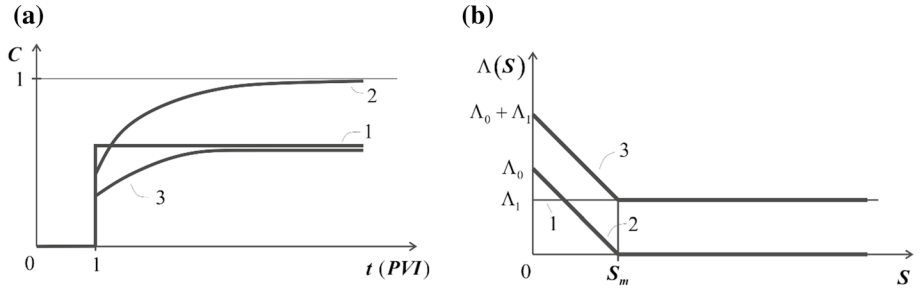


Fig. 3 Illustration of three different shapes of filtration function: **a** breakthrough curves (BTCs) and **b** shapes of filtration function. Curves 1, 2, and 3 correspond to constant filtration coefficient, Langmuir blocking, and combined (binary) filtration function for two simultaneous mechanisms, respectively

particle concentration reached its maximum value s_{m}, the particle attachment on the solid matrix surfaces stops. Note that the above-mentioned scenario corresponds to the case of solid matrix–particle attraction and particle–particle repulsion (Kuhnen et al. 2000; Bennacer et al. 2017). The Langmuir blocking filtration function (6) is usually used for monolayer electrostatic attachment of particles on solid matrix surfaces, but is also applicable for straining and size exclusion (Herzig et al. 1970; Kuhnen et al. 2000).

For a small retained particle concentration ($s \ll s_{\mathrm{m}}$), the filtration coefficient is assumed to be constant, $\lambda(s) = \lambda_1$ (curve 1 in Fig. 3b). The probability of particle capture remains constant for low-retention concentrations, because the particles do not compete for the same vacancy. For this case, the breakthrough concentration is expected to be initially equal to zero and subsequently to jump up to some value that remains constant (curve 1 in Fig. 3a). In the present work, to be specific but without loss of generality, this low-retention mechanism is referred to as size exclusion, whereas attachment corresponds to the Langmuir's blocking capture.

Regarding deep bed filtration with multiple particle capture mechanisms, Appendix A proves that the total retention rate for a multiple capture system can be represented by a single-capture mechanism given by Eq. (2). The overall filtration function $\lambda(s)$ is a total of individual filtration functions (λ_1, λ_2… λ_n), i.e. λ is also a function of all individual retention concentrations s_i, $i = 1,2…n$. However, solution of system of retention rate Eq. (A1), where time T is parametrised by the total retention concentration $s(x_0, t)$, allows expressing all individual retention concentrations via the overall s, yielding the aggregated filtration function $\lambda = \lambda(s)$.

In particular, the filtration function that aggregates two capture mechanisms with Langmuir's and constant filtration functions can be approximated by the following piecewise function with high accuracy (Zhang et al. 2018):

$$\lambda(s) = \begin{cases} \lambda_0\left(1 - \frac{s}{s_{\mathrm{m}}}\right) + \lambda_1, & s \le s_{\mathrm{m}} \\ \lambda_1, & s \le s_{\mathrm{m}} \end{cases}, \tag{7}$$

where the filtration coefficient λ_0 corresponds to monolayer attachment where no particles were attached yet, and λ_1 corresponds to low-retention size exclusion. So, the filtration function given by Eq. (7) consists of two simultaneous particle capture mechanisms and is called the binary filtration function further in the text. Curve 3 in Fig. 3b corresponds to

a binary filtration function. It should be noted that the filtration model (7) contains three parameters (λ_0, λ_1, and s_m). Model (7) can describe other couples of particle retention mechanisms.

Note that BTCs, which are initially equal to zero, jump up to some value and then monotonically increase to a limit that is lower than the injected concentration as time tends to infinity, have been observed in laboratory breakthrough experiments with kaolinite colloid particles and graphene oxide nanoparticles conducted by Chrysikopoulos et al. (2017).

In this study, we show that such BTCs can be represented by a binary filtration function.

Further in this paper, the filtration coefficients are determined by tuning the experimental data (Sect. 3). Theoretical calculations of straining filtration coefficient accounting for effects of attached particles can be performed from reconstruction of CT or NMR images using digital core techniques (Wang et al. 2018a, b; Shikhov and Arns 2015). The approach is similar to calculation of permeability or electrical conductivity from rock geometry at pore scale (Yanici et al. 2013; Arns and Adler 2018).

Introducing the following dimensionless definitions for time, x-coordinate, filtration coefficients, suspended and attached concentrations:

$$T = \frac{Ut}{\phi L},\ X = \frac{x}{L},\ \Lambda_i = \lambda_i L,\ C = \frac{c}{c^0},\ S = \frac{s}{\phi c^0}, \tag{8}$$

the governing model (1, 2) becomes:

$$\frac{\partial (C+S)}{\partial T} + \frac{\partial C}{\partial X} = 0, \tag{9}$$

$$\frac{\partial S}{\partial T} = \Lambda(S) C, \tag{10}$$

Here, the filtration function (7) is given by:

$$\Lambda(S) = \begin{cases} \Lambda_0 \left(1 - \frac{S}{S_m}\right) + \Lambda_1, & S \le S_m \\ \Lambda_1, & S \le S_m \end{cases}, \tag{11}$$

and the initial and boundary conditions (4, 5) become:

$$C(X,0) = S(X,0) = 0, \tag{12}$$

$$C(0,T) = 1. \tag{13}$$

2.2 Analytical Model for 1D Flow of Single-Population Colloids

In this section, we present the final formulae for the analytical model for 1D flow of single-population colloids, derived in Appendix A. The formulation of the problem (9–13) corresponds to injection of particles with given suspended concentration into a porous specimen (Fig. 2).

Briefly, introducing the following integral potential from Eq. (10)

$$\Psi(S) = \int_0^S \frac{\mathrm{d}y}{\Lambda(y)} \tag{14}$$

yields the following solution:

$$\int_{S(0,T-X)}^{S(X,T)} \frac{\mathrm{d}S}{S\Lambda(S)} = -X, \quad \Psi(S(0,T-X)) = T-X, \quad T > X. \tag{15}$$

Equation (15) is the solution for retained particle concentration $S(X, T)$ at $T > X$. The solution for suspension concentration $C(X, T)$ follows from Eq. (B8) and boundary condition (13):

$$C(X,T) = \frac{S(X,T)}{S(0,T-X)}, \quad T > X. \tag{16}$$

The concentration front $X = T$ moves along the porous medium with a velocity equal to unity. Ahead of this front, initial conditions (12) hold: $C(X, T) = S(X, T) = 0$. Along the front, the concentration of deposited particles equals zero, $S(T, T) = 0$. Therefore, as it follows from Eqs. (9, 10), the concentration of suspended particles along the front, $C(T, T)$, is expressed as:

$$C(T,T) = \exp\left(-\Lambda(0)T\right). \tag{17}$$

Equations (15, 16) determine the retained particle concentration $S(X, T)$ for $T > X$. For $T < X$, integration along the characteristics of Eq. (A4) gives: $S(X, T) = 0$. Substitution of Eq. (10) into Eq. (9) and integration along its characteristics for $T < X$ gives: $C(X, T) = 0$.

Equation (15) provides an exact solution in the implicit form of two transcendental equations for unknowns $S(X, T)$ and $S(0, T)$. Using $S(0, T)$ as an independent variable allows for explicit calculation of T. The explicit formulae for suspended and retained particle concentrations are given in Table 1 for a binary filtration function.

2.3 Qualitative Analysis of the Flux Structure and Type Curves

Figure 3a presents three breakthrough curves simulated by the analytical solutions given in Table 1, for the three different filtration functions presented in Fig. 3b. The analytical solutions for the case of constant filtration coefficient are obtained by fixing $\Lambda_0 = 0$ and $S_m \to \infty$, and for Langmuir blocking function by setting $\Lambda_1 = 0$. The BTC corresponding to the constant filtration function is shown in Fig. 3a (curve 1), to the Langmuir filtration function is shown in Fig. 3a (curve 2), and to the case of combined constant and Langmuir filtration is shown in Fig. 3a (curve 3). The Langmuir mechanism exhibits blocking under conditions of substantial particle attachment. The Langmuir mechanism is usually applied for monolayer particle attachment onto the solid matrix, where the attachment rate is proportional to number of vacant sites for retention on the surfaces of solid matrix.

Figure 4a shows the plane (X, T), three concentration fronts, and the corresponding flow zones: 0, I, II, and III, as obtained by the exact analytical solutions listed in Table 1. The four different zones are separated by the trajectories of three concentration fronts: $T_{\mathrm{I}}(X)$, $T_{\mathrm{II}}(X)$, and $T_{\mathrm{III}}(X)$. The corresponding domains separated by those fronts are presented in Table 1. The cotangents of the trajectory slopes $(\mathrm{d}T_k(X)/\mathrm{d}X)^{-1}$, $k = \mathrm{I}, \mathrm{II}, \mathrm{III}$, are equal to the front speeds. Note that the method of characteristics was used for the derivation of the exact solutions presented in Table 1, and the characteristics are the particle trajectories. The initial conditions hold in zone 0 ahead of the concentration front $T_{\mathrm{I}}(X)$ that moves

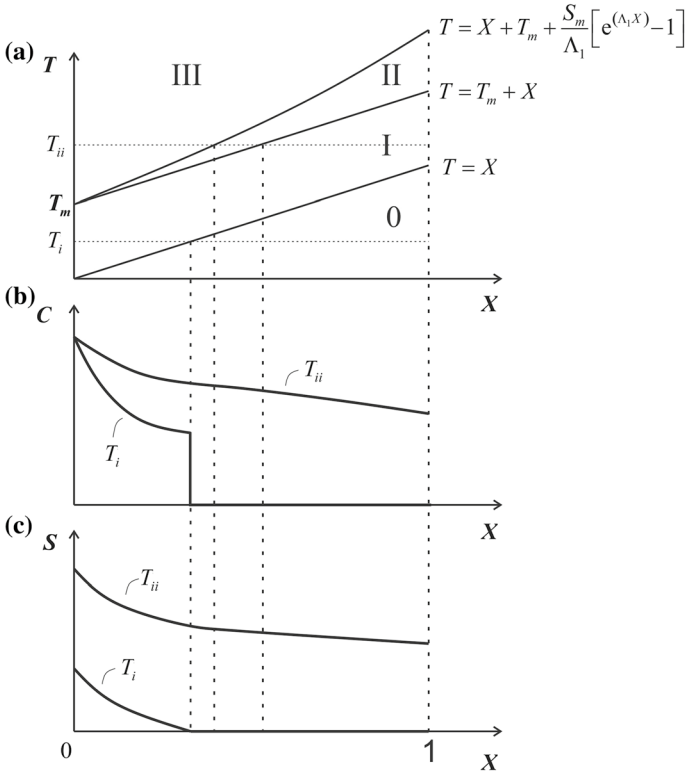


Fig. 4 Exact solution for particle transport in porous media with piecewise-linear filtration function: **a** structure of the flow pattern, **b** suspended particle concentration profiles at three instances, and **c** retained particle concentration profiles at three instances

with unitary speed. Zone I behind this front corresponds to flow with retained concentration $S(X, T) < S_m$, where the particles migrate subject to binary filtration function (7). Two capture mechanisms act in zone I. The filtration function is constant in zone III, where the suspended particles move from the inlet $X = 0$ to the boundary between zones III and II, $T_{III}(X)$, where the retained particle concentration increases up to the maximum value S_m. Migration of suspended particles continues in zone II subject to linear filtration. Only straining occurs in zone III, while both retaining mechanisms act in zone II. The suspended particle concentration is at a steady state in zone III, so the capture rate is constant, and the retained particle concentration accumulates linearly with time. The structure of the flow pattern is as follows: (Zone 0)—initial conditions of no suspended and retained particles are held ahead of the first concentration front; (Zone I)—two simultaneous capture mechanisms act, front and rear boundaries of this zone move with unitary speed; (Zone II)—starts at the inlet at the moment T_m, when the maximum attached value S_m is reached by the retained particle concentration; subsequently, only straining occurs in zone III; and (Zone III)—steady-state suspended particle concentration decreases exponentially due to constant filtration. Figure 4b, c present profiles of suspended and retained particles at three different points in time. At T_i, the particle front did not breakthrough yet. Both dimensionless particle concentrations C and S are zero ahead of this front. The suspended particle

concentration jumps from zero at the front and increases behind the front, while the suspended particle concentration is continuous. At T_{ii}, after the front has breakthrough, the profiles of particle concentration decrease exponentially from the inlet in zone III, and continue to decrease in zones II and I. Suspended particle concentrations coincide at T_{ii} and T_{iii} in zone III.

2.4 Cotransport Model

For the case of cotransport of two different populations of suspended particles, it was assumed that the concentration of each population of suspended particles was low, so that the suspended particles from one population do not compete for the same vacancies with suspended particles from the other population (Fig. 1b). The particle capture by the solid matrix for each population follows linear kinetics with capture rate proportional to the particle advective flux and occurs by either two mechanisms of size exclusion, straining, attachment, segregation, diffusion into dead-end pores, etc. (see Fig. 1a). Therefore, the maximum attached particle concentration S_{m} and attachment filtration coefficient Λ_0 of each population during cotransport are assumed to be identical to those during transport of each individual population. The suspended particles of each population are uniformly sized and, being attached, occupy the same surface area. The interstitial carrier fluid is incompressible. Particle concentration in each population is low, so that the carrier fluid density is not altered. Consequently, for the case of kaolinite colloids and NPs cotransport the governing partial differential equations are (Bedrikovetsky 2013):

$$\frac{\partial C_i}{\partial T} + \frac{\partial C_i}{\partial X} = -\left[\Lambda_{0i}\left(1 - \frac{S_N}{S_{mN}} - \frac{S_K}{S_{mK}}\right) + \Lambda_{1i}\right] C_i, \tag{18}$$

$$\frac{\partial S_i}{\partial T} = \left[\Lambda_{0i}\left(1 - \frac{S_K}{S_{mK}} - \frac{S_N}{S_{mN}}\right) + \Lambda_{1i}\right] C_i \tag{19}$$

where index $i = K, N$ corresponds to kaolinite colloids and NPs, respectively. It should be noted that S_{mN}, $\Lambda_{0\mathrm{N}}$, S_{mK}, and $\Lambda_{0\mathrm{K}}$ are equal to those for the case of transport of each population of suspended particles, but $\Lambda_{1\mathrm{N}}$ and $\Lambda_{1\mathrm{K}}$ are different because particle onto the surfaces of the solid matrix can affect pore throat radii (Fig. 1b), which in turn can affect straining (Fig. 1b) (Alem et al. 2015). Therefore, the filtration coefficients for straining during cotransport are assumed to be different from those corresponding to transport of each individual population. The cotransport model contains six independent parameters: S_{mN}, $\Lambda_{0\mathrm{N}}$, S_{mK}, $\Lambda_{0\mathrm{K}}$, $\Lambda_{1\mathrm{N}}$ and $\Lambda_{1\mathrm{K}}$. Four parameters (S_{mN}, $\Lambda_{0\mathrm{N}}$, S_{mK}, and $\Lambda_{0\mathrm{K}}$) are determined from experimental breakthrough data of individual population transport, whereas two parameters ($\Lambda_{1\mathrm{N}}$ and $\Lambda_{1\mathrm{K}}$) are obtained by fitting the cotransport experimental breakthrough curves.

The initial and boundary conditions for system (18, 19) corresponding to commingled injection of kaolinite and NPs are

$$C_K(X,0) = C_N(X,0) = S_K(X,0) = S_N(X,0) = 0, \tag{20}$$

$$C_K(0,T) = C_N(0,T) = 1. \tag{21}$$

2.5 Numerical Modelling of Single and Binary Suspension-Colloidal Populations

The governing equations subject to initial and boundary conditions for individual transport (9–13) and for cotransport (18–21) were solved numerically using the computer code developed by Shampine (2005a). The inbuilt algorithm implements a two-step Lax–Friedrichs finite-difference method (Shampine 2005b). The method allows for vectorisation of the problem, taking advantage of MATLAB's matrices and vectors optimisation. The MATLAB computer program and pertinent supporting information are available from http://faculty.smu.edu/shampine/current.html. We divide the spatial domain [0,1] into 1000 evenly spaced intervals, so $\Delta X = 0.001$. The time steps employed in the finite-difference method is selected to satisfy the Courant–Friedrichs–Lewy stability condition, $\Delta T = 0.0009$. Both species during the individual and binary flows move with the carrier water velocity (see Eqs. 9 and 18), so time step ΔT is taken the same for individual flow and for cotransport.

Figure 5 presents a comparison of the analytical solution with the numerical solution for individual transport of NPs and kaolinite colloids at pH = 7 and $I_S = 27$ mM. The values of the parameters Λ_0, Λ_1, and S_{m} used are listed in Table 2. The exact analytical and numerical solutions are almost identical. Smoothing of the concentration jump in the numerical solution is almost invisible, suggesting that the numerical scheme exhibited very low numerical dispersion.

Figures 8 and 9b present BTCs, calculated numerically for NPs and kaolinite fines during the cotransport.

3 Results

The new transport and cotransport mathematical models were used to match the experimental data reported by Chrysikopoulos et al. (2017) for transport and cotransport of graphene oxide (GO) NPs and kaolinite (KGa-1b) colloids in columns packed with glass beads and quartz sand under various water chemistry conditions (pH = 4, 7, 10 and $I_S = 7$, 12, 27 mM). The unknown parameters were determined with a nonlinear least squares method, which minimises the normalised deviation between the model and the experimental data (Coleman and Li 1996). Specifically, the Trust-Region-Reflective optimisation algorithm

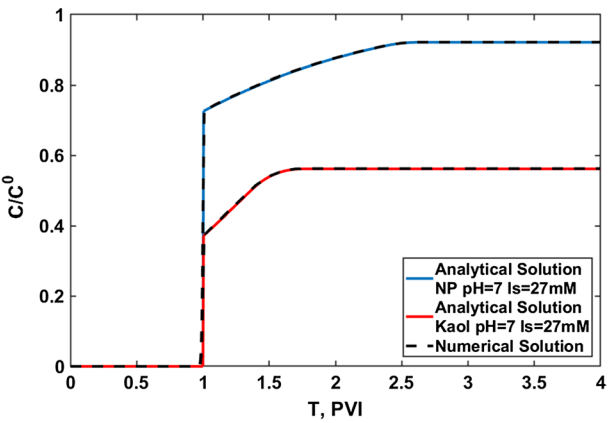


Fig. 5 Comparison between the analytical and numerical modelling for individual suspended particle transport

Table 2 Fitted parameters for GO NPs and kaolinite colloids individual transport experimental data

	Glass beads									
	GO NPs					Kaolinite colloids				
Figure	Λ_0	Λ_1	S_M	T_m	R^2	Λ_0	Λ_1	S_M	T_m	R^2
(a) pH = 4 I_S = 7 mM	0.4888	0.0910	0.5953	2.2555	0.9536	0.3506	0.5110	0.7629	1.1368	0.8815
(b) pH = 7 I_S = 7 mM	0.3045	0.0451	0.1216	0.8180	0.9598	0.2536	0.4395	0.3113	0.5592	0.9754
(c) pH = 10 I_S = 7 mM	0.1684	–	0.0731	–	0.9863	0.2211	0.4233	0.3898	0.7409	0.9751
(e) pH = 7 I_S = 12 mM	0.1956	0.0465	0.1233	1.0402	0.9851	0.6283	0.3526	0.3032	0.4938	0.9841
(f) pH = 7 I_S = 27 mM	0.2395	0.0821	0.2433	1.3870	0.9807	0.4130	0.5813	0.2847	0.3700	0.9276
	Sand									
	Nanoparticles					Kaolinite				
	Λ_0	Λ_1	S_M	T_m	R^2	Λ_0	Λ_1	S_M	T_m	R^2
pH = 7 I_S = 7 mM	0.9279	0.0529	0.2542	0.7998	0.9396	0.7186	0.1371	0.2542	0.6478	0.9597

of MATLAB was used for the solution of the resulting quadratic-deviation minimisation problem. Note that the steep continuous growth of a BTC around its breakthrough time ($T = 1$) is treated in this work as a concentration jump from zero, before the breakthrough to continuously growing BTC after the breakthrough. The areas between the continuous and discontinuous BTCs before and after the breakthrough time are equal. This procedure used here for matching BTCs is analogous to matching of inner and outer asymptotic expansions when dispersion is small (Polyanin and Dil′man 1994; Polyanin 2004).

3.1 Matching of the Transport Experimental Data

The experimental data for NPs and for kaolinite colloids individual transport in a column packed with glass beads at five different sets of water chemistry conditions reported by Chrysikopoulos et al. (2017) are presented in Fig. 6, together with the corresponding fitted analytical model simulations. Furthermore, the experimental data for NPs and for kaolinite colloids individual transport in a column packed with quartz sand for just one set of water chemistry conditions are presented in Fig. 9a, together with the corresponding fitted analytical model simulations. All fitted parameters for the individual transport experiments are listed in Table 2. Based on the R^2 values listed in Table 2, the analytical model fitted adequately the experimental data for both NPs and kaolinite colloids. This validates the proposed binary model given by Eq. (7).

For all cases presented in Fig. 6 (except the NP case in Fig. 6c), the experimental data were fitted with the analytical model utilising the filtration piecewise function (7). The unfavourable attachment conditions (high pH and low I_S) in Fig. 6c lead to large

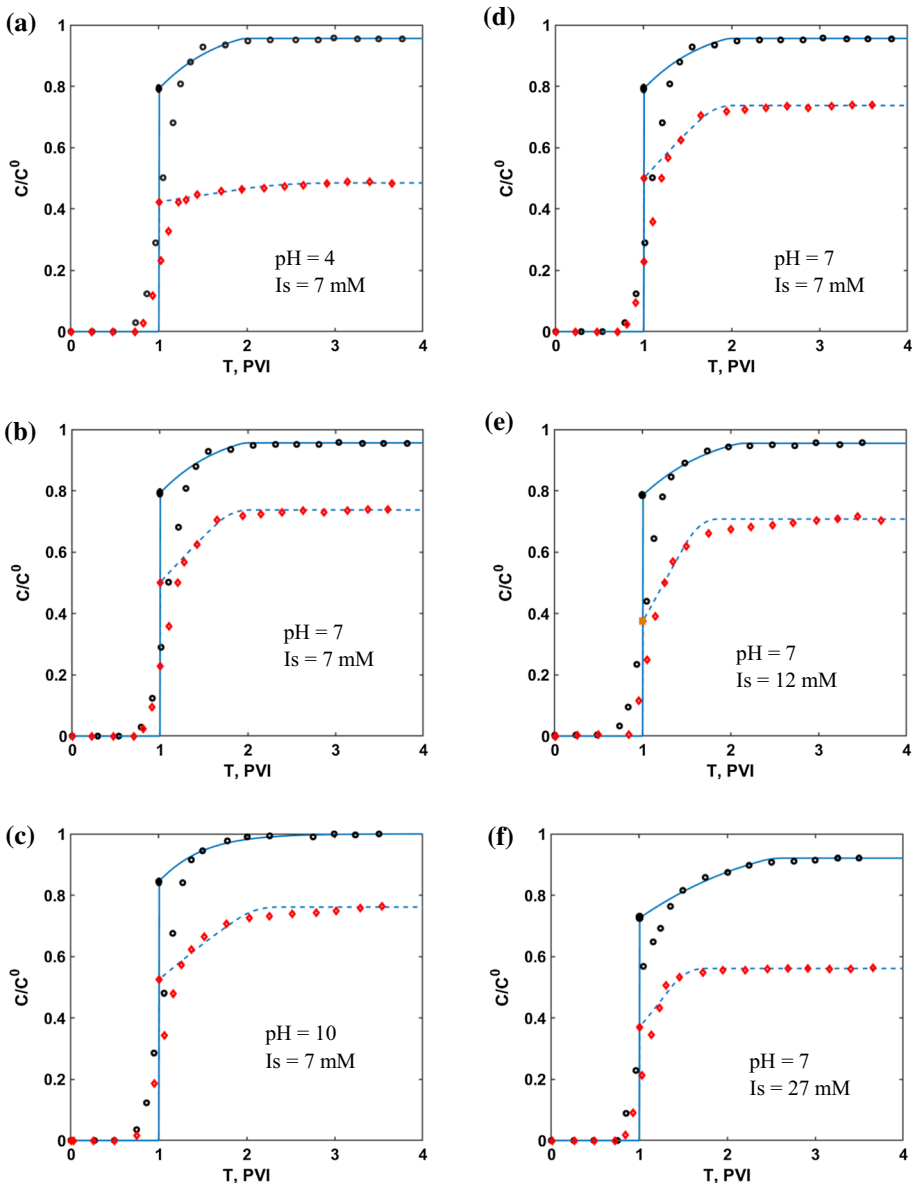


Fig. 6 Fitted breakthrough data reported by Chrysikopoulos et al. (2017) for individual transport experiments of GO NPs (open black circles) and kaolinite colloids (red diamonds) in columns packed with glass beads at different conditions: **a** pH = 4, Is = 7 mM, **b** and **d** pH = 7, I_S = 7 mM, **c** pH = 10, I_S = 7 mM, **e** pH = 7, I_S = 12 mM, and **f** pH = 7, I_S = 27 mM. BTC tending to unity is fitted with a Langmuir function (solid curves in **c**), while those tending to the limit below unity are fitted with a piecewise filtration function

solid matrix–particle repulsion, as suggested by (Derjaguin–Landau–Verwey–Overbeek) DLVO theory (Chrysikopoulos et al. 2017). Consequently, suspended particles are mobile and unstable (Bennacer et al. 2017). Furthermore, attachment onto the solid matrix under

unfavourable attachment conditions can be better represented by the Langmuir filtration function.

The fitted parameters listed in Table 2 are also presented graphically in Fig. 7 as a function of pH and I_S. Parameter values, corresponding to transport experiments in columns packed with glass beads and quartz sand, are represented by circles and squares, respectively. Figures 7a and 4d show the initial filtration coefficient variability with pH, at $I_S = 7$ mM for NPs and kaolinite colloids, respectively. The higher is the pH, the lower is the electrostatic solid matrix–particle attraction, and the lower is the Λ_0 as well as the straining Λ_1 (Bradford et al. 2009a). Figures 7b and 7e show the initial filtration coefficient variability with I_S, at pH = 7 for NPs and kaolinite colloids, respectively. The higher is the I_S, the larger is the expected electrostatic attraction between the suspended particles and the solid matrix, and in turn the higher the expected value for both filtration coefficients (Λ_0 and Λ_1). The Λ_0 fitted values for both NPs and kaolinite colloids do not exhibit a clear increasing trend with increasing I_S. However, the fitted values for Λ_1 for both NPs and

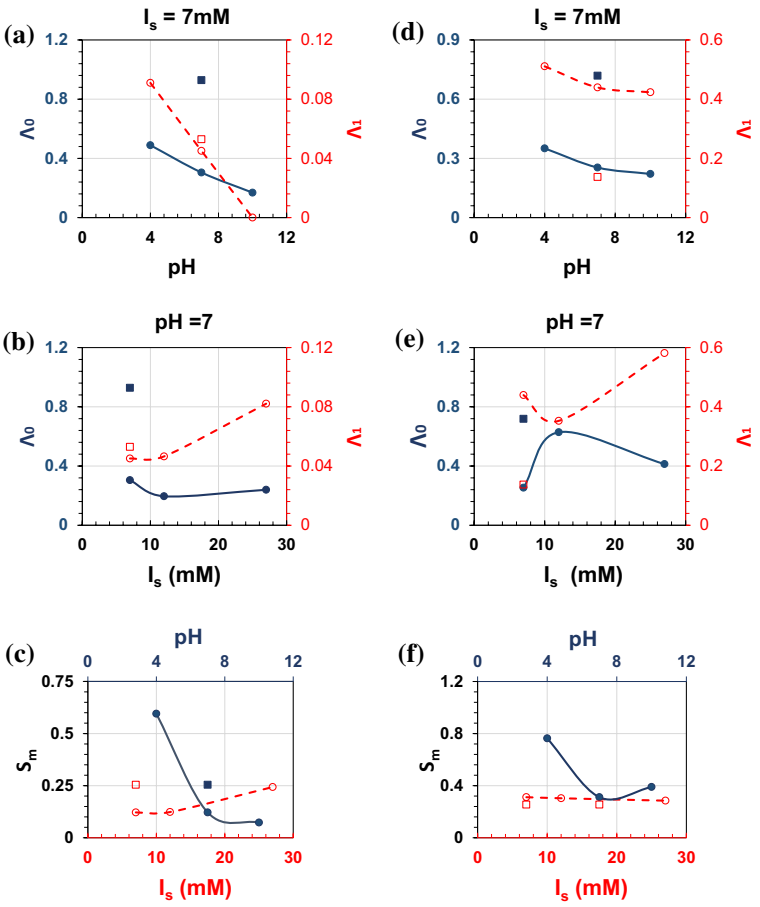


Fig. 7 Behaviour of fitted parameters for individual transport experiments of: **a–c** GO NPs and **d–e** kaolinite colloids as a function of pH and I_S. Circles and squares correspond to columns packed with glass beads and quartz sand, respectively. Solid and open symbols in **a**, **b**, **d**, **e** correspond to parameters Λ_0 and Λ_1, respectively. Solid and open symbols in **c**, **f** correspond to parameter variation with pH and I_S, respectively

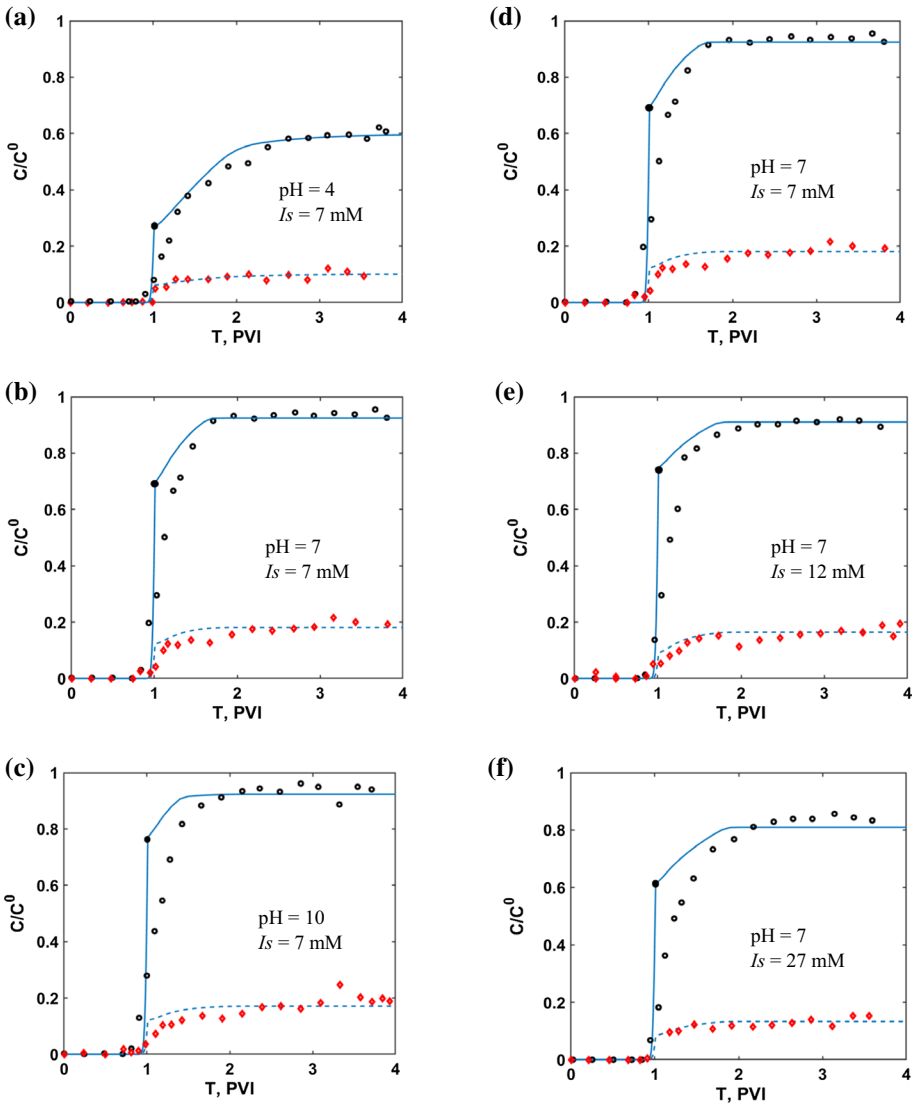


Fig. 8 Fitted breakthrough data reported by Chrysikopoulos et al. (2017) for cotransport experiments of GO NPs (open black circles) and kaolinite colloids (red diamonds) in columns packed with glass beads at different conditions: **a** pH = 4, Is = 7 mM, **b** and **d** pH = 7, I_S = 7 mM, **c** pH = 10, I_S = 7 mM, **e** pH = 7, I_S = 12 mM, and **f** pH = 7, I_S = 27 mM. The matched modelling data are given by continuous curves

kaolinite colloids generally fulfil this tendency. Figure 7c and f shows the maximum retention concentration variability with I_S and pH for both NPs and kaolinite colloids, respectively. For increasing pH and decreasing I_S, both the electrostatic attraction between the suspended particles and the solid matrix and S_{m} are expected to decrease. This is clearly the case for NPs, but it is somewhat less pronounced for kaolinite colloids.

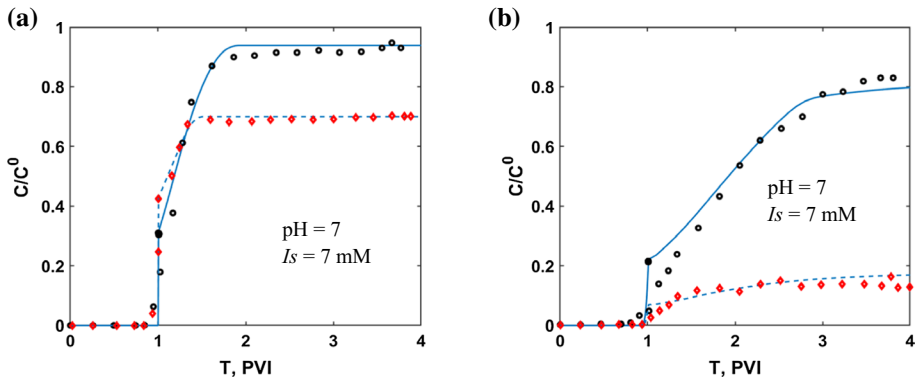


Fig. 9 Fitted breakthrough data reported by Chrysikopoulos et al. (2017) for **a** individual transport experiments of NPs (open black circles) and kaolinite colloids (red diamonds), and **b** cotransport experiments of GO NPs (open black circles) and kaolinite colloids (red diamonds) in columns packed with sand at pH = 7 and $Is = 7$ mM. The matched modelling data are given by continuous curves

Table 3 Fitted parameters for GO NPs and kaolinite colloids cotransport experimental data

	Glass beads			
	GO NPs		Kaolinite colloids	
Figures 6, 7	$\Lambda_{1,N}$	R^2	$\Lambda_{1,K}$	R^2
(a) pH = 4 $I_S = 7$ mM	0.59	0.9142	2.32	0.9263
(b) pH = 7 $I_S = 7$ mM	0.22	0.9426	2.00	0.9296
(c) pH = 10 Is = 7 mM	0.14	0.8925	1.95	0.8805
(e) pH = 7 $I_S = 12$ mM	0.21	0.9144	2.25	0.8968
(f) pH = 7 $I_S = 27$ mM	0.23	0.8770	2.20	0.8992
	Quartz sand			
	GO NPs		Kaolinite colloids	
Figure 8	$\Lambda_{N,coinj}$	R^2	$\Lambda_{k,coinj}$	R^2
pH = 7 $I_S = 7$ mM	1.00	0.9710	2.60	0.9381

The mean radius of the glass beads employed in this study was 1 mm, while the mean radius of quartz sand grain was 0.3 mm. So, the sand grains were smaller than the glass beads; thus, the solid matrix surface area was larger in the columns packed with quartz sand. Furthermore, sand grain shapes are irregular, so the surface area was larger than that

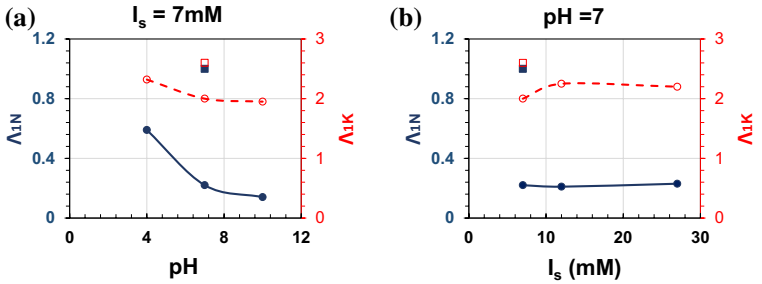


Fig. 10 Behaviour of fitted parameters associated with the cotransport experiments of GO NPs and kaolinite colloids as a function of: **a** pH and **b** IS. Circles and squares correspond to columns packed with glass beads and quartz sand, respectively. Solid and open symbols in **a**, **b** correspond to parameters Λ1N (for GO NPs) and Λ1K (for kaolinite), respectively

for the glass beads. Consequently, Λ_0 must be greater for quartz sand. This is clearly the case for both NPs and kaolinite colloids (see Fig. 7a, b, d, e) (Bradford et al. 2003, 2009a). The pore throats in columns packed with quartz sand are smaller than those packed with glass beads. Also, sand has rougher surface than glass beads, which facilitates size exclusion. The average radii for nanoparticles and kaolinite colloids were 0.4 μm and 0.6 μm, respectively, i.e. they are almost the same. Therefore, size exclusion filtration coefficient Λ_1 must be higher for sand than for glass beads. This is the case for NPs (see Fig. 7a, b), but not for kaolinite colloids (see Fig. 7d, e). The maximum retention concentration for columns packed with quartz sand is higher due to the larger solid matrix surface area of the smaller irregular grains. Therefore, S_m must be higher for columns packed with quartz. This is the case for NPs (see Fig. 7c), but not for kaolinite colloids (see Fig. 7f). The deviation of kaolinite colloids from expected behaviour is attributed to kaolinite particle aggregation. It should be noted that based on DLVO theory, kaolinite aggregation is significant (Chrysikopoulos et al. 2017).

3.2 Matching of the Cotransport Experimental Data

The experimental data for NPs and for kaolinite colloids cotransport in a column packed with glass beads at five different sets of water chemistry conditions reported by Chrysikopoulos et al. (2017) are presented in Fig. 8, together with the corresponding fitted numerical model simulations. Furthermore, the experimental data for NPs and for kaolinite colloids cotransport in a column packed with quartz sand for just one set of water chemistry conditions are presented in Fig. 9b, together with the corresponding fitted numerical model simulations. All fitted parameters for the cotransport experiments are listed in Table 3. Based on the R^2 values listed in Table 3, the numerical model (Eqs. 18 and 19) fitted adequately the experimental data for both NPs and kaolinite colloids. It should be noted that for individual suspended particle transport, the BTCs have an exponential form, so the number of degrees of freedom for each BTC is three. Therefore, three coefficients (Λ_0, Λ_1 and S_m) are determined from experimental BTC. However, for the case of cotransport (Eqs. 18 and 19), there are two breakthrough curves with six degrees of freedom, and the number of fitted parameters is only two (Λ_{1N} and Λ_{1K}).

The fitted parameters listed in Table 3 are also presented graphically in Fig. 10 as a function of pH and I_S. Both Λ_{1N} and Λ_{1K} corresponding to NPs and kaolinite colloids, respectively, decrease with increasing pH, at $I_S = 7$ mM (see Fig. 10a), whereas both Λ_{1N} and Λ_{1K}, at pH = 7, are not strongly affected by I_S (see Fig. 10b). The unexpected behaviour of kaolinite colloids (Fig. 10b) is attributed to kaolinite–kaolinite particle aggregation, which is far more significant than that of kaolinite–NP and NP–NP (Chrysikopoulos et al. 2017). It should be noted that based on DLVO theory, kaolinite aggregation is significant (Chrysikopoulos et al. 2017). However, particle aggregation was beyond the scope of this study and has not been accounted for by the proposed transport and cotransport models.

4 Discussion

The fate and transport of nanoparticles and clays in subterranean waters are highly affected by the nanoparticle–clay interactions, cotransport and their capture by the porous matrix. In this study, a novel 1D transport model with binary filtration functions was developed to simulate the transport of suspended colloidal particles as well as the cotransport of colloids and NPs. The proposed cotransport model assumes that the different types of suspended particles have electrostatic interactions with the solid matrix, which are similar under both transport and cotransport conditions. Also, the initial attachment filtration coefficient for each particle type in the mixture is equal to that for transport of each individual particle type, which implies that the maximum retention concentration for attachment for each particle type is the same under both transport and cotransport conditions.

4.1 Validity of the Single-Population and Cotransport Models

The Langmuir's mechanism is usually applied for monolayer particle attachment to the rock, where the rate is proportional to number of vacant sites for retention on rock surface. However, for size exclusion in two-sized rock with mono-sized suspension transport, the filtration function also has the blocking form (Bedrikovetsky 2008).

The individual binary filtration function, given by Eq. (7), contains three constants, namely λ_0, s_m, and λ_1. The breakthrough curve, typical for individual corefloods by nanoparticles and kaolinite particles, has three degrees of freedom (Figs. 6, 7, 8). For 11 tests, the mathematical model for single-population deep bed filtration with binary function (7) closely matches the laboratory data. However, the degree of freedom of the matched numerical array does not exceed the number of the model constants, so the model validity cannot be claimed.

The cotransport model (18, 19) contains six constants, from which four constants are determined from the individual transport experimental data. This leaves just two tuning parameters λ_{1N} and λ_{1K}. Two BTCs for each component are closely matched, so the degree of freedom of the matched information array is six. High match between the laboratory and modelling data for six cotransport experiments performed allows validating the binary deep bed filtration model given by Eq. (18, 19). In particular, the assumption that the Langmuir coefficients for transport and cotransport of NPs and kaolinite colloids are the same is valid.

4.2 Effects of Rock Properties, Salinity, and pH

Comparison between columns packed by sand and by glass beads allows qualitative prediction for straining and attachment filtration coefficients, and also for maximum attached concentration S_m. The same relates to pH and salinity for water. Those dependencies are very clearly confirmed during corefloods by nanoparticles. However, the results for kaolinite injection do not follow the trend.

DLVO energy potentials show that the particle–particle attraction is significantly weaker than that for particle–rock (Sotirelis and Chrysikopoulos 2017; Chrysikopoulos et al. 2017). Besides, the attraction force kaolinite–kaolinite is significantly stronger than those for kaolinite–NP and NP–NP. Thus, aggregation of kaolinite–NP and NP–NP can be neglected, while the kaolinite–kaolinite aggregation must be accounted for in the basic model. The luck of aggregation for kaolinite in the model can be blamed for non-monotonic behaviour of the curves shown in Figs. 7 and 10. Therefore, the model for kaolinite should include aggregation, which is outside the scope of the present study and is the next stage of the work.

4.3 Front for Discontinuity of First Derivatives

First derivatives of the solution for piecewise-linear filtration function suffer discontinuity on the boundary between zones II and III, where $S(X, T) = S_m$, and the derivative of the filtration function is also discontinuous. This phenomenon has been observed from the exact solution for flow with deposit dissolution, where the dissolution rate becomes zero when the deposit vanishes (Sorbie and Stamatiou 2018). Apart from the derivative discontinuity front, the system with deposit dissolution is linear, and the complete dissolution front propagates with constant speed. The problem (9, 10) is nonlinear, so the front trajectory in Fig. 4a is curvilinear.

4.4 Application of the Model

The proposed cotransport model with two capture mechanisms can be also used for prediction of simultaneous flows of bacteria, viruses, clays, NPs, etc. Section 2.1 shows that the filtration coefficient is constant for small retained concentration under any capture mechanism (Fig. 3b). For intermediate retained concentrations, for any capture mechanism, keeping zero and first terms in the Tailor's series yields linear filtration function (6). Zhang et al. (2018) show that binary filtration function (7) is an approximation of any two simultaneous mechanisms with constant and linear filtration functions.

The exact solution for homogeneous colloid transport has been used to fit the laboratory data and obtain model coefficients. The matching process requires computing the direct (forward) model many times; and consequently, any incremental computation time introduced by numerical techniques can be prohibitive to convergence of the fitting procedure. Therefore, derived analytical model for binary particle capture mechanisms is preferred over computationally expensive numerical solutions of inverse problem for history matching. In addition, the exact solution presented here can be used as a benchmark for numerical models. The explicit analytical solution provided in Table 1 allows for direct numerical implementation without going through complicated mathematical derivations. The analytical model developed can also be used in three-dimensional reservoir simulation using stream-line techniques (Oladyshkin and Panfilov 2007).

5 Conclusions

Analytical modelling of separate and commingled transport of clay particles and nanoparticles and matching the laboratory data allow drawing the following conclusions:

1. The breakthrough curves for *individual deep bed filtration* of kaolinite and nanoparticles exhibit the behaviour typical for two simultaneous particle capture mechanisms with binary filtration function. Tuning of six corefloods by kaolinite and six corefloods by nanoparticles and high agreement between the modelling and experimental data validate the two capture models for individual flows of both populations.
2. The proposed model for *commingled injection* of kaolinite and nanoparticles assumes the same electrostatic interaction between the species and the rock, as for the individual flows. Therefore, the initial attachment filtration coefficient for each species in the mixture is equal to that for the individual flow.
3. Another assumption of cotransport model is independent occupation of the attachment vacancies by both species, so the individual maximum retention concentration for attachment for each species is equal to that in the mixture.
4. The tuning parameters during matching the breakthrough curves with commingled injection are size exclusion filtration coefficients for straining, $\lambda_{1,\mathrm{K}}$, and $\lambda_{1,\mathrm{N}}$. High precision of the matching of eight-parametric experimental data array by two tuning parameters only for six commingled corefloods validates the cotransport model developed.

Appendix A: Aggregation of Multiple Particle Capture Mechanisms in One Mechanism

Following works by Guedes et al. (2009) and Zhang et al. (2018), in this Appendix we present the aggregation procedure for multiple particle capture mechanisms.

Consider single-population colloidal-suspension flow with n particle retention mechanisms that correspond to different filtration functions:

$$\frac{\partial S_i}{\partial T} = \lambda_i\left(S_1, S_2 \ldots S_n\right)C, \tag{A1}$$

where the total retention concentration is a sum of individual retention concentrations

$$S = \sum_{i=1}^{n} S_i. \tag{A2}$$

As it follows from Eq. (A2), mass balance for suspended particles and the particles retained by all capture mechanisms is given by Eq. (9).

The sum of n retention rates (A1) leads to the total retention rate of the overall colloidal suspension

$$\frac{\partial S}{\partial T} = \lambda\left(S_1, S_2 \ldots S_n\right)C, \quad \lambda\left(S_1, S_2 \ldots S_n\right) = \sum_{i=1}^{n} \lambda_i\left(S_1, S_2 \ldots S_n\right). \tag{A3}$$

Here, $\lambda(S_1, S_2 \ldots S_n)$ is the overall filtration function.

Fixing $x=x_0$, assuming that $C(X, T)$ is already known, and changing independent variable in system of ordinary differential equations (A3) from T to S yield

$$\frac{\partial S_i}{\partial S} = \frac{\Lambda_i\left(S_1, S_2 \dots S_n\right)}{\Lambda\left(S_1, S_2 \dots S_n\right)}, \frac{\partial T}{\partial S} = \frac{1}{\Lambda\left(S_1, S_2 \dots S_n\right)}, \quad i = 1, 2 \dots n. \tag{A4}$$

Zero initial conditions for all retention concentrations yield initial condition (12) for the total retention concentration

$$S = 0 : S_i = 0, \quad i = 1, 2 \dots n. \tag{A5}$$

Substitution of solution of the problem (A4) $S_i=S_i(S)$ into Eq. (A5) yields

$$\frac{\partial S}{\partial T} = \Lambda\left(S_1(S), S_2(S) \dots S_n(S)\right)C, \quad \Lambda(S) = \sum_{i=1}^{n} \Lambda_i\left(S_1(S), S_2(S) \dots S_n(S)\right), \tag{A6}$$

and reduces system of $n+1$ Eqs. (9, A1) to two Eqs. (9, 10).

Appendix B. Exact Solution for 1D Transport of Single-Population Colloids

Following works by Polyanin and Manzhirov 2006; Polyanin and Zaitsev (2012); Alvarez et al. (2005, 2007); Bedrikovetsky et al. (2017), in this Appendix we derive an analytical solution to the model Eqs. (9–13).

Introduction of function $\Psi(S)$ by formula (14) yields the following form for Eq. (10):

$$\frac{\partial \Psi(S)}{\partial T} = C. \tag{B1}$$

Substituting expression (B1) for $C(X, T)$ into Eq. (9) and changing the order of differentiation by X and T in second derivative yield

$$\frac{\partial}{\partial T}\left[\frac{\partial \Psi(S)}{\partial T}\right] + \frac{\partial S}{\partial T} + \frac{\partial}{\partial T}\left[\frac{\partial \Psi(S)}{\partial X}\right] = 0. \tag{B2}$$

Integrating Eq. (B2) in T from 0 to T leads to the following expression:

$$\frac{\partial \Psi(S)}{\partial T} + S + \frac{\partial \Psi(S)}{\partial X} = \left.\frac{\partial \Psi(S)}{\partial T}\right|_{T=0} + S|_{T=0} + \left.\frac{\partial \Psi(S)}{\partial X}\right|_{T=0}. \tag{B3}$$

The constant of integration is situated in the right-hand side of Eq. (B3) and is calculated from initial conditions (12). So, the right-hand side of the previous equation is equal to zero. Consequently, Eq. (B3) reduces to:

$$\frac{\partial \Psi(S)}{\partial T} + \frac{\partial \Psi(S)}{\partial X} = -S \tag{B4}$$

where $\Psi(X, T)$ is unknown, and $S(\Psi)$ is the inverse function to $\Psi=\Psi(S)$.

The initial and boundary conditions (12), (13) for Eq. (B4) become:

$$\Psi[S(X, 0)] = 0, \quad \Psi[S(0, T)] = T, \tag{B5}$$

respectively.

Along the characteristic lines $X=T–T_0$, $T_0>0$, Eq. (B4) can be transformed as follows:

$$\frac{1}{\Lambda(S)}\frac{\mathrm{d}S}{\mathrm{d}X}=-S. \tag{B6}$$

Note that the characteristic lines $X=T-T_0$, $T_0>0$ cover the overall domain $T>X$. Integrating Eq. (B6) over X and imposing boundary condition (B5) yield solution $S(X, T)$ in the form (15).

Taking derivative with respect to T on both sides of Eq. (15) yields

$$\frac{1}{S\Lambda(S)}\frac{\partial S(X,T)}{\partial T}=\frac{1}{S(0,T-X)\Lambda[S(0,T-X)]}\frac{\mathrm{d}S(0,T-X)}{\mathrm{d}T}. \tag{B7}$$

Substitution of Eq. (10) into Eq. (B7) yields

$$\frac{C(X,T)}{S(X,T)}=\frac{C(0,T-X)}{S(0,T-X)},\quad T>X. \tag{B8}$$

As it follows from Eq. (B8), the value C/S is constant along the characteristic lines $X=T–T_0$, $T_0>0$, i.e. C/S is Riemann invariant. Accounting for boundary condition (13) in Eq. (B8) yields formula (16) for suspension concentration in the domain $T>X$.

References

Abdel-Salam, A., Chrysikopoulos, C.V.: Modeling of colloid and colloid-facilitated contaminant transport in a two-dimensional fracture with spatially variable aperture. Transp. Porous Med. **20**(3), 197–221 (1995)

Alem, A., Ahfir, N.-D., Elkawafi, A., Wang, H.: Hydraulic operating conditions and particle concentration effects on physical clogging of a porous medium. Transp. Porous Med. **106**(2), 303–321 (2015)

Alvarez, A., Bedrikovetsky, P., Hime, G., Marchesin, A., Marchesin, D., Rodrigues, J.: A fast inverse solver for the filtration function for flow of water with particles in porous media. Inverse Probl. **22**(1), 69 (2005)

Alvarez, A.C., Hime, G., Marchesin, D., Bedrikovetsky, P.G.: The inverse problem of determining the filtration function and permeability reduction in flow of water with particles in porous media. Transp. Porous Med. **70**(1), 43–62 (2007)

Arab, D., Pourafshary, P.: Nanoparticles-assisted surface charge modification of the porous medium to treat colloidal particles migration induced by low salinity water flooding. Colloids Surf. A Physicochem. Eng. Asp. **436**, 803–814 (2013)

Arab, D., Pourafshary, P., Ayatollahi, S.: Mathematical modeling of colloidal particles transport in the medium treated by nanofluids: deep bed filtration approach. Transp. Porous Med. **103**(3), 401–419 (2014)

Araújo, J.A., Santos, A.: Analytic model for DBF under multiple particle retention mechanisms. Transp. Porous Med. **97**(2), 135–145 (2013)

Arns, C., Adler, P.: Fast Laplace solver approach to pore-scale permeability. Phys. Rev. E **97**(2), 023303 (2018)

Bashtani, F., Taheri, S., Kantzas, A.: Scale up of pore-scale transport properties from micro to macro scale; network modelling approach. J. Petrol. Sci. Eng. **170**, 541–562 (2018)

Bedrikovetsky, P.: Upscaling of stochastic micro model for suspension transport in porous media. Transp. Porous Med. **75**(3), 335–369 (2008)

Bedrikovetsky, P.: Mathematical Theory of Oil and Gas Recovery: With Applications to Ex-USSR Oil and Gas Fields, vol. 4. Springer, Berlin (2013)

Bedrikovetsky, P., You, Z., Badalyan, A., Osipov, Y., Kuzmina, L.: Analytical model for straining-dominant large-retention depth filtration. Chem. Eng. J. **330**, 1148–1159 (2017)

Bekhit, H.M., El-Kordy, M.A., Hassan, A.E.: Contaminant transport in groundwater in the presence of colloids and bacteria: model development and verification. J. Contam. Hydrol. **108**(3–4), 152–167 (2009)

Bennacer, L., Ahfir, N.-D., Alem, A., Wang, H.: Coupled effects of ionic strength, particle size, and flow velocity on transport and deposition of suspended particles in saturated porous media. Transp. Porous Med. **118**(2), 251–269 (2017)
Bradford, S.A., Kim, H.N., Haznedaroglu, B.Z., Torkzaban, S., Walker, S.L.: Coupled factors influencing concentration-dependent colloid transport and retention in saturated porous media. Environ. Sci. Technol. **43**(18), 6996–7002 (2009)
Bradford, S.A., Simunek, J., Bettahar, M., van Genuchten, M.T., Yates, S.R.: Modeling colloid attachment, straining, and exclusion in saturated porous media. Environ. Sci. Technol. **37**(10), 2242–2250 (2003)
Bradford, S.A., Torkzaban, S., Leij, F., Šimůnek, J., van Genuchten, M.T.: Modeling the coupled effects of pore space geometry and velocity on colloid transport and retention. Water Resour. Res. **45**(2) (2009b)
Chequer, L., Russell, T., Behr, A., Genolet, L., Kowollik, P., Badalyan, A., Zeinijahromi, A., Bedrikovetsky, P.: Non-monotonic permeability variation during colloidal transport: governing equations and analytical model. J. Hydrol. **557**, 547–560 (2017)
Chrysikopoulos, C.V., Sotirelis, N.P., Kallithrakas-Kontos, N.G.: Cotransport of graphene oxide nanoparticles and kaolinite colloids in porous media. Transp. Porous Med. **119**(1), 181–204 (2017)
Civan, F.: Reservoir Formation Damage. Gulf Professional Publishing, Houston (2015)
Coleman, T.F., Li, Y.: An interior trust region approach for nonlinear minimization subject to bounds. SIAM J. Optim. **6**(2), 418–445 (1996)
Elimelech, M., Gregory, J., Jia, X.: Particle Deposition and Aggregation: Measurement, Modelling and Simulation. Butterworth-Heinemann, Oxford (2013)
Farajzadeh, R., Guo, H., van Winden, J., Bruining, J.: Cation exchange in the presence of oil in porous media. ACS Earth Space Chem. **1**(2), 101–112 (2017)
Guedes, R.G., Al-Abduwani, F., Bedrikovetsky, P., Currie, P.: Injectivity decline under multiple particle capture mechanisms. J. Soc. Pet. Eng. **14**, 477–487 (2009)
Hammadi, A., Ahfir, N.-D., Alem, A., Wang, H.: Effects of particle size non-uniformity on transport and retention in saturated porous media. Transp. Porous Med. **118**(1), 85–98 (2017)
Hayek, M.: Exact solutions for one-dimensional transient gas flow in porous media with gravity and Klinkenberg effects. Transp. Porous Med. **107**(2), 403–417 (2015)
Hayek, M., Kosakowski, G., Jakob, A., Churakov, S.V.: A class of analytical solutions for multidimensional multispecies diffusive transport coupled with precipitation-dissolution reactions and porosity changes. Water Resour. Res. **48**(3) (2012)
Herzig, J., Leclerc, D., Goff, P.L.: Flow of suspensions through porous media—application to deep filtration. Ind. Eng. Chem. **62**(5), 8–35 (1970)
Katzourakis, V.E., Chrysikopoulos, C.V.: Mathematical modeling of colloid and virus cotransport in porous media: application to experimental data. Adv. Water Resour. **68**, 62–73 (2014)
Katzourakis, V.E., Chrysikopoulos, C.V.: Modeling dense-colloid and virus cotransport in three-dimensional porous media. J. Contam. Hydrol. **181**, 102–113 (2015)
Kuhnen, F., Barmettler, K., Bhattacharjee, S., Elimelech, M., Kretzschmar, R.: Transport of iron oxide colloids in packed quartz sand media: monolayer and multilayer deposition. J. Colloid Interface Sci. **231**(1), 32–41 (2000)
Kuzmina, L.I., Osipov, Y.V., Galaguz, Y.P.: A model of two-velocity particles transport in a porous medium. Int. J. Non Linear Mech. **93**, 1–6 (2017)
Mansouri, M., Nakhaee, A., Pourafshary, P.: Effect of SiO_2 nanoparticles on fines stabilization during low salinity water flooding in sandstones. J. Petrol. Sci. Eng. **174**, 637–648 (2019)
Mikhailov, D., Zhvick, V., Ryzhikov, N., Shako, V.: Modeling of rock permeability damage and repairing dynamics due to invasion and removal of particulate from drilling fluids. Transp. Porous Med. **121**(1), 37–67 (2018)
Mirabolghasemi, M., Prodanović, M., DiCarlo, D., Ji, H.: Prediction of empirical properties using direct pore-scale simulation of straining through 3D microtomography images of porous media. J. Hydrol. **529**, 768–778 (2015)
Oladyshkin, S., Panfilov, M.: Streamline splitting between thermodynamics and hydrodynamics in a compositional gas–liquid flow through porous media. C. R. Méc. **335**(1), 7–12 (2007)
Polyanin, A.: EqWorld, The World of Mathematical Equations. http://eqworld.ipmnet.ru/ (2004). Accessed 01/06/2018
Polyanin, A., Zaitsev, V.: Handbook of Nonlinear Partial Differential Equations. CRC Press, Boca Raton (2012)
Polyanin, A.D., Dil′man, V.V.: Methods of Modeling Equations and Analogies in Chemical Engineering. CRC Press, Boca Raton (1994)
Polyanin, A.D., Manzhirov, A.V.: Handbook of Mathematics for Engineers and Scientists. CRC Press, Boca Raton (2006)

Rottman, J., Sierra-Alvarez, R., Shadman, F.: Real-time monitoring of nanoparticle retention in porous media. Environ. Chem. Lett. **11**(1), 71–76 (2013)
Russell, T., Pham, D., Neishaboor, M.T., Badalyan, A., Behr, A., Genolet, L., Kowollik, P., Zeinijahromi, A., Bedrikovetsky, P.: Effects of kaolinite in rocks on fines migration. J. Nat. Gas Sci. Eng. **45**, 243–255 (2017)
Santos, A., Bedrikovetsky, P.: A stochastic model for particulate suspension flow in porous media. Transp. Porous Med. **62**(1), 23–53 (2006)
Sefrioui, N., Ahmadi, A., Omari, A., Bertin, H.: Numerical simulation of retention and release of colloids in porous media at the pore scale. Colloids Surf. A Physicochem. Eng. Asp. **427**, 33–40 (2013)
Shampine, L.: Solving hyperbolic PDEs in MATLAB. Appl. Numer. Anal. Comput. Math. **2**(3), 346–358 (2005a)
Shampine, L.F.: Two-step Lax–Friedrichs method. Appl. Math. Lett. **18**(10), 1134–1136 (2005b)
Shapiro, A., Wesselingh, J.: Gas transport in tight porous media: gas kinetic approach. Chem. Eng. J. **142**(1), 14–22 (2008)
Shapiro, A., Yuan, H.: Application of stochastic approaches to modelling suspension flow in porous media. In: Skogseid, A., Fasano, V. (eds.) Statistical Mechanics and Random Walks: Principles, Processes and Applications. Hauppauge, New York (2012)
Shapiro, A.A., Bedrikovetsky, P.G., Santos, A., Medvedev, O.O.: A stochastic model for filtration of particulate suspensions with incomplete pore plugging. Transp. Porous Med. **67**(1), 135–164 (2007)
Shapiro, A., Bedrikovetsky, P.: Elliptic random-walk equation for suspension and tracer transport in porous media. Phys. A: Stat. Mech. Appl. **387**(24), 5963–5978 (2008)
Shapiro, A., Bedrikovetsky, P.: A stochastic theory for deep bed filtration accounting for dispersion and size distributions. Phys. A: Stat. Mech. Appl. **389**, 2473–2494 (2010)
Sharma, M., Yortsos, Y.: Transport of particulate suspensions in porous media: model formulation. AlChE J. **33**(10), 1636–1643 (1987)
Shikhov, I., Arns, C.H.: Evaluation of capillary pressure methods via digital rock simulations. Transp. Porous Med. **107**(2), 623–640 (2015)
Sorbie, K., Stamatiou, A.: Analytical solutions of a one-dimensional linear model describing scale inhibitor precipitation treatments. Transp. Porous Med. **123**, 271–287 (2018)
Sotirelis, N.P., Chrysikopoulos, C.V.: Heteroaggregation of graphene oxide nanoparticles and kaolinite colloids. Sci. Total Environ. **579**, 736–744 (2017)
Syngouna, V.I., Chrysikopoulos, C.V., Kokkinos, P., Tselepi, M.A., Vantarakis, A.: Cotransport of human adenoviruses with clay colloids and TiO_2 nanoparticles in saturated porous media: effect of flow velocity. Sci. Total Environ. **598**, 160–167 (2017)
Wang, Y., Arns, C.H., Rahman, S.S., Arns, J.-Y.: Porous structure reconstruction using convolutional neural networks. Math. Geosci. **50**, 1–19 (2018a)
Wang, Y., Rahman, S.S., Arns, C.H.: Super resolution reconstruction of μ-CT image of rock sample using neighbour embedding algorithm. Phys. A: Stat. Mech. Appl. **493**, 177–188 (2018b)
Yanici, S., Arns, J.-Y., Cinar, Y., Pinczewski, W., Arns, C.: Percolation effects of grain contacts in partially saturated sandstones: deviations from Archie's law. Transp. Porous Med. **96**(3), 457–467 (2013)
You, Z., Bedrikovetsky, P., Badalyan, A., Hand, M.: Particle mobilization in porous media: temperature effects on competing electrostatic and drag forces. Geophys. Res. Lett. **42**(8), 2852–2860 (2015)
Yuan, B., Moghanloo, R.G.: Analytical model of well injectivity improvement using nanofluid preflush. Fuel **202**, 380–394 (2017). https://doi.org/10.1016/j.fuel.2017.04.004
Yuan, B., Moghanloo, R.G., Zheng, D.: Analytical evaluation of nanoparticle application to mitigate fines migration in porous media. SPE J. **21**(06), 2–317 (2016a)
Yuan, B., Wang, W., Moghanloo, R.G., Su, Y., Wang, K., Jiang, M.: Permeability reduction of berea cores owing to nanoparticle adsorption onto the pore surface: mechanistic modeling and experimental work. Energy Fuels **31**(1), 795–804 (2016b)
Yuan, H., Shapiro, A., You, Z., Badalyan, A.: Estimating filtration coefficients for straining from percolation and random walk theories. Chem. Eng. J. **210**, 63–73 (2012)
Yuan, H., Shapiro, A.A.: Modeling non-Fickian transport and hyperexponential deposition for deep bed filtration. Chem. Eng. J. **162**(3), 974–988 (2010)
Zhang, H., Malgaresi, G.V.C., Bedrikovetsky, P.: Exact solutions for suspension-colloidal transport with multiple capture mechanisms. Int. J. Non Linear Mech. **105**, 27–42 (2018)

Publisher's Note Springer Nature remains neutral with regard to jurisdictional claims in published maps and institutional affiliations.

4 Exact Upscaling for Transport of Size-Distributed Colloids

P. Bedrikovetsky, Y. Osipov, L. Kuzmina and, **G. Malgaresi**.

Water Resources Research Journal

Statement of Authorship

Title of Paper	Exact Upscaling for Transport of Size-Distributed Colloids
Publication Status	☑ Published ☐ Accepted for Publication ☐ Submitted for Publication ☐ Unpublished and Unsubmitted work written in manuscript style
Publication Details	Bedrikovetsky, P., Osipov, Y., Kuzmina, L. and Malgaresi, G., 2019. Exact Upscaling for Transport of Size-Distributed Colloids. Water Resources Research, 55(2), pp.1011-1039.

Principal Author

Name of Principal Author	Pavel Bedrikovetsky
Contribution to the Paper	Derivation of the mathematical model for multicomponent transport in porous media, performed analysis of the results and, mathematical properties of the model.
Signature	Date 23/10/2019

Co-Author Contributions

By signing the Statement of Authorship, each author certifies that:

i. the candidate's stated contribution to the publication is accurate (as detailed above);

ii. permission is granted for the candidate in include the publication in the thesis; and

iii. the sum of all co-author contributions is equal to 100% less the candidate's stated contribution.

Name of Co-Author	Yuri Osipov
Contribution to the Paper	Helped with the derivation of the mathematical model for multicomponent in porous media, analysis of the results, and mathematical properties of the model.
Signature	Date 28/10/2019

Name of Co-Author	Liudmila Kuzmina
Contribution to the Paper	Helped with the derivation of the mathematical model for multicomponent in porous media and, analysis of the results.
Signature	Date 28/10/2019

Name of Co-Author	Gabriel Malgaresi
Contribution to the Paper	Helped with the derivation of analytical solution and numerical solution. Helped in laboratory data interpretation, and developed the DLVO calculation.
Overall percentage (%)	40%
Certification:	This paper reports on original research I conducted during the period of my Higher Degree by Research candidature and is not subject to any obligations or contractual agreements with a third party that would constrain its inclusion in this thesis.
Signature	Date 25/10/2019

Water Resources Research

RESEARCH ARTICLE
10.1029/2018WR024261

Exact Upscaling for Transport of Size-Distributed Colloids

P. Bedrikovetsky[1], Y. Osipov[2], L. Kuzmina[3], and G. Malgaresi[1]

[1]Australian School of Petroleum, University of Adelaide, Adelaide, South Australia, Australia, [2]Applied Mathematics Department, Moscow State University of Civil Engineering, Moscow, Russia, [3]Department of Mathematics, National Research University Higher School of Economics, Moscow, Russia

Key Points:
- Exact averaging of colloidal, nanotranspost, and reactive transport with distributed particle properties in porous media is performed
- The upscaled 3 x 3 system significantly differs from the classical 2 x 2 system for deep bed filtration or reactive flow in porous media
- Microscale multicomponent particle properties are reflected in the large-scale model by newly introduced nonlinear suspension function

Correspondence to:
P. Bedrikovetsky,
pavel@asp.adelaide.edu.au

Citation:
Bedrikovetsky, P., Osipov, Y., Kuzmina, L., & Malgaresi, G. (2019). Exact upscaling for transport of size-distributed colloids. *Water Resources Research*, *55*, 1011–1039. https://doi.org/10.1029/2018WR024261

Received 25 OCT 2018
Accepted 10 JAN 2019
Accepted article online 17 JAN 2019
Published online 6 FEB 2019

Abstract The article investigates one-dimensional (1-D) suspension-colloidal transport of size-distributed particles with particle attachment. A population balance approach is presented for computing the particle transport and capture by porous media. The occupied area of each attached particle is particle size-dependent. The main model assumption is the retention rate dependency of the overall vacancy concentration for all particle sizes. For the first time, we derive an exact averaging (upscaling) procedure resulting in a closed system of large-scale equations for average concentrations of suspended and retained particles and of occupied rock surface area. The resulting large-scale 3×3 system significantly differs from the traditional 2×2 deep bed filtration model. However, the traditional model becomes a particular case that corresponds to an equal occupied area for all particles. The averaging yields the appearance of two empirical suspension and site occupation functions, which govern the kinetics of particle retention and site occupation, respectively. One-dimensional flow problems for the averaged equations are essentially nonlinear. However, they allow for exact solutions. We derive novel exact solutions for three 1-D problems: continuous injection of particulate colloidal suspension, injection of colloidal suspension bank with particle-free chase drive, and fines migration induced by high-rate flows. The analytical model for continuous injection closely matches three series of laboratory tests on nanofluid transport.

1. Introduction

We consider porous-media flows of suspension, colloids, and nanofluids whose properties vary by orders of magnitude. The focus is on solving nonsteady state one-dimensional (1-D) problems of either injection of water with "foreign" particles in aquifers or lifting, mobilization, and migration of natural reservoir fines. Those flows occur in numerous areas of environmental, chemical, and petroleum engineering. The incomplete list of topics includes disposal of industrial wastes in aquifers, propagation of viruses and bacteria in subterranean waters, industrial filtering of water and technical fluids, cold-water injection into geothermal reservoirs, exploitation of geothermal wells, mass exchange by waters with different salinities between aquifers and ocean, migration of natural reservoir fines, injection of water with solid and liquid particles into oilfields during waterflooding, and reinjection of water produced from oilfields (Bradford, Torkzaban, & Simunek, 2011; Bradford, Torkzaban, & Wiegmann, 2011; Chrysikopoulos & Syngouna, 2012; Chrysikopoulos et al., 2012; Elimelech et al., 2013; Rosenbrand et al., 2015).

Physical mechanisms of particle capture by the rock during suspension-colloidal flows may include size exclusion, straining, attachment, segregation, adsorption, and diffusion into dead end pores (Bradford et al., 2015; Chrysikopoulos et al., 2017; Chrysikopoulos & Syngouna, 2012; Civan, 2015). The effects of particle retention are decrease in suspension concentration and permeability. The suspension concentration decline due to retention is important for industrial waste disposal and aquifer contamination, while the permeability decline yields well productivity and injectivity decline.

Governing equations of deep bed filtration in porous media contain mass balance for suspended and retained particles, particle capture rate that is proportional to the particle advective flux, and Darcy's law accounting for permeability decline due to particle retention (Bradford, Torkzaban, & Simunek, 2011; Yuan & Shapiro, 2010, 2012; Xu, 2016):

$$\frac{\partial}{\partial t}(\phi c + s) + U\frac{\partial c}{\partial x} = 0, \tag{1}$$

$$\frac{\partial s}{\partial t} = \lambda(1 - b_0 s)cU, \tag{2}$$

©2019. American Geophysical Union. All Rights Reserved.

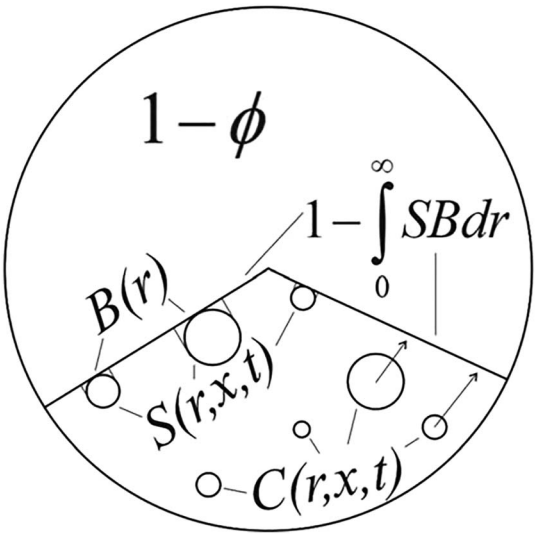


Figure 1. Schematic for fines suspension in pore space and attachment to the rock surface. C and S are suspended and retained concentrations, respectively; B is the surface area occupied by a single attached particle.

$$U = -\frac{k(s)}{\mu(c)}\frac{\partial p}{\partial x}, \tag{3}$$

where x is the linear coordinate in the flow direction, t is the time, c and s are suspended and attached concentrations, ϕ is the porosity, U is the fluid velocity, λ is the filtration coefficient, b_0 is the fraction of the vacancies occupied by a single retained particle, k is the permeability, μ is the viscosity, and p is the pressure. Suspension concentration c is determined as the number of suspended particles in a unitary volume of carrier fluid, while the attached concentration s is defined as the number of attached particles in a unitary volume of the rock (Figure 1). The fraction of the vacant area for attachment of suspended particles is equal to $1\text{-}b_0s$; here dimension of constant is L^3 that corresponds to the product of the grain system dispersivity and the area occupied by a single attached particle (Shapiro et al., 2007).

The assumption leading to equation (2) is monolayer Langmuir's attachment where one attached particle occupies one vacancy. This assumption yields the "active-mass" law for the particle vacancy 1:1 "reaction," where the reaction rate is proportional to the product of "reactive vacancy" and suspension concentrations, $1\text{-}b_0s$ and c, respectively (Elimelech et al., 2013; Fogler, 2006). Other assumptions are small suspended and attached concentrations. For large suspended and vacancy concentrations in the rate equation (2), vacancy concentration ($1\text{-}b_0s$) and suspension concentration c are substituted by their nonlinear functions, like the large concentrations of reacting species, which are substituted by their activities in the active mass law (Fogler, 2006)

$$\frac{\partial s}{\partial t} = h(s)f(c)U. \tag{4}$$

Therefore, equations (1), (3), and (4) also model reactive transport with chemical fluid-rock reactions (Lasaga, 1998; Polyanin & Dil'man, 1994). So far extended equation (4) for deep bed filtration was not derived from either first principles or microscale mechanics but is used for matching the laboratory data (Bradford et al., 2015; Civan, 2015; Kuzmina et al., 2017).

One-dimensional problems for any arbitrary filtration function $h(s)$ and linear suspension function $f(c) = \lambda c$ allow for exact solutions (Goldberg et al., 2014; Polyanin & Manzhirov, 2006; Polyanin & Zaitsev, 2012). For the forward problem, the exact solution determines concentrations c and s from 2×2 system ((1) and (4)), and then pressure $p(x,t)$ is calculated from equation (3). The inverse problems determine filtration function $h(s)$ from the breakthrough concentration $c(L,t)$ and formation damage function $k(s)$ from the pressure drop across the core $\Delta p = p(0,t)\text{-}p(L,t)$, where L is the core length. The exact solutions provide the regularization for both inverse problems (Alvarez et al., 2007). The exact solutions for direct problems and well-posed inverse solutions yield the original laboratory test design for determining $h(s)$ and $k(s)$ from the experimental data (Vaz et al., 2016, 2017).

The filtration and formation damage functions depend on sizes and shapes of particles and pores, z-potentials of rock and particle surfaces, mineral compositions of carrier fluids and solids, etc. The above mentioned parameters can vary by several orders of magnitude and are randomly distributed at the microscale (Bradford et al., 2013; Brady et al., 2015; Elimelech et al., 2013; Yu et al., 2018). The effects of microscale parameters on suspension-colloidal flows in porous media are captured by stochastic mathematical models, where the particles are distributed by physical parameters like size, shape factor, and z-potential.

The microscale (pore-scale) mathematical models include trajectory analysis (Payatakes et al., 1974), numerical solutions of Navier-Stokes equations at the pore scale and predicting the filtration coefficient λ as a function of microparameters (Bradford, Torkzaban, & Wiegmann, 2011; Tufenkji & Elimelech, 2004), random-walk modeling using the Master equation (Boccardo, Sethi, & Marchisio, 2018; Boccardo, Sokolov, & Paster, 2018; Paster et al., 2014; Shapiro, 2007; Shapiro & Yuan, 2012; Yuan & Shapiro, 2012), 3-D micromodeling on pore scale (Bianco et al., 2016; Bradford, Torkzaban, & Wiegmann, 2011;

Mirabolghasemi et al., 2015), Boltzmann's equation (Shapiro & Wesselingh, 2008), and population balance modeling (Boccardo, Sethi, & Marchisio, 2018; Boccardo, Sokolov, & Paster, 2018). The population balance models, proposed by Sharma and Yortsos (1987a, 1987b), account for particle and pore size distributions, straining and attachment capture mechanisms, pore connectivity, and permeability damage. More detailed models account for inaccessible pore volume and fractional flow of particles, size-exclusion percolation, and incomplete pore plugging (Bedrikovetsky, 2008; Yuan et al., 2012).

Upscaling of porous media flows with a heterogeneous microstructure has highly developed considerably in the last 20 years (Dagan et al., 2013; Tartakovsky et al., 2017). The dispersivity coefficient is the size of quasiperiodical structure for deterministic problems, and the correlation length for the problems with stochastic heterogeneity (Arns & Adler, 2018; Arns et al., 2005; Boso & Tartakovsky, 2016; Fiori et al., 2015; Rabinovich et al., 2013; Winter & Tartakovsky, 2002). An important particular case is uncorrelated stochastic properties, which corresponds to zero dispersivity of the microscale system (Dagan et al., 2013; Efendiev et al., 2016). In the present paper, we discuss this particular case. Therefore, further in the text we apply both terms upscaling and averaging.

The upscaling of population balance equations for monosized particles and size exclusion capture yields two traditional equations ((1) and (2)) for deep bed filtration (Bedrikovetsky, 2008). Moreover, due to exact averaging procedure, the upper-scale exact 1-D solutions allow for downscaling (Bedrikovetsky et al., 2017). Yet the upscaled equations for multisized particle transport with attachment are not available.

The current paper fills the gap. For the first time, we derive averaged equations for suspended colloidal transport of size-distributed particles accompanied by particle capture by the rock. The microscale system consists of two governing equations for particle conservation law and kinetics of their attachment, while the upscaled system contains three equations for particle conservation law and kinetics of their attachment and occupation of the vacancies. The upscaled particle capture law has the form given by equation (4), where the formulae for suspension function $f(c)$ is derived from individual suspension functions at the microscale. The upscaled 3×3 system significantly differs from the traditional 2×2 system ((1) and (4)) but degenerates into it for the case where different-size attached particles occupy the same area. The upscaled 3×3 system allows for exact solutions for the case of Langmuir (blocking) filtration function. Novel exact solutions are derived for three cases of 1-D suspension-colloidal flow: continuous and pulse-like suspension injection into a clean bed and also for fines migration of mobilized particles. The typical shapes of the model functions as well as for suspended, retained, and site occupation profiles are predicted by the analytical model of a binary suspension injection. Matching the laboratory data on colloidal and nanoparticle injections into porous columns by the upscaled model yields a close match, while matching by the traditional model exhibits significant deviation.

The structure of the text is as follows. Section 1 introduces the classical model for suspension-colloidal flow in porous media and its nonlinear modifications. Section 2 presents the microscale equations for suspension-colloidal-nanotransport with size-distributed particles. Section 3 derives the upscaled equations for averaged (total) particle and occupied vacancy concentrations. Section 4 presents averaged equations for systems with discrete particle size distributions. Section 5 derives exact solutions for 1-D continuous and bank suspension-colloidal injections in porous media. Section 6 derives exact solutions for 1-D fines migration. Section 7 discusses the results of analytical modeling of 1-D suspension-colloidal injections. Section 8 presents treatment of laboratory data by the analytical model. Sections 9 and 10 discuss the microscale and macroscale models and conclude the paper.

2. Population Balance Model With Particle Attachment

This section lists the main assumptions of the population balance model for multisize particle transport (section 2.1), introduces microscale and macroscale parameters (section 2.2), presents microscale equations (section 2.3), and formulates initial-boundary value problems for 1-D flows with suspension injection and fines migration for continuous and discrete particle systems (section 2.4).

2.1. Assumptions of the Model

We consider incompressible carrier fluids (water, oil, and air) with low-concentration suspension, so variations of suspended or attached concentrations do not affect the fluid density, which remains constant. The assumptions of volume additivity with suspension of particles in water and with the particle attachment

(Amagat's law) and incompressibility of aqueous and solid components yield the same system of equations for volumetric concentrations even for high suspended and retained concentrations (Bedrikovetsky, 2013). The suspension incompressibility yields flow rate conservation $U = U(t)$. Here we discuss the particular case where $U =$ constant.

Particle diffusion is negligible if compared with the advective flux. The dispersion is proportional to flow velocity $D = \alpha_L U$, where α_L is the dispersivity coefficient. The inverse to Peclet number is D/LU = α_L/L. For laboratory porous columns or reservoir cores with moderate heterogeneity, α_L varies from 10^{-4} to 10^{-2} m, while typical core length is $L = 0.1$ m (Dagan et al., 2013; Fiori et al., 2015). Thus, the dispersivity coefficient is negligible if compared with the core length, that is, dispersion is negligible if compared with the advective flux (Dagan et al., 2013; Polyanin & Dil'man, 1994).

The filtration coefficient in equation (2) and suspension function in equation (4) are assumed to be independent of velocity, and the retention rate is proportional to velocity. In reality, filtration coefficient λ is the probability of particle capture per unit of its trajectory (Bedrikovetsky, 2008). This probability depends on velocity via various dimensionless groups (Pan & Tartakovsky, 2013; Tufenkji & Elimelech, 2004). Here we discuss 1-D transport, where constant U is a parameter with given value.

Attached and suspended particles are distributed by size r. The attachment rate is equal to the product of two functions, where the first filtration function depends on the fraction of the vacant rock surface, and the second suspension function depends on suspension concentration, like in equation (4). For each r population, the suspension function depends on suspension concentration of this population and of particle size r, while the filtration function depends on the overall vacancy concentration and is independent of r. So the filtration function $h(s)$ at the microscale is the same for particles with different radii. It means that different particle populations compete for the same set of vacancies.

2.2. Introduction of Basic Parameters

Consider suspended and attached particles randomly distributed by size or any other property, C and S, respectively. The particle properties can include radius, shape factor, z-potential, density, and surface charge; in general, r is the vector of those properties. Further in the text, for the sake of simplicity but without loss of generality, r is the particle size. The overall suspended and attached concentrations are

$$c(x,t) = \int_0^\infty C(r,x,t)\mathrm{d}r,\ \ s(x,t) = \int_0^\infty S(r,x,t)\mathrm{d}r. \tag{5}$$

We consider a monolayer of attached particles with different sizes. The fraction of the occupied attachment vacancies of the overall rock surface is

$$b(x,t) = \int_0^\infty B(r)S(r,x,t)\mathrm{d}r, \tag{6}$$

where $B(r)$ is the ratio between the area occupied by a single attached particle and the overall rock surface, and b is the overall fraction of the rock surface occupied by the attached particles. The probability distribution functions for suspended and retained particles and for occupied vacancies are C/c, S/s, and BS/b, respectively.

2.3. Basic Equations

The system of governing equations for suspension-colloidal transport with particle attachment and size-distributed particles is obtained by random distribution of particles in system (1) and (4).

The suspended particles are transported by the advective flux of the carrier fluid, while the attached particles stay either at the rock or internal cake surface (Figure 1). Therefore, mass balance equation for suspended and attached particles of any given size r is (Shapiro et al., 2007)

$$\frac{\partial(\phi C(r,x,t) + S(r,x,t))}{\partial t} + U\frac{\partial C(r,x,t)}{\partial x} = 0 \tag{7}$$

By analogy to equation (4), the attachment rate for particles with size r is a product of two functions that depends on each "reagent" concentration, that is, of vacant attachment sites and suspended particles (Katzourakis & Chrysikopoulos, 2018; Kuzmina et al., 2017)

$$\frac{\partial S(r,x,t)}{\partial t} = h\left(\int_0^\infty B(r)S(r,x,t)\mathrm{d}r\right)F(C(r,x,t),r)U. \tag{8}$$

Here $h(b)$ is the filtration function that depends on the overall area occupied by the attached particles. Because the total of attached and vacant areas is constant, the vacant area can serve as a variable for the filtration function. $F(C,r)$ is a suspension function that is defined for each particle size r. The retention rate of rth population is independent of concentrations for other populations. In the particular case where the individual attachment area $B(r)$ is the same for all populations, h becomes a function of suspended concentration, given by equation (2) or (4).

For small suspension concentrations C, considering Taylor's series for suspension function and keeping zero and first-order terms yield the capture rate proportional to the advective flux

$$F(C,r) = \lambda(r)C, \tag{9}$$

resulting in the following properties of the microscale suspension function $F(C(r),r)$:

$$F(0,r) = 0,\ \ \frac{\partial F}{\partial C}(0,r) = \lambda(r). \tag{10}$$

For small retention concentrations and, consequently, small occupied vacancy concentrations, considering Taylor's series for filtration function and keeping zero and first-order terms yield the capture rate proportional to the number of vacant sizes, like in equation (2)

$$h(y) = 1 - b_0 y, \tag{11}$$

This results in the following properties of the nonlinear filtration function $h(s)$ from equation (4):

$$h(0) = 1,\ \ h'(0) = -b_0. \tag{12}$$

Equations (7) and (8) form 2×2 system of partial differential equations for two unknowns $C(r,x,t)$ and $S(r,x,t)$. Properties given by equations (10) and (12) correspond to any suspension and filtration functions. However, forms (9) and (11) correspond to small suspension and retained concentrations, respectively, and are used further in the text in the analytical modeling.

2.4. One-Dimensional Flows for Suspension Injection and Fines Migration

The problem of suspension injection into clean-bed porous media corresponds to the following initial and boundary conditions:

$$t = 0 : C = S = 0, x = 0 : C = C^0(r), \tag{13}$$

where $C^0(r)$ is the particle size-distribution in the injected suspension.

The following dimensionless parameters and variables are introduced:

$$x \to \frac{x}{L}, t \to \frac{Ut}{\phi L}, c^0 = \int_0^\infty C^0(r)\mathrm{d}r, C \to \frac{C}{c^0}, S \to \frac{S}{\phi c^0}, F(C,r) \to \frac{F(C,r)L}{c^0},$$
$$C^0(r) \to \frac{C^0(r)}{c^0}, r \to \frac{rc^0}{\int_0^\infty rC^0(r)\mathrm{d}r},\ \ B \to \phi c^0 B, \tag{14}$$

Here the dimensionless linear coordinate x is expressed as a fraction of the core (reservoir) length L; the dimensionless time t is expressed in pore volumes injected (PVI); for each size particle, the injected

concentration $C^0(r)$, the suspension function $F(C,r)$, and the suspended concentration C are normalized by the total injected concentration c^0; radius r is normalized using the average particle radius in the injected fluid.

Introduction of dimensionless parameters and variables (14) transforms system (7) and (8) to the following form:

$$\frac{\partial(C(r,x,t)+S(r,x,t))}{\partial t}+\frac{\partial C(r,x,t)}{\partial x}=0, \tag{15}$$

$$\frac{\partial S(r,x,t)}{\partial t}=h\left(\int_0^\infty B(r)S(r,x,t)\mathrm{d}r\right)F(C(r,x,t),r). \tag{16}$$

Now consider the initial-boundary problem for initial release of the attached fines with further migration and capture. Here we assume torque balance of drag, electrostatic, lift, and gravitational forces exerting a single particle at the rock or internal cake surface as a mechanical equilibrium of the particle (Bradford et al., 2013). The torque balance allows determining how much particles of each size are released by the drag force created by injection at $t = 0$ using so-called maximum retention function (Bedrikovetsky et al., 2011). Fines release occurs instantly due to fluid incompressibility. The remaining attached particles are assumed to be part of the rock. So the initial and boundary conditions for *migration of fines* released by the injection of particle-free water are

$$t=0: C=C^0(r), S=0; \quad x=0: C=0. \tag{17}$$

Further at $t > 0$, the mobilized particles migrate in the porous space and are captured by the rock. It yields the increase of retaining fines S and decrease in suspended particle concentration C.

Introduce a new variable τ and the corresponding mapping

$$\tau = t-x, \ \ (x,t)\rightarrow(x,\tau), \tag{18}$$

where τ is the time counted from the moment where the concentration front $x = t$ passes point x.

Changing variables $(x,t) \rightarrow (x,\tau)$ in system (15) and (16) yields

$$\frac{\partial S(r,x,\tau)}{\partial \tau}+\frac{\partial C(r,x,\tau)}{\partial x}=0, \tag{19}$$

$$\frac{\partial S(r,x,\tau)}{\partial \tau}=h\left(\int_0^\infty B(r)S(r,x,\tau)dr\right)F(C(r,x,\tau),r). \tag{20}$$

This change of variables transforms the initial and boundary conditions (13) for the suspension injection problem into

$$\tau=-x: C=S=0, \quad x=0: C=C^0(r), \tag{21}$$

The mapping (18) transforms the initial and boundary conditions (17) for instant *fines mobilization* with further migration and capture during the particle-free water injection, into the following conditions

$$\tau=-x: \ \ C=C^0(r), S=0, \quad x=0: C=0, \tag{22}$$

Figure 2 reflects mapping (18) and transformation of the flow domain and of initial and boundary conditions. Straight lines $t = 0$, $x = t$, $x = t$-Δ, and $x = 0$ in plane (x,t) map into straight lines $\tau = -x$, $\tau = 0$, $\tau = \Delta$, and $x = 0$ in plane (x,τ), respectively. Consequently, zones 0, I, and II in plane (x,t) map into the same zones in plane (x,τ).

Now we discuss boundary conditions of equation (13) pertaining to suspension injection. Attachment rate equation (20) does not contain x-derivative, so the axis $x = 0$ is a characteristic line, that is, the boundary

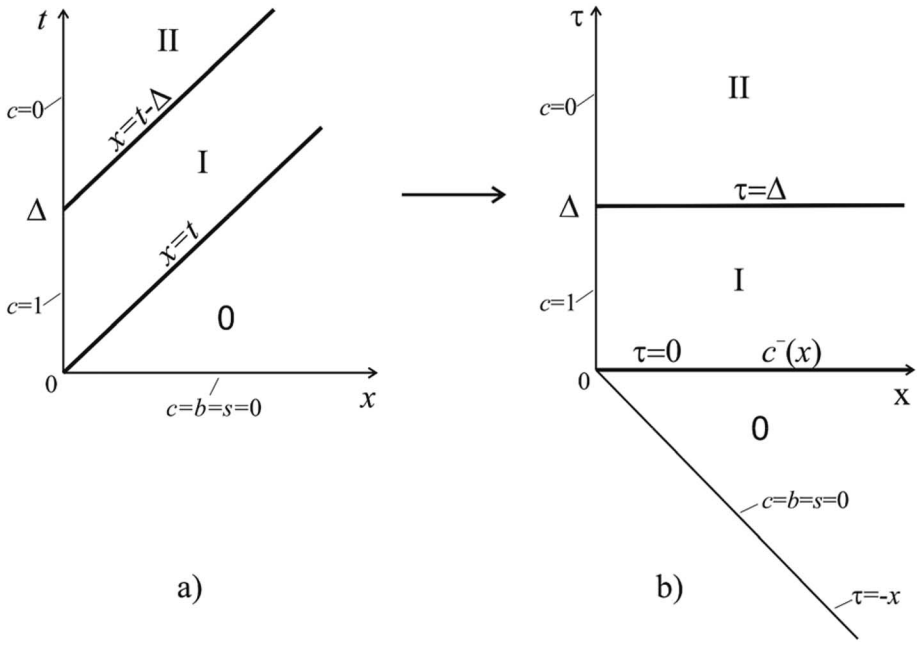


Figure 2. Change of independent variables in suspension-colloidal-nanotransport system for continuous or bank suspension injection: (a) initial coordinates (x, t); (b) introduction of Lagrangian coordinate $\tau = t - x$.

problem (21) is Goursat type (Courant & Hilbert, 1989; Polyanin & Zaitsev, 2012). The attachment rate equation (20) at the inlet accounting for boundary condition (21) is

$$x = 0 : \frac{\mathrm{d}S(r,x,\tau)}{\mathrm{d}\tau} = h(b)F\left(C^0(r),r\right). \tag{23}$$

Multiplying both sides of equation (23) by $B(r)$ and integrating in r yields the equation for boundary value of site occupation concentration $b(0,\tau)$:

$$\frac{\mathrm{d}b(0,\tau)}{\mathrm{d}\tau} = \Lambda h(b(0,\tau)), \Lambda = \int_0^\infty B(r)F\left(C^0(r),r\right)\mathrm{d}r, b(x=0,\tau=0) = 0, \tag{24}$$

where constant Λ is defined by injected concentrations and occupied attachment areas for particles with various radii.

The solution of ordinary differential equation (24) is obtained by separation of variables and accounting for "initial" condition (24):

$$\int_0^{b(0,\tau)} \frac{\mathrm{d}u}{h(u)} = \frac{\tau}{\Lambda}. \tag{25}$$

Substituting solution (25) into equation (23) yields the boundary value of retained concentration distribution:

$$x = 0 : \frac{\mathrm{d}S(r,0,\tau)}{\mathrm{d}\tau} = h(b(0,\tau))F\left(C^0(r),r\right), \tag{26}$$

resulting in explicit formula for attached concentration distribution at the inlet:

$$S(r,0,\tau) = F\left(C^0(r),r\right)\int_0^\tau h(b(0,y))\mathrm{d}y. \tag{27}$$

Here occupied concentration at the inlet $b(0,\tau)$ is implicitly expressed by equation (25).

For *fines migration* with particle-free water injection, initial and boundary conditions (22) yield

$$S(r,x,-x)=0, C(r,x,-x)=C^0(r), C(r,0,\tau)=0. \tag{28}$$

System of two equations ((19) and (20)) subject to either initial-boundary condition (21) or (22) defines two unknowns $C(r,x,\tau)$ and $S(r,x,\tau)$ during suspension injection into porous media. The microscale system ((19) and (20)) contains the model phenomenological functions of filtration, suspension, and vacancy occupation

$$h=h(b),\ \ F=F(c,r),\ \ B=B(r). \tag{29}$$

For injection or mobilization of suspension with n different-size particles, either boundary condition (21) or initial condition (22) yield

$$C^0(r)=\sum_{k=1}^{n} C_k^0\delta(r-r_k). \tag{30}$$

Looking for solution of system ((19) and (20)) in terms of discrete particle population (30) results in the following system

$$\frac{\partial S_k}{\partial \tau}+\frac{\partial C_k}{\partial x}=0, \qquad \frac{\partial S_k}{\partial \tau}=h\left(\sum_{k=1}^{n} C_k^0 B_k S_k\right)F_k(C_k), \quad k=1,2...n. \tag{31}$$

Initial and boundary conditions for injection into clean bed (21) become

$$x=0: C_k=C_k^0,\ \ \tau=-x: C_k=S_k=0. \tag{32}$$

For migration of fines with discrete particle size distribution, initial and boundary conditions (22) become

$$x=0: C_k=0,\ \ \tau=-x: C_k=C_k^0, S_k=0. \tag{33}$$

The model (31) also describes reactive flows with chemical reactions between multiple aqueous components and a single mineral in the rock, and irreversible ion exchange with clay (Bradford et al., 2015; Lasaga, 1998).

3. Upscaling

This section derives upscaled equations for microscale system presented in the previous section, that is, for transport of continuously distributed particles (section 3.1) and then for particular cases of constant areas occupied by different size particles (section 3.2) and small suspended concentrations (section 3.3).

3.1. Continuous System With Injection of Size-Distributed Particles

Substitution of equation (20) into mass balance equation (19) yields

$$\frac{\partial C(r,x,\tau)}{\partial x}=-h\left(\int_0^\infty b(r)S(r,x,t)\mathrm{d}r\right)F(C(r,x,\tau),r). \tag{34}$$

As it follows from equation (34) and initial conditions (21), suspended concentration ahead of the concentration front in the 0 domain in Figure 2 ($x>t$, or $\tau<0$) is equal to 0. Consequently, as it follows from equation (20), retained concentration is also 0.

Consider the domain I behind the concentration front for $t>x$, or $\tau>0$. Equation (34) allows for separation of variables and can be transformed to the following form

$$\frac{\partial G(C(r),r)}{\partial x}=-h\left(\int_0^\infty b(r)S(r,x,\tau)\mathrm{d}r\right),\ \ G(C(r),r)=\int_{C^0(r)}^{C(r)}\frac{\mathrm{d}u}{F(u,r)}. \tag{35}$$

Discussing the initial-boundary problem with fixed conditions (32), we omit the dependency on $C^0(r)$ while defining functions G in equation (35).

The right-hand side of equation (35) is independent of r, so its value for any arbitrary r is equal to that at the mean radius $r = 1$:

$$\frac{\partial G(C(r),r)}{\partial x} = \frac{\partial G(C(1),1)}{\partial x}. \tag{36}$$

The mean radius value is used in equation (14) for nondimensionalization of parameter r, so $r = 1$ is a mean radius.

Consider characteristic line for system ((20), (34)) $\tau = \tau_0$. Integrate both sides of equation (36) in x. Functions $G(C(r), r)$ are equal to 0 for any $r > 0$ at $x = 0$, so the integration constant is also 0. Therefore, the following equality takes place along the line $\tau = \tau_0$:

$$\tau = \tau_0 : \ G(C(r),r) = G(C(1),1). \tag{37}$$

Equation (37) allows expressing concentration of suspended particles with size r via the concentration of suspended particles with average size $r = 1$, using the inverse function

$$C(r) = g(C(1),r), \ \ g = G^{-1}(C,r). \tag{38}$$

The obtained relationship (38) allows deriving the averaged equations. Averaged concentration $c(x,\tau)$ can be expressed via the concentration of average-size particle $C(1,x,\tau)$, and vice versa, using the inverse function

$$c = \int_0^\infty g(C(1),r)\mathrm{d}r, C(1) = a(c). \tag{39}$$

Multiplying both parts of equation (20) by $B(r)$, integrating in r, and taking function h, which is independent of r, out of integral, yields the occupation rate equation

$$\frac{\partial b(x,\tau)}{\partial \tau} = h(b)\int_0^\infty B(r)F(C(r,x,\tau),r)\mathrm{d}r. \tag{40}$$

The integral in the right-hand side of equation (40) accounting for expression (39) becomes

$$\int_0^\infty B(r)F(C(r,x,t),r)dr = \int_0^\infty B(r)F(g(C(1),r),r)dr = D(C(1)) = D(a(c)) = d(c). \tag{41}$$

equation (40) accounting for equation (41) becomes

$$\frac{\partial b(x,\tau)}{\partial \tau} = h(b)d(c). \tag{42}$$

Here the large-scale function $d(c)$ is called the occupation function.

Integrate both sides of equation (34) in r and take r-independent function h out of the integral

$$\frac{\partial c(x,\tau)}{\partial x} = -h(b(x,\tau))\int_0^\infty F(C(r,x,\tau),r)dr. \tag{43}$$

Integral in right-hand side of equation (43) accounting for expression (39) becomes

$$\int_0^\infty F(C(r,x,\tau),r)\mathrm{d}r = \int_0^\infty F(g(C(1,x,\tau),r),r)\mathrm{d}r = e(C(1,x,\tau)) = e(a(c(x,\tau))) = f(c). \tag{44}$$

Equation (43) accounting for averaged relationship (44) becomes

$$\frac{\partial s(x,\tau)}{\partial \tau} = h(b(x,\tau))f(c). \tag{45}$$

Here function $f(c)$ is the suspension function at the upper scale; that is, it is the result of upscaling of suspension function $F(C,r)$ defined by equation (20).

Integration of both parts of equation (19) in r yields

$$\frac{\partial s}{\partial \tau} + \frac{\partial c}{\partial x} = 0. \tag{46}$$

Equations (46), (45), and (42) form a 3×3 system for three unknowns of overall concentrations of suspended and attached particles and of the occupied surface area, c, s, and b, respectively.

The clean-bed initial conditions for the upscaled system for suspension injection follow from equation (21):

$$\tau = -x: \ c = s = b = 0. \tag{47}$$

The boundary condition follows from equations (13) and (14):

$$x = 0: \ c = 1. \tag{48}$$

System (46), (42), and (45) subject to initial and boundary conditions ((47) and (48)) is the result of upscaling of equations (19) and (20). The macroscale system ((46), (42), and (45)) contains the model phenomenological functions of filtration $h(b)$, suspension $f(c)$ and vacancy occupation $d(c)$:

$$h = h(1-b), \ f = f(c), \ d = d(c). \tag{49}$$

For fines migration with initial conditions (17), formulae (34)–(46) hold. Functions $G(C(r), r)$ are equal to 0 for any $r > 0$ along the initial data line $x = -\tau$. The derivations (34)–(46) hold, yielding the same upscaled system. The initial and boundary conditions for the upscaled system for fines migration follow from initial and boundary conditions (17):

$$\tau = -x: \ c = 1, s = b = 0, \tag{50}$$

$$x = 0: \ c = 0. \tag{51}$$

3.2. System With Constant Single-Particle Occupied Area

Consider the high-suspended concentration case with nonlinear suspension function $F(C(r),r)$, where the attached different-size particles occupy the same area on the rock surface: $B(r) = b_0 = \text{const}$. In this case,

$$b(x,\tau) = b_0 s(x,\tau). \tag{52}$$

Overall mass balance equation (46) remains the same. Attachment rate equation (45) also remains the same. Yet occupation rate equation (42) degenerates into equation (45). The initial and boundary conditions for 1-D flows are obtained from equations ((47), (48)) and ((50), (51)) by waving the conditions on the occupied area $b(x,\tau)$.

Therefore, the result of upscaling of the system where the area engaged by the attached particle is independent of its radius is the classical nonlinear deep bed filtration model, given by equations ((1), (2)) or ((1), (4)). The filtration function after upscaling remains the same. The upscaled functions of suspension $f(c)$ and occupation $d(c)$ are obtained from the small-scale function $F(C,r)$ by integration, inversion and convolution, given by equations (38), (39), (41), and (44).

3.3. System With Linear $F(C,r)$ and Constant Single-Particle Occupied Area B

Consider the case of small injected concentrations; that is, the suspension functions are linear

$$F(C(r),r)=\lambda(r)C(r). \tag{53}$$

Performing calculations by equations (38), (39), and (41), we obtain the particular form of the expression of $C(r)$ via c:

$$G(C(r),r)=\ln\left[\frac{C(r)}{C^0(r)}\right]^{1/\lambda(r)},\ C(r)=C^0(r)\left[\frac{C(1)}{C^0(1)}\right]^{\lambda(r)/\lambda(1)},\ c=\int_0^\infty C^0(r)\left[\frac{C(1)}{C^0(1)}\right]^{\lambda(r)/\lambda(1)}dr,\quad C(1)=a(c). \tag{54}$$

where function $a(c)$ is determined from the previous transcendental equation.

Equations ((53), (54)) result in the following upscaled function $f(c)$:

$$f(c)=\int_0^\infty \lambda(r)C^0(r)\left[\frac{a(c)}{C^0(1)}\right]^{\lambda(r)/\lambda(1)}\mathrm{d}r. \tag{55}$$

Equation (55) shows that upscaling of linear suspension functions for individual populations (53) result in nonlinear suspension function $f(c)$ at the large scale.

4. Upscaling in Discrete Systems

This section derives upscaled equations for transport of discrete particle systems for any $n>1$ (section 4.1), and the particular case of $n=2$ (section 4.2).

4.1. Discrete Systems of Multisized Suspensions

Consider injection of suspension with concentrations ${C_k}^0$ for particles with radii r_k. System of microscale equations is given by equation (31). The initial and boundary conditions corresponding to suspension injection into clean bed are given by equation (32).

Similar to equations ((37), (38)), concentration of kth population is expressed via the concentration of first population particles (with $r=r_1$):

$$G_k(C_k)=G_1(C_1),\ C_k=g_k(C_1),\ g_k={G_k}^{-1}(G_1),\ k=1,2...n. \tag{56}$$

It allows expressing concentration of particles with $r=r_k$ via concentration of the first population, and vice versa, by analogy to equation (39):

$$c=\sum_{k=1} g_k(C_1), g_1(C_1)=C_1,\ C_1=a(c). \tag{57}$$

Similar to equation (44), the total of individual suspension functions can be expressed via the function of total concentration, resulting in an expression for upscaled suspension function

$$\sum_k F_k(C_k)=\sum_{k=1} F_k(g_k(C_1))=e(C_1)=e(a(c))=f(c). \tag{58}$$

Upscaled occupation function is determined by analogy to equation (41):

$$\sum_k B_kF_k(C_k)=\sum_{k=1} B_kF_k(g_k(C_1))=D(C_1)=D(a(c))=d(c). \tag{59}$$

For fines migration, formulae (56)–(59) hold for initially mobilized fines with concentrations ${C_k}^0$. Equations (56)–(58) provide the model functions $f(c)$ and $d(c)$ for upscaled system (31) of discrete multisized colloidal flow.

4.2. Binary System

We discuss deep bed filtration of a binary system as a particular case $n = 2$ of the system discussed in the previous section. We consider the case where $\lambda_1 = 2\lambda_2$.

Similar to equation (56), the relationship between two individual concentrations is

$$G_1(C_1) = \ln\left(\frac{C_1}{C_1^0}\right)^{1/\lambda_1} = G_2(C_2) = \ln\left(\frac{C_2}{C_2^0}\right)^{1/\lambda_2}. \tag{60}$$

Equation (60) allows expressing the first population concentration C_1 and the total concentration c via concentration of second particle population C_2, like in equation (57)

$$c = C_1^0\left(\frac{C_2}{C_2^0}\right)^2 + C_2. \tag{61}$$

Solving quadratic equation (61) yields expressing two individual concentrations C_1 and C_2 via total concentration c:

$$\frac{C_2}{C_2^0} = \sqrt{\frac{c}{C_1^0} + \left(\frac{C_2^0}{2C_1^0}\right)^2} - \frac{C_2^0}{2C_1^0}, \quad \frac{C_1}{C_1^0} = \left(\sqrt{\frac{c}{C_1^0} + \left(\frac{C_2^0}{2C_1^0}\right)^2} - \frac{C_2^0}{2C_1^0}\right)^2. \tag{62}$$

Upscaled suspension function, like in equation (58), is

$$f(c) = \lambda_1 C_1 + \lambda_2 C_2 = \lambda_2 C_2^0\left(\sqrt{\frac{c}{C_1^0} + \left(\frac{C_2^0}{2C_1^0}\right)^2} - \frac{C_2^0}{2C_1^0}\right)\left(\frac{2C_1^0}{C_2^0}\left(\sqrt{\frac{c}{C_1^0} + \left(\frac{C_2^0}{2C_1^0}\right)^2} - \frac{C_2^0}{2C_1^0}\right) + 1\right). \tag{63}$$

Suspension function $f(c)$ depends on individual filtration coefficients of the populations and on the injected population concentrations.

Figure 3a shows a plot of the suspension function for five filtration coefficients of the second population for the case $\lambda_1 = 2\,\lambda_2$ and ${C_2}^0 = {C_1}^0$. The higher are the individual filtration coefficients, the higher is the suspension function. The suspension function can be approximated by quadratic parabola $f(c) = Ac(1 + Ec)$, A, $E > 0$, with high accuracy.

The expression for upscaled occupation function $d(c)$ for a binary suspension follows from equation (59) for $n = 2$:

$$d(c) = \phi C_1^0 B_1 \lambda_1 C_1(c) + \phi C_2^0 B_2 \lambda_2 C_2(c) =$$
$$\phi\left(C_2^0\right)^2 B_2 \lambda_2\left(\sqrt{\frac{c}{C_1^0} + \left(\frac{C_2^0}{2C_1^0}\right)^2} - \frac{C_2^0}{2C_1^0}\right)\left(\frac{2\left(C_1^0\right)^2}{\varepsilon\left(C_2^0\right)^2}\left(\sqrt{\frac{c}{C_1^0} + \left(\frac{C_2^0}{2C_1^0}\right)^2} - \frac{C_2^0}{2C_1^0}\right) + 1\right), \quad \varepsilon = \frac{B_2}{B_1}. \tag{64}$$

Figure 3b displays the plot of the upscaled vacancy occupation function $d(c)$ for three values of filtration coefficient λ_2 and three values of the ratio ε between the occupied areas B_2 and B_1. Other conditions are $\lambda_1 = 2\,\lambda_2$, $B_1 = 0.2$, and ${C_2}^0 = {C_1}^0$. The higher the ratio ε between the individual occupied areas $\varepsilon = B_2/B_1$ for the constant B_1, the higher is the vacancy occupation function—the black curve is located above the blue curve, which is above the red curve. The vacancy occupation function increases as the individual filtration coefficients increase—the green curve is placed above the black curve, which is located above the dark blue curve. The higher the ratio ε, the more curvilinear is the line $d(c)$. The vacancy occupation function can be also approximated by quadratic parabola $d(c) = Ac(1 + Ec)$ with high accuracy. Figure 3b shows both concave and convex forms, so constant E can be either positive or negative.

Figures 3c and 3d depict the effect of injected concentration of the second population ${C_2}^0$ on suspension and site occupation functions, respectively. The plots have been calculated for $B_1 = 0.2$; $B_2 = \varepsilon\, B_1$; $\lambda_2 = 3$;

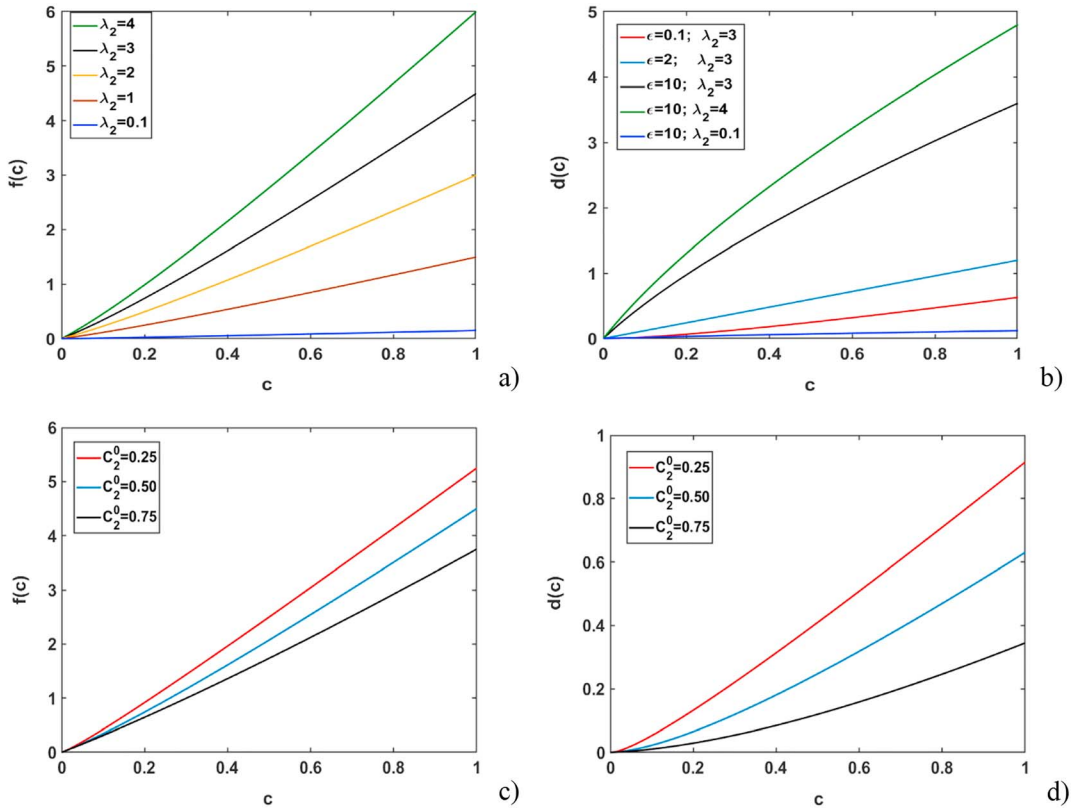


Figure 3. Typical forms for suspension and occupation curves for a binary suspension: (a) suspension function for five values of microscale filtration coefficient $\lambda_2 = 0.1$, 1.0, 2.0, 3.0, and 4.0; (b) site occupation function for three ratios of $\varepsilon = B_2/B_1 = 0.1$, 2.0, and 10.0 and three values of filtration coefficient $\lambda_2 = 0.1$, 3.0 and 4.0, here $B_1 = 0.2$, $\lambda_1 = 2\,\lambda_2$, and ${C_2}^0 = {C_1}^0$; (c) suspension functions for various ${C_2}^0$; and (d) forms of site occupation function for various ${C_2}^0$, here $B_1 = 0.2$, $B_2 = 0.02$, $\lambda_1 = 6$, and $\lambda_2 = 3$.

$\lambda_1 = 2\,\lambda_2$; $\varepsilon = 0.1$. The higher the concentration of component with lower filtration coefficient, the lower is the suspension function $f(c)$. The higher the concentration of component with lower individual occupation area, the lower is the vacancy occupation function.

The suspension function $f(c)$ depends on both individual filtration coefficients λ_1 and λ_2 and the component concentrations. The suspension function monotonically increases over both variables λ_1 and λ_2. The higher the ratio between filtration coefficients λ_1 and λ_2 under fixed λ_2, the higher is the deviation of suspension function $f(c)$ from straight line given by equation (2); so the higher the difference between the individual filtration coefficients of the particle populations, the more curvilinear is the suspension function at the upper scale. The suspension function $f(c)$ monotonically increases with increase of the component concentration with larger filtration coefficient. The vacancy occupation function $d(c)$ depends on individual filtration coefficients of the populations, on the injected population concentrations, and on individual surface area fractions B_1 and B_2. The vacancy occupation function monotonically increases over both variables λ_1 and λ_2. It also monotonically increases over both variables B_1 and B_2. It monotonically increases with increase of the component concentration with larger individual surface area ${C_2}^0$.

5. Exact Solutions for Upscaled Suspension Injection

In this section we derive exact solution of upscaled system ((46), (42), and (45)) subject to initial and boundary conditions (47) and (48) for the particular case where filtration function has Langmuir's form given by equation (11). The detailed derivations and calculations of Riemann invariants are presented in Appendixes A and B.

5.1. Upscaled System for Langmuir's Filtration Function and Solution in Zone 0

Equations (42) and (45) for Langmuir's form of filtration function, given by equation (11), are

$$\frac{\partial b}{\partial \tau} = (1-b)d(c), \tag{65}$$

$$\frac{\partial s}{\partial \tau} = (1-b)f(c). \tag{66}$$

Substitution of equation (66) into equation (46) yields

$$\frac{\partial c}{\partial x} = -(1-b)f(c). \tag{67}$$

Initial and boundary conditions (47) and (48) define the unique solution of the system (65)–(67) in the domain

$$\Omega = \{x, \tau : \ x \geq 0; \ \tau \geq -x\}.$$

The domain Ω is divided into three zones where the solution has a different form (Figure 2b). Equation (67) and boundary condition (47) for suspension concentration imply that suspension concentration is equal to 0 in zone 0. As it follows from equation (65) and initial conditions (47), concentration of occupied vacancies b in zone 0 is also equal to 0. Equation (66) and initial conditions (47) yield that $s = 0$ in zone 0.

Zone 0 is separated from zone I by the concentration front with trajectory $\tau = 0$ (or $x = t$ in plane (x,t)). The solution $c(x,t)$ is discontinuous on the concentration front because the initial-boundary conditions (47) and (48) do not match at the origin. The solutions $s(x,t)$ and $b(x,t)$ are continuous in Ω due to accumulative kinetics given by equations (65) and (66).

5.2. Solution and Riemann Invariants in Zone I

As it follows from equation (65) and boundary condition (48), at the inlet $x = 0$ the vacant concentration $1-b(0,\tau)$ exponentially decays with time with the decrement $d(1)$. From equation (66), as time tends to infinity, the vacant concentration tends to 0 and the retained concentration $s(0,\tau)$ tends to $f(1)/d(1)$. Retained concentration $s(x, \tau)$ increases in τ and tends to finite limit $s_{max}(x)$ as $\tau \to \infty$. The stabilized retention profile $s_{max}(x)$ is nonuniform.

Consider the solution on the concentration front. Kinetics equation (65) implies continuity of occupied vacancies b on the front. Since $b = 0$ in zone 0, the occupied vacancy concentration b remains equal to 0 along the front. For $b = 0$ and suspended concentration $c^{-}(x)$ on the front with trajectory $\tau = 0$, equation (67) becomes

$$\frac{\mathrm{d}c^{-}(x)}{\mathrm{d}x} = -f(c^{-}). \tag{68}$$

Separating variables and accounting for boundary condition (48)

$$x = 0 : \ c^{-} = 1, \tag{69}$$

yield the following implicit expression for suspension concentration $c^{-}(x)$ behind the concentration front at $\tau = +0$

$$\int_{c^{-}(x)}^{1} \frac{\mathrm{d}y}{f(y)} = x. \tag{70}$$

The function $w(c)$ is introduced

$$w(c) = \int_{c}^{1} \frac{\mathrm{d}(y)}{f(y)} \mathrm{d}y. \tag{71}$$

The solution $c(x,\tau)$ in zone I is (see derivations (A1)–(A8) in Appendix A):

$$\int_{c^-(x)}^{c} \frac{dy}{f(y)w(y)} = \tau. \tag{72}$$

For known solution $c(x,\tau)$, the retained concentration $s(x,\tau)$ is obtained from equations (66) and (72) by integration in τ and accounting for value $s = 0$ along the front $\tau = 0$:

$$s(x,\tau) = -\int_0^{\tau} \frac{\partial c(x,y)}{\partial x} dy; \tag{73}$$

The occupied area concentration $b(x,\tau)$ in zone I is determined from equation (67).

Using variables (x, t) in zone I (Figure 2), the solution $c(x,\tau)$ given by equation (72) becomes

$$\int_{c^-(x)}^{c(x,t)} \frac{dy}{f(y)w(y)} = t - x. \tag{74}$$

For known solution $c(x,\tau)$, Riemann invariant I_b for quasi-linear hyperbolic system (65)–(67), given by equation (B3), allows for explicit expression of the occupied site concentration:

$$b(x,\tau) = 1 - \frac{w(c(x,\tau))}{w(c^-(x))}; \tag{75}$$

Riemann invariant I_s, expressed by equation (B8), yields explicit solution for the retained concentration:

$$s(x,\tau) = \frac{c(x,\tau) - c^-(x)}{w(c^-(x))}. \tag{76}$$

5.3. Injection of Colloidal Bank With Particle-Free Water Chase Drive

We consider injection of colloidal slug with volume Δ followed by particle-free water chase drive into clean bed. The initial conditions remain the form given by equation (47). The boundary condition is

$$x = 0: \; c(0,t) = \begin{cases} 1, & t < \Delta \\ 0, & t > \Delta \end{cases}. \tag{77}$$

Solution in zones 0 and I remains the same as in the problem of continuous colloid-suspension injection (Figure 2). Suspension concentration in zone II is equal to 0. Retained and vacancy occupation concentrations in zone II remain the same as those reached before passing the rear slug front:

$$\begin{aligned} &t > x + \Delta: \\ &s(x,t) = s(x, x+\Delta), b(x,t) = b(x, x+\Delta). \end{aligned} \tag{78}$$

6. Analytical Model for Migration of Size-Distributed Fines

Accounting for boundary condition (51) of particle-free flow through the inlet in the retention rate expression (66) and for the property of suspension function $f(0) = 0$ yields no retention at the inlet; that is, $s(0,\tau) = 0$. The same considerations with vacancy occupation kinetics and $d(0) = 0$ show that the vacancy concentration at the inlet remains the same, $b(0,\tau) = 0$.

Equation (67) and boundary condition (51) for suspension concentration imply that suspension concentration is equal to 0 in zone I. As it follows from equations (65) and (66), since $f(0) = d(0) = 0$, time derivatives of retained and occupied vacancy concentrations are 0; that is, no retention and vacancy occupation occur in zone I. The retained and occupied vacancy concentrations in zone I remain the same as those along the concentration front $\tau = 0$ (Figure 2).

The solution $c(x,\tau)$ in zone 0 is (see equation (C6), Appendix C)

$$\int_1^{c(x,\tau)} \frac{dy}{f(y)(w(y)-1)} = \tau + x. \tag{79}$$

The suspended concentration $c^+(x)$ on the concentration front is determined by equation (79) ahead of the concentration front at $\tau = -0$

$$\int_1^{c^+(x)} \frac{dy}{f(y)(w(y)-1)} = x. \tag{80}$$

The occupied vacancy concentration $b(x,\tau)$ in zone 0 is obtained using Riemann invariant I_{b0}, given by equation (C10)

$$b(x,\tau) = w(c(x,\tau)). \tag{81}$$

The retained concentration $s(x,\tau)$ in zone 0 is determined by Riemann invariant I_{s0}, given by equation (C13)

$$s(x,\tau) + c(x,\tau) = 1. \tag{82}$$

Equations (81) and (82) are derived in Appendix C.

In zone I, the occupied vacancy and retained concentrations are inherited from the values on the concentration front

$$b(x,\tau) = w(c^+(x)), \ \ \tau > 0, \tag{83}$$

$$s(x,\tau) = 1-c^+(x), \ \ \tau > 0, \tag{84}$$

respectively.

The solution (79)–(82) in zone 0 takes the following form in coordinates (x,t):

$$\int_1^{c(t)} \frac{dy}{f(y)(w(y)-1)} = t; \ \ b(t) = w(c(t)); \ \ s(t) = 1-c(t). \tag{85}$$

In zone 0, ahead of the concentration front, uniform initial distributions of suspended and attached fines and vacancies provide equal capture probability for all suspended particles. Therefore, the capture and vacancy occupation rates remain the same, and concentration profiles for c, s, and b remain uniform. Solution (85) is independent of x. In zone I, behind the concentration front, the initially mobilized suspended fines are completely displaced by the particle-free injected water. At the absence of suspended fines, both capture and occupation rates remain 0, and solution (83) and (84) is steady state.

7. Results of Analytical Modeling

In this section, the analytical solution for suspension injection ((70), (72), (75), and (76)) is used to produce breakthrough curves and concentration profiles for transport of binary mixture. Quadratic approximation of suspension and vacancy occupation functions simplify the formulae for solution.

Figures 4a and 5 show the breakthrough curves and concentration profiles for suspension and vacancy occupation functions from Figures 3a and 3b. Black, red, green, blue, and dark blue curves in Figures 3a, 3b, 4a, and 5, correspond to the same values of model constants. All breakthrough curves exhibit the colloid's arrival at $t = 1$ PVI, jump on the concentration front, and continuous growth until stabilization. The exact solution shows that the breakthrough curves asymptotically stabilize as time tends to infinity at $c = 1$; corresponding values of retained and vacancy occupation concentrations are $s = f(1)/d(1)$ and $b = 1$. The breakthrough value at the arrival time, given by equation (70), is independent of the individual occupation areas;

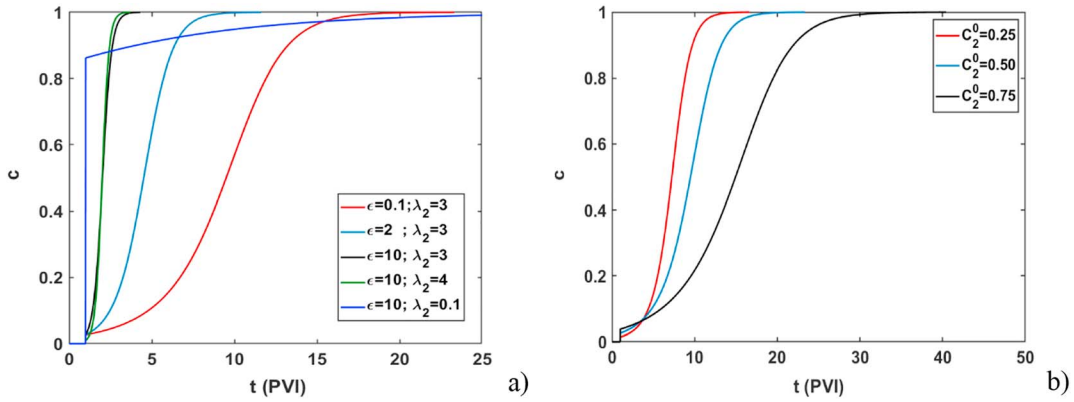


Figure 4. Typical breakthrough curves for a binary system: (a) for three occupation-area ratios of $\varepsilon = B_2/B_1 = 0.1, 2.0, 10.0$ and three values of filtration coefficient $\lambda_2 = 0.1, 3.0, 4.0$, other parameters are $B_1 = 0.2$, $\lambda_1 = 2\,\lambda_2$, and $C_2{}^0 = C_1{}^0$; (b) for three concentrations of the second component $C_2{}^0$ for $\lambda_1 = 6$, $\lambda_2 = 3$, $B_1 = 0.2$, and $B_2 = 0.02$. PVI = pore volumes injected.

therefore, the values for red, blue, and black curves in Figure 4a coincide. The higher the filtration coefficient, the higher is the capture rate, the higher is the retained concentration s, the lower is the breakthrough concentration at some period after $t = 1$ PVI, and the faster is the breakthrough curve stabilization. Figure 4a depicts that the dark blue, black, and green curves follow this order.

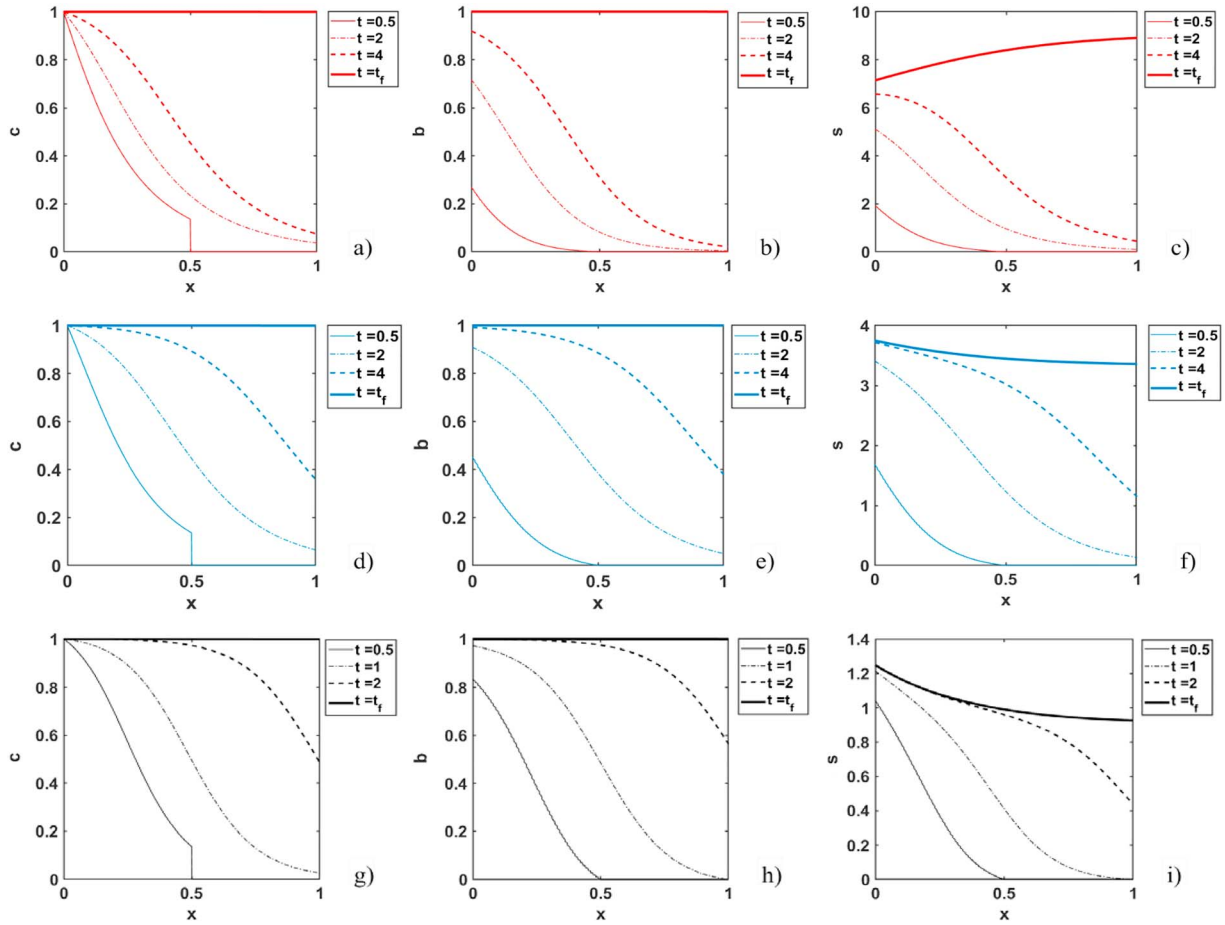


Figure 5. Effects of ratio $\varepsilon = B_2/B_1$ on profiles of suspended concentration, occupied sites, and retained concentration at four instances (first column a, d, g, second column b, e, h, and third column c, f, i, respectively). Red, blue, and black curves correspond to those in Figures 3b and 4a ($\varepsilon = 0.1$, 2.0, and 10.0). The model parameters are $B_1 = 0.2$, $B_2 = \varepsilon B_1$, $\lambda_2 = 3$, $\lambda_1 = 2\,\lambda_2$, and $C_2{}^0 = C_1{}^0$.

For the same values of individual filtration coefficients and the individual occupation area for the first component, the higher is the ratio $\varepsilon = B_2/B_1$, the higher is the capture rate, and the faster is its stabilization (the red, blue, and black curves in Figure 4a follow this order).

At the moment $t = 0.5$, the concentration front has not reached the outlet yet. The suspension profiles in Figures 5a, 5d, and 5g exhibit concentration jump on the front. Suspension profiles are continuous at $t = 2$, 4, and t_f because the concentration front has already passed the position $x = 1$. As individual occupation area B_2 increases from red curve to blue curve, and then to black curve in Figures 3b and 4a, the occupied area b increases, the vacant area 1-b decreases, the retention concentration decreases, and the suspended concentration increases. Those tendencies are clear by comparison of Figures 5a, 5d, and 5g; Figures 5b, 5e, and 5h; and Figures 5c, 5f, and 5i.

Figures 5b, 5c, 5e, 5f, 5h, and 5i present the concentration profiles for retained particles and occupied vacancies. Both concentrations monotonically increase with time during the accumulation of the retained particles. With time, the concave shape changes to an S shape and then to a convex shape.

Figures 4b and 6 correspond to suspension and vacant occupation functions shown in Figure 3c and 3d. The higher the concentration of component with lower individual occupation area C_2^0, the lower is the vacancy occupation function $d(c)$, the higher is the retention rate and retention concentration s, the lower is the breakthrough concentration, and the slower is the stabilization. Breakthrough curves in Figure 4b and profiles in Figure 6 follow those tendencies.

8. Treatment of Laboratory Data

Consider whether the differences between the traditional and upscaled models in breakthrough concentrations and attachment profiles are significant for laboratory coreflood conditions. Goldberg et al. (2014) report multiple laboratory data where the breakthrough concentration and retention profile cannot be simultaneously fitted by the traditional model, given by equations (1) and (2).

Chen et al. (2017) injected biochar nanoparticles into a porous column. The so-called paddy soil consists of quartz, clay minerals, and iron oxides. The study investigated particle retention by the rock under changing z-potential of the particles. The concentration of humic acid in the injected fluid controls z-potential of the particles under fixed concentration of either salt NaCl or $CaCl_2$. Straining did not play a significant role in nanoparticles (NP) retention due to jamming ratio that was significantly lower than the threshold value; that is, particle attachment under the strong DLVO (Derjaguin, Landau, Verwey, and Overbeek) particle-rock attraction was the main particle capture mechanism. Wide particle size variation (261–365 nm) has been reported.

Table 1 shows the results of fitting the laboratory data by tuning five model coefficients B_1, B_2, λ_1, λ_2, and C_2^0. Here we use the upscaled model for transport of binary colloids, given by equations (56)–(59). Lines 2, 4, 6, 8, 10, 12, 14, 16, and 18 correspond to matching the breakthrough and retention curves by the upscaled model for binary colloids. Lines 3, 5, 7, 9, 11, 13, 15, 17, and 19 present the data matching by the traditional model, given by equations (1) and (2); here $B_1 = b_0$, and we tune only two parameters: occupied area of a single particle b_0 and filtration coefficient λ_1. The coefficients of determination are given separately for breakthrough histories and for retention profiles (columns 9 and 10, respectively).

The data sets for breakthrough concentration and retention profile were tuned simultaneously within Matlab R2016 with Statistics Toolbox (MathWorks Inc, Natick, MA) using a genetic least squares algorithm. We chose this method because it avoids convergence to local minima. The algorithm minimized the observed difference between the experimental data and five-parametric binary model and biparametric classical model.

Figures 7a–7d present the results of simultaneous tuning of the breakthrough curves and retention profiles by the binary model. Matching of both NaCl and $CaCl_2$ series exhibits close agreement between the laboratory and modeling data. The coefficient of determination R^2 while matching by the binary model has order of magnitude 0.87 for breakthrough curves and 0.97 for retention profiles (Table 1). The corresponding R^2 values for matching by the traditional model are 0.31 for breakthrough curves and 0.46 for retention profiles; that is, the matching quality is poor. It is common that the breakthrough concentration history and retention

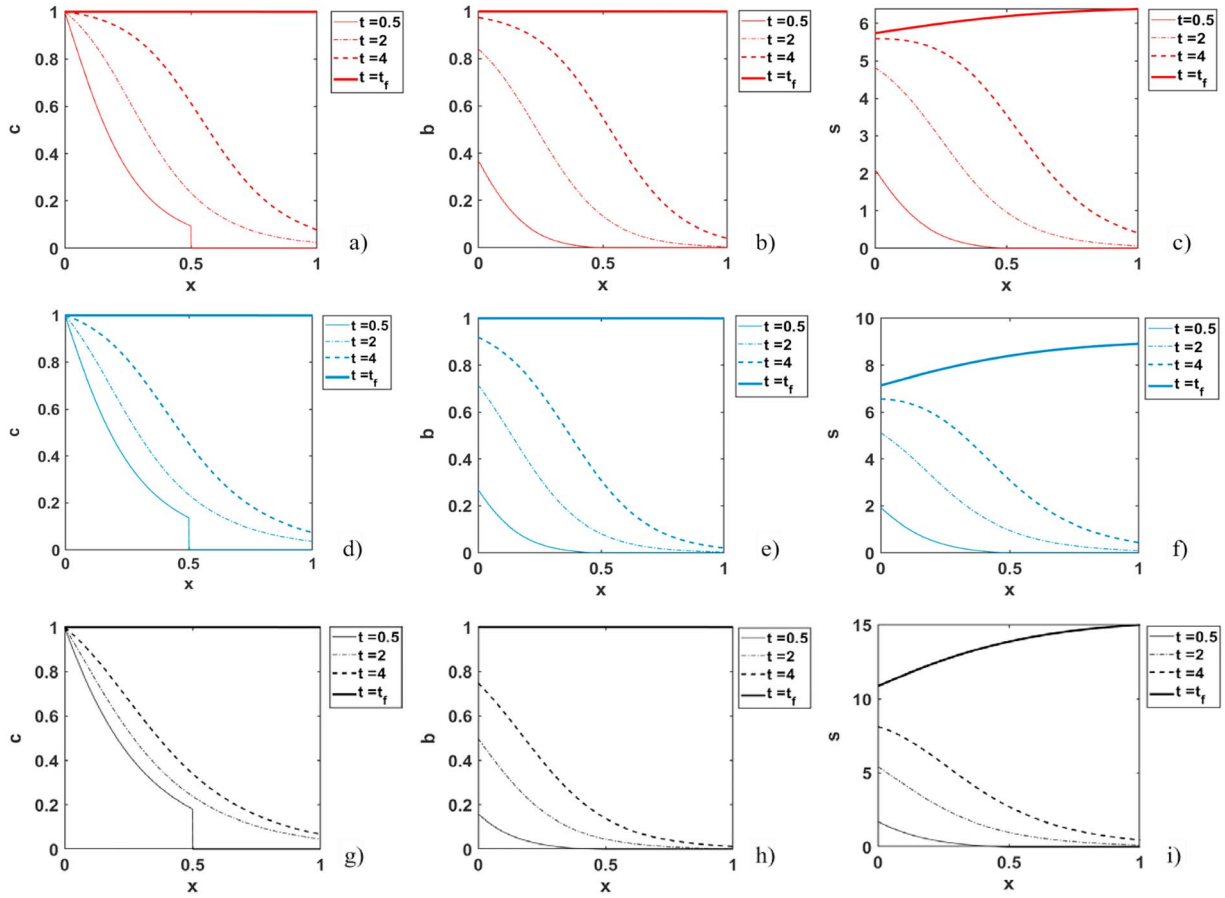


Figure 6. Effects of injected concentration C_2^0 on profiles of suspended concentration, occupied sites, and retained concentration at four instances (first column a, d, g, second column b, e, h, and third column c, f, i, respectively). Red, blue, and black curves correspond to those in Figures 3d and 4b ($C_2^0 = 0.25$, 0.5, and 0.75). The model parameters are $B_1 = 0.2$, $B_2 = \varepsilon B_1$, $\lambda_2 = 3$, $\lambda_1 = 2\,\lambda_2$, and $\varepsilon = 0.1$.

Table 1
Tuning Model Parameters of Three Coreflood Series From Figure 7 by the Binary and Monosize Analytical Models

Reference	Experiment	Model	B_1	B_2	λ_1	λ_2	C_2^0	R_c^2	R_S^2
Chen et al. (2017)	NaCl, 0 mg/L HA	Binary	0.02103	0.1077	6.5631	0.6415	0.6759	0.9385	0.9704
		Mono	0.067385	—	1.1822	—	—	0.0012	0.4222
	NaCl, 5 mg/L HA	Binary	0.01716	0.1645	9.4055	0.6283	0.7316	0.9660	0.9603
		Mono	0.0427456	—	0.7646	—	—	0.3197	0.4199
	NaCl, 10 mg/L HA	Binary	0.02699	0.1840	11.9538	0.5248	0.7527	0.8719	0.9700
		Mono	0.0029	—	0.5459	—	—	0.3806	0.5520
	$CaCl_2$, 0 mg/L HA	Binary	0.01232	0.2464	12.4382	0.6555	0.6868	0.8273	0.9827
		Mono	0.0026	—	0.6362	—	—	0.4556	0.4796
	$CaCl_2$, 5 mg/L HA	Binary	0.02242	0.3397	6.9175	0.4831	0.6349	0.8338	0.9476
		Mono	0.0028	—	0.6020	—	—	0.3504	0.5813
	$CaCl_2$, 10 mg/L HA	Binary	0.01237	0.3708	6.2513	0.2977	0.8403	0.7518	0.9558
		Mono	0.0023	—	0.2783	—	—	0.3576	0.3393
Sun et al. (2015)	$C^0 = 5$ mg/L	Binary	0.1614	0.5615	2.2731	0.7220	0.1643	0.9549	0.8579
		Mono	0.1697	—	1.7991	—	—	0.9514	0.8494
	$C^0 = 10$ mg/L	Binary	0.1081	0.7985	2.6233	0.7219	0.4847	0.9274	0.9603
		Mono	0.2805	—	1.412	—	—	0.9339	0.8338
	$C^0 = 25$ mg/L	Binary	0.4941	0.7855	3.5496	0.7573	0.7894	0.9850	0.9386
		Mono	0.5571	—	0.8448	—	—	0.9428	0.9230

Note. HA = humic acid.

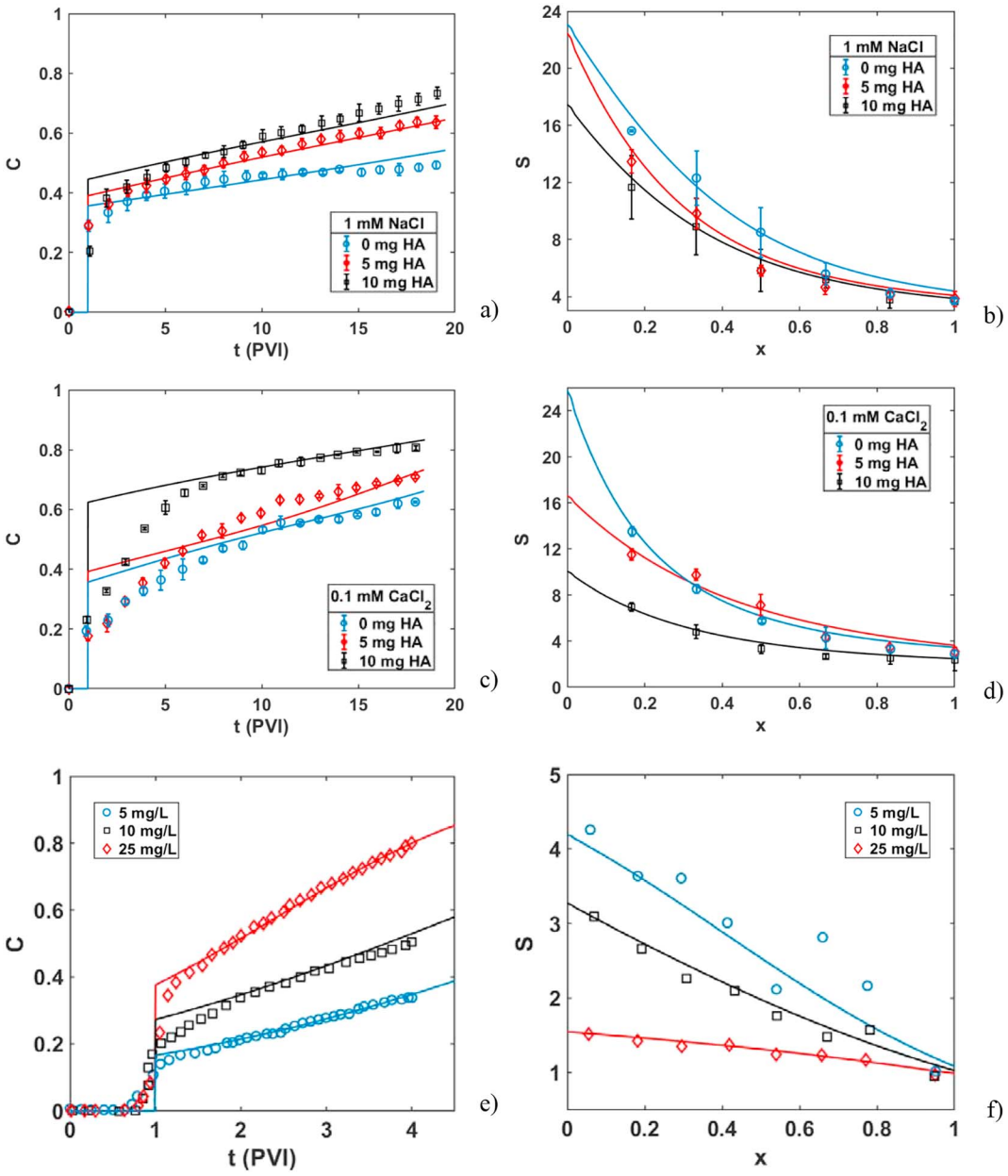


Figure 7. Matching the laboratory data of coreflooding by the analytical model given by equations (54), (55), (70), (71), and (81): (a, c, e) breakthrough curves; (b, d, f) retention profiles. Data a, b, c, and d with changing z potential are obtained by Chen et al. (2017); data e and f with changing injected colloidal concentration are presented by Sun et al. (2015).

profile cannot be fitted simultaneously by the traditional model ((1) and (2)) (Alvarez et al., 2007; Bradford et al., 2015; Goldberg et al., 2014; Shapiro & Yuan, 2012). Comparison of coefficients of determination for traditional and upscaled models in the ninth and tenth columns of Table 1 indicates that the breakthrough curves and retention profiles can be highly fitted simultaneously by the averaged binary model.

Close matching of the NP transport data by the binary model and poor matching quality using the traditional model are explained by wide variation of the particle sizes in the laboratory tests by Chen et al. (2017).

Sun et al. (2015) conducted sand column experiments injecting graphene oxide nanoparticles. DLVO calculations exhibits rock-particle attachment. Low jamming ratio in the course sand tests allows excluding straining and size exclusion particle capture mechanisms. Figures 7e and 7f show close match of the laboratory data by the analytical binary-particle model—the coefficient of determination is around 0.95 for

breakthrough concentrations and 0.92 for retention profiles (Table 1). However, the gain in matching accuracy if compared with the traditional model for monosized particles is negligibly small. The paper reports very narrow injected particle size distribution—the variation coefficient is 0.08. It explains the negligible difference between the modeling results using the binary and monosized models.

Matching laboratory data by a five-parametric model yields higher accuracy than that by a model with two free model parameters. Chen et al. (2017) performed the laboratory tests using colloid with wide particle size distributions, so the real model is closer to a binary colloid model than for a model with monosized colloid. Therefore, R^2 for the binary model is significantly higher than that for the monosized model. On the contrary, Sun et al. (2015) performed the tests using almost monosized colloids, so the real system is close enough to the traditional model. Therefore, the gain in R^2 accuracy with the binary model is insignificantly higher than that for the traditional model.

9. Discussions

9.1. General

Averaging of particle populations in suspension-colloidal porous media flows, where the particle and rock properties are randomly distributed, is needed in order to reduce the numerical burden. Permanent progress in computer capabilities may make simulations of numerous particle populations more feasible, but the gained accuracy is of limited benefit in view of the large uncertainty of rock and suspension characterization on one hand and the need of averaged particle concentrations and rock permeability on the other (Dagan et al., 2013; Tosco et al., 2014). Consequently, averaging/upscaling will remain in the foreseeable future a useful procedure in suspension-colloidal-nanotransport modeling.

The same applies to exact direct solutions of the averaged systems. Using exact solutions in iterative minimization algorithms for inverse problems significantly reduces calculations if compared with the forward numerical solutions. Moreover, exact solutions of direct problems often regularize usually ill-posed inverse problems, yielding unique and stable inverse solutions for system characterization from laboratory or field data (Alvarez et al., 2007; Bianco et al., 2016; Chrysikopoulos et al., 2012; Chrysikopoulos & Syngouna, 2012; Tosco et al., 2014). Besides, exact solutions benchmark numerical methods, optimize the numerical schemas, select proper time and areal steps, etc.

9.2. The Role of Filtration Function

The Langmuir blocking function, given by equation (11), is derived for monolayer attachment of particles on the rock surface. However, the nonlinear modification of the Langmuir's filtration function $h(s)$ can be applied for several other particle capture mechanisms. For the cases of size exclusion and straining, the capture probability decreases as the number of vacant thin pores or fissures decreases, and the capture-free flow starts when the corresponding vacancies vanish. In particular, the Langmuir blocking function corresponds to flow of binary suspension in rock with monosized pores, where the small particles are smaller than pores and the large particles are larger than pores. Various forms of filtration function $h(s)$ correspond to different pore size distributions in the rock during monosized colloidal-suspension flows (Bedrikovetsky, 2008).

The Langmuir's blocking filtration function assumes no capture after filling all vacant sites, that is, $h(s_0) = 0$ for $s > s_0$. In this case, the retained concentration cannot exceed value s_0 for the process determined by the initial and boundary conditions (13). Consider the form $h(s) = A(s_0\text{-}s)^n$ near the point s_0. For $n > 1$, s tends to s_0 asymptotically at time tending to infinity together with c tending to injected value $c = 1$; the flow pattern during continuous injection consists of two zones 0 and I (Figure 2). For $n < 1$, s reaches value s_0 at the finite moment $t_0(x)$. Therefore, for $n > 1$ and $t > t_0(x)$, $s = s_0$, and $c = 1$. This constant-value zone appears in the flow pattern during continuous injection inside zone I.

9.3. Inverse Problems for Laboratory Corefloods and Downscaling

The modified model ((42), (45), (46)) degenerates into the extended traditional model (1, 4) for the case where the attached particles with different size occupy the same number of vacancies, that is, $B(r) = b_0$. The traditional equations ((1), (3), (4)) contain empirical filtration and formation damage functions, $h(s)$ and $k(s)$, respectively. Those functions cannot be determined by direct measurement; they are

calculated from the laboratory coreflood measurements using the inverse solutions. The filtration function can be determined from breakthrough concentration $c(L,t)$, while the formation damage function $k(s)$ can be determined from pressure drop history across the core (Alvarez et al., 2007). Regularization of those ill-posed inverse problems, which is based on exact solutions of direct problem, yields an algorithm that provides well-posed solutions.

A similar role plays the direct Buckley-Leverett solution for immiscible displacement in inverse solution for coreflood data treatment. Welge's method of determining the fractional flow function from the breakthrough water cut is an exact solution for inverse problem (Bedrikovetsky, 2013). JBN's method (Johnson-Bossler-Naumann method) is an exact solution for inverse determination of total two-phase mobility from the history of pressure drop across the core.

For both suspension and two-phase transport in porous media, kinematics equations (mass balance and capture kinetics) separate from dynamic Darcy's equation for hydraulic resistance. Therefore, the inverse kinematic problem separates from the inverse dynamic problem for both flow problems. In particular, kinematic filtration function $h(s)$ governing the particle capture rate in equation (4) is determined from breakthrough concentration, while the dynamic formation damage function $k(s)$ is calculated from the "hydraulic resistance forces" associated with the pressure drop history (Alvarez et al., 2007). The kinematic fractional flow function, which distributes the total two-phase rate between immiscible phases, is determined from the produced fractions of each phase in the effluent (water cut history). The dynamic total mobility function, which governs the friction between the rock and two-phase flow, is calculated from the pressure drop.

The analogous inverse problem for the modified system ((42), (45), (46)) also involves breakthrough concentration $c(L,t)$ that is measured by turbidimeter during corefloods with either suspension-colloidal injection or high-rate injection of colloid-free water (Vaz et al., 2016, 2017). Modern scanning computational tomography provides retention profile measurements $s(x,t_k)$, k = 1, 2 ... at discrete moments (Arns, 2004; Arns et al., 2005; Yu et al., 2018). The inverse problem formulates as determination of suspended, filtration, and occupation functions, $f(c)$, $h(s)$ and $d(c)$, respectively, from breakthrough concentration and retention profiles. For Langmuir's filtration function, given by equation (11), the exact solution of direct problem ((70), (72), (75), (76)) can yield regularization of the inverse problem, similar to the above mentioned deep bed filtration and waterflooding problems.

On the microscale, particle counting determines size distribution of injected and breakthrough colloids, $C(r,0,t)$ and $C(r,L,t)$ respectively. Retention profiles $S(r,x,t)$ and $s(x,t)$ can be measured by the methods of computational tomography, nuclear magnetic resonance or chemical analysis. The inverse problem can be formulated as determination of the microscale model functions $B(r)$ and $F(C,r)$ from the above mentioned data of the coreflood measurements.

Exact upscaling of the population balance equations for transport of monosized colloids yields unique solution for the downscaling problem (Bedrikovetsky et al., 2017). Filtration function $h(s)$ defines the pore size distribution. The downscaling formulation for the modified system ((42), (45), (46)) is the determination of functions $F(C,r)$ and $B(r)$ from known upper-scale model functions $h(s)$, $f(c)$ and $d(c)$.

As well as filtration function $h(s)$ for the traditional model, the functions $B(r)$ and $F(C,r)$ for the microscale model cannot be determined by direct measurements. The model functions $B(r)$ and $F(C,r)$ can be determined only from the laboratory data by solution of the inverse problems.

If pressure drop across the core is measured during the suspension-colloidal flow, the formation damage function $k(s)$ can also be estimated in these experiments (Alvarez et al., 2007). Pressure measurements in intermediate core ports (so-called three-point pressure method) allows capturing either extra model functions or core heterogeneity (Vaz et al., 2016, 2017). The permeability distribution can be estimated from the suspension-colloidal flow tests with monitoring pressure along the core (Krause et al., 2011; Rabinovich, 2017).

9.4. Applications

The developed averaging approach can be applied for two-phase suspension-colloidal-nanotransport in porous media (Borazjani & Bedrikovetsky, 2017). For particles suspended in aqueous phase and attached to the surface, the splitting method separating two-phase multicomponent system into one-phase solute

system and one equation for phase saturation yields one-phase solute system ((19), (20)) (Borazjani et al., 2015). So the averaging procedure given by equations (35)–(44) is valid for two-phase suspension-colloidal systems. For two-phase suspension-colloidal-nanotransport, where the particles are captured on the water-air interface, the equations for interface transport separating water and air flows must be applied (Shapiro, 2015, 2016).

Equations (1) and (4) are also valid for mineral replacement reactions between the rock and brine. The upscaled technique can be applied to aggregate multiple chemical reactions involving a single mineral.

The procedure for exact upscaling and the analytical model can be extended for quasi 3-D flows for the case of immobile streamlines. Consider 3-D transport of colloids or nanoparticles with significant particle size variation (the same applies to variation of shapes, surface charge, z-potentials, etc.). We consider small suspended and retention concentrations, so the fluid viscosity and rock permeability are constant. Therefore, the streamlines remain immobile during flow of different particle populations with varying suspended and retention concentrations. Introduction of one potential coordinate along the streamlines (pressure) and two transversal coordinates transforms 3-D transport equations into two-dimensional set of independent 1-D problems. Descriptions of streamline parametrization for different flow geometries are presented by Oladyshkin and Panfilov (2007) and Bedrikovetsky (2013). The procedure for exact upscaling, given by equations (34)–(45), along each streamline yields the upscaled system ((42), (45), (46)). Application of exact solution ((70), (72), (75), (76)) for 1-D flow along each streamline yields exact solution for 3-D colloidal transport. Double integration in the transversal coordinates results in breakthrough concentrations.

The comparison between the upscaled modeling data and the averaged results of microscale calculations usually validate asymptotic and approximate averaging procedures (Dagan et al., 2013; Efendiev et al., 2016; Fiori et al., 2015). The presented upscaled method is exact, so this validating comparison is not necessary.

10. Conclusions

Averaging of suspension-colloidal transport of size-distributed particles and particle retention and analytical modeling of large-scale equations allow for the following conclusions.

Population balance system for multisized colloidal-suspension transport with particle attachment allows for exact upscaling. The microscale system with distributed parameters contains two equations, one for particle conservation law and another for attachment kinetics. In contrast, the derived upscaled system consists of three equations: particle conservation law, kinetics of particle attachment, and kinetics of vacancy occupation. The upscaled system degenerates into the traditional 2×2 deep bed filtration system for the particular case where the attached different size particles occupy the same area.

The microscale system contains filtration function of the total occupied area $h(b)$, individual suspension function $F(C,r)$, and occupied vacancy concentration for each particle $B(r)$. The upscaled system contains the same filtration function $h(b)$ as at the microscale, and also the suspension function $f(c)$ and the occupied vacancy function $d(c)$. The suspension function $f(c)$ is the averaged individual suspension function $F(C,r)$. The occupied vacancy function $d(c)$ is the averaged product of individual suspension function $F(C,r)$ and the occupied area for each particle size $B(r)$.

The averaging procedure contains implicit formulae for upscaled suspension and the occupied vacancy functions. The functions $f(c)$ and $d(c)$ depend on the microscale initial and boundary conditions. For suspension injection into clean bed, the upscaled functions depend on the injected composition. For fines migration, the upscaled equations depend on the composition of mobilized fines.

The filtration functions $h(b)$ on the microscale and macroscale coincide.

Even for linear suspension function in multisized attachment kinetics, the upscaling yields nonlinear suspension function $f(c)$.

One-dimensional large-scale problems for continuous injection of suspended colloid, for injection of colloidal bank with particle-free chase drive, and for fines mobilization and migration allow exact solutions for the case of the Langmuir (blocking) filtration function.

Appendix A: Exact Solution in Integral Form

In this Appendix, we derive solution $c(x,\tau)$ for system ((65)–(67)) subject to initial and boundary conditions (47) and (48).

Express occupied vacancy concentration b from equation (67)

$$b = 1 + \frac{1}{f(c)}\frac{\partial c}{\partial x}, \tag{A1}$$

and substitute it into equation (65):

$$\frac{\partial}{\partial \tau}\left(1 + \frac{1}{f(c)}\frac{\partial c}{\partial x}\right) = -\frac{1}{f(c)}\frac{\partial c}{\partial x}d(c). \tag{A2}$$

Direct differentiation in the left-hand side of equation (A2) shows that change of order of partial derivatives does not change the equation

$$\frac{\partial}{\partial x}\left(\frac{1}{f(c)}\frac{\partial c}{\partial \tau}\right) + \frac{d(c)}{f(c)}\frac{\partial c}{\partial x} = 0. \tag{A3}$$

The function $w(c)$ is introduced

$$w(c) = \int_c^1 \frac{\mathrm{d}(y)}{f(y)}\mathrm{d}y. \tag{A4}$$

Equation (A3) takes the form

$$\frac{\partial}{\partial x}\left(\frac{1}{f(c)}\frac{\partial c}{\partial \tau}\right) - \frac{\partial w(c)}{\partial x} = 0. \tag{A5}$$

Integration of equation (A5) in x yields

$$\frac{1}{f(c)}\frac{\partial c}{\partial \tau} - w(c) = K(\tau). \tag{A6}$$

The integration constant $K(\tau)$ can be found from boundary condition (48):

$$K(\tau) = 0. \tag{A7}$$

Equation (A6) takes the form:

$$\frac{1}{f(c)}\frac{\partial c}{\partial \tau} = w(c). \tag{A8}$$

Separating variables in equation (A8) and accounting for suspended concentration $c^{-}(x,0)$ at $\tau = +0$ results in the solution $c(x,\tau)$ in zone I, given by implicit formula (72).

Appendix B: Riemann Invariants for Suspension Injection System

In this appendix, we derive Riemann invariants of the upscaled equations (65)–(67) subject to initial and boundary conditions (47) and (48).

Differentiation of equation (72) with respect to x yields

$$\frac{1}{f(c)w(c)}\frac{\partial c}{\partial x} - \frac{1}{f(c^{-})w(c^{-})}\frac{\partial c^{-}}{\partial x} = 0 \tag{B1}$$

From equations (68) and (B1) it follows that

$$\frac{\partial c}{\partial x} = \frac{f(c)w(c)}{f(c^-)w(c^-)}\frac{\partial c^-}{\partial x} = -\frac{f(c)w(c)}{w(c^-)}. \tag{B2}$$

Substitution of equation (B2) into equation (A1) gives

$$b = 1 - \frac{w(c)}{w(c^-)}. \tag{B3}$$

Due to continuity of $b(x,0)$ across the concentration front $\tau = 0$, the relation (B3) can be written as

$$\frac{1-b}{1-b^-} = \frac{w(c)}{w(c^-)}. \tag{B4}$$

Formula (B4) determines the Riemann invariant I_b for system (65)–(67).

Substitution of Riemann invariant I_b (B3) in the right side of the equation (66) yields

$$\frac{\partial s}{\partial \tau} = \frac{w(c)}{w(c^-)}f(c). \tag{B5}$$

Now we express $w(c)$ from equation (B5)

$$w(c) = w(c^-)\frac{1}{f(c)}\frac{\partial s}{\partial \tau}. \tag{B6}$$

Combining equations (A8) and (B6) results in

$$\frac{\partial c}{\partial \tau} = w(c^-(x))\frac{\partial s}{\partial \tau}. \tag{B7}$$

Integration of equation (B7) over the variable τ from 0 to τ using solution (70) on the concentration front

$$\tau = 0: \quad c(x,\tau) = c^-(x); \quad s(x,\tau) = 0,$$

yields

$$c(x,\tau) - c^-(x) = w(c^-(x))s(x,\tau). \tag{B8}$$

In zone I, equation (B8) defines Riemann invariant I_s for the system (65)–(67) with conditions (47) and (48).

Appendix C: Riemann Invariants for Fines Migration System

In this appendix, we derive Riemann invariants of the upscaled equations (65)–(67) subject to initial and boundary conditions (50) and (51).

Formulae (A1)–(A6) are valid for system (65)–(67) and are independent of initial and boundary conditions. Now we calculate constant $K(\tau)$ in zone 0. Rewriting initial condition (50) in the form

$$c(x,-x) = 1, \tag{C1}$$

and taking derivative of both sides of equation (C1) yields

$$\frac{\partial c}{\partial x}(x,-x) = \frac{\partial c}{\partial \tau}(x,-x). \tag{C2}$$

As it follows from equation (67), along the initial axes $x = -\tau$,

$$\frac{\partial c}{\partial x}(x,-x) = -f(1). \tag{C3}$$

Substituting equation (C3) in equation (A6) yields the value of constant $K(\tau)$:

$$K(\tau) = -1. \tag{C4}$$

Equation (A6) takes the form:

$$\frac{1}{f(c)}\frac{\partial c}{\partial \tau} = w(c)-1. \tag{C5}$$

Separating variables in equation (C5), integrating over the variable τ from $-x$ to τ, and using condition (C1) results in the solution $c(x,\tau)$ in zone 0:

$$\int_1^{c(x,\tau)} \frac{dy}{f(y)(w(y)-1)} = \tau + x. \tag{C6}$$

The suspended concentration $c^+(x)$ ahead of the concentration front is given by formula (C6) at $\tau = -0$

$$\int_1^{c^+(x)} \frac{dy}{f(y)(w(y)-1)} = x. \tag{C7}$$

Riemann invariant I_{b0} in zone 0 can be derived by differentiation of equation (C6) with respect to x:

$$\frac{1}{f(c)(w(c)-1)}\frac{\partial c}{\partial x} = 1. \tag{C8}$$

From equation (C8) it follows that

$$\frac{\partial c}{\partial x} = f(c)(w(c)-1). \tag{C9}$$

Comparison of equations (67) and (C9) yields

$$b(x,\tau) = w(c(x,\tau)). \tag{C10}$$

Differentiation of equation (C6) in τ gives

$$\frac{\partial c}{\partial \tau} = f(c)(w(c)-1). \tag{C11}$$

From equations (C10), (C11), and (66) follows

$$\frac{\partial s}{\partial \tau} = -\frac{\partial c}{\partial \tau}. \tag{C12}$$

Integration of (C12) in respect to τ from $-x$ to τ using condition (50) leads to Riemann invariant I_{s0} in zone 0

$$s(x,\tau) = 1-c(x,\tau). \tag{C13}$$

Nomenclature

English Letters

B – surface area fraction occupied by a single particle with radius r, L^4.
b – overall concentration of occupied sites on the rock surface.

C – suspended concentration distribution $C(r,x,t)$, L^{-4}.
c – total suspended particle concentration, L^{-3}.
d – site occupation function $d(c)$,
F – individual suspension function for particles with size r, L^{-5}.
f – upscaled suspension function $f(c)$, L^{-4}.
h – filtration function $h(s)$,
k – permeability, L^2.
L – core length, L.
p – pressure, MLT^{-2}.
r – particle radius, L.
S – attached concentration distribution $S(r,x,t)$, L^{-4}.
s – total attached particle concentration $s(x,t)$, L^{-3}.
t – time, T.
U – Darcy's velocity of the carrier fluid, LT^{-1}.
x – Cartesian coordinate.

Greek Letters

λ – filtration coefficient, L^{-1}.
μ – viscosity, $ML^{-1}\,T^{-1}$.
ϕ – porosity.
τ – time counted from the moment of front arrival to point x, T.

Acknowledgments
Special thanks are due to A. Roberts (University of Adelaide) for very useful discussions, and B. Collins and P. Alvaro for fruitful cooperation and significant improvement of the text. Many thanks are due to David H. Levin (Murphy, NC, USA) who provided professional English language editing of this article. This research did not receive any specific grant from funding agencies in the public, commercial, or not-for-profit sectors. The data used in this paper are available in the cited references or are included in the table and figures. There are no data-sharing issues in the paper.

References

Alvarez, A. C., Hime, G., Marchesin, D., & Bedrikovetsky, P. G. (2007). The inverse problem of determining the filtration function and permeability reduction in flow of water with particles in porous media. *Transport in Porous Media*, *70*(1), 43–62. https://doi.org/10.1007/s11242-006-9082-3

Arns, C. H. (2004). A comparison of pore size distributions derived by NMR and X-ray-CT techniques. *Physica A: Statistical Mechanics and its Applications*, *339*(1–2), 159–165. https://doi.org/10.1016/j.physa.2004.03.033

Arns, C. H., & Adler, P. M. (2018). Fast Laplace solver approach to pore-scale permeability. *Physical Review E*, *97*(2), 023303. https://doi.org/10.1103/PhysRevE.97.023303

Arns, C. H., Knackstedt, M. A., & Martys, N. S. (2005). Cross-property correlations and permeability estimation in sandstone. *Physical Review E*, *72*(4), 046304. https://doi.org/10.1103/PhysRevE.72.046304

Bedrikovetsky, P. (2008). Upscaling of stochastic micro model for suspension transport in porous media. *Transport in Porous Media*, *75*(3), 335–369. https://doi.org/10.1007/s11242-008-9228-6

Bedrikovetsky, P. (2013). *Mathematical theory of oil and gas recovery: With applications to ex-USSR oil and gas fields*. Springer Science & Business Media.

Bedrikovetsky, P., Siqueira, F. D., Furtado, C. A., & Souza, A. L. S. (2011). Modified particle detachment model for colloidal transport in porous media. *Transport in Porous Media*, *86*(2), 353–383. https://doi.org/10.1007/s11242-010-9626-4

Bedrikovetsky, P., You, Z., Badalyan, A., Osipov, Y., & Kuzmina, L. (2017). Analytical model for straining-dominant large-retention depth filtration. *Chemical Engineering Journal*, *330*, 1148–1159. https://doi.org/10.1016/j.cej.2017.08.031

Bianco, C., Tosco, T., & Sethi, R. (2016). A 3-dimensional micro-and nanoparticle transport and filtration model (MNM3D) applied to the migration of carbon-based nanomaterials in porous media. *Journal of Contaminant Hydrology*, *193*, 10–20. https://doi.org/10.1016/j.jconhyd.2016.08.006

Boccardo, G., Sethi, R., & Marchisio, D. L. (2018). Fine and ultrafine particle deposition in packed-bed catalytic reactors. *Chemical Engineering Science*. https://doi.org/10.1016/j.ces.2018.09.024

Boccardo, G., Sokolov, I. M., & Paster, A. (2018). An improved scheme for a Robin boundary condition in discrete-time random walk algorithms. *Journal of Computational Physics*, *374*, 1152–1165. https://doi.org/10.1016/j.jcp.2018.08.009

Borazjani, S., & Bedrikovetsky, P. (2017). Exact solutions for two-phase colloidal-suspension transport in porous media. *Applied Mathematical Modelling*, *44*, 296–320. https://doi.org/10.1016/j.apm.2016.12.023

Borazjani, S., Roberts, A. J., & Bedrikovetsky, P. (2015). Splitting in systems of PDEs for two-phase multicomponent flow in porous media. *Applied Mathematics Letters*, *53*, 25–32.

Boso, F., & Tartakovsky, D. M. (2016). The method of distributions for dispersive transport in porous media with +uncertain hydraulic properties. *Water Resources Research*, *52*, 4700–4712. https://doi.org/10.1002/2016WR018745

Bradford, S. A., Torkzaban, S., Leij, F., & Simunek, J. (2015). Equilibrium and kinetic models for colloid release under transient solution chemistry conditions. *Journal of Contaminant Hydrology*, *181*, 141–152. https://doi.org/10.1016/j.jconhyd.2015.04.003

Bradford, S. A., Torkzaban, S., & Shapiro, A. (2013). A theoretical analysis of colloid attachment and straining in chemically heterogeneous porous media. *Langmuir*, *29*(23), 6944–6952. https://doi.org/10.1021/la4011357

Bradford, S. A., Torkzaban, S., & Simunek, J. (2011). Modeling colloid transport and retention in saturated porous media under unfavorable attachment conditions. *Water Resources Research*, *47*, W10503. https://doi.org/10.1029/2011WR010812

Bradford, S. A., Torkzaban, S., & Wiegmann, A. (2011). Pore-scale simulations to determine the applied hydrodynamic torque and colloid immobilization. *Vadose Zone Journal*, *10*(1), 252–261. https://doi.org/10.2136/vzj2010.0064

Brady, P. V., Morrow, N. R., Fogden, A., Deniz, V., & Loahardjo, N. (2015). Electrostatics and the low salinity effect in sandstone reservoirs. *Energy & Fuels*, *29*(2), 666–677. https://doi.org/10.1021/ef502474a

Chen, M., Wang, D., Yang, F., Xu, X., Xu, N., & Cao, X. (2017). Transport and retention of biochar nanoparticles in a paddy soil under environmentally-relevant solution chemistry conditions. *Environmental Pollution*, *230*, 540–549. https://doi.org/10.1016/j.envpol.2017.06.101

Chrysikopoulos, C. V., Sotirelis, N. P., & Kallithrakas-Kontos, N. G. (2017). Cotransport of graphene oxide nanoparticles and kaolinite colloids in porous media. *Transport in Porous Media*, *119*(1), 181–204. https://doi.org/10.1007/s11242-017-0879-z

Chrysikopoulos, C. V., & Syngouna, V. I. (2012). Attachment of bacteriophages MS2 and ΦX174 onto kaolinite and montmorillonite: Extended-DLVO interactions. *Colloids and Surfaces B: Biointerfaces*, *92*, 74–83. https://doi.org/10.1016/j.colsurfb.2011.11.028

Chrysikopoulos, C. V., Syngouna, V. I., Vasiliadou, I. A., & Katzourakis, V. E. (2012). Transport of Pseudomonas putida in a 3-D bench scale experimental aquifer. *Transport in Porous Media*, *94*(3), 617–642. https://doi.org/10.1007/s11242-012-0015-z

Civan, F. (2015). *Reservoir formation damage*. Norman, OK: Gulf Professional Publishing.

Courant, R., & Hilbert, D. (1989). Partial differential equations, Reprint of the 1962 Original, Edited, A Wiley-Interscience Publication. New York.

Dagan, G., Fiori, A., & Jankovic, I. (2013). Upscaling of flow in heterogeneous porous formations: Critical examination and issues of principle. *Advances in Water Resources*, *51*, 67–85. https://doi.org/10.1016/j.advwatres.2011.12.017

Efendiev, Y., Hou, T., Durlofsky, L., & Tchelepi, H. (2016). *Multiscale analysis and computation for flows in heterogeneous media*. College Station, TX: Texas A & M Univ.

Elimelech, M., Gregory, J., & Jia, X. (2013). *Particle deposition and aggregation: measurement, modelling and simulation*. Oxford, UK: Butterworth-Heinemann.

Fiori, A., Bellin, A., Cvetkovic, V., de Barros, F., & Dagan, G. (2015). Stochastic modeling of solute transport in aquifers: From heterogeneity characterization to risk analysis. *Water Resources Research*, *51*, 6622–6648. https://doi.org/10.1002/2015WR017388

Fogler, H. (2006). *Elements of chemical reaction engineering*. *International Series in the Physical and Chemical Engineering Sciences*. NJ: Prentice Hall.

Goldberg, E., Scheringer, M., Bucheli, T. D., & Hungerbühler, K. (2014). Critical assessment of models for transport of engineered nanoparticles in saturated porous media. *Environmental Science & Technology*, *48*(21), 12,732–12,741. https://doi.org/10.1021/es502044k

Katzourakis, V. E., & Chrysikopoulos, C. V. (2018). Impact of spatially variable collision efficiency on the transport of biocolloids in geochemically heterogeneous porous media. *Water Resources Research*, *54*, 3841–3862. https://doi.org/10.1029/2017WR021996

Krause, M. H., Perrin, J. C., & Benson, S. M. (2011). Modeling permeability distributions in a sandstone core for history matching coreflood experiments. *SPE Journal*, *16*(04), 768–777. https://doi.org/10.2118/126340-PA

Kuzmina, L. I., Osipov, Y. V., & Galaguz, Y. P. (2017). A model of two-velocity particles transport in a porous medium. *International Journal of Non-Linear Mechanics*, *93*, 1–6. https://doi.org/10.1016/j.ijnonlinmec.2017.04.015

Lasaga, A. (1998). *Kinetic theory in the Earth sciences*. Princeton, NJ: Princeton University Press.

Mirabolghasemi, M., Prodanović, M., DiCarlo, D., & Ji, H. (2015). Prediction of empirical properties using direct pore-scale simulation of straining through 3D microtomography images of porous media. *Journal of Hydrology*, *529*, 768–778. https://doi.org/10.1016/j.jhydrol.2015.08.016

Oladyshkin, S., & Panfilov, M. (2007). Limit thermodynamic model for compositional gas–liquid systems moving in a porous medium. *Transport in Porous Media*, *70*(2), 174–165.

Pan, W., & Tartakovsky, A. M. (2013). Dissipative particle dynamics model for colloid transport in porous media. *Advances in Water Resources*, *58*, 41–48. https://doi.org/10.1016/j.advwatres.2013.04.004

Paster, A., Bolster, D., & Benson, D. A. (2014). Connecting the dots: Semi-analytical and random walk numerical solutions of the diffusion–reaction equation with stochastic initial conditions. *Journal of Computational Physics*, *263*, 91–112. https://doi.org/10.1016/j.jcp.2014.01.020

Payatakes, A. C., Rajagopalan, R., & Tien, C. (1974). Application of porous media models to the study of deep bed filtration. *The Canadian Journal of Chemical Engineering*, *52*(6), 722–731. https://doi.org/10.1002/cjce.5450520605

Polyanin, A., & Dil'man, V. V. (1994). *Methods of modeling equations and analogies in chemical engineering*. Boca Raton, FL: CRC Press.

Polyanin, A., & Zaitsev, V. (2012). *Handbook of nonlinear partial differential equations*. Boca Raton: Chapman & Hall/CRC Press.

Polyanin, A. D., & Manzhirov, A. V. (2006). *Handbook of mathematics for engineers and scientists*. Boca Raton, FL: CRC Press. https://doi.org/10.1201/9781420010510

Rabinovich, A. (2017). Estimation of sub-core permeability statistical properties from coreflooding data. *Advances in Water Resources*, *108*, 113–124. https://doi.org/10.1016/j.advwatres.2017.07.012

Rabinovich, A., Dagan, G., & Miloh, T. (2013). Dynamic effective properties of heterogeneous geological formations with spherical inclusions under periodic time variations. *Geophysical Research Letters*, *40*, 1345–1350. https://doi.org/10.1002/grl.50319

Rosenbrand, E., Kjøller, C., Riis, J. F., Kets, F., & Fabricius, I. L. (2015). Different effects of temperature and salinity on permeability reduction by fines migration in Berea sandstone. *Geothermics*, *53*, 225–235. https://doi.org/10.1016/j.geothermics.2014.06.004

Shapiro, A., & Wesselingh, J. (2008). Gas transport in tight porous media: Gas kinetic approach. *Chemical Engineering Journal*, *142*(1), 14–22.

Shapiro, A., and H. Yuan (2012), Application of stochastic approaches to modelling suspension flow in porous media. In A. Skogseid & V. Fasano (Eds.), *Statistical mechanics and random walks: Principles, processes and applications* (pp. 1–36). Hauppauge, New York: Nova Science Publishers, Incorporated.

Shapiro, A. A. (2007). Elliptic equation for random walks. Application to transport in microporous media. *Physica A: Statistical Mechanics and its Applications*, *375*(1), 81–96. https://doi.org/10.1016/j.physa.2006.08.033

Shapiro, A. A. (2015). Two-phase immiscible flows in porous media: The Mesocopic Maxwell–Stefan approach. *Transport in Porous Media*, *107*(2), 335–363. https://doi.org/10.1007/s11242-014-0442-0

Shapiro, A. A. (2016). Mechanics of the separating surface for a two-phase co-current flow in a porous medium. *Transport in Porous Media*, *112*(2), 489–517. https://doi.org/10.1007/s11242-016-0662-6

Shapiro, A. A., Bedrikovetsky, P. G., Santos, A., & Medvedev, O. O. (2007). A stochastic model for filtration of particulate suspensions with incomplete pore plugging. *Transport in Porous Media*, *67*(1), 135–164. https://doi.org/10.1007/s11242-006-0029-5

Sharma, M., & Yortsos, Y. (1987a). Transport of particulate suspensions in porous media: Model formulation. *AICHE Journal*, *33*(10), 1636–1643. https://doi.org/10.1002/aic.690331007

Sharma, M., & Yortsos, Y. (1987b). Fines migration in porous media. *AICHE Journal*, *33*(10), 1654–1662. https://doi.org/10.1002/aic.690331009

Sun, Y., Gao, B., Bradford, S. A., Wu, L., Chen, H., Shi, X., & Wu, J. (2015). Transport, retention, and size perturbation of graphene oxide in saturated porous media: Effects of input concentration and grain size. *Water Research*, *68*, 24–33. https://doi.org/10.1016/j.watres.2014.09.025

Tartakovsky, A. M., Panzeri, M., Tartakovsky, G. D., & Guadagnini, A. (2017). Uncertainty quantification in scale-dependent models of flow in porous media. *Water Resources Research*, *53*, 9392–9401. https://doi.org/10.1002/2017WR020905

Tosco, T., Gastone, F., & Sethi, R. (2014). Guar gum solutions for improved delivery of iron particles in porous media (part 2): Iron transport tests and modeling in radial geometry. *Journal of Contaminant Hydrology*, *166*, 34–51. https://doi.org/10.1016/j.jconhyd.2014.06.014

Tufenkji, N., & Elimelech, M. (2004). Correlation equation for predicting single-collector efficiency in physicochemical filtration in saturated porous media. *Environmental Science & Technology*, *38*(2), 529–536. https://doi.org/10.1021/es034049r

Vaz, A., Fernandes, P., Badalyan, A., Carageorgos, T., & Bedrikovetsky, P. (2017). Determining model parameters for non-linear deep-bed filtration using laboratory pressure measurements. *Journal of Petroleum Science and Engineering*, *151*, 421–433. https://doi.org/10.1016/j.petrol.2017.01.001

Vaz, A., Maffra, D., Carageorgos, T., & Bedrikovetsky, P. (2016). Characterisation of formation damage during reactive flows in porous media. *Journal of Natural Gas Science and Engineering*, *34*, 1422–1433. https://doi.org/10.1016/j.jngse.2016.08.016

Winter, C. L., & Tartakovsky, D. M. (2002). Groundwater flow in heterogeneous composite aquifers. *Water Resources Research*, *38*(8), 1148. https://doi.org/10.1029/2001WR000450

Xu, J. (2016). Propagation behavior of permeability reduction in heterogeneous porous media due to particulate transport. *Europhysics Letters*, *114*(1), 14001. https://doi.org/10.1209/0295-5075/114/14001

Yu, M., Hussain, F., Arns, J.-Y., Bedrikovetky, P., Genolet, L., Behr, A., et al. (2018). Imaging analysis of fines migration during water flow with salinity alteration. *Advances in Water Resources*, *121*, 150–161. https://doi.org/10.1016/j.advwatres.2018.08.006

Yuan, H., & Shapiro, A. (2012). Colloid transport and retention: recent advances in colloids filtration theory. In P. C. Ray (Ed.), *Colloids: Classification, properties and applications* (Chap. 9, pp. 1–36). Hauppauge, New York: Nova Science Publishers, Incorporated.

Yuan, H., Shapiro, A., You, Z., & Badalyan, A. (2012). Estimating filtration coefficients for straining from percolation and random walk theories. *Chemical Engineering Journal*, *210*, 63–73. https://doi.org/10.1016/j.cej.2012.08.029

Yuan, H., & Shapiro, A. A. (2010). Modeling non-Fickian transport and hyperexponential deposition for deep bed filtration. *Chemical Engineering Journal*, *162*(3), 974–988. https://doi.org/10.1016/j.cej.2010.07.003

5 Model to match hyper-exponential retention profiles

5.1 A modified model for colloidal transport to match hyper-exponential particle retention

Chengyuan Xu, **Gabriel Malgaresi**, Yuri Osipov, Liudmila Kuzmina, Pavel Bedrikovetsky

Chemical Engineering Journal

Statement of Authorship

Title of Paper	A modified model for colloidal transport to match hyper-exponential particle retention
Publication Status	☐ Published ☐ Accepted for Publication ☑ Submitted for Publication ☐ Unpublished and Unsubmitted work written in manuscript style
Publication Details	Xu, C., Malgaresi, G., Osipov, Y., Kuzmina, L. and Bedrikovetsky, P., 2019. A modified model for colloidal transport to match hyper-exponential particle retention. Chemical Engineering Journal.

Principal Author

Name of Principal Author	Chengyuan Xu		
Contribution to the Paper	Derivation of the model. Found the activity function to use as a suspension function in the traditional model for DBF.		
Signature	[redacted]	Date	29/10/2019

Co-Author Contributions

By signing the Statement of Authorship, each author certifies that:

i. the candidate's stated contribution to the publication is accurate (as detailed above);

ii. permission is granted for the candidate in include the publication in the thesis; and

iii. the sum of all co-author contributions is equal to 100% less the candidate's stated contribution.

Name of Co-Author	Gabriel Malgaresi		
Contribution to the Paper	Development of the analytical model. Tuned all sets of experiments. Helped with the analysis of the tuned parameters, sensitivity analysis and preparation of the manuscript.		
Overall percentage (%)	50%		
Certification:	This paper reports on original research I conducted during the period of my Higher Degree by Research candidature and is not subject to any obligations or contractual agreements with a third party that would constrain its inclusion in this thesis.		
Signature	[redacted]	Date	25/10/2019

Name of Co-Author	Yuri Osipov		
Contribution to the Paper	Helped with the derivation of the mathematical model, analysis of the results, and mathematical properties of the model.		
Signature	[redacted]	Date	28/10/2019

Name of Co-Author	Liudmila Kuzmina		
Contribution to the Paper	Helped with the derivation of the mathematical model, analysis of the results, and mathematical properties of the model.		
Signature	[redacted]	Date	28/10/2019

Name of Co-Author	Pavel Bedrikovetsky		
Contribution to the Paper	Problem formulation and supervision of the development of the whole work.		
Signature		Date	23/10/2013

A modified model for colloidal transport to match hyper-exponential particle retention

Chengyuan Xu[1], Gabriel Malgaresi[1], Yuri Osipov[2], Liudmila Kuzmina[3], Pavel Bedrikovetsky[1]

1- University of Adelaide, Australia

2- Moscow State University of Civil Engineering, Russia

3- National Research University Higher School of Economics, Russia

Abstract Hyper-exponential retention profiles (HERPs) are often observed during laboratory tests on colloidal and nano-suspension transport in porous media. The aim of this work is an extension of the traditional model for suspended particle transport (deep bed filtration) to match HERPs. Interpreting particle capture in the framework of active mass law for the "chemical reaction" particle-rock, we substitute suspension concentration in the traditional expression for capture rate by non-linear "activity" function, called suspension function. We show that this extended model can be obtained by averaging of the particulate flows with distributed particle properties; this explains non-linearity of the suspension function by heterogeneity of the colloidal flux. One-dimensional (1D) suspension flow problem allows for exact analytical solution for any arbitrary suspension function. The analytical model is applied to laboratory data treatment. For matching purposes, we proposed a one-parametric suspension functions. Numerous laboratory tests, exhibiting HERPs, have been matched by the traditional and extended models. The traditional modelling data significantly deviate from the laboratory data, while the extended model, which uses only one extra parameter exhibits high agreement with the laboratory data. For those tests, the dimension of experimental data array exceeds the number of model parameters, which validates the extended deep bed filtration model.

1. Introduction

Colloidal and nano-suspension flow in porous media is of fundamental importance to environmental, chemical, civil and petroleum engineering. Deep bed filtration (DBF) includes propagation of viruses, bacteria and other contaminants in ground waters, disposal of industrial wastes in aquifers, industrial filtering of technical fluids, transport of nanoparticles, injection of water with solid and liquid particles in oilfields during waterflooding, size-exclusion chromatography, and technical fluid invasion during well drilling and completion [1-13]. The major

features of the processes are particle transport and capture by the porous medium, and the consequent permeability decline.

The mathematical model for colloidal and nano- suspension transport in porous media includes mass balance for the suspended and retained particles, expression for particle capture rate, and Darcy´s law that accounts for permeability decline during particle retention [14, 15]

$$\phi \frac{\partial c}{\partial t} + U \frac{\partial c}{\partial x} = -\frac{\partial s}{\partial t} \tag{1}$$

$$\frac{\partial s}{\partial t} = \lambda \left(1 - \frac{s}{s_m}\right) cU \tag{2}$$

$$U = -\frac{k}{\mu(1+\beta s)} \frac{\partial p}{\partial x} \tag{3}$$

Here ϕ is the porosity, U is the Darcy's flow velocity, c is the suspension concentration, s is the retained concentration, s_m is the maximum retained concentration that corresponds to filling all vacancies for the particle capture, λ is the filtration coefficient, p is the pressure, k is the permeability, and μ is the carrier water viscosity. The suspension concentration is defined as the number of particles per unit volume of the fluid, and the retained concentration is equal to the number of particles per unit of the rock volume. The filtration coefficient λ is the probability of particle capture per unit length of its trajectory [16-18].

Fig. 1 presents multiple particle capture mechanisms that may occur simultaneously during flow of colloidal and nano-suspensions in porous media: size exclusion, straining, attachment, incomplete pore plugging with internal cake, diffusion into dead-end pores, bridging, and segregation [19-21]. Particle capture is analogous to chemical reaction between the particle and vacancy. Vacancy for size exclusion is a pore throats that is smaller than the particle [15]. Vacancy for attachment is a site on the rock surface that attracts the particle by electrostatic forces. Kinetics equation (2) corresponds to the total particle capture rate by the rock.

The initial and boundary conditions that correspond to colloid injection with constant concentration into a clean bed are:

$$t = 0: \; c = s = 0; \quad x = 0: \; c = c^0 \tag{4}$$

In the clean bed case, the initial vacancy concentration is s_m, and concentration of remaining vacancies is s_m-s. So, kinetics equation (2) is analogous to active mass law in chemical reaction kinetics with both stoichiometric coefficients equal one, as if one vacancy "reacts" with the captured particle [22]. For small concentrations of suspended particles and vacancies, the particle capture is a result of simultaneous appearance of a suspended particle and a vacancy in the same reference volume. In this case, the simultaneous appearances are independent events, so the probability of "reaction" is equal to product of the individual probabilities. Therefore, the capture rate is proportional to the product of reacting species concentrations $c(s_m-s)$. This form of the active mass law is valid for low concentrations of both reagents [23].

The term in brackets in Eq. (2), which is proportional to the concentration of remaining vacancies is called the blocking (Langmuir's) function [15]. The blocking function corresponds to mono-layer particle attachment to the rock surface. It also describes suspension-colloidal transport with mono-sized particles through porous media with two-size pores, where the particles move via large pores and strain the small pores [18]; here s_m is the initial concentration of small pores. However, in the case where pore plugging increases the particle path tortuosity and lengthens the trajectory, the particle straining increases the capture probability; matching of the laboratory data yields a negative value of the phenomenological constant s_m.

For low retention $s << s_m$, the term in the brackets in Eq. (2) has small deviation from unity. The solution of the problem (1-4) exhibits constant breakthrough concentration c^L and exponential retention profiles $s(x,t_f)$ at all times t_f [14]. The extension of the model (1-3) by changing the linear expression in the brackets by any arbitrary filtration function $h(s)$ is [18, 20]

$$\frac{\partial s}{\partial t} = \lambda h(s) c U \qquad (5)$$

The model transformation from Eq. (2) to Eq. (5) is analogous to substituting the specie concentration by its activity in the law of acting masses [22]. Eq. (5) is valid for high retention concentrations, where the retention significantly changes the pore space geometry and affects the capture probability. A single function $h(s)$ in Eq. (2) represents the total retention rate. Exact solution of the problem (1, 3-5) for any arbitrary filtration function

73 $h(s)$ exhibits varying breakthrough concentration $c^L(t)$ and an exponential shape of the retention profile $s(x,t_f)$.
74 Further in the text, we call Eq. (5) the traditional model.
75 Fig. 2 shows the schematic for laboratory test on injection of colloidal or nano-suspension with concentration c^0.
76 The breakthrough concentration $c^L(t)$ and pressure drop $\Delta p(t)$ are measured in line while the suspension
77 concentration is injected. The retention profile $s(x,t_f)$ is measured after colloidal injection at the moment t_f (called
78 *post-mortem time)* where the core is dissected in section and the numbers of colloids are quantified. Numerous
79 corefloods by suspensions and colloids exhibit HERPs [10, 24-32]. Those profiles correspond to retention rate
80 decrease along the core. The traditional filtration model does not match the HERPs [33]. In particular, Tufenkji
81 and Elimelech [25], [34] highlight that the measured retained concentrations are in marked discrepancy with
82 those predicted by Eq. (5). To match the retained profiles, Tufenkji and Elimelech [10] assumed probabilistic
83 distribution of the filtration coefficient. This model assumes bimodal distribution with five constants,
84 corresponding to fast and slow capture due to favourable and unfavourable particle-surface interactions. The
85 proposed stochastic model successfully matches the retention profiles using those five constants.
86 Schijven, et al. [7] proposed a two-capture model for colloidal-suspension transport in porous media. The model
87 uses four constants for tuning. This model successfully matches either of HERP or BTC; simultaneous match of
88 two curves cannot be achieved [33].
89 Another way around the matching of HERPs was developed by Bradford, et al. [35], where the filtration function
90 for straining is depth-dependent, i.e. $h=h(s,x)$. Power-law is assumed for this depth-dependency. The model also
91 included kinetics of simultaneous attachment and detachment. The model successfully matched BTCs and
92 HERPs simultaneously. Currently, this model is widely used for matching of numerous laboratory data sets [19,
93 32, 36, 37]. However, Goldberg, et al. [33] suggested that x-dependency of the filtration function must be
94 justified with more physical background.
95 Numerous authors attribute HERPs to distributed properties of colloidal particles [24, 25, 27, 34]. In particular,
96 Tong and Johnson [24] explain HERPs by multiple populations in the colloidal fluids. The same size particles
97 can have different surface charges and zeta-potentials, so the particles with high filtration coefficients retain near

to the inlet, while those with lower filtration coefficient move further in the core. The total of two exponential RPs with highly different decrements is non-exponential.

Yuan and Shapiro [38] also discuss multi-component colloids, extending the random walk model with stochastically distributed lengths and durations of jumps [39], in order to match simultaneously retention profile and breakthrough curve. Averaging of the Master equation with distributed jump lengths and flight times results in elliptic transport equation. The filtration coefficient is assumed to be dependent of a particle property, like size, shape, surface charge, etc. Introduction of probabilistic distributions of the filtration coefficient and of the particle flight time into Master equation yields system of elliptic transport equations, where each equation corresponds to a particle population. The derived "integral" system successfully matches HERPs and BTCs simultaneously.

Exact averaging of a stochastic system results in representation of a distributed parameter by a number (function). For example, jump length distribution in random walks and consequent averaging result in diffusion coefficient [40]. Averaging of stochastically distributed lengths and durations of jumps leads to diffusion and timely-diffusion coefficients [39]. Discretisation of a wide filtration-coefficient distribution in the system with distributed lengths and durations of jumps requires numerous values for filtration coefficient, and leads to solution of the system containing the same number of elliptic equations. This results in cumbersome and computer time consuming calculations for direct runs and for iterative data-matching procedures. Averaging of this system would significantly simplify solutions of forward and inverse problems.

In the current work, we transform the traditional DBF model to reproduce HERPS. Suspension concentration in the particle capture rate is substituted by nonlinear suspension function. We show that the extended model can be obtained by averaging of micro-scale DBF equations with distributed particle properties, which supports the extended model. For a binary colloid, the suspension function is bi-parametric, i.e. the extended model contains two extra model parameters if compared with the traditional model. We derive an exact analytical solution for 1D flow problem that reproduces HERPs. We propose one-parametric exponential-quadratic suspended function, which successfully matches numerous laboratory tests with HERPs. Close precision of matching and prediction of the laboratory data, where the number of degrees of freedom of the experimental data array exceeds the number of model coefficients by one to six, validates the modified mathematical model. The averaging of the colloidal

system with distributed parameters and validation of the upscaled system explains HERPs by heterogeneity of the colloidal flux.

The structure of the text is as follows. Section 2 presents the extended model for suspension and colloidal transport in porous media. Section 3 derives exact solution for 1D transport and exhibits HERPs. Section 4 discusses the results of experimental data matching by the traditional and modified models. Section 5 discusses the limitations and applications of the extended DBF model. Section 6 concludes the paper.

2. FORMULATION OF THE MODEL

This section formulates the extended DBF model, including the assumptions (section 2.1) and governing equations (section 2.2). Appendix A derives the extended model by averaging the micro-scale colloidal transport equations with distributed particle properties. Section 2.3 proposes the forms of suspension function that are used further for matching the laboratory data.

2.1. Assumptions of the model

Exploring further the analogy between the particle capture rates (2) and (5) and the mass action law for the "reaction" pore-particle, we substitute suspension concentration c in Eq. (5) by its "activity" $f(c)/\lambda$ for the case of dense suspensions and colloids:

$$\frac{\partial s}{\partial t} = h(s)\, f(c) U \tag{6}$$

where $f(c)$ is called the suspension function. Non-linear suspension function $f(c)$ reflects the competition between high-concentration suspended particles for the vacancies, so the meetings between the particles and vacancies are not independent events for high suspension concentrations.

The carrier fluid is assumed to be incompressible. We discuss small concentrations for attached and retained particles, so it does not affect the suspension density, which is equal to the carrier fluid density. It results in conservation of the suspension flux: $U=U(t)$. The assumptions of incompressible fluid and the particle matter, and volume additivity during particle suspension in the carrier fluid and particle capture by the rock (Amagat's law), also result in the suspension flux conservation, even for high suspension concentrations [41].

We discuss large-scale approximation of the flow equations, where the diffusive/dispersive flux is negligibly small if compared with the advective flux [41, 42]. Let us calculate the ratio between the dispersive and advective fluxes, which is equal to reciprocal of Peclet's number. Dispersive flux is proportional to flow velocity: $D=LU$, where L is the dispersivity coefficient that has the order of magnitude of the size of micro heterogeneity [43]. For natural porous media with small to moderate micro heterogeneity, L varies from 10^{-4} to 10^{-2} m, while the typical core length is 0.1m, so $1/Pe=\alpha_L/L=10^{-3}$-10^{-1}. Dispersivity in glass-bead or sand packs is one-two orders of magnitude lower than in natural rocks. Molecular diffusion is two-three orders of magnitude lower than dispersion in porous media. The above speculations justify ignoring the diffusion and dispersion during coreflooding in natural and artificial porous media.

For small suspension concentrations, the retention rate expression (6) tends to (5), yielding the following properties of suspension function:

$$f(0)=0,\ f'(0)=\lambda \tag{7}$$

2.2. System of governing equations

This section formulates 1D DBF problem for the modified model (1, 3, 6). We introduce the following dimensionless variables and parameters:

$$\begin{gathered} x\to\frac{x}{L},\ t\to\frac{Ut}{L\phi},\ c\to\frac{c}{c^0},\ s\to\frac{s}{\phi c^0},\ p\to\frac{kp}{U\mu L} \\ \lambda\to\lambda L,\ s_m\to\frac{s_m}{\phi c^0},\ f(c)\to\frac{Lf(c)}{c^0} \end{gathered} \tag{8}$$

Introduction of dimensionless parameters (8) transforms system (1, 3, 6) to the following dimensionless form:

$$\frac{\partial c}{\partial t}+\frac{\partial c}{\partial x}=-\frac{\partial s}{\partial t} \tag{9}$$

$$\frac{\partial s}{\partial t}=h(s)\,f(c) \tag{10}$$

$$1=-\frac{1}{1+\beta\phi c^0 s}\frac{\partial p}{\partial x} \tag{11}$$

The initial conditions correspond to injection into a clean bed:

$$t = 0 : c = s = 0 \tag{12}$$

The injected suspension concentration and pressure are set as the boundary conditions:

$$x = 0 : c = 1,\ p = \frac{kp_0}{U\mu L} \tag{13}$$

2.3. Forms for suspension function

Consider possible forms of the "particle activity" suspension function *f*(c). For dimensionless suspension function, Taylor's expansion accounting for properties given by Eq. (7) is:

$$f\left(c\right) = \lambda c + \frac{f''(0)}{2}c^2 + \frac{f'''(0)}{6}c^3 + O\left(c^4\right) \tag{14}$$

First, consider second-order Taylor's expansion of the suspension function *f(c)* near to *c*=0, fulfilling the properties given by Eq. (7):

$$f\left(c\right) = \lambda c\left(1 + bc\right),\ b = \frac{f''(0)}{2\lambda} \tag{15}$$

The traditional model (1, 3, 5) corresponds to *b*=0. The model (15) contains an extra parameter *b* if compared with the traditional model. Further in the text, the model (15) is called quadratic.

Then, consider the shape of suspension function analogous to so-called two-suffix Margules expression of activity coefficient for non-ideal solutions [22, 44]

$$f\left(c\right) = \lambda c e^{Ac^2} \tag{16}$$

where the interaction parameter *A* is an empirical coefficient, typically obtained by fitting experimental data. The *A*-value is affected by molecular size, shape and polarity, etc. Further in the text, Eqs. (6, 16) are called the modified model. The modified model contains an extra model parameter *A* compared with the traditional model (1, 3, 5), where *A*=0.

For small *c*, Taylor's series for the model (14, 16) is

$$f\left(c\right) = \lambda c\left(1 + Ac^2\right),\ A = \frac{f'''(0)}{6\lambda},\ f''(0) = 0 \tag{17}$$

3. ANALYTICAL MODEL

This section derives exact analytical solution of 1D problem (9-13) for any arbitrary form of the particle activity function (section 3.1). Appendix B derives simplified forms of the analytical model for various particular cases of the suspension function *f(c)*. Section 3.2 validates the analytical model by comparison with the numerical solution. Section 3.3 presents the type curves for RPs, BTCs, and pressure drop, generated by the analytical model.

3.1. Exact analytical solution for 1D clean bed filtration

Introduction of a new independent variable [42, 45]

$$\tau = t - x, \tag{18}$$

yields the following form of system (9, 10)

$$\frac{\partial c}{\partial x} = -\left(1 - \frac{s}{s_m}\right) f(c) \tag{19}$$

$$\frac{\partial s}{\partial \tau} = \left(1 - \frac{s}{s_m}\right) f(c) \tag{20}$$

Initial conditions (12) become:

$$\tau = -x:\ c = s = 0 \tag{21}$$

Boundary condition at the inlet (13) remains the same.

As it follows from initial condition (12) and Eq. (9), in zone $-x<\tau<0$

$$c(x,t) = s(x,t) = 0 \tag{22}$$

From (20) follows that solution $s(x,\tau)$ is a continuous function. Therefore, s=0 at the line τ=0. Substituting s=0 into Eq. (19), we obtain suspension concentration just behind the front τ=0, which is $c^{-}(x)=c(x,0)$:

$$\int_{c^{-}(x)}^{1} \frac{du}{f(u)} = x, \tag{23}$$

Expression (23) can be rewritten as

$$\varphi(1) - \varphi\left(c^{-}(x,0)\right) = x, \quad \varphi'(c) = \frac{1}{f(c)} \tag{24}$$

Expressing retained concentration from Eq. (19)

$$s(x,\tau) = s_m\left[\frac{1}{f(c)}\frac{\partial c}{\partial x}+1\right] = s_m\left[\frac{\partial \varphi(c)}{\partial x}+1\right] \tag{25}$$

and substituting it in Eq. (20) results in

$$\frac{\partial}{\partial \tau}\left(\frac{\partial \varphi(c)}{\partial x}\right)+\frac{\partial c}{\partial x} = 0 \tag{26}$$

Changing the order of derivatives in Eq. (26) and integrating in x accounting for boundary conditions (13) yields

$$\frac{\partial \varphi(c)}{\partial \tau}+c = 1 \tag{27}$$

Dividing variables in obtained ordinary differential equation (27) results in solution $c(x,\tau)$

$$\int_{c^-(x)}^{c}\frac{du}{(1-u)\,f(u)} = \tau \tag{28}$$

where suspension concentration just behind the front $c^-(x)=c(x,x)$ is given by Eq. (23).

Taking derivative in x of both sides of Eq. (28) leads to:

$$\frac{1}{(1-c)\,f(c)}\frac{\partial c}{\partial x}-\frac{1}{\left(1-c^-(x,0)\right)f\left(c^-(x,0)\right)}\frac{dc^-(x,0)}{dx} = 0 \tag{29}$$

Accounting for Eq. (23) in (29) yields the expression for Riemann invariant [42, 45]

$$\frac{s(x,\tau)-s_m}{1-c(x,\tau)} = \frac{-s_m}{\left(1-c(x,0)\right)} \tag{30}$$

which determines solution $s(x,\tau)$.

Changing variable $t=\tau+x$ in solution (28, 30) yields the solution in (x,t)-plane. The corresponding formula are presented in Table 1. Explicit expressions for solution in cases of modified, quadratic, and traditional models are presented in Appendix B.

Expression of the pressure gradient from Eq. (11) and integration in x from zero to one yields the pressure drop across the core

$$\Delta p(t) = 1 + \beta\phi c^0 \int_0^1 s(u,t)\,du \tag{31}$$

The dimensionless pressure drop

$$J(t) = \frac{\Delta p(t)}{\Delta p(t=0)} \tag{32}$$

is called the impedance. The initial value of impedance is equal to one.

3.2. Validation of the analytical model by numerical solution

System of two equations (9, 10) subject to initial and boundary conditions (12, 13) is solved numerically using the hyperbolic partial differential equation solver presented by Shampine [46].

The method allows for vectorisation of the problem, taking advantage of MATLAB's matrices and vectors optimisation. The algorithm implements a two-step Lax–Friedrichs finite-difference method [47].

The calculation results are presented in Fig. 3. Here the areal and time steps for finite-difference method are Δx=0.001 and Δt=0.0009, i.e. the linear stability condition $\Delta t / \Delta x < 1$ is fulfilled. BTCs (Fig. 3a) and RPs (Fig. 3b) for exact and numerical solutions almost coincide exhibiting high agreement between the solutions.

3.3. Type curves calculated by the analytical model

Fig. 4 presents the analytical modelling results using the modified, quadratic, and traditional models. The values of the model parameters are typical for those tuned from the laboratory tests and presented in Tables 2 and 3.

Fig. 4a presents schematic of the flow zone in plane *(x,t)*. Flow of particle-free water is going on ahead of the concentration front $x=t$ (Table 1). Retention concentration is continuous across the front, while suspension concentration suffers shock. Suspension concentration just behind the front $c^-(t,t)$ is given by Eq. (23), presented in the second line of the Table 2. Suspension concentration in zone $x<t$ is expressed by Eq. (28) via $c^-(t,t)$ (second line in the Table 2). Retention concentration expressed via suspension concentration (Eq. (30)). Figs. 4b, 4c, 4d, and 4e present the solution in three moments.

Let us compare the type curves for linear, quadratic, and exponential forms of the suspension functions *f(c)*. Figs. 4b and 4c show that positions of the concentration front and values ahead of the front coincide for all models. Suspension concentrations in the zone behind the front decrease with time. Quadratic and modified RPs near to

the core entrance exhibit significantly higher slopes, which are typical for HERPs, than those by the traditional model. Fig. 4d shows the same breakthrough moment and zero earlier breakthrough values for all models. Comparing with the traditional model, quadratic and modified models accelerate particle retention, therefore suspension concentration for traditional model converges to the injected value slower. Fig. 4e presents pressure drop histories.

The case discussed corresponds to negative s_m, which usually appears by matching the laboratory tests, where filtration function increases during particle retention. For the case $s_m>0$, like in Langmuir's blocking function, BTCs tend to injected concentration, retention concentration tends to s_m, and the impedance curve is concave.

4. ANALYSIS OF LABORATORY-DATA MATCHING BY THE ANALYTICAL MODELS

This section presents results of treatment of the laboratory data using the traditional model (1, 3, 5) and the modified models with quadratic (15) and exponential-quadratic suspension functions (16); the corresponding analytical models are given by Eqs. (23), (28), and (30), respectively. Section 4.1 matches the laboratory data on pressure drop with varying flow rates and injected concentrations. Section 4.2 matches the tests with BTCs and RPs for different values of solute ionic strength and pH.

4.1. Matching pressure drop data

Ramachandran and Fogler [48], [49] injected charged polystyrene microspheres dispersed in water into multi-layer porous membranes. A significant number of overlapping pores and strong inter-pore connections allowed claiming the porous space structure as an irregular pore network. Zeta-potential measurements and DLVO calculations revealed strong electrostatic `particle-particle` and `particle-matrix` repulsion, so the capture mechanisms by aggregation and consequent aggregate straining were excluded. Size exclusion and straining were also excluded under the pores radii that highly exceed the particle radii. However, the experiments show substantial particle retention. The established mechanism causing particle retention under the test conditions was a flow-induced hydrodynamic bridging.

The experimental data matching by three models are performed using nonlinear least square method, which minimises the normalised deviation between the modelling and the experimental data [50]. So-called Trust-Region-Reflective optimisation algorithm solves the problem of quadratic-deviation minimisation. This

algorithm is implemented in Matlab. Besides high agreement with the experimental data, the model validation must include some predictive modelling, i.e. the number of tuned model coefficients must be smaller than the dimension (number of degrees of freedom) of the matched data array [43].

Figs. 5 and 6 present pressure drop measurements for three series per three tests each, with injection of particles with different rates and injected concentrations. The points $(J(t_k)-1)/t_k$, k=1, 2… as calculated from the laboratory data do not fit to straight lines for all the tests, but can be closely approximated by quadratic parabolas. So, each of the nine experimental curves has three degrees of freedom. Blue, green, and red curves are calculated using the modified, quadratic, and traditional models, respectively. Table 2 presents the tuned parameters and corresponding coefficients of determination.

Curves 1, 2, and 3 in Fig. 5 correspond to injected conventions 1235, 720, and 220 ppm, respectively. Four model parameters λ, s_m, β, and A or b are tuned from the tests with c^0= 1235 and 720 ppm. The predictive impedance curves based on those parameters is compared with the experimental data for injection with c^0=220 ppm. The values of coefficients of determination, presented in eighths column of Table 2 show significant deviation of the traditional model data from the experimental results. Using the quadratic model significantly improves the accuracy of matching. The modified model presents high agreement with the experimental data. High match of two curves, which have six degrees of freedom, by four-parametric model, and of one curve by pure prediction, validates the model developed. Moreover, high agreement with three data sets that correspond to different injected concentrations is achieved using the same values of four model parameters, i.e. the filtration and formation damage coefficients, maximum retention value, and constant A are independent of the injected concentration, which accords to the model assumptions.

Fig. 6a shows the results of tests with the same particles and porous media, as in the previous tests, but with varying injection rate. The formation damage coefficient is determined by the rock and retained particle geometry and is independent of the flow rate [51, 52]. Maximum retained concentration shows how many attached particles completely populate the rock surface, and s_m is also rate-independent. We assume that parameter A is independent of rate too. Therefore, the values β, s_m, and A are taken from tuning of three previous tests (these parameter values in lines 2 and 3 in Table 2 are the same). The only parameter tuned from three

306 curves in Fig. 6a is filtration coefficient λ. The curves 1, 2, and 3, and the coefficient of determination in
307 sevenths column of Table 2 show high deviation of the traditional model from the laboratory data. Using
308 quadratic model significantly improves the matching accuracy. The modified model provides high agreement.
309 So, for each test, three-parametric curve is matched by single parameter, which validates the model proposed.
310 Besides, matching of the three tests exhibit filtration coefficient that monotonically increases with velocity (Fig.
311 7a), which agrees with the classical filtration theory [15].
312 The laboratory data shown in Fig. 6b correspond to carboxylate particles of almost the same size as polystyrene
313 sulphate particles used in two previous series. Therefore, the value of maximum retention concentrations is taken
314 from the previous tests (the s_m-values in column 5 in Table 2 coincide for those three tests). Four parameters –
315 formation damage coefficient β, A-value, and two values of filtration coefficient – are determined from two
316 curves that correspond to velocities U=6.0·10^{-3} and 6.0·10^{-4} m/s. The third curve determines just one parameter,
317 which is the filtration coefficient. High agreement (Table 2) is achieved by tuning of nine-parametric data array
318 by tuning five parameters, which validates the model developed. The filtration coefficients increase with velocity
319 increase (Fig. 7b), as it is predicted by the classical filtration theory [25, 34].

320 **4.2. Matching the laboratory tests measuring the RPs and BTCs**

321 The large-scale models (9, 10) are diffusion / dispersion free, yielding suspension concentration discontinuity
322 across the front, while the concentration jumps in BTCs are smoothed by micro-scale dissipative processes.
323 Therefore, we treat the steep continuous growth of a BTC around its breakthrough time of 1 PVI as a
324 concentration jump. Suspension concentration before the breakthrough is zero. The jump occurs to continuously
325 growing BTC after the breakthrough. The areas between the continuous and discontinuous BTCs before and
326 after the breakthrough time are equal. This BTC-treatment procedure is analogous to matching of inner and outer
327 asymptotic expansions in the case of small diffusion and dispersion [43, 53-56].
328 Fig. 8 shows the laboratory data on injection of spherical fluorescent carboxylate-modified polystyrene latex
329 particles with diameter 1.0 μm into quartz sand packs with grain sizes 417-600 μm with length 20 cm, diameter
330 3.81 cm and salinity 1.0 mM for NaHCO3 [28]. The breakthrough concentration remains constant during the
331 test, so we chose $h(s)$=1. Filtration coefficient and A-value are determined from matching BTC and RP. Both
332 traditional and quadratic models significantly deviate from the laboratory data, while the modified model shows
333 high agreement. Change of filtration coefficient $h(s)$=1 to blocking function yields high value of maximum
334 retained concentration s_m and insignificant improvement of accuracy (Table 3, lines 2 and 3).
335 Fig. 9 shows the laboratory data where different salinities were injected [27]. Spherical soda lime glass beads
336 have been used for packing the column with length 20 cm and diameter 3.81 cm. Spherical fluorescent
337 carboxylate-modified polystyrene latex particles with diameter 1.1 μm were used. For each test, filtration
338 coefficient, maximum retained concentration, and A-value are determined by simultaneous matching BTC and
339 RP. Like in the previous test, traditional and quadratic models significantly deviate from the laboratory data,
340 while the modified model shows high agreement. So, for each test, four-parametric data arrays is matched by
341 three constants. Moreover, for both cases, the higher is the salinity the higher is the filtration coefficient (lines 3
342 and 4 in Table 3); this is explained by increase in electrostatic attraction as the solute ionic strength increases.
343 Fig. 10 presents the results of colloidal injection into porous column packed by quartz sand with 425-600 μm
344 [57]. The column length was 12 cm and diameter is 2.5 cm. BTCs and RPs with injection of biochar colloids are
345 shown in Figs. 8a – 8f for three different pH values. BTC shows the tendency of low decrease, so the model with

346 blocking filtration function (19, 20) was used. Three constants λ, s_m, and A were determined from each test. The
347 data are presented in Table 3.
348 Three tests, presented in Figs. 10a and 10b, 10c and 10d, 10e and 10f correspond to injection of biochar colloids,
349 biochar colloids coated by Bull serum albumin protein, and biochar colloids coated by Cytochrome protein,
350 respectively. For all tests, traditional model significantly deviates from the laboratory data; quadratic model
351 significantly improves the matching accuracy, and the modified model presents high agreement (columns 7 and
352 8 in Table 3). For all tests, the higher is the pH, the lower is the filtration coefficient, which is explained by
353 weakening of the electrostatic forces with increase in pH of the carrier fluid (Fig. 11).
354 Liang, et al. [58] injected graphene oxide colloid at two concentrations 10 and 100 ppm. The saturated transport
355 experiments have been performed in a stainless-steel column with 3 cm inner diameter and 12 cm length filled
356 with wet-packed quartz sand. The particle size varied between 0.5-2.0 μm. The grain size varied from 330 to 519
357 μm. The salinity of the injected colloid was 50 mM of NaCl. The rate $1.17 \cdot 10^{-4}$ m/s was maintained during all
358 injections. The tuned coefficients are given in Table 3, lines 14-17. Fig. 12 shows the coefficient of
359 determination by matching using the traditional and modified models.
360 For all tests, the tuned model coefficients λ, s_m, and A vary in the common intervals [3-5, 8, 15, 19-21, 23, 28,
361 35, 51, 52, 59-62]. The A-data presented in Tables 2 and 3 can be used for predictive modelling.

362 **5. DISCUSSION**

363 The motivation of this work stems from failure of the traditional DBF equations (1, 3, 5) to match simultaneously
364 BTC and PR for frequently encountered cases of HERPs. Therefore, the main aim of the work is a simplest possible
365 extension of the traditional model to reproduce HERPs. The present paper transforms the traditional model to Eqs.
366 (1, 3, 6) by introducing a new phenomenological suspension function $f(c)$. The extended model exhibits HERPs.
367 The numerous laboratory data sets can be closely fitted and predicted using suspension function $f(c)=\lambda \cdot c \cdot exp(A \cdot c^2)$,
368 which adds just one extra parameter into the traditional model.
369 *The role of high suspension concentrations* Fig. 12 shows the matching accuracy by the traditional and modified
370 models for different injected concentrations. The traditional model significantly deviates from the laboratory data,

while the modified model exhibits high match. Ramachandran and Fogler [48] used high-concentration colloids, which correspond to right side of the figure. Lower concentrations correspond to tests by Liang, et al. [58]. Fig. 12 indicates that the accuracy of matching by the traditional model decreases with increase of injected concentrations, for three sets of the above-mentioned tests. It substantiates the logic for extending the analogy to active mass law, given by Eq. (5), to large suspension concentrations, Eq. (6). Fig. 12 also shows that the accuracy of match by the modified model increases with injected concentration, i.e. the developed model modification achieves the aim of precise predictions at high suspension concentrations.

Physics interpretation of the modified model Let us explain how high suspension concentration transforms the capture rate by traditional mathematical model to that by the modified model. "High concentration" means that it is comparable with the vacancy concentration. In the case of bridging, increase of suspension concentration increases the retention rate faster than it does in the traditional model, where the rate is proportional to suspension concentration – a bridge across pore throat yields significant acceleration of the capture and plugging (Fig. 1).

The same effect takes place for size exclusion with incomplete pore plugging, where all forthcoming particles entering the throat after size exclusion of the first particle are trapped. In this case, the first size exclusion acts as a centre of condensation, yielding hyper-exponential deposition. Incomplete pore plugging corresponds to widely spread internal cake at deep bed filtration (Fig. 1).

Another case corresponds to fines attachment in pore throats, yielding decreasing in throat radii and size exclusion acceleration. The higher is the carrier water velocity, the higher is the probability of particle collision with grain. It explains predominant attachment in pore throats, where the particle speed significantly exceeds the mean velocity. Under the attachment in pore throats, the increase in suspension concentration yields acceleration of size exclusion rate faster than that expressed by the traditional model [15].

Tufenkji and Elimelech [25] and Li, et al. [27] link HERPs with existence of secondary minimum in DLVO potential and favourable and unfavourable attachment conditions, along with distributed properties of colloidal particles.

Validity of the assumptions and of the extended model Failure of the traditional model to match HERPs is usually attributed to distributed properties of the suspended particles [10, 24, 33, 34]. We show that the proposed model

(6) can be obtained by averaging of the suspension-colloidal flow with distributed filtration coefficient, which in turn can be attributed to distributed size, shape, surface charge and other particle properties (Appendix A). Therefore, the proposed model implicitly accounts for the particle property distribution. Moreover, calculations by Eqs. (A12-A16) show that, the wider is the continuous filtration coefficient distribution the higher is the second derivative of suspension function, and the higher is the deviation between the RPs predicted by the traditional and modified models [63]. The same applies to a binary colloid – the higher is the ratio between the filtration coefficients of two populations, the higher is the deviation between the two models. This averaging strongly supports the modified model and explains HERPs by heterogeneity of the colloidal flux.

The experimental verification of the above claim would include injection of binary colloids with various properties in identical porous columns. To the best of our knowledge, those laboratory data are not available in the literature.

We propose an alternative reason for deviation between the laboratory data and traditional modelling that is high suspension concentration, which promotes the competition between the suspended particles for the vacancies. At high suspension concentrations, where the particles compete for vacancies, the events of particle appearance near the vacancies are not independent, so Eq. (5) is not valid. The calculations show that the higher is second derivative of the suspension function (or the higher is A-value in expression (16)), the higher is the deviation between the extended and traditional models.

Fig. 5 shows that deviation between the curve generated by the traditional model and laboratory data for large injected concentration 1235 ppm is significantly higher than that for low injected concentration 220 ppm; the modified model (16) highly matches the experimental points for both tests. Eighth column in Table 2 presents the coefficient of determination for matching by three models. The matching accuracy by the traditional model decreases as the injected concentration increases (rows ten, seven, and two). For the modified model, R^2 exceeds 0.979 for all injected concentrations (second, fifth, and eighth rows).

Comparison between columns 7 and 8 in Tables 2 and 3 show that using the exponential-quadratic suspension function yields closer match and prediction than using the quadratic suspension function.

Figs. 7a and 7b shows the velocity-dependency of the tuned filtration coefficient as obtained by matching the laboratory data presented in Figs. 5 and 6a, respectively. The higher is the velocity the higher is the filtration coefficient, which is explained by high particle-grain collision probability at high particle speeds [15].

Fig. 11 shows the pH-dependency of the tuned filtration coefficient; the corresponding laboratory data are presented in Fig. 10. The higher is the pH the weaker is the electrostatic particle-rock attraction, and the lower is the capture probability [15, 64]. Fig. 9 shows the results of injections at different ionic strengths. Lines 3 and 4 in Table 3 show that the higher is the ionic strength the larger is the filtration coefficient, which is explained by higher electrostatic particle-grain attraction at higher salinity.

Different formulations of laboratory tests Field-scale predictions of colloidal and nano-suspension transport are based on the core-scale data. The corresponding coreflood tests are usually performed in laboratories, but also on-site in the fields. The main quality requirements to corefloods are precision of measurements, robust and simple equipment, and cost efficiency. Pressure drop measurements are precise and cost effective, requiring simple and robust pump and pressure transducers (Fig. 2). Measurements of breakthrough concentrations require cumbersome particle counters and usually yield high data scattering during particle counting; using particle counters in field conditions is problematic. Retention profile measurements require sophisticated computational tomography (CT), which is feasible at laboratory conditions only. The exception is *post mortem* retention profile determination by dividing the core into small sections and performing chemical analysis of the rock matter.

Therefore, the most widely spread data in the literature are pressure drop [65]; BTCs can be found for numerous tests; RPs are less available [35, 61, 62]. In section 4, we treat the pressure-drop tests, and also the tests with measurements of BTCs and RPs.

The justification for the extended model validity can be enforced by treatment of more complete laboratory data sets. One possibility would be simultaneous measurements of BTC and pressure drop, and post-mortem RPs. Besides, computational tomography can deliver RPs at several moments [66, 67]. Another extended laboratory formulation would be pressure measurements in a few intermediate core points [51]; the so-called three-point pressure method can substitute BTC measurements. This explains the advantage of three-point-pressure method, which measures pressure in several core points, and allows avoiding the concentration measurements.

Phenomenological modified model vs averaged multicomponent model The modified model with exponent-quadratic suspension function contains just one extra parameter if compared with the traditional model. We found that this model successfully matches and predicts numerous laboratory data sets. However, A is an effective phenomenological parameter, which makes it difficult to analyse its dependencies of the colloid and rock properties.

On the contrary, averaging of multicomponent colloidal transport yields multi-parametric suspension functions. The suspension function for binary colloid contains two extra parameters – λ_1/λ_2 and C_1^0. The ternary modified model contains four extra parameters, which makes the model more complex. More laboratory data are required for unique determination of the model parameters. However, tuning of multicomponent models allows for downscaling [63], i.e. it provides concentrations for all populations. This is not the case for phenomenological exponent-quadratic suspension function.

The limitation of the upscaled model (9, 10) is the same filtration function for all populations; yet the suspension function is specific for each population. The analytical model (23, 28, 30) used for matching contains Langmuir's blocking filtration function. However, the proposed extended model contains any arbitrary filtration and suspension functions $h(s)$ and $f(c)$ and is not limited to those assumptions.

Inverse problem for the modified model 1D flow problem (4) for the traditional model (1, 3, 5) allows for exact solution, yielding simple iterative algorithms for inverse problems [52, 59, 60]. BTC allows determination of the filtration function $h(s)$ [59]. RP also determines $h(s)$ [52]. The inverse solution $h(s)$ is stable with respect to small perturbations of RPs, i.e. the inverse problem is well-posed, while the problem of $h(s)$-determination from BTC is ill-posed and requires regularisation.

Those properties of the inverse problems for the traditional model are illustrated by red curves in Fig. 4. The breakthrough moment t=1 PVI cannot be distinguished at the scale 300 PVI, so Fig. 4d shows the BTC after the breakthrough only. The figure exhibits almost steady-state suspension concentration in the flow zone behind the front (Fig. 4b) and constant breakthrough concentration (Fig. 4d), which is the case for the linear system where $h(s)$=1. However, contrary to the linear system, impedance growth is non-linear. Eq. (31) shows that impedance is determined by the RP. Non-linear $J(t)$ suggests that $h(s)$-variation affects RP significantly stronger than the

BTCs. This explains why the problem of filtration function determination from the BTC is ill-posed, while the inverse problem using RP is well-posed.

Pressure drop data defines formation damage function $k(s)$. For all three above-mentioned inverse problems, the stable solution exists and is unique. Therefore, the inverse problem for the modified model (1, 6) is formulated as determination of formation damage and suspended functions from BTC and RP.

The solution for $h(s)=1$ and any arbitrary suspension function yields steady-state suspension concentration behind the concentration front (see formulae (B3) and (B9) in Appendix B). Almost steady-state suspension concentrations in the zone behind the front (Fig. 4b) and constant breakthrough concentration (Fig. 4d) for blue and green curves suggest that for the modified model, $h(s)$-variation also affects RP significantly stronger than the BTCs.

Applications The upscaling procedure, presented in Appendix A can be extended for any 3D flow, where the permeability is not affected by the retained particles, i.e. where the formation damage coefficient is zero. Transferring 3D micro-scale equations (A3, A4) into the curvilinear coordinates associated with streamlines and the averaging yield 3D equations (9, 10) [41, 68]. The analytical model (23, 28, 30) can be implemented into quasi 3D streamline simulator. So, the laboratory-based model with the tuned A-value can be used for reservoir behaviour prediction in numerous engineering areas listed in the beginning of introduction. High match and prediction by the modified model allow recommending it for treatment of laboratory data on colloidal and nano-suspension transport and for laboratory-based field-scale forecasts.

Extension of DBF models for two-phase flow in under-saturated porous media accounts for particle capture on the interface, i.e. water-air menisci. The models contain equations for dynamics of the interphase surface, derived by Shapiro [69], [70].

6. CONCLUSIONS

Development of the modified deep bed filtration equations, derivation of the analytical model, and matching the experimental data allow drawing the following conclusions.

The analogy between the particle capture and chemical reaction, expressed by action mass law with the reactive species activities used for high-concentration species, allows introducing nonlinear suspension function into the

capture rate equation. Introduction of one-parametric exponential-quadratic suspension function into the traditional deep bed filtration model allows successfully matching hyper-exponential retention profiles, simultaneously with the breakthrough curves.

The close match and prediction have been achieved for the tests with pressure drop measurements, and also for the tests where the breakthrough curves and retention profiles have been measured. The tuned model parameters vary in their common intervals. The filtration coefficient, as tuned from numerous laboratory tests, is a monotonically increasing function of velocity and of ionic strength, and is a monotonically decreasing function of pH, which agrees with the traditional filtration theory.

For the above-mentioned experiments, the number of degree of freedom of the laboratory data exceeds the number of tuned model parameters by one and six. Therefore, high agreement between the laboratory and modelling data validates the modified model for colloidal-suspension flow in porous media.

The modified model is derived from the micro-scale colloidal transport equations with distributed parameters, which supports the modified model and explains HERPs by heterogeneity of the colloidal flux.

Appendix A. Averaging of multicomponent colloidal flow with size-distributed particles

This Appendix derives the extended model (1, 3, 6) by upscaling the micro-scale DBF equations, where the particles are distributed by any property like radius, shape factor, z-potential, density, surface charge, etc. Let r be a vector of particle properties $r=(r_1,r_2...r_n)$ and use the following notation for integral over n properties:

$$\int_0^\infty u(r,x,t)\,dr = \int_0^\infty\int_0^\infty ...\int_0^\infty u(r_1,r_2...r_n,x,t)\,dr_1dr_2...dr_n\,. \tag{A1}$$

Average suspension and retention concentrations are

$$c(x,t)=\int_0^\infty C(r,x,t)\,dr,\;\; s(x,t)=\int_0^\infty S(r,x,t)\,dr\,. \tag{A2}$$

Mass balance for suspended and retained particles is valid for each population with given property r [63]

$$\frac{\partial\left(\phi C(r,x,t)+S(r,x,t)\right)}{\partial t}+U\frac{\partial C(r,x,t)}{\partial x}=0 \tag{A3}$$

We consider filtering of different particle populations in the same rock, so the filtration function is the same for all populations, but suspension function depends on the particle radius

$$\frac{\partial S(r,x,t)}{\partial t}=h\left(\int_0^\infty S(r,x,t)\,dr\right)F\left(C(r,x,t),r\right)U\,. \tag{A4}$$

We use dimensionless parameters (8) with

$$c^0=\int_0^\infty C^0(r)\,dr,\; C\to\frac{C}{c^0},\; S\to\frac{S}{\phi c^0},\; F(C,r)\to\frac{F(C,r)L}{c^0},$$
$$C^0(r)\to\frac{C^0(r)}{c^0},\; r\to\frac{rc^0}{\int_0^\infty rC^0(r)\,dr}\,, \tag{A5}$$

System (A3, A4) takes the form

$$\frac{\partial\left(C(r,x,t)+S(r,x,t)\right)}{\partial t}+\frac{\partial C(r,x,t)}{\partial x}=0\,, \tag{A6}$$

$$\frac{\partial S(r,x,t)}{\partial t}=h(s)F\left(C(r,x,t),r\right)\,. \tag{A7}$$

System of two equations (A6, A7) subject to initial and boundary conditions (4) that correspond to colloid injection into clean porous bed defines two unknowns *C(r,x,t)* and *S(r,x,t)*. The micro-scale system (A6, A7) contains the model phenomenological functions of filtration and suspension

$$h = h(s),\ F = F(C,r),\ r = (r_1, r_2 ... r_n)\ . \tag{A8}$$

Using timely variable τ and the corresponding mapping (18) in system (A6, A7) yields

$$\frac{\partial S(r,x,\tau)}{\partial \tau} + \frac{\partial C(r,x,\tau)}{\partial x} = 0\,, \tag{A9}$$

$$\frac{\partial S(r,x,\tau)}{\partial \tau} = h(s) F\left(C(r,x,\tau), r\right). \tag{A10}$$

Substituting Eq. (A10) in Eq. (A9) yields

$$\frac{\partial C(r,x,\tau)}{\partial x} = -h(s) F\left(C(r,x,\tau), r\right). \tag{A11}$$

As it follows from clean-bed initial conditions and characteristic form of Eq. (A11), $C=S=0$ for $\tau<0$.

Separating variables in Eq. (A11) at $\tau>0$ yields

$$\frac{\partial G(C(r),r)}{\partial x} = -h\left(\int_0^{\infty} S(r,x,\tau)\,dr\right),\ G(C(r),r) = \int_{C^0(r)}^{C(r)} \frac{du}{F(u,r)}\,. \tag{A12}$$

Right hand side of Eq. (A12) is independent of *r*, so its value for any arbitrary *r* is equal to that at the mean radius $r=(1,1\ldots1)$:

$$\frac{\partial G(C(r),r)}{\partial x} = \frac{\partial G(C(1),1)}{\partial x}\,. \tag{A13}$$

Integrate both sides of Eq. (A13) in *x* characteristic line $\tau=\tau_0$. Functions *G(C(r), r)* are equal zero for any $r>0$ at $x=0$, so the integration constant is also zero. Therefore, along the characteristic line $\tau=\tau_0$, the following equality takes place:

$$\tau = \tau_0 :\ G(C(r),r) = G(C(1),1)\,. \tag{A14}$$

By using the inverse function in Eq. (A14), express concentration *C(r,x,t)* via concentration *C(1,x,t)*:

549 $$C(r) = g(C(1), r),\ g = G^{-1}(C, r).$$ (A15)

550 Now averaged concentration $c(x, \tau)$ can be expressed via the concentration of average-size particle $C(1, x, \tau)$, and

551 *vice versa,* using the inverse function:

552 $$c = \int_0^\infty g(C(1), r)dr,\ C(1) = a(c).$$ (A16)

553 Integrate both sides of Eq. (A11) in r and take r-independent function h out of the integral

554 $$\frac{\partial c(x, \tau)}{\partial x} = -h(s(x, \tau)) \int_0^\infty F(C(r, x, \tau), r)\, dr.$$ (A17)

555 Integral in right hand side of Eq. (A17) accounting for expression (A15) becomes

556 $$\int_0^\infty F(C(r, x, \tau), r)\, dr = \int_0^\infty F(g(C(1, x, \tau), r), r)\, dr = e(C(1, x, \tau)) = e(a(c(x, \tau))) = f(c).$$ (A18)

557 Eq. (A10) accounting for averaged relationship (A18) becomes

558 $$\frac{\partial s(x, \tau)}{\partial \tau} = h(s(x, \tau))\, f(c).$$ (A19)

559 The averaged suspension function $f(c)$ is the result of upscaling of micro-scale suspension function $F(C,r)$ that is

560 individual for each population.

561 Integration of both parts of Eq. (A9) in r yields

562 $$\frac{\partial s}{\partial \tau} + \frac{\partial c}{\partial x} = 0\ .$$ (A20)

563 The derived macro-scale system (A19, A20) contains the model phenomenological functions of filtration $h(s)$

564 and of suspension $f(c)$. The upscaled suspension function depends not only of the suspension functions for each

565 population, but also on the injected concentrations $C^0(r)$.

566 So, the modified model (9, 10) can be obtained by averaging of micro-scale system with multiple distributed

567 particle properties, where the property distributions are independent.

568 *Example* Consider binary colloid described by the traditional DBF model with constant filtration coefficients λ_1

569 and λ_2, and C_1^0 is the injected concentration of the first component in the overall colloid. Assuming low retained

concentrations for both components, the filtration functions are considered to be equal one. As it follows from Eq. (A18), suspension function is [63]

$$f(c)=\lambda_1\left[c_1+\frac{\lambda_2}{\lambda_1}(c-c_1)\right], \tag{A21}$$

where expression $c_1=c_1(c)$ follows from Eq. (A16):

$$c=c_1+C_2^{\,0}\left(\frac{c_1}{C_1^{\,0}}\right)^{\frac{\lambda_1}{\lambda_2}}. \tag{A22}$$

Appendix B. Analytical models for different suspension functions

For the case of traditional model (1, 3-5) where $f=\lambda c$, taking integrals in Eqs. (23) and (28) yields the explicit formulae for solution [14, 42, 45]

$$c(x,t)=\frac{1}{1-e^{-\frac{\lambda}{s_m}(t-x)}+e^{\left[-\frac{\lambda}{s_m}(t-x)+\lambda x\right]}}, \tag{B1}$$

$$s(x,t)=\frac{s_m\left(1-e^{-\frac{\lambda}{s_m}(t-x)}\right)}{1-e^{-\frac{\lambda}{s_m}(t-x)}+e^{\left[-\frac{\lambda}{s_m}(t-x)+\lambda x\right]}}. \tag{B2}$$

The particular case of traditional model corresponds to low retention concentrations $s<<s_m$, where the filtration function $h(s)$ (the term in brackets in Eq. (5)) is equal one:

$$c(x,t)=e^{-\lambda x}, \tag{B3}$$

$$s(x,t)=\lambda_0(t-x)\mathrm{e}^{-\lambda x}. \tag{B4}$$

Integration in Eq. (23) for the case of quadratic suspension function $f(c)=\lambda(c+bc^2)$, yields explicit expression for suspension concentration just behind the concentration front $x=t$:

$$c^{-}(x,x)=\frac{e^{-\lambda x}}{1+b\left(1-e^{-\lambda x}\right)},\ x=t. \tag{B5}$$

Integration in Eq. (28) yields transcendental equation for suspension concentration

$$(1+b)\ln\frac{c(x,t)}{c^{-}(x,x)}+\ln\frac{1-c^{-}(x,x)}{1-c(x,t)}-b\ln\left|\frac{bc(x,t)+1}{bc^{-}(x,x)+1}\right|=\frac{\lambda}{s_m}(1+b)(x-t). \quad \text{(B6)}$$

In the case of the modified model with exponential-quadratic suspension function $f(c)=\lambda c\exp(Ac^2)$, Eqs. (23) and (28) become

$$ei(-A)-ei\left(-A\left[c^{-}(x,x)\right]^2\right)=2\lambda x,\ ei(y)=-\int_{-y}^{\infty}\frac{e^{-u}}{u}du; \quad \text{(B7)}$$

$$\int_{c^{-}(x,x)}^{c(x,t)}\frac{e^{-Au^2}du}{\lambda(1-u)u}=\frac{1}{s_m}(t-x). \quad \text{(B8)}$$

The particular case of formulae (B8) corresponds to low retention concentrations $s<<s_m$, where the filtration function $h(s)=1$ in Eq. (6). The solution is obtained by tending s_m to infinity in formulae (B8):

$$ei(-A)-ei\left(-A\left[c(x,t)\right]^2\right)=2\lambda x,\ ei(y)=-\int_{-y}^{\infty}\frac{e^{-u}}{u}du. \quad \text{(B9)}$$

Consider the particle capture by bridging, where n particles simultaneously plug one pore (Fig. 1). By active mass law for small suspension concentrations, the suspension function has power-law form $f(c)=\lambda c^n$. Performing integration in Eq. (23) yields:

$$c^{-}(x,x)=\left(1-(1-n)\lambda x\right)^{\frac{1}{1-n}},\ n\neq 1,\ x=t, \quad \text{(B10)}$$

$$\int_{c^{-}(x,x)}^{c}\frac{du}{\lambda(1-u)u^n}=\frac{1}{s_m}(t-x)\ . \quad \text{(B11)}$$

For the case of power-law suspension function with threshold value $f(c)=\lambda(c-c_{cr})^n$

$$c^{-}(x,x)=\begin{cases}c_{cr}+\left(1-(1-n)\lambda x\right)^{\frac{1}{1-n}}, & n\neq 1\\ c_{cr}+e^{-\lambda x}, & n=1\end{cases},\ x=t, \quad \text{(B12)}$$

$$\int_{c^{-}(x,x)}^{c(x,t)}\frac{du}{\lambda(1-u)(u-u_{cr})^n}=\frac{1}{s_m}(t-x). \quad \text{(B13)}$$

For all the above-discussed cases, expressions for retained concentration follows from Eq. (30).

Acknowledgements. Authors are grateful to Prof. C. Alexander (Russian Gubkin Oil-Gas University) for fruitful discussions of the current paper in particular, and generally for extremely encouraging co-operation since early 80-th. Many thanks are due to Dr. T. Carageorgos for improvement of the text.

NOMENCLATURE

A	-	coefficient
b	-	coefficient
C	-	distributed particle concentration, L^{-4}, m^{-4}
c^0	-	injected particle concentration
c	-	total suspended particle concentration
J	-	Impedance
k	-	permeability, L^2, m^2
L	-	core length, L, m
p	-	pressure, $ML^{-1}T^{-2}$, N m^{-2}
p_0	-	initial pressure, $ML^{-1}T^{-2}$, N m^{-2}
P	-	dimensionless pressure
S	-	distributed deposit concentration, L^{-4}, m^{-4}
s	-	total deposit concentration
s_m	-	dimensionless concentration of the capture vacancies
t	-	time, T, s
U	-	Darcy flow velocity, LT^{-1}, ms^{-1}
x	-	coordinate, L, m

Greek Letters

μ	-	viscosity, $ML^{-1}T^{-1}$, kg m^{-1} s^{-1}
ϕ	-	porosity
β	-	formation damage coefficient
λ	-	filtration coefficient, L^{-1}, m^{-1}
Δp	-	pressure drop across the core, $ML^{-1}T^{-2}$, N m^{-2}
ΔP	-	dimensionless pressure drop across the core

REFERENCES

[1] R. Anders, C.V. Chrysikopoulos, Evaluation of the Factors Controlling the Time-Dependent Inactivation Rate Coefficients of Bacteriophage MS2 and PRD1, Environ. Sci. Technol. 40 (2006) 3237-3242.

[2] M. Asraf-Snir, V. Gitis, Tracer studies with fluorescent-dyed microorganisms—A new method for determination of residence time in chlorination reactors, Chem. Eng. J. 166 (2011) 579-585.

[3] M.D. Becker, Y. Wang, K.D. Pennell, L.M. Abriola, A multi-constituent site blocking model for nanoparticle and stabilizing agent transport in porous media, Environmental Science: Nano 2 (2015) 155-166.

[4] C. Bianco, T. Tosco, R. Sethi, A 3-dimensional micro-and nanoparticle transport and filtration model (MNM3D) applied to the migration of carbon-based nanomaterials in porous media, J. Contam. Hydrol. 193 (2016) 10-20.

[5] C.V. Chrysikopoulos, N.P. Sotirelis, N.G. Kallithrakas-Kontos, Cotransport of Graphene Oxide Nanoparticles and Kaolinite Colloids in Porous Media, Transp. Porous Med. 119 (2017) 181-204.

[6] Y. Li, Y. Wang, K.D. Pennell, L.M. Abriola, Investigation of the Transport and Deposition of Fullerene (C60) Nanoparticles in Quartz Sands under Varying Flow Conditions, Environ. Sci. Technol. 42 (2008) 7174-7180.

[7] J.F. Schijven, S.M. Hassanizadeh, R.H. de Bruin, Two-site kinetic modeling of bacteriophages transport through columns of saturated dune sand, J. Contam. Hydrol. 57 (2002) 259-279.

[8] V. Sygouni, C.V. Chrysikopoulos, Characterization of TiO2 nanoparticle suspensions in aqueous solutions and TiO2 nanoparticle retention in water-saturated columns packed with glass beads, Chem. Eng. J. 262 (2015) 823-830.

[9] E. Timchak, V. Gitis, A combined degradation of dyes and inactivation of viruses by UV and UV/H2O2, Chem. Eng. J. 192 (2012) 164-170.

[10] N. Tufenkji, M. Elimelech, Spatial distributions of Cryptosporidium oocysts in porous media: Evidence for dual mode deposition, Environ. Sci. Technol. 39 (2005) 3620-3629.

[11] E.D. Vecchia, M. Luna, R. Sethi, Transport in Porous Media of Highly Concentrated Iron Micro- and Nanoparticles in the Presence of Xanthan Gum, Environ. Sci. Technol. 43 (2009) 8942-8947.

[12] Y. Wang, Y. Li, H. Kim, S.L. Walker, L.M. Abriola, K.D. Pennell, Transport and Retention of Fullerene Nanoparticles in Natural Soils, Journal of Environmental Quality 39 (2010) 1925-1933.

[13] Y. Wang, M.D. Becker, V.L. Colvin, L.M. Abriola, K.D. Pennell, Influence of residual polymer on nanoparticle deposition in porous media, Environ. Sci. Technol. 48 (2014) 10664-10671.

[14] J. Herzig, D. Leclerc, P.L. Goff, Flow of suspensions through porous media—application to deep filtration, Ind. Eng. Chem. 62 (1970) 8-35.

[15] M. Elimelech, J. Gregory, X. Jia, Particle deposition and aggregation: measurement, modelling and simulation, Butterworth-Heinemann 2013.

[16] H. Yuan, A. Shapiro, Z. You, A. Badalyan, Estimating filtration coefficients for straining from percolation and random walk theories, Chem. Eng. J. 210 (2012) 63-73.

[17] A. Shapiro, H. Yuan, Application of stochastic approaches to modelling suspension flow in porous media, Statistical Mechanics and Random Walks: Principles, Processes and Applications, Nova Science Publishers, Incorporated2012, pp. 1-36.

[18] P. Bedrikovetsky, Upscaling of stochastic micro model for suspension transport in porous media, Transp. Porous Med. 75 (2008) 335-369.

[19] S.A. Bradford, M. Bettahar, J. Simunek, M.T. Van Genuchten, Straining and attachment of colloids in physically heterogeneous porous media, Vadose Zone Journal 3 (2004) 384-394.

[20] H. Zhang, G. Malgaresi, P. Bedrikovetsky, Exact solutions for suspension-colloidal transport with multiple capture mechanisms, Int J. Non-linear Mech. 105 (2018) 27-42.

675 [21] V. Gitis, I. Rubinstein, M. Livshits, G. Ziskind, Deep-bed filtration model with multistage deposition kinetics,
676 Chem. Eng. J. 163 (2010) 78-85.

677 [22] S.H. Fogler, Elements of chemical reaction engineering, Prentice Hall 2016.

678 [23] F. Kuhnen, K. Barmettler, S. Bhattacharjee, M. Elimelech, R. Kretzschmar, Transport of iron oxide colloids in
679 packed quartz sand media: monolayer and multilayer deposition, J. Colloid Interface Sci. 231 (2000) 32-41.

680 [24] M. Tong, W.P. Johnson, Colloid Population Heterogeneity Drives Hyperexponential Deviation from Classic
681 Filtration Theory, Environ. Sci. Technol. 41 (2007) 493-499.

682 [25] N. Tufenkji, M. Elimelech, Breakdown of colloid filtration theory: Role of the secondary energy minimum and
683 surface charge heterogeneities, Langmuir 21 (2005) 841-852.

684 [26] O. Albinger, B.K. Biesemeyer, R.G. Arnold, B.E. Logan, Effect of bacterial heterogeneity on adhesion to uniform
685 collectors by monoclonal populations, FEMS Microbiol. Lett. 124 (1994) 321-326.

686 [27] X. Li, T.D. Scheibe, W.P. Johnson, Apparent Decreases in Colloid Deposition Rate Coefficients with Distance of
687 Transport under Unfavorable Deposition Conditions: A General Phenomenon, Environ. Sci. Technol. 38 (2004) 5616-
688 5625.

689 [28] X. Li, W.P. Johnson, Nonmonotonic Variations in Deposition Rate Coefficients of Microspheres in Porous Media
690 under Unfavorable Deposition Conditions, Environ. Sci. Technol. 39 (2005) 1658-1665.

691 [29] X. Jiang, M. Tong, R. Lu, H. Kim, Transport and deposition of ZnO nanoparticles in saturated porous media,
692 Colloids and Surfaces A: Physicochemical Eng. Aspects 401 (2012) 29-37.

693 [30] D. Wang, M. Paradelo, S.A. Bradford, W.J. Peijnenburg, L. Chu, D. Zhou, Facilitated transport of Cu with
694 hydroxyapatite nanoparticles in saturated sand: effects of solution ionic strength and composition, Water Res. 45 (2011)
695 5905-5915.

696 [31] D. Kasel, S.A. Bradford, J. Šimůnek, M. Heggen, H. Vereecken, E. Klumpp, Transport and retention of multi-
697 walled carbon nanotubes in saturated porous media: Effects of input concentration and grain size, Water Res. 47 (2013)
698 933-944.

699 [32] D. Wang, W. Zhang, X. Hao, D. Zhou, Transport of biochar particles in saturated granular media: effects of
700 pyrolysis temperature and particle size, Environ. Sci. Technol. 47 (2013) 821-828.

701 [33] E. Goldberg, M. Scheringer, T.D. Bucheli, K. Hungerbühler, Critical assessment of models for transport of
702 engineered nanoparticles in saturated porous media, Environ. Sci. Technol. 48 (2014) 12732-12741.

703 [34] N. Tufenkji, M. Elimelech, Deviation from the classical colloid filtration theory in the presence of repulsive DLVO
704 interactions, Langmuir 20 (2004) 10818-10828.

705 [35] S.A. Bradford, J. Simunek, M. Bettahar, M.T. van Genuchten, S.R. Yates, Modeling colloid attachment, straining,
706 and exclusion in saturated porous media, Environ. Sci. Technol. 37 (2003) 2242-2250.

707 [36] S.A. Bradford, M. Bettahar, Concentration dependent transport of colloids in saturated porous media, J. Contam.
708 Hydrol. 82 (2006) 99-117.

709 [37] H. Bai, L. Lassabatere, E. Lamy, Colloid Transport in Aggregated Porous Media with Intra-and Interaggregate
710 Porosities, Industrial & Engineering Chemistry Research 57 (2018) 6553-6567.

711 [38] H. Yuan, A.A. Shapiro, Modeling non-Fickian transport and hyperexponential deposition for deep bed filtration,
712 Chem. Eng. J. 162 (2010) 974-988.

[39] A.A. Shapiro, Elliptic equation for random walks. Application to transport in microporous media, Physica A: Statistical Mech. its Applic. 375 (2007) 81-96.

[40] A. Einstein, Investigations on the theory of Brownian motion. Translated by AD Cowper, 1905.

[41] P. Bedrikovetsky, Mathematical theory of oil and gas recovery: with applications to ex-USSR oil and gas fields, Springer Science & Business Media 2013.

[42] A. Polyanin, V. Zaitsev, Handbook of nonlinear partial differential equations. Chapman & Hall/CRC Press, Boca Raton, (2012).

[43] A. Polyanin, V.V. Dil′man, Methods of modeling equations and analogies in chemical engineering, CRC Press, Boca Raton 1994.

[44] M. Margules, Über die Beziehung zwischen Barometerschwankungen und Konitinuitätsgleichung, JA Barth 1904.

[45] A.D. Polyanin, A.V. Manzhirov, Handbook of mathematics for engineers and scientists, CRC Press, Boca Raton 2006.

[46] L. Shampine, Solving hyperbolic PDEs in MATLAB, Appl. Num. Anal. Comp. Math. 2 (2005) 346-358.

[47] L.F. Shampine, Two-step Lax–Friedrichs method, Appl. Math. Lett. 18 (2005) 1134-1136.

[48] V. Ramachandran, H.S. Fogler, Plugging by hydrodynamic bridging during flow of stable colloidal particles within cylindrical pores, J. Fluid Mech. 385 (1999) 129-156.

[49] V. Ramachandran, R. Venkatesan, G. Tryggvason, H.S. Fogler, Low Reynolds number interactions between colloidal particles near the entrance to a cylindrical pore, J. Colloid Interface Sci. 229 (2000) 311-322.

[50] T.F. Coleman, Y. Li, An interior trust region approach for nonlinear minimization subject to bounds, SIAM J. Optim. 6 (1996) 418-445.

[51] P. Bedrikovetsky, D. Marchesin, F. Shecaira, A. Souza, P. Milanez, E. Rezende, Characterisation of deep bed filtration system from laboratory pressure drop measurements, Journal of Petroleum Science and Engineering 32 (2001) 167-177.

[52] A.C. Alvarez, G. Hime, D. Marchesin, P.G. Bedrikovetsky, The inverse problem of determining the filtration function and permeability reduction in flow of water with particles in porous media, Transp. Porous Med. 70 (2007) 43-62.

[53] A. Polyanin, EqWorld, The World of Mathematical Equations. http://eqworld.ipmnet.ru/, 2004 (accessed 10/09/2019).

[54] J.P. Guerrero, L. Pimentel, T. Skaggs, M.T. Van Genuchten, Analytical solution of the advection–diffusion transport equation using a change-of-variable and integral transform technique, Int. J. Heat Mass Transfer 52 (2009) 3297.

[55] J.P. Guerrero, E. Pontedeiro, M.T. van Genuchten, T. Skaggs, Analytical solutions of the one-dimensional advection–dispersion solute transport equation subject to time-dependent boundary conditions, Chem. Eng. J. 221 (2013) 487-491.

[56] G. Ziskind, H. Shmueli, V. Gitis, An analytical solution of the convection–dispersion–reaction equation for a finite region with a pulse boundary condition, Chem. Eng. J. 167 (2011) 403-408.

[57] W. Yang, S.A. Bradford, Y. Wang, P. Sharma, J. Shang, B. Li, Transport of biochar colloids in saturated porous media in the presence of humic substances or proteins, Environ. Pollut. 246 (2019) 855-863.

[58] Y. Liang, S.A. Bradford, J. Simunek, E. Klumpp, Mechanisms of graphene oxide aggregation, retention, and release in quartz sand, Sci. Total Environ. 656 (2019) 70-79.

[59] A. Alvarez, P. Bedrikovetsky, G. Hime, A. Marchesin, D. Marchesin, J. Rodrigues, A fast inverse solver for the filtration function for flow of water with particles in porous media, Inverse Probl. 22 (2005) 69.

[60] A. Alvarez, G. Hime, J. Silva, D. Marchesin, Analytic regularization of an inverse filtration problem in porous media, Inverse Probl. 29 (2013) 025006.

[61] S.A. Bradford, S. Torkzaban, A. Shapiro, A theoretical analysis of colloid attachment and straining in chemically heterogeneous porous media, Langmuir 29 (2013) 6944-6952.

[62] V. Gitis, C. Dlugy, G. Ziskind, S. Sladkevich, O. Lev, Fluorescent clays—similar transfer with sensitive detection, Chem. Eng. J. 174 (2011) 482-488.

[63] P. Bedrikovetsky, Y. Osipov, L. Kuzmina, G. Malgaresi, Exact Upscaling for Transport of Size-Distributed Colloids, Water Resour. Res. 55 (2019) 1011-1039.

[64] J.N. Israelachvili, Intermolecular and surface forces, Academic press 2015.

[65] K.C. Khilar, H.S. Fogler, Migrations of fines in porous media, Springer Science & Business Media 1998.

[66] C.H. Arns, A comparison of pore size distributions derived by NMR and X-ray-CT techniques, Physica A: Statistical Mech. its Applic. 339 (2004) 159-165.

[67] C.H. Arns, M.A. Knackstedt, N.S. Martys, Cross-property correlations and permeability estimation in sandstone, Physical Review E 72 (2005) 046304.

[68] S. Oladyshkin, M. Panfilov, Streamline splitting between thermodynamics and hydrodynamics in a compositional gas–liquid flow through porous media, Comptes Rend. Mécan. 335 (2007) 7-12.

[69] A.A. Shapiro, Two-phase immiscible flows in porous media: The Mesocopic Maxwell–Stefan approach, Transp. Porous Med. 107 (2015) 335-363.

[70] A.A. Shapiro, Mechanics of the separating surface for a two-phase co-current flow in a porous medium, Transp. Porous Med. 112 (2016) 489-517.

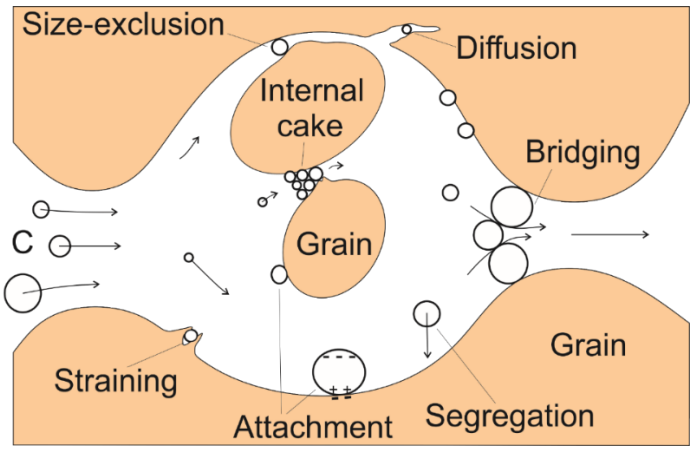


Fig. 1. Multiple capture mechanisms during colloidal and nano-suspension transport in porous media.

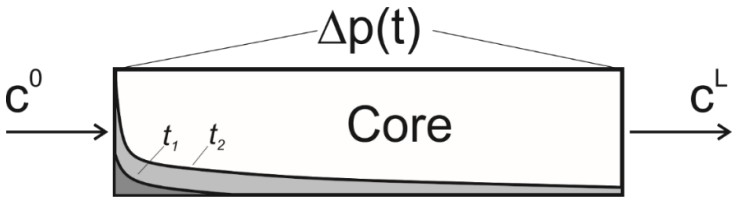
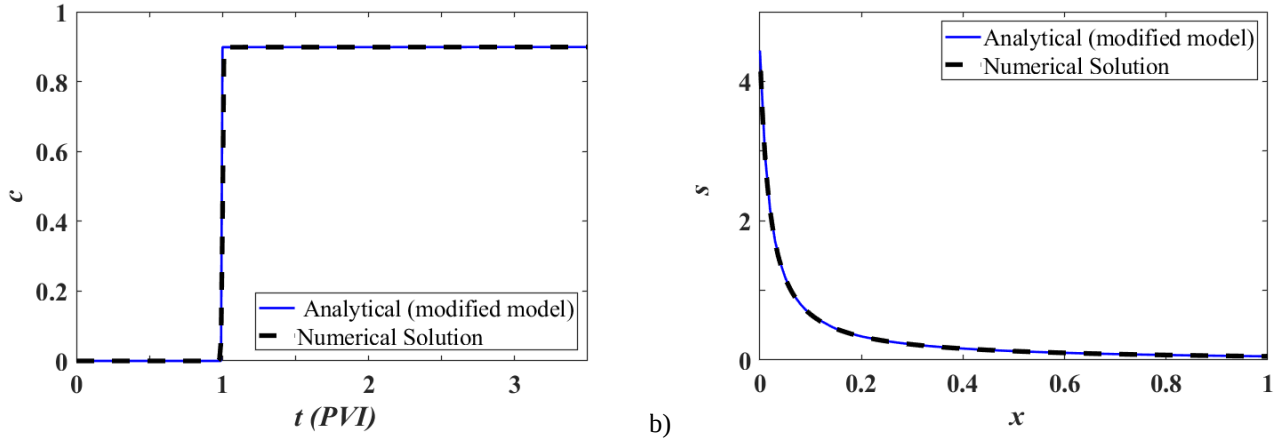


Fig. 2. Schematic of laboratory test on colloidal and nano-suspension flow in porous media. Where c^0 corresponds to an injected colloidal concentration, while c^L represents the concentration at the outlet, c^L is measured continually during suspension injection and it is used to plot the breakthrough curve. $\Delta p(t)$ is the pressure drop across the core and is also measured continually during colloidal injection. The pressure drop data is used to plot the impedance curve over time. During colloidal injection, some particles are captured into the core, these captured particles are named retention profile $s(x,t)$, and it can be measured over time as shown by the continuous line inside the core.



a) b)

Fig. 3. Validation of the analytical model by comparison between the exact and numerical solutions.

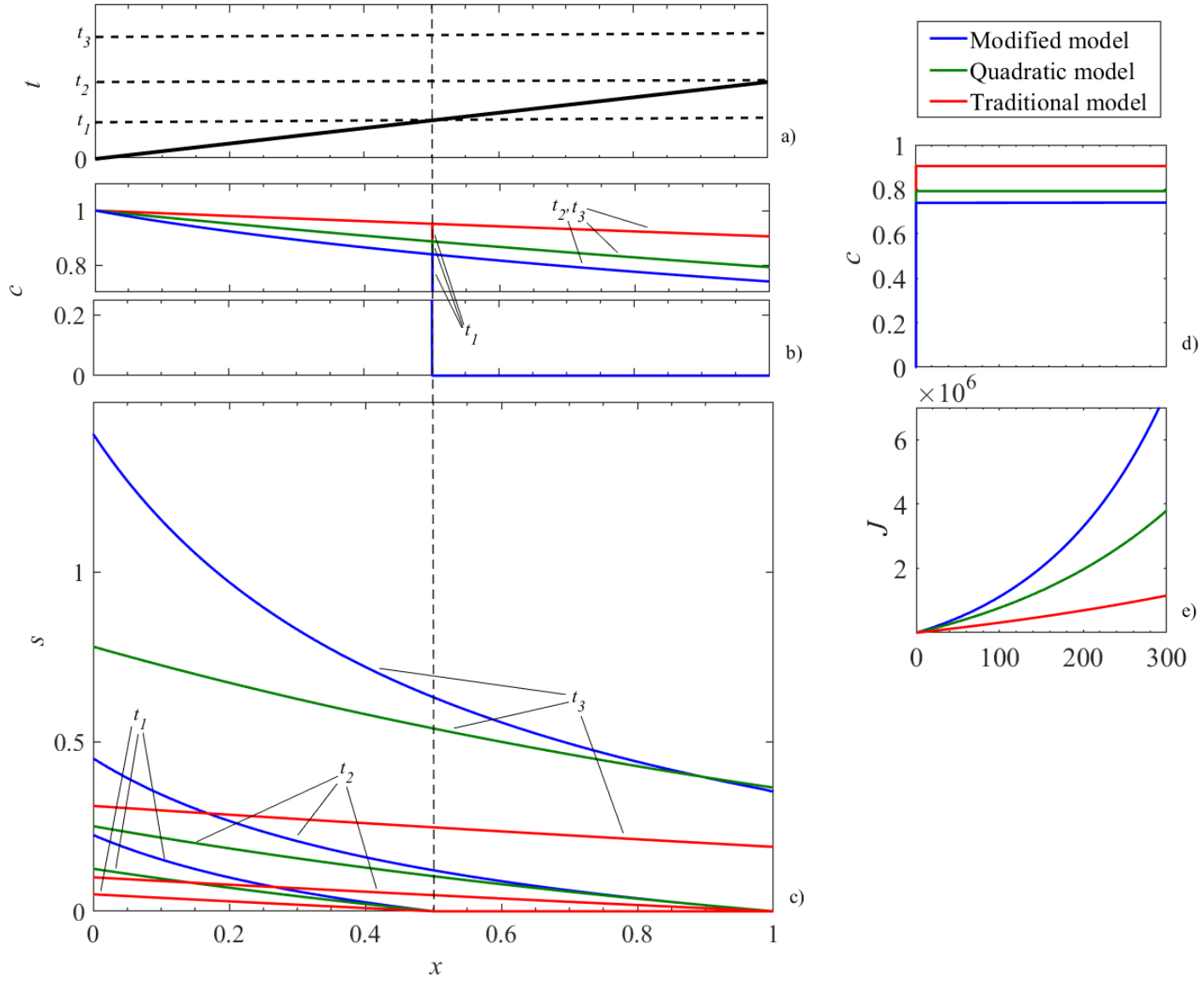


Fig. 4. Type curves from analytical modelling by the modified, quadratic, and traditional models: (a) concentration front trajectory in (x,t)-plane; (b) suspension concentration profiles at three moments; (c) retention profiles; (d) breakthrough curves. The calculations were performed for c^0=1000 ppm; ϕ=0.3; λ=001 1/m; s_m=-0.015 1/m^3, A=15·10^5, b=1.5·10^4; β=10^5.

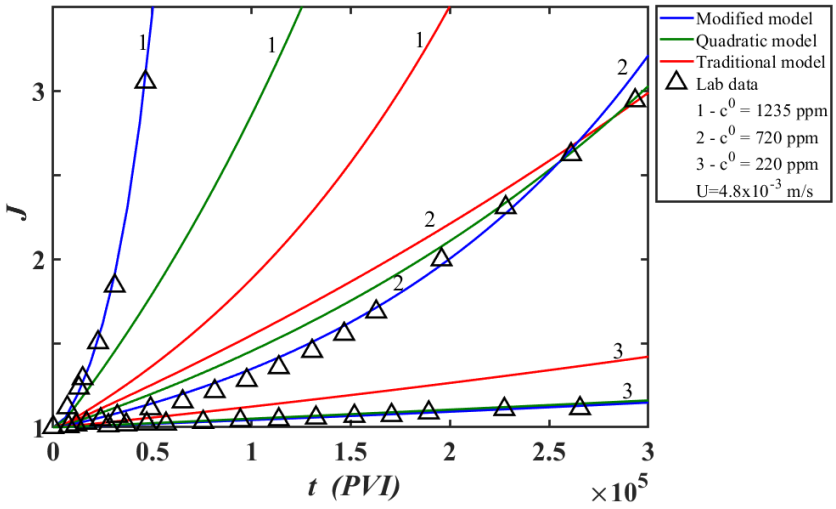


Fig. 5. Pressure drop growth during suspension flows under different injected concentrations.

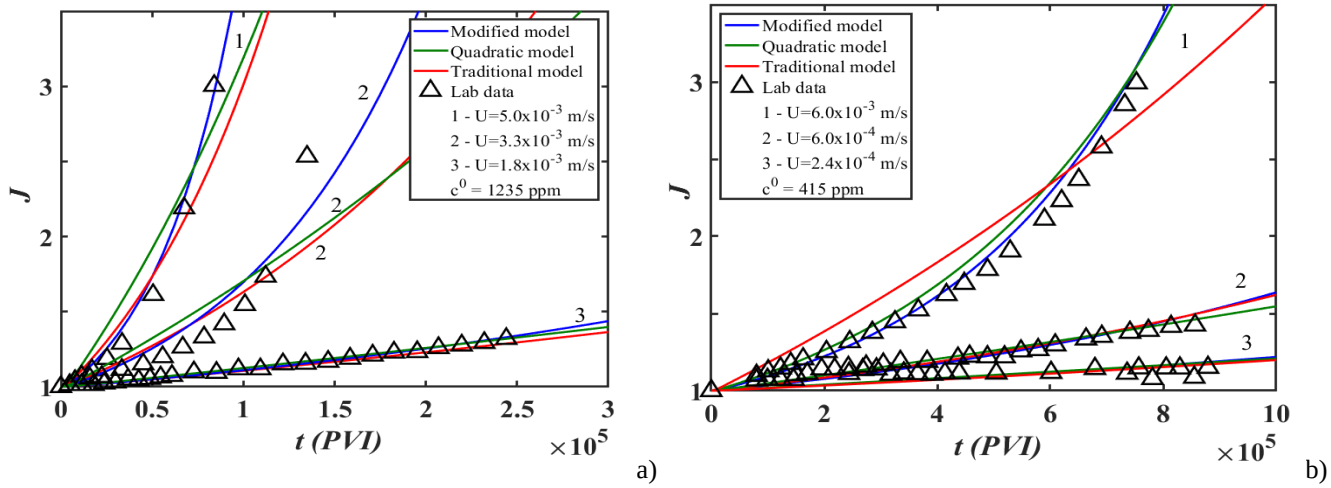


Fig. 6. Increase in pressure drop for suspension flow under different velocities at different injection concentrations: (a) c^0=1235 ppm; (b) c^0=415 ppm.

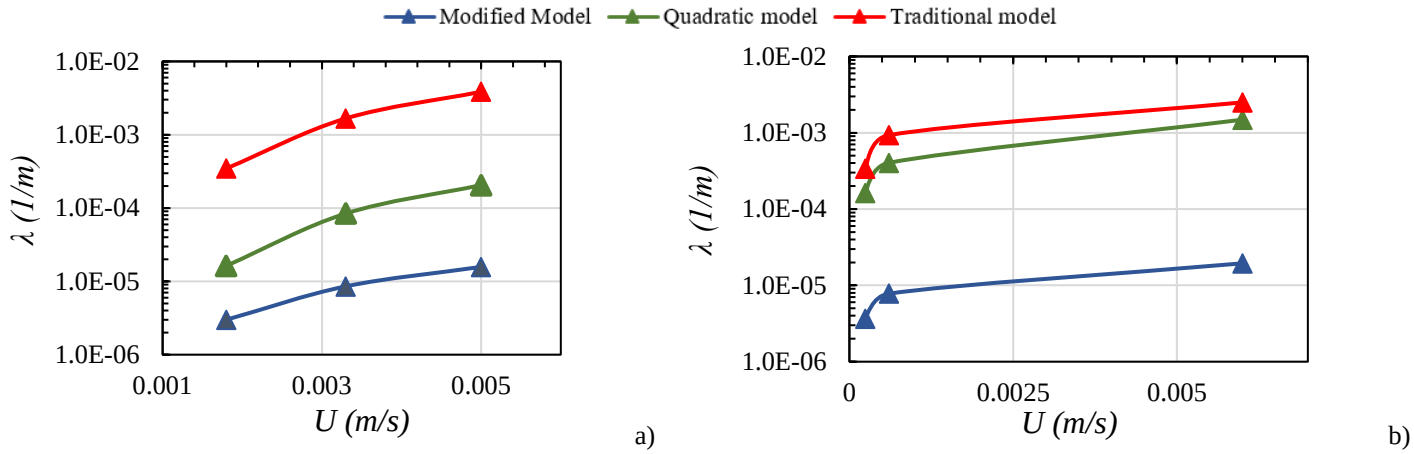


Fig. 7. Velocity-dependency for filtration coefficient λ as obtained from matching the laboratory data using the traditional, quadratic and modified (exponential-quadratic) models: (a) based on the injection data with c^0= 1235 ppm shown in Fig. 4a; (b) based on injection with c^0= 415 ppm, Fig. 4b.

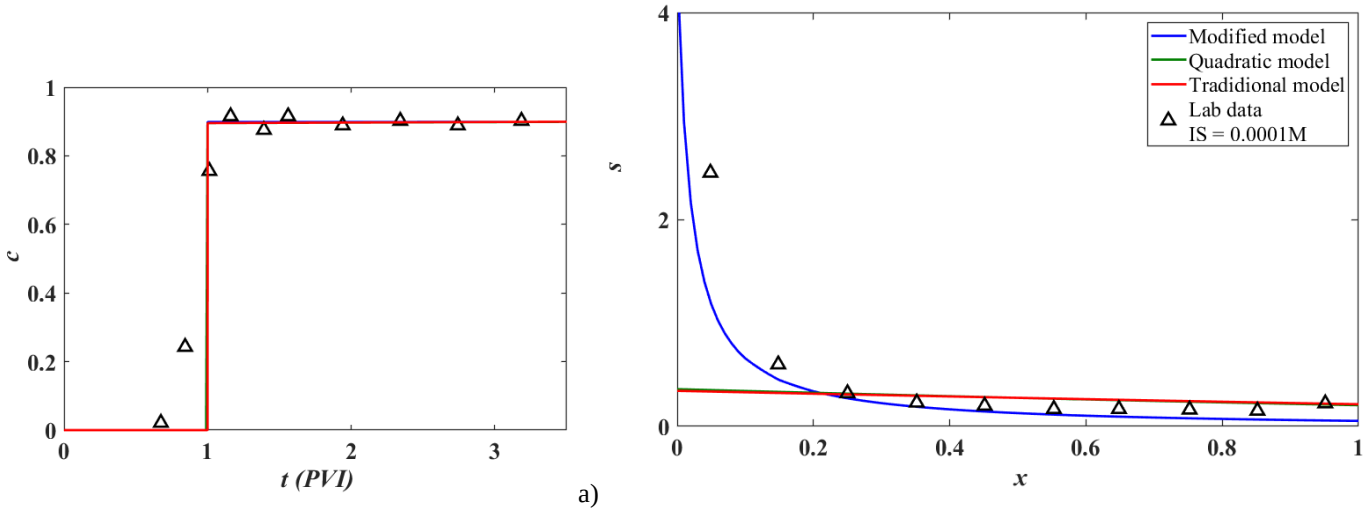


Fig. 8. Matching of laboratory data on colloidal flow by the traditional, quadratic and modified models: (a) breakthrough concentration; (b) retention concentration profile at *IS*=0.001M and flow rate $9.26 \cdot 10^{-5}$ m/s.

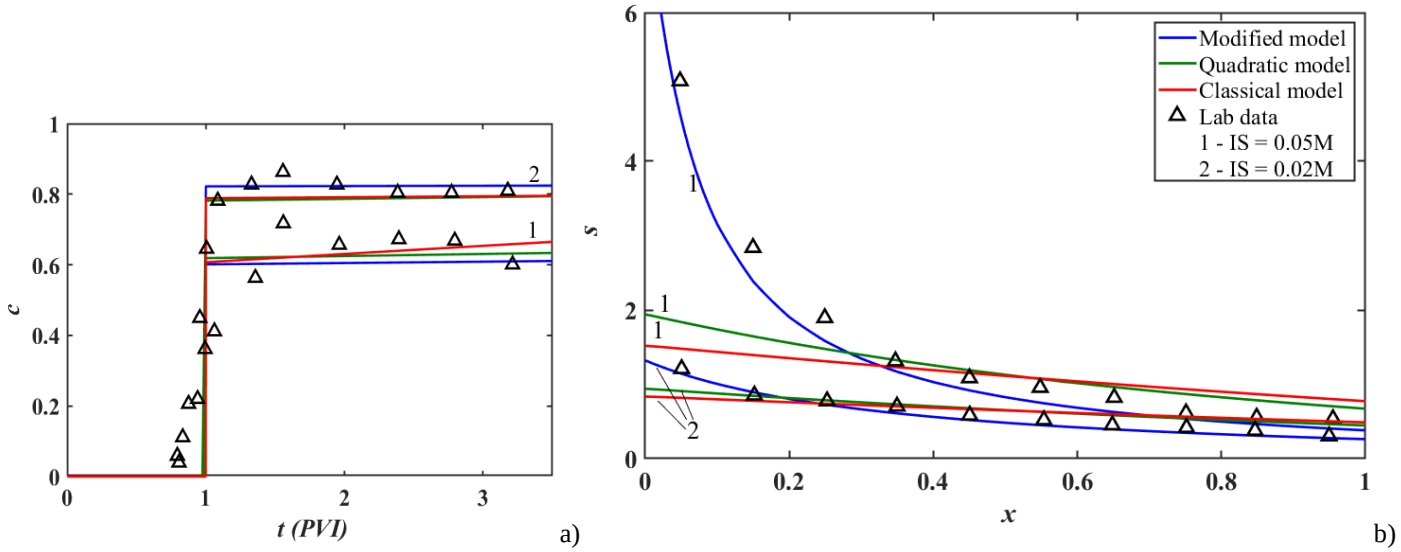


Fig. 9. Matching of laboratory data on colloidal flow by the traditional, quadratic and modified models at jamming ratio *j*=0.017 – 0.012 and different salinities: (a) breakthrough curves BTC for *IS*=0.02M; (b) retention profiles RP for *IS*=0.02M; (c) BTC for *IS*=0.05M; (d) RP for *IS*=0.05M.

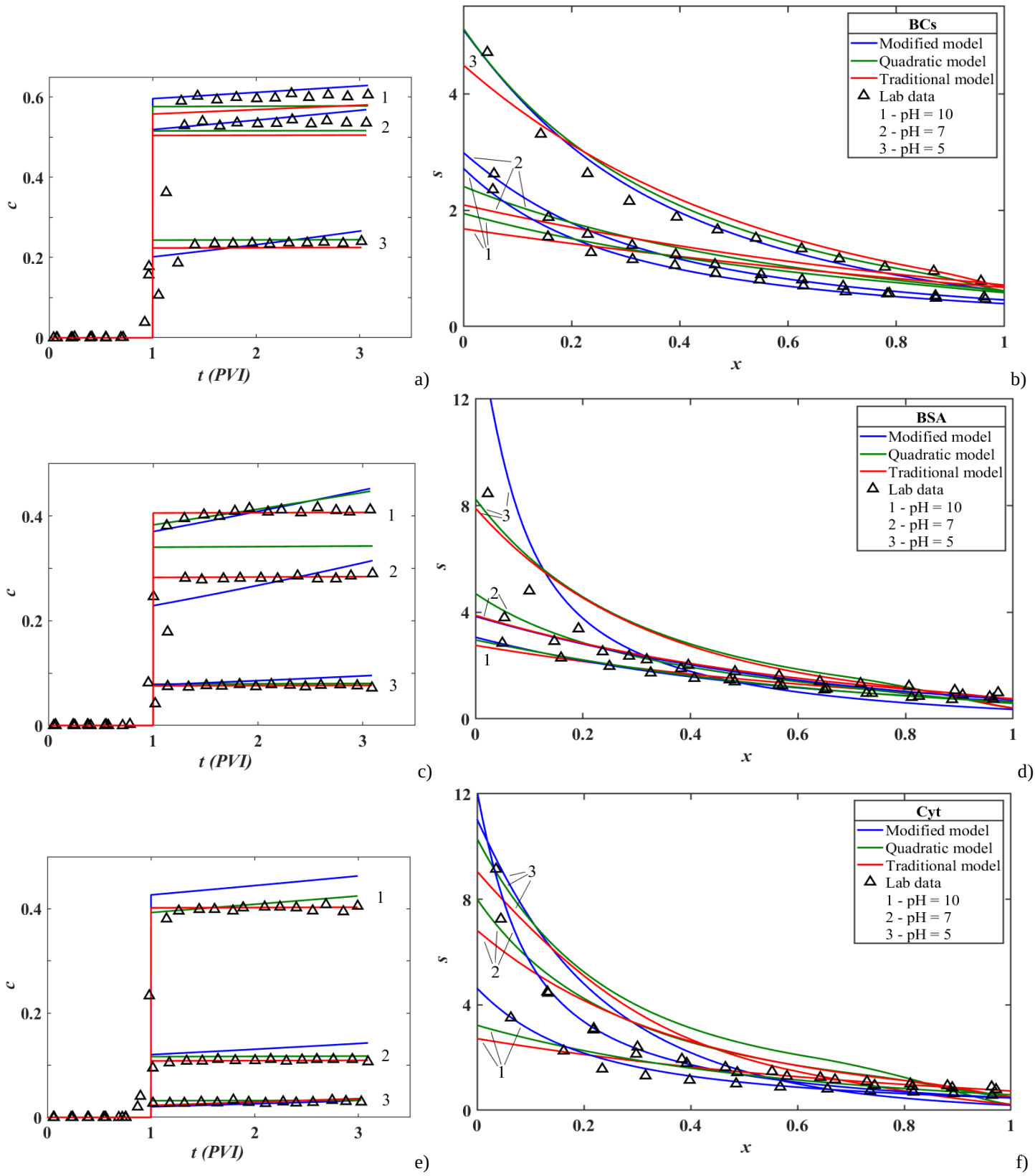


Fig. 10. Matching the tests with three different colloids at different pH-values: (a,b) biochar colloids (BCs); (c, d) biochar colloids coated by Bull serum albumin protein (BSA); (e, f) biochar colloids coated by Cytochrome protein (Cyt).

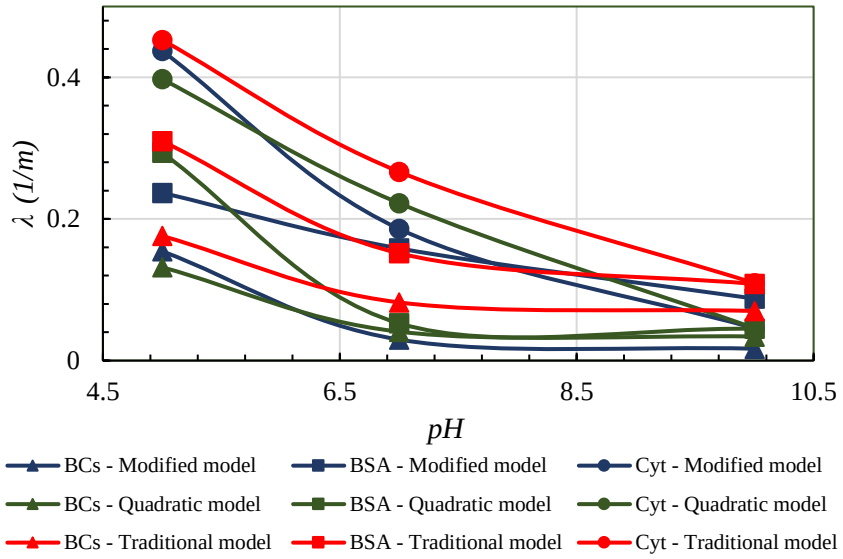


Fig. 11. Dependency of filtration coefficient of pH as obtained by tuning the laboratory data from Fig. 10.

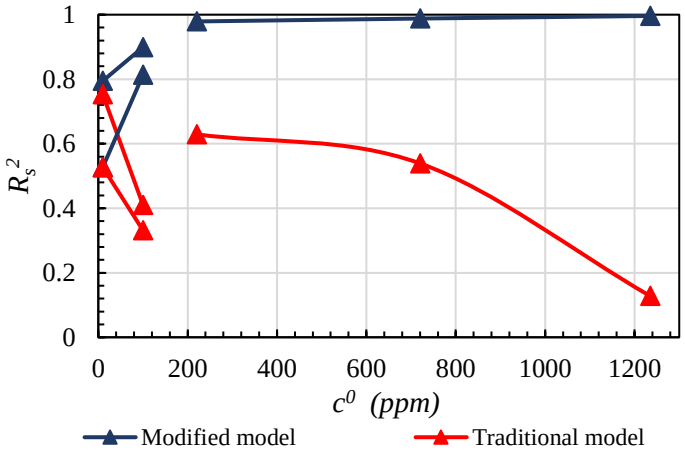


Fig. 12. Deviation between the traditional model and the experimental data increases with increase in the injected concentration, while for modified model the deviation decreases.

Table 1: Exact solution for 1D particle transport for any arbitrary suspension function *f(c)*

Flow zone	*c(x,t)*	*s(x,t)*
x>t>0	*0*	*0*
0>t>x	$\int_{c^-(x,x)}^{1} \frac{du}{f(u)} = x$ $\int_{c^-(x,x)}^{c(x,t)} \frac{du}{(1-u)\,f(u)} = \frac{1}{s_m}(t-x)$	$s(x,t) = s_m\left[\frac{c(x,t)-c^-(x,x)}{1-c^-(x,x)}\right]$

Table 2: Tuned parameters for the modified, quadratic and traditional models using the pressure drop data

Laboratory study	Test conditions	$A \times 10^{-5}$	$b \times 10^{-4}$	s_m [L^{-3}] Modified Quadratic Traditional models	λ [1/m] Modified Quadratic Traditional models	β Modified Quadratic Traditional models	R_p^2
Ramachandran and Fogler [48] (Fig. 5)	c^0=1235 720, and 220 ppm $U = 4.8\times10^{-3}$ m/s	13.494	4.00	-3.080e-8 -29.156e-6 -4.608e-6	1.306e-4 21.831e-3 21.870e-4	2.772e6 0.223e6 0.502e6	0.996 – tuning 0.524 – tuning 0.128 – tuning 0.988 – tuning 0.753 – tuning 0.539 – tuning 0.979 – prediction 0.902 – prediction 0.629 – prediction
Ramachandran and Fogler [48] (Fig. 6a)	$U = 5.0\times10^{-3}$ 3.2×10^{-3} and 1.8×10^{-3} m/s c^0=1235 ppm	13.494	4.00	-3.080e-8 -29.156e-6 -4.608e-6	0.1576e-4 2.0550e-4 38.5609e-4 0.0855e-4 0.8418e-4 16.6701e-4 0.030e-4 0.1632e-4 3.4678e-4	2.772e6 0.223e6 0.502e6	0.995 – tuning 0.725 – tuning 0.501 – tuning 0.935 – tuning 0.675 – tuning 0.604 – tuning 0.946 – tuning 0.936 – tuning 0.973 – tuning
Ramachandran and Fogler [48] (Fig. 6b)	$U = 6.0\times10^{-3}$ 6.0×10^{-4} and 2.4×10^{-4} m/s c^0=415 ppm	-0.0071	0.4841	-3.080e-8 -29.156e-6 -4.608e-6	0.1944e-4 1.4828e-3 24.989e-4 0.0778e-4 4.0311e-4 9.2850e-4 0.0366e-4 1.6193e-4 3.3772e-4	11.1685e6 0.1001e6 0.1038e6	0.996 – tuning 0.949 – tuning 0.805 – tuning 0.955 – tuning 0.936 – tuning 0.901 – tuning 0.802 – prediction 0.758 – prediction 0.744 – prediction

847 Table 3: Tuned model parameters by matching BTCs and RPs for modified, quadratic and traditional models

Laboratory study	Test conditions		$A \times 10^{-5}$	$b \times 10^{-4}$	s_m [L^{-3}] Modified Quadratic Traditional models	λ [1/m] Modified Quadratic Traditional models	R_c^2	848 R_s^2
Li and Johnson [28] (Fig. 7)	c^0= 193 ppm *IS* = 0.001 M		5826.73	1.062	8.22e-4 1.82e-4 2.7e-4	3.28e-9 9.50e-2 1.134	0.901 0.901 0.902	0.911 0.163 0.101
Li, et al. [27] (Fig. 8a,b)	c^0= 193 ppm *IS* = 0.02 M		939.62	9.824	1.46e-3 5.23e-4 1.02e-3	0.057 0.070 1.187	0.791 0.806 0.790	0.941 0.728 0.580
Li, et al. [27] (Fig. 8c,d)	c^0= 193 ppm *IS* = 0.05 M		1012.10	1.346	1.07e-3/ 1.19e-3/ 3.60e-4	0.395 0.790 2.494	0.842 0.886 0.860	0.928 0.329 0.134
Yang, et al. [57] (Fig. 10a,b)	c^0= 50 ppm *IS* = 0.001 M pH=10		8921.2	2.4874	1.14E-04 2.97E-03 3.07E-04	0.016752 0.03402 0.070068	0.955 0.950 0.956	0.981 0.797 0.658
	pH=7		7526	2.6418	1.04E-04 9.81E-03 8.82E-03	0.02964 0.040788 0.082164	0.948 0.948 0.946	0.994 0.890 0.764
	pH=5		3180	1.1108	1.75E-04 9.93E-03 1.07E-02	0.154368 0.131784 0.176004	0.932 0.879 0.911	0.980 0.969 0.938
Yang, et al. [57] (Fig. 10c,d)	*BSA* c^0= 50 ppm *IS* = 0.001 M pH=10		2980.4	5.0968	1.18E-04 1.41E-04 1.02E-02	0.087552 0.04488 0.10818	0.961 0.955 0.947	0.996 0.991 0.954
	pH=7		1424	5.0338	1.52E-04 4.05E-03 7.72E-03	0.158448 0.052632 0.15156	0.947 0.748 0.938	0.965 0.928 0.964
	pH=5		6835.6	0.2106	4.23E-04 8.99E-03 1.17E-02	0.236904 0.293532 0.309828	0.892 0.921 0.922	0.928 0.844 0.843
Yang, et al. [57] (Fig. 10e,f)	*Cyt* c^0= 50 ppm *IS* = 0.001 M pH=10		7391.2	4.6432	1.75E-04 2.65E-04 8.73E-03	0.045708 0.045864 0.109404	0.808 0.862 0.878	0.960 0.800 0.681
	pH=7		6795.6	0.8242	4.00E-04 9.69E-03 1.17E-02	0.186036 0.222288 0.266712	0.911 0.923 0.957	0.917 0.875 0.864
	pH=5		2291.2	0.2106	3.60E-04 8.98E-03 5.57E-04	0.437436 0.397524 0.452808	0.882 0.774 0.814	0.907 0.727 0.829
Yang, et al. [57]	d_g= 590 μm	10 ppm	2500.1	-	9.66E-05 - 1.10E-04	0.13704 - 0.14854	0.8861 - 0.8693	0.7947 - 0.7529
		100 ppm			5.50E-04 - 5.49E-04	0.12600 - 0.20915	0.9178 - 0.9207	0.8993 - 0.4102
	d_g= 330 μm	10 ppm	2999.8	-	7.60E-05 - 1.20E-4	0.28801 - 0.29867	0.6321 - 0.6112	0.5270 - 0.5271
		100 ppm			6.01E-04 - 7.96E-04	0.14416 - 0.26143	0.7954 - 0.7814	0.8133 - 0.3315

5.2 A Transport of high-concentration colloids with two particle-capture mechanisms

Gabriel Malgaresi, Yuri Osipov, Liudmila Kuzmina, Pavel Bedrikovetsky

Water Resources Research Journal (to be submitted)

Statement of Authorship

Title of Paper	Transport of high-concentration colloids with two particle-capture mechanisms
Publication Status	☐ Published ☐ Accepted for Publication ☐ Submitted for Publication ☑ Unpublished and Unsubmitted work written in manuscript style
Publication Details	Malgaresi, G., Osipov, Y., Kuzmina, L. and Bedrikovetsky, P., 2019. Transport of high-concentration colloids with two particle-capture mechanisms.

Principal Author

Name of Principal Author (Candidate)	Gabriel Malgaresi
Contribution to the Paper	Development of the analytical model. Tuned all sets of experiments. Helped with the analysis of the tuned parameters, sensitivity analysis and preparation of the manuscript.
Overall percentage (%)	60%
Certification:	This paper reports on original research I conducted during the period of my Higher Degree by Research candidature and is not subject to any obligations or contractual agreements with a third party that would constrain its inclusion in this thesis. I am the primary author of this paper.
Signature	Date 23/10/2019

Co-Author Contributions

By signing the Statement of Authorship, each author certifies that:

i. the candidate's stated contribution to the publication is accurate (as detailed above);

ii. permission is granted for the candidate in include the publication in the thesis; and

iii. the sum of all co-author contributions is equal to 100% less the candidate's stated contribution.

Name of Co-Author	Yuri Osipov
Contribution to the Paper	Development and derivation of the mathematical model, analysis of the results, and mathematical properties of the model
Signature	Date 28/10/2019

Name of Co-Author	Liudmila Kuzmina
Contribution to the Paper	Helped with the derivation of the mathematical model and analysis of the results.
Signature	Date 28/10/2019

Name of Co-Author	Pavel Bedrikovetsky
Contribution to the Paper	Problem formulation and supervision of the development of the whole work.
Signature	Date 23/10/2019

Transport of high-concentration colloids with two particle-capture mechanisms

Gabriel Malgaresi[1], Yuri Osipov[2], Liudmila Kuzmina[3], Pavel Bedrikovetsky[1]

1- University of Adelaide, Australia

2- Moscow State University of Civil Engineering, Russia

3- National Research University Higher School of Economics, Russia

Abstract

Understanding of complex behaviour of colloidal-suspension fluxes in porous media is extremely important for numerous technologies in environmental, water-resource, and chemical engineering. The work aims transformation of the traditional deep-bed filtration model that reproduces breakthrough curves (BTCs) with stabilisation below the injected level, and hyper-exponential retention profiles (HERPs). Based on the upscaling of multicomponent colloidal flow and the analogy with chemical-reaction active-mass law, we propose transport equations with nonlinear suspension function and binary-blocking filtration function. One-dimensional (1D) flow problem that corresponds to laboratory tests on colloidal transport in porous columns allows for exact analytical solution. The developed model reproduces HERPs and BTCs stabilised at the level below the injected value. Close match and prediction have been observed in 24 laboratory tests. Moreover, the dependencies of the tuned model coefficients are explained by Derjaguin-Landau-Verwey-Overbeek (DLVO) theory.

1. Introduction

Colloidal, suspension, and nanoparticle transport in natural reservoirs and engineered porous columns occurs in numerous areas of environmental, water-resource, chemical, and petroleum engineering. The decision making in those areas rely on laboratory studies, experimental data treatment by the mathematical models, and laboratory-based large-scale modelling predictions. This explains the intensive development of mathematical modelling in industrial waste disposal in subterranean water, fresh water storage in aquifers, management of water resources, contamination of aquifers by viruses and bacteria, and vadoze zone hydrology [*Bradford et al.*, 2011; *Rabinovich et al.*, 2013; *Tartakovsky et al.*, 2017].

The contemporary mathematical models for colloidal transport in porous media account for simultaneous attachment and detachment of particles, attachment sites of the primary and secondary

DLVO energy minima, diffusion and hydrodynamic dispersion, and consequent permeability decline [*Bradford et al.*, 2003; *Elimelech et al.*, 2013; *Hilpert and Johnson*, 2018].

Mass balance equation accounts for suspended and retained particles

$$\phi \frac{\partial c}{\partial t} + U \frac{\partial c}{\partial x} = -\frac{\partial s}{\partial t} \tag{1}$$

where ϕ is the porosity, c and s are the concentrations of suspended and retained particles, respectively, and U is Darcy's velocity. Suspended concentration is a number of particles per unit volume of the carrier water, while retained concentration is a number of particles per unit of the rock volume. Fig 1a shows the suspended particles in the porous space and the retained particles on the rock surface.

Fig. 1b shows multiple particle capture mechanisms. The multiple capture corresponds to a sequence of sieves in Fig. 2; here l is the distance between the sieves, α is the particle capture probability, and B is the cross-section. The retention rate is equal to a number of particles captured during unit of time in unit volume and corresponds to the total retained concentration s:

$$\frac{\Delta s}{\Delta t} = \frac{\alpha c U B \Delta t}{\Delta t B l} \tag{2}$$

As it follows from Eq. (2), retention rate is proportional to particle flux cU

$$\frac{\partial s}{\partial t} = \lambda c U, \;\; \lambda = \frac{\alpha}{l} \tag{3}$$

and the proportionality coefficient – filtration coefficient λ - is the capture probability per unit length of the particle trajectory α/l. The capture probability is retained-concentration dependent for large s-concentrations, adding the filtration function $h(s)$ to the capture rate expressed by Eq. (3):

$$\frac{\partial s}{\partial t} = h(s) \lambda c U \tag{4}$$

In particular, linear filtration function

$$h(s) = \begin{cases} \left(1 - \dfrac{s}{s_m}\right), & 0 \le s \le s_m \\ 0, & s > s_m \end{cases} \tag{5}$$

is called the Langmuir's blocking function and corresponds to proportionality between the capture rate and concentration of vacant sites for capture s_m-s, where s_m is the maximum retained concentration.

After retained concentration reaches its maximum value, i.e. all vacancies are occupied, the rock does not capture particles any more. The particular case of Langmuir's blocking function (5) corresponds to low retention concentrations s<<sm, yielding a constant filtration coefficient h(s)=1, Eq. (3).

For colloids with multiple particle capture mechanisms and *n* filtration functions $h_k(s_1,s_2\ldots s_n)$, the overall filtration function *h* depends on the total retention concentration, like in Eq. (4). The overall filtration function $h(s)$ is obtained from the individual filtration functions $h_k(s_1,s_2\ldots s_n)$ by solving system of ordinary differential equations [*Zhang et al.*, 2018]. In particular, close approximation of $h(s)$ for two populations with constant filtration function $h_1=\lambda_1/\lambda$ and blocking function given by Eq. (5) is their total

$$h(s)=\begin{cases}\left(1-\dfrac{s}{s_m}\right)+\Lambda, & 0\le s\le s_m \\ \Lambda, & s>s_m\end{cases} \quad ;\ \Lambda=\frac{\lambda_1}{\lambda} \tag{6}$$

Further in the text, the traditional model (4) with filtration function (6) is called the binary-blocking model (BBM).

Fig. 3a presents individual constant and blocking filtration functions (lines 1 and 2) and the overall filtration function for two simultaneous capture mechanisms (line 3). Fig. 3b presents BTCs that follow exact solutions of 1D problems with filtration functions 1, 2, and 3, given by Eqs. (3), (5), and (6), respectively. Constant BTC 1 corresponds to constant filtration coefficient; BTC corresponding to Langmuir's blocking tends to one as time tends to infinity [*Polyanin and Manzhirov*, 2006; *Polyanin and Zaitsev*, 2012; *Elimelech et al.*, 2013]. BTC that corresponds to filtration function (6) for two simultaneous particle capture mechanisms tends to constant that is below the injected concentration [*Zhang et al.*, 2018].

For large suspension concentrations *c*, the extension to capture rate Eq. (4) is obtained by upscaling (averaging) of multicomponent colloids with distributed particle properties

$$\frac{\partial s}{\partial t}=h(s)\,f(c)U \tag{7}$$

where $f(c)$ is called the suspension function [*Bedrikovetsky et al.*, 2019]. The upscaling is valid for colloids where each population filtrates with its own suspension function $f_i(c_i)$ but the filtration function

is the same for all populations. Averaging of colloidal transport with multiple populations that follow linear filtration given by the rate equations (4) and individual filtration constants λ_k, k=1,2…n results in nonlinear suspension function in Eq. (7).

Particle retention causes permeability decline, so the modified Darcy's law

$$U = -\frac{k}{\mu(1+\beta s)}\frac{\partial p}{\partial x} \tag{8}$$

includes the formation damage effect. Here k is the initial rock permeability, μ is the viscosity, β is the formation damage coefficient.

The traditional mathematical models (4) exhibit exponential RPs. However, hyper-exponential retention profiles (HERP) are often observed in laboratory corefloods [*Albinger et al.*, 1994; *Li et al.*, 2004; *Li and Johnson*, 2005; *Tufenkji and Elimelech*, 2005a, b; *Tong and Johnson*, 2007; *Wang et al.*, 2011; *Jiang et al.*, 2012; *Kasel et al.*, 2013; *Wang et al.*, 2013]. Significant deviation of the modelling data from the experimentally obtained HERPs has been reported in numerous works [*Tufenkji and Elimelech*, 2004, 2005a; *Goldberg et al.*, 2014]. This explained various approaches to reproduce HERPs by mathematical modelling [*Tong and Johnson*, 2007; *Yuan and Shapiro*, 2010; *Yuan and Sin*, 2011].

HERPs as a total of multiple exponents is attributed to multicomponent colloidal flows, where the populations differ from each other by particle size, shape, zeta-potential, etc. [*Li et al.*, 2004; *Tufenkji and Elimelech*, 2004, 2005a; *Tong and Johnson*, 2007]. In particular, *Tufenkji and Elimelech* [2005b] assumed probabilistic distribution of the filtration coefficient and slow and fast capture rates by favourable and unfavourable sites, corresponding to primary and secondary minima, respectively. The model successfully matches HERPs.

The suspension-colloidal flow model developed by *Schijven et al.* [2002] assumes two independent particle capture mechanisms. Close matching of experimental data can be achieved for either BTCs or HERPs; matching of both curves simultaneously hasn't been performed [*Goldberg et al.*, 2014].

Bradford et al. [2003] noted that HERPs correspond to retention rate decrease along the core, and proposed the filtration function that decreases with depth. The mass balance equation accounts for two-site attachment, straining, diffusion, and detachment kinetics. This model achieves simultaneous close match of RPs and BTCs. This model is currently widely used to reproduce HERPs by mathematical

104 modelling [*Bradford et al.*, 2004; *Bradford and Bettahar*, 2006; *Wang et al.*, 2013; *Bai et al.*, 2018].
105 Yet, the filtration-coefficient dependency of the depth should be substantiated by deeper physics
106 fundamentals [*Goldberg et al.*, 2014].
107 The model for multi-component colloidal flow based on Master equation with randomly distributed
108 jump lengths and times [*Shapiro*, 2007] was derived by *Yuan and Shapiro* [2010]. The model assumes
109 particle-property distribution. The filtration coefficient for each population is a function of size, shape,
110 surface charge, etc. Averaging over probabilistic distributions of population parameters yields system
111 of elliptic equations, which simultaneously closely matches BTCs and RPs. However, the effective
112 averaged model is cumbersome and yields to significant computer time consumption during iterative
113 processes of data matching and inverse problem solution.
114 Numerous laboratory observations of HERPs also include BTC stabilisation at concentrations lower
115 than the injected concentration [*Tufenkji and Elimelech*, 2005a; *Wang et al.*, 2011; *Wang et al.*, 2012b;
116 *Wang et al.*, 2012a; *Yang et al.*, 2017]. This results in continuous growth of retained concentration and
117 permeability damage. BTC stabilisation at the level lower than the injected concentration indicates
118 particle capture by two independent and simultaneous mechanisms [*Zhang et al.*, 2018], which is
119 already widely reflected in the contemporary mathematical models [*Wang et al.*, 2011; *Wang et al.*,
120 2012b; *Wang et al.*, 2012a; *Yang et al.*, 2017]. However, simultaneous matching of BTCs with stabilised
121 level lower than one and HERPs is not available; this behaviour cannot be reproduced by the available
122 mathematical models.
123 The current paper fills the gap. We transform the traditional colloidal transport model by introduction
124 of nonlinear suspension function *f(c)* and binary blocking filtration function. This transformation is
125 based on the upscaling results and analogy with active mass law for chemical reactions. The modified
126 model reproduces the stabilised BTC concentration that is below the injected value, and HERPs. It was
127 proven that the aggregation of multiple particle-capture mechanisms for the model with nonlinear
128 suspension function results in an overall filtration function for an equivalent single-capture rate. We
129 derived exact solution for 1D transport problem that corresponds to laboratory flow-in-column tests.
130 The model closely matches HERPs and BTCs simultaneously. The number of degrees of freedom of
131 experimental data arrays in every of 24 matched tests exceeds the number of model parameters by two.

Moreover, the dependencies of the tuned model parameters of salinity and pH is explained by DLVO theory. Those allow claiming the validity of the model developed.

The text structure is as follows. Section 2 presents major physics assumptions of the model and introduces governing equations. Section 3 derives exact solution for 1D flow problem and calculates the type curves. Section 4 presents the results and analysis of the laboratory data matching by the proposed mathematical model. Section 5 discusses shortcomings and applications of the model. Section 6 concludes the paper.

2. Governing system of equations

2.1. Assumptions of the model

We assume the rate equation (7). The rate expression (4) is valid for small suspension and retention concentrations, where, by analogy with the active mass law, the probability of the meeting is the product of individual probabilities that are proportional to the specie concentrations. For the particle capture, the concentrations of particles and sites are c and s_m-s, respectively. Extension of the low-concentration rate expression (7) for the case of large suspension and retention concentrations corresponds to change the concentrations by their activities $f(c)$ and $h(s)$, respectively. In particular cases we are using the suspension function that is analogous to two-suffix Margules expression of activity coefficient for non-ideal solutions in the equation chemical-reaction rate [*Margules*, 1904; *Fogler*, 2016]

$$f\left(c\right)=ce^{Ac^2},\ \ A>0 \tag{9}$$

Further in the text, the model (7) with suspension function (9) and blocking filtration function (5) is called Langmuir exponential-quadratic model (LEQM).

At small concentrations, the suspension function tends to λc and filtration function tends to Eq. (3), which yields

$$f\left(0\right)=0,\ f'\left(0\right)=\lambda,\ h\left(0\right)=1,h'\left(0\right)=-\ {}^{1}\!\!\diagup\!\!{}_{S_m} \tag{10}$$

We consider concentrations to be large enough for significantly nonlinear suspension and filtration functions, but low enough not to affect the suspension density and rock porosity. In other words, the colloid is assumed to be incompressible and the flux is conserved $U=U(t)$. The same model can be obtained for large suspension and retained concentrations with incompressible water and particles, and

159 the volume additivity during the suspension and retention of the particles (so-called Amagat's law)
160 [*Bedrikovetsky*, 2013].
161 The model is valid in large scale approximation, where the diffusive and dispersion fluxes are negligible
162 if compared with the advective particle flux. We also assume two independent particle-capture
163 mechanisms, one with Langmuir's blocking (Eq. (5)) and another one with low retention concentration
164 $s<<s_m$ and constant filtration coefficient λ_1. The aggregation lemma, derived in Appendix A.

165 **2.2. Governing equations**

166 Les us consider colloid injection into clean bed, where the initial vacancy concentration is equal to s_m.
167 The corresponding initial and boundary conditions are:

168 $$t=0:\ c=s=0;\quad x=0:\ c=c^0,\ p=p^0 \tag{11}$$

169 Introduce dimensionless variables and parameters as

170 $$x\to\frac{x}{L}, t\to\frac{Ut}{L\phi}, c\to\frac{c}{c^0}, s\to\frac{s}{\phi c^0}, p\to\frac{kp}{U\mu L}$$
$$\lambda\to\lambda L,\ \lambda_1\to\lambda_1 L,\ s_m\to\frac{s_m}{\phi c^0}, f(c)\to\frac{Lf(c)}{c^0} \tag{12}$$

171 System of equations (1, 7) in dimensionless variables takes the following form

172 $$\frac{\partial c}{\partial t}+\frac{\partial c}{\partial x}=-\frac{\partial s}{\partial t} \tag{13}$$

173 $$\frac{\partial s}{\partial t}=h(s)\,f(c) \tag{14}$$

174 $$1=-\frac{1}{1+\beta\phi c^0 s}\frac{\partial p}{\partial x} \tag{15}$$

175 The initial and boundary conditions (11) in dimensionless variables become:

176 $$t=0: c=s=0 \tag{16}$$

177 $$x=0: c=1,\ p=\frac{kp_0}{U\mu L} \tag{17}$$

178 Properties of suspension function (10) remain the same.

179 **3. Mathematical modelling**

180 This section presents semi-analytical solution for 1D problem (13), derived in Appendix B (section 3.1)
181 and the numerical model based on finite-difference method (section 3.2).

182 **3.1. Semi-analytical model and flow zone structure**

183 System (B2-B3) subject to initial and boundary conditions (B4) allows for exact solution, which is
184 derived in Appendix B. Table 2 presents implicit formulae for $c(x,t)$ and $c(x,t)$ in the four zones and
185 formulae for boundaries between the zones.

186 Fig. 4 shows the structure of flow domain. Zone *0* ahead of the concentration front is non-perturbed
187 zone of the initial conditions. Zone *I* behind the concentration front is covered by the fluid trajectories,
188 which passed the inlet before the maximum retention value $s(0,t)=s_m$ was reached. In zone *III*, $s>s_m$, i.e.
189 the filtration function is constant and equal Λ. The value $s>s_m$ is reached at the front $\tau=\tau_m(x)$. Ahead of
190 this front in zone *II*, $s<s_m$. Exact solution is presented by series of transcendental equations () in
191 Appendix B and in Table 1.

192 Solution in zone *III* allows calculating BTC that stabilises at the moment $\tau= \tau_m(1)$ at x=1. The equation
193 for stabilised BTC $c_m(1)$ is obtained from Eq. (B):

194 $$\int_{c_m(1)}^{1} \frac{dy}{f(y)} = \Lambda \tag{22}$$

195 Suspension concentration just behind the concentration front $c^-(x)$ allows calculating the BTC at the
196 breakthrough moment at x=1:

197 $$\varphi(1) - \varphi\left(c^-\left(x=1,0\right)\right) = 1+\Lambda\,, \tag{23}$$

198 Suspension concentration at the breakthrough moment $c^-(x)$ at x=1 is

199 $$\int_{c^-(1)}^{1} \frac{dy}{f(y)} = 1+\Lambda \tag{24}$$

200 In particular, expressions (22) and (24) for the case of exponential-quadratic suspension function (9)
201 defining stabilized and breakthrough concentrations become

202 $$\Lambda = \frac{ei\left[-A\right] - ei\left[-A\left(c_m(1)\right)^2\right]}{2\lambda} \tag{25}$$

$$1+\Lambda=\frac{ei[-A]-ei\left[-A\left(c^{-}(1)\right)^{2}\right]}{2\lambda} \tag{26}$$

Expressions (25) and (26) allow determining filtration constants λ and λ_1 from stabilized and breakthrough concentrations.

The modified model contains four constants: λ, λ_1, s_m, and A. Relationships (25, 26) allow tuning two free model coefficients A and s_m to match BTC and RP.

3.2. Type curves and fingerprints of different models

Fig. 5 shows typical BTCs, RPs, and impedance (dimensionless pressure drop across the core)

$$J(t)=p(0,t)-p(1,t) \tag{27}$$

for LEQM, BBM, and modified model.

The LEQM contains blocking filtration function (5), so BTC tends to the injected concentration c=1 (Fig. 5a). The BBM and the modified model contain binary blocking filtration function (6), so BTCs stabilise at the limit lower than the injected concentration c<1. Fig. 5b shows that both LEQM and modified models exhibit HERPs, while the BBM reproduces exponential RPs. The LEQM presents BTCs that stabilise at the injected value, i.e. no fines are retained afterward; thus the model predicts stabilisation of the impedance (Fig. 5c). BBM and modified model exhibit BTCs stabilised at the value lower that injected, so particle retention continues throughout the overall injection period, and impedance does not stabilise.

The above-mentioned fingerprints of three models allow choosing the model from the experimental data. Exponential RP and BTC stabilised at the injected value indicate the traditional model (4). Exponential RP and BTC stabilised below the injected value suggest the BBM (4, 6). HERP and BTC stabilised at the injected value indicate the LEQM (5, 7). HERP and BTC stabilised below the injected value suggest using the modified model (6, 7). So, measurements of BTC and RP allows to choose the model for matching the laboratory experiments for further performance of laboratory-based predictions. Simultaneous measurements of BTC and impedance do not allow to choose the model.

3.3. Numerical model

Governing system (13, 14) subject to initial and boundary conditions (16, 17) is solved numerically using the hyperbolic partial differential equation solver presented by *Shampine* [2005a]. The method allows for vectorisation of the problem, taking advantage of MATLAB's matrices and vectors optimisation. The algorithm implements a two-step Lax–Friedrichs finite-difference method [*Shampine*, 2005b].

The areal and time steps for finite-difference method are selected to satisfy the Courant–Friedrichs–Lewy stability condition: ΔX=0.001, ΔT=0.0009.

4. Matching of laboratory data

This section analysis matching of the laboratory tests on colloidal and nanoparticles injection into porous media by the modified model with binary filtration function and exponential-quadratic suspension function, developed in the present work, and the model with binary filtration function and linear suspension function (so-called binary blocking model proposed by [*Zhang et al.*, 2018]).

Tests by Wang et al. [2012a] *with NaCl salinity variation* Hydroxyapatite nanoparticles (nHAP) were injected with concentration 100 ppm into the column packed by quartz sand with grain size 0.55-0.65 mm and porosity 0.38-0.40. The Darcy's velocity was $7.5 \cdot 10^{-5}$ m/s. Four tests were carried out at different salinities shown in Fig. 5a. The injection was carried out in the presence of 10 ppm humic acid. The results of the tests and their match by the model with binary filtration function and linear suspension function (red lines) and the modified model (blue lines) are shown in Fig. 5. Table 3 presents the tuned parameters for both models in fourth, fifth, sixth, and seventh lines. The accuracy of matching for BTC and RP are given in last and penultimate columns, respectively.

Fig. 5a and Table 3 show that both models exhibit high match of BTCs. The match of RPs by the BBM is poor, while the modified model closely agrees with the laboratory data. The maximum attached concentration s_m as tuned using both models has the same order of magnitude. Filtration coefficients λ and λ_1 for both models have the same orders of magnitude at high salinities and become significantly different at low salinities. The lower is the salinity, the higher is the laboratory-data deviation from the BBM, and the higher is the A-value.

Fig. 6a shows the salinity-dependencies for filtration coefficients λ and λ_1. The higher is the salinity the stronger is the electrostatic particle-grain attraction, and the higher are the attachment filtration coefficients. The original paper by *Wang et al.* [2012a] shows that the particle size increases as salinity increases, so the filtration coefficient for straining and size exclusion also increases. *Wang et al.* [2012a] highlight the particle capture by two retention mechanisms. The above speculations explain increase in both filtration coefficients with salinity increase.

Fig. 6b shows the increase in the maximum attached concentration s_m with salinity increase. Two competitive factors affect sm with salinity variation. The higher is the salinity the larger are the particles. Yet, it yields the stronger the electrostatic particle-particle and particle-grain attachment, resulting in particle clustering on the grain surfaces [*Chequer et al.*, 2019]. The dependencies of s_m versus salinity shows that the electrostatic attraction effect dominates.

The last column in Table 3 shows that the lower is the salinity the higher is the deviation between the laboratory data and the binary blocking model. The same effect has been observed by *Tufenkji and Elimelech* [2005a]. So, the valid model must be more nonlinear at low salinities. This explains why *A*-value increases as salinity decreases (Fig. 6b).

Tests by Wang et al. [2011] *with CaCl2 salinity variation* The explanations of results of the previous tests are valid for this series of tests where aqueous colloids of nanoparticles have been injected with five *IS*s of $CaCl_2$ (Fig. 7 and lines 14-17 in Table 3). Salinity increase yields increase of both filtration coefficients and of maximum attached concentration (Figs. 8a and 8b). Decrease in accuracy of experimental data match by the BBM yields increase in *A*-value.

Tests by Wang et al. [2012b] *with pH variation* have been performed under the same conditions of experiments performed by *Wang et al.* [2011], except that the grains were coated by iron oxy-hydroxide, and water with 0.1 mM NaCl and three different pH-values have been used.

Fig. 9a shows high match of BTCs by both models. The BBM exhibits poor match of RPs, while the modified model shows high match (Figs 9b, 9c and 9d). High electrostatic particle-grain attraction at low pH-values yields more intensive particle attachment to the grain surfaces. In particular, the particles attach to the pore throat surfaces, results in the increase of size-exclusion rates. Indeed, both filtration coefficients λ and λ_1 decrease as pH increases (Fig. 10a). The higher are electrostatic particle-particle

and particle-grain attractions, the denser are the attached clusters. Indeed, maximum retention concentrations decreases at pH increase (Fig. 10b). The accuracy of matching the experimental data with pH increase has the same order of magnitude, so the *A*-value variation is insignificant (columns eleven and nine in Table 3).

Tests by Yang et al. [2017] with changing HA concentration Biochar colloids with concentration 250 ppm have been injected with three different concentrations of humic acid in the column packed by sand grains with sizes 0.425-0.60 mm. The BTC and RP results are presented in Fig. 11. Increase of humic acid concentration results in increase of repulsion component of the grain-particle and particle-particle electrostatic forces. Consequently, as discussed above in this section, the increase in humic acid concentration yields decrease in both filtration coefficients (Fig. 12a) and in s_m decrease (Fig. 12b).

Table 3 also presents the results of matching of the tests on injection of surfactant-free fluorescent polystyrene latex particles with varying salinity - NaCl [*Tufenkji and Elimelech*, 2005a], injection of hydroxyapatite nanoparticles (nHAP) with varying salinity (NaCl) [*Wang et al.*, 2011], and injection of biochar colloids with varying naphthalene concentration [*Yang et al.*, 2017]. In all the tests, BTCs are highly matched by both models. Regarding the RPs, the coefficient of determination for the modified model is significantly higher than that for the BBM. This can be attributed to the high concentration of colloids in the suspension solution. At high colloidal suspension concentration, colloids do not behave as an ideal solution, where one particle does not interact with other particles, and just one particle "reacts" with one site into porous media. The modified model uses a non-linear function of concentration, e.g., activity in chemical reaction, that describe the behaviour of high colloidal suspension concentration, where particles do interact with each other and, more than one particle "reacts" with one site into porous media, simultaneously. Therefore, the modified model presents better results them BBM.

Appendix A. Aggregation lemma for multi-capture filtration with high concentrations and particle dispersion

In this Appendix, we show that the colloidal transport *(n+1)×(n+1)* system with *n* independent capture mechanisms is equivalent to *2×2* system with a single mechanism of the particle capture.

The mass balance equation for suspension and nano-colloidal transport in porous media accounts for suspended particles and the particles retained by *n* capture mechanisms:

$$\frac{\partial}{\partial t}(c\phi + \sum_{i=1}^{n} s_i) + \frac{\partial}{\partial x}\left(cU - D\frac{\partial c}{\partial x} \right) = 0 , \quad \text{(A1)}$$

where *D* is the effective dispersion coefficient ().

The capture rate equations for each individual mechanism assume large suspension concentration and contain suspension function

$$\frac{\partial s_i}{\partial t} = h_i\left(s_1, s_2 \cdots s_n\right) f\left(c\right) U, i = 1, 2 \cdots n \quad \text{(A2)}$$

The total of n kinetics rates (A.2) is

$$\frac{\partial s}{\partial t} = \sum_{i=1}^{n} \frac{\partial s_i}{\partial t} = \left(\sum_{i=1}^{n} h_i(s_1, s_2 \cdots s_n) \right) f\left(c\right) U = h(s_1, s_2 \cdots s_n) f\left(c\right) U, \; s = \sum_{i=1}^{n} s_i, \; h = \sum_{i=1}^{n} h_i(s_1, s_2 \cdots s_n) \quad \text{(A3)}$$

Assume the solution *c(x,t)* is known. For any arbitrary 0<*x*<L, PDEs (A2) and (A3) are transformed to ODEs. Change of independent variables in these ODEs from t to s yields

$$\frac{ds_i}{ds} = \frac{h_i(s_1, s_2 \cdots s_n)}{\left[\sum_{i=1}^{n} h_i(s_1, s_2 \cdots s_n) \right]} \quad \text{(A4)}$$

Initial condition for system (A2, A3) follows from initial conditions (16) for each retained concentration:

$$s = 0 : \; s_i = 0, \; i = 1, 2...n \quad \text{(A5)}$$

Substituting solution $s_i(s)$ of system of ODEs Eq. (A4) subject to Cauchy conditions (A5) into Eq. (A3) reduces system with *n* capture mechanisms (A1, A2) to a single capture system (1, 4, 5).

Appendix B. Exact solution for the proposed model

This Appendix derives exact analytical solution of system (13, 14) subject to initial and boundary conditions (16, 17).

Introduce Lagrangian time τ as an independent variable instead of time t. The corresponding mapping

$$(x,t)\to(x,\tau),\ \ \tau=t-x, \tag{B1}$$

is shown in Fig. 4. In plane (x,τ), boundary condition (17) remains the same; initial conditions (16) are set along the bisectrix of the third coordinate quadrant. System of equations (13, 14) takes the form

$$\frac{\partial c}{\partial x}=-\left[\left(1-\frac{s}{s_m}\right)+\Lambda\right]f(c) \tag{B2}$$

$$\frac{\partial s}{\partial \tau}=\left[\left(1-\frac{s}{s_m}\right)+\Lambda\right]f(c) \tag{B3}$$

Initial and boundary conditions (16, 17) become

$$\begin{array}{l} x=0:\quad c=1 \\ \tau=-x:\ c=s=0 \end{array} \tag{B4}$$

Quasilinear 2×2 system (B2, B3) has two families of characteristic lines: τ=const, and x=const, with relationships along characteristics given by Eqs. (B2) and (B3), respectively (Polyanin, Zaitsev, Polyanin, Sh).

Solution at the inlet (x=0) The Goursat initial-boundary problem (B2-B4) allows determining retention concentration along characteristic line x=0 without derivation of the global solution. At x=0 for small τ where $s(0,\tau)<s_m$, boundary condition (B4) gives c=1, and Eq. (B3) takes the form

$$\frac{\partial s}{\partial \tau}=\left[\left(1-\frac{s}{s_m}\right)+\Lambda\right]f(1) \tag{B5}$$

Integration of Eq. (B5) by separation of variables and accounting for initial condition (B4) yields

$$\int_0^{s(0,\tau)}\frac{du}{\left[\left(1-\frac{u}{s_m}\right)+\Lambda\right]}=f(1)\tau \tag{B6}$$

Calculation of integral in the left side of Eq. (B6) yields the explicit expression for retained concentration

$$s(0,\tau)=s_m(1+\Lambda)\left(1-e^{-\frac{f(1)}{s_m}\tau}\right). \tag{B7}$$

Formula (B7) is valid for $0 \le \tau \le \tau_m(0)$, where $s(0,\tau)<s_m$ (Fig. 4b). At the moment $\tau=\tau_m(0)$, retention concentration reaches value s_m, which determines this moment from Eq. (B7)

$$\tau_m(0) = \frac{s_m}{f(1)} \ln(1+\Lambda). \tag{B8}$$

For $\tau \ge \tau_m(0)$ Eq. (B3) takes the form, yielding

$$\frac{\partial s}{\partial \tau} = \Lambda f(1). \tag{B9}$$

Integration of the Eq. (B9) with condition $s=s_m$ at $\tau=\tau_m(0)$ gives

$$s(0,\tau) = s_m + \Lambda f(1)\left(\tau - \tau_m(0)\right). \tag{B10}$$

The solution at the inlet $x=0$ is obtained by combining formulas (B7) and (B10)

$$s(0,\tau) = \begin{cases} s_m(1+\Lambda)\left(1 - e^{-\frac{f(1)}{s_m}\tau}\right), & 0 \le \tau \le \tau_m(0) \qquad (a) \\ s_m + \Lambda f(1)\left(\tau - \tau_m(0)\right), & \tau > \tau_m(0) \qquad (b) \end{cases} \tag{B11}$$

Solution in Zone 0 ($-x<\tau<0$) Ahead of the concentration front for $\tau<0$, both Eq. (B2), (B3) are subject to zero Cauchy's conditions. The solution

$$c(x,\tau) = s(x,\tau) = 0 \tag{B12}$$

means, that the porous medium in zone 0 does not contain any suspended and retained particles (Fig. 4b)

Solution on the characteristic line ($\tau=0$) just behind the concentration front:

On the concentration front, the solution $c(x,\tau)$ is discontinuous. As it follows from the accumulation rate equation (B3), the solution $s(x,\tau)$ is continuous and $s(x,0)=0$. Denote the solution on just behind the concentration front as

$$c^{-}(x) = c(x,0) \tag{B13}$$

Function $c^{-}(x)$ is determined by equation (B2) on the front $\tau=0$, which is a characteristic line

$$\frac{dc^{-}}{dx} = -(1+\Lambda)\, f\left(c^{-}\right) \tag{B14}$$

Solution of Eq. (B14) with Cauchy condition (B4) is obtained by separation of variables

$$\int_{c^{-}(x)}^{1} \frac{du}{f(u)} = (1+\Lambda)\, x\,. \tag{B15}$$

Denote by $\varphi(c^{-})$ the integral in the left-hand side of equation (B15). Eq. (B15) can be written in a form

$$\varphi\left(c^{-}(x)\right) = (1+\Lambda)\, x, \;\; \varphi'(c) = -\frac{1}{f(c)}, \tag{B16}$$

Eq. (B16) implicitly defines suspension concentration just behind the front and provides boundary condition for solution in zone I.

Solution in Zone I ($0 \le \tau \le \tau_m(0)$): Expressing retained concentration from Eq. (B2)

$$s(x,\tau) = s_m\left(1+\Lambda+\frac{1}{f(c)}\frac{\partial c}{\partial x}\right) = s_m\left(1+\Lambda-\frac{\partial \varphi(c)}{\partial x}\right) \tag{B17}$$

and substituting it in Eq. (B3) results in

$$\frac{\partial}{\partial \tau}\left(\frac{\partial \varphi(c)}{\partial x}\right) = \frac{1}{s_m}\frac{\partial c}{\partial x} \tag{B18}$$

Changing the order of derivatives in Eq. (B18) and integrating in x accounting for boundary conditions (B4) yields

$$-s_m\frac{\partial \varphi(c)}{\partial \tau} + c = 1 \tag{B19}$$

Dividing variables in obtained ordinary differential equation (B19) results in solution $c(x,\tau)$

$$\int_{c^{-}(x)}^{c} \frac{dy}{f(y)(1-y)} = \frac{1}{s_m}\tau \tag{B20}$$

Defining indefinite integral as $w(c)$ allows for implicit expression for solution $c(x,\tau)$:

$$w(c) - w\left(c^{-}(x,0)\right) = \frac{\tau}{s_m};\;\; w'(c) = \frac{1}{f(c)(1-c)}, \tag{B21}$$

Taking derivative in x of both sides of Eq. (B20) leads to relationship

$$\frac{1}{(1-c)\,f(c)}\frac{\partial c}{\partial x}-\frac{1}{\left(1-c^{-}(x,0)\right)f\left(c^{-}(x,0)\right)}\frac{dc^{-}(x,0)}{dx}=0 \qquad \text{(B22)}$$

Accounting for Eq. (B14), (B17) in (B22) yields the expression for Riemann invariant in zone I

$$\frac{s(x,\tau)-s_m(1+\Lambda)}{(1-c)}=\frac{-s_m(1+\Lambda)}{\left(1-c^{-}\right)}, \qquad \text{(B23)}$$

which expresses solution $s(x,\tau)$ versus already known solution $c(x,\tau)$.

Solution in Zone III ($\tau \geq \tau_m(x)$): In Zone III (Fig. 4b) the filtration function $h(s)$ is constant. Integration of Eq. (B2) gives steady-state solution, which we denote as $c_m(x)$:

$$\int_{c_m(x)}^{1}\frac{dy}{f(y)}=\Lambda x \qquad \text{(B24)}$$

Solution $s(x,\tau)$ in Zone III is determined from Eq. (B3) and is expressed via $c(x,\tau)$

$$s(x,\tau)=s_m+\Lambda f\left(c_m(x)\right)\left(\tau-\tau_m(x)\right) \qquad \text{(B25)}$$

Formulae (B24, B25) determining the boundary $\tau_m(x)$ are given in the next subsection.

Solution at the boundary between zones II and III ($\tau=\tau_m(x)$):

Denote the solution of the system in *zone I* on the boundary $\tau=\tau_m(0)$ as

$c(x,\tau=\tau_m(0))=c_1(x)$; $s(x,\tau=\tau_m(0))=s_1(x)$, *i.e.*

408 Table 1. Exact solution of system () subject to initial and boundary conditions () in coordinates (x,τ)

Zone/line	$c(x,\tau)$	$s(x,\tau)$
Zone 0	0	0
Inlet $x=0$	$c(0,\tau)=1$	$s(0,\tau)=\begin{cases} s_m(1+\Lambda)\left[1-\exp\left(-\dfrac{f(1)}{s_m}\tau\right)\right], & 0\le\tau\le\tau_m(0) \\ s_m+\Lambda f(1)\left(\tau-\tau_m(0)\right), & \tau>\tau_m(0) \end{cases}$ $\tau_m(0)=\dfrac{s_m}{f(1)}\ln(1+\Lambda)$
Concentration front $\tau=0$	$\int\limits_{c^-(x)}^{1}\dfrac{du}{f(u)}=(1+\Lambda)x,\ c^-(x)=c(x,0)$	$s(x,0)=0$
Zone I $\tau\le\tau_m(0)$ $0<x<\infty$	$\int\limits_{c^-(x)}^{c}\dfrac{dy}{f(c)(1-c)}=\dfrac{\tau}{s_m}$	$s(x,\tau)=s_m(1+\Lambda)\dfrac{c-c^-}{1-c^-}$
Zone II $\tau_m(0)\le\tau\le\tau_m(x)$	$s_m\dfrac{1}{f(c)}\dfrac{\partial c}{\partial\tau}+c=s_m\Lambda x_m'(\tau)+c_m(x_m(\tau))$ $\tau=\tau_m(0):\ c(x,\tau)=c_1(x)$	$s(x,t)=s_m(1+\Lambda)-$ $-\left(s_m(1+\Lambda)-s_1(x)\right)\exp\left(-\dfrac{1}{s_m}\int\limits_{\tau_m(0)}^{\tau}f(c(x,z))dz\right)$
Boundary Γ $\tau=\tau_m(x)$	$c(x,\tau_m(x))=c_m(x)$	$s(x,\tau_m(x))=s_m$
Zone III	$\int\limits_{c_m(x)}^{1}\dfrac{dy}{f(y)}=\Lambda x$	$s(x,\tau)=s_m+\Lambda f(c_m(x))(\tau-\tau_m(x))$

409

Table 2. Exact solution for 1D suspension-colloidal transport in coordinates *(x,t)*

Zone/line	$c(x,t)$	$s(x,t)$
Zone 0	0	0
Inlet $x=0$	$c(0,t)=1$	$s(0,t)=\begin{cases} s_m(1+\Lambda)\left[1-\exp\left(-\frac{f(1)}{s_m}t\right)\right], 0\le t\le t_m(0) \\ s_m+\Lambda f(1)\left(t-\tau_m(0)\right) \quad , \quad t>\tau_m(0) \end{cases}$ $\tau_m(0)=\frac{s_m}{f(1)}\ln(1+\Lambda)$
Concentration front $t=x$	$\int\limits_{c^-(x)}^{1}\frac{du}{f(u)}=(1+\Lambda)x,\ c^-(x)=c(x,x)$	$s(x,x)=0$
Zone I $x\le t\le\tau_m(0)+x$	$\int\limits_{c^-(x)}^{c}\frac{dy}{f(c)(1-c)}=\frac{t-x}{s_m}$	$s(x,t)=s_m(1+\Lambda)\frac{c(x,t)-c^-(x)}{(1-c^-(x))}$
Zone II $\tau_m(0)+x\le t\le\tau_m(x)+x$	$s_m\frac{1}{f(c)}\frac{\partial c}{\partial t}+c=s_m\Lambda x_m'(t-x)+c_m(x_m(t-x))$ $t=\tau_m(0)+x:\ c(x,t)=c_1(x)$	$s(x,t)=s_m(1+\Lambda)-\left[s_m(1+\Lambda)-s_1(x)\right]\cdot$ $\cdot\exp\left(-\frac{1}{s_m}\int\limits_{\tau_m(0)+x}^{t}f(c(x,z))dz\right)$
Boundary Γ $t=\tau_m(x)+x$	$c(x,\tau_m(x)+x)=c_m(x)$	$s(x,\tau_m(x)+x)=s_m$
Zone III $t\ge\tau_m(x)+x$	$\int\limits_{c_m(x)}^{1}\frac{dy}{f(y)}=\Lambda x$	$s(x,t)=s_m+\Lambda f(c_m(x))(t-\tau_m(x)-x)$

Table 3. The results of laboratory data matching by the modified and binary-blocking models and model tuned coefficients

Refs.	Test Conditions			s_m	λ	λ_1	A	R_c^2	R_s^2
				Modified Binary-blocking models	Modified Binary-blocking models	Modified Binary-blocking models	Modified model	Modified Binary-blocking models	Modified Binary-blocking models
Wang et al. [2012a]	c^0 *(ppm)*	NaCl (mM)	pH						
	100	0.1	7.2	0.072 0.064	0.025 0.209	0.0095 0.216	4	0.9453 0.9423	0.8533 0.2567
		1		0.178 0.164	0.120 0.259	0.0913 0.543	3.01	0.9625 0.9697	0.9382 0.4446
		10		0.232 0.238	0.439 0.604	0.230 0.751	2.5	0.9710 0.9766	0.9369 0.4555
		50		13.408 18.192 24.000[#]	0.874 1.402 1.649[#]	0.756 0.910 -	1.9 - 1.9[#]	0.9332 0.9650 0.9210[#]	0.9806 0.7471 0.9734[#]
Wang et al. [2011]	c^0 *(ppm)*	NaCl (mM)	CaCl2 (mM)						
	200	0	-	0.098 0.063	0.035 0.294	0.0045 0.1844	4.40	0.9903 0.9895	0.8017 0.2758
		1	-	0.134 0.088	0.05 0.324	0.006 0.2294	4.40	0.9791 0.9899	0.8033 0.0711
		10	-	0.154 0.097	0.074 0.313	0.022 0.3286	3.80	0.9972 0.9927	0.8607 0.2630
		50	-	0.616 0.452	0.58 0.742	0.22 0.6539	1.75	0.9424 0.9573	0.6492 0.2847
		100	-	0.074 0.045	0.56 0.47	1.25 2.012	0.50	0.8916 0.8548	0.7250 0.4489
		-	0.1	0.083 0.043	0.014 0.086	0.018 0.298	3.80	0.9387 0.9316	0.8341 0.1967
		-	0.3	0.076 0.061	0.03 0.157	0.029 0.354	3.82	0.9588 0.9635	0.7989 0.1812
		-	0.5	0.124 0.090	0.042 0.218	0.043 0.387	3.85	0.8502 0.8598	0.7978 0.1952
		-	1.0	0.367 0.223	0.32 0.507	0.22 0.899	3.50	0.9881 0.9828	0.8015 0.4340
Wang et al. [2012b]	c^0 *(ppm)*	NaCl (mM)	pH						
	100	0.1	6	0.341 0.362	0.760 1.130	0.110 0.585	3.13	0.9795 0.9838	0.9935 0.4321
			8	0.217 0.272	0.260 0.610	0.052 0.357	3.10	0.9664 0.9707	0.9664 0.2720
			10.5	0.104 0.073	0.040 0.179	0.037 0.315	3.25	0.9316 0.9306	0.9483 0.2566
Tufenkji and Elimelech [2005a]	c^0 *(ppm)*	NaCl (mM)	pH						
	10	20	8	0.125 0.105	0.016 0.131	0.0095 0.120	3.15	0.9330 0.9340	0.8190 0.3404
		30		0.135 0.119	0.250 0.282	0.490 0.663	0.51	0.9319 0.9325	0.9701 0.8324
		33		0.049 0.052	0.270 0.282	2.05 2.12	0.15	0.8901 0.8668	0.9509 0.9450
Yang et al. [2017]	c^0 *(ppm)*	Humic Acid	Naph*						
	250	0		0.211 0.186	0.320 0.895	0.028 0.213	3.20	0.9716 0.9842	0.9685 0.2352
		10		0.121 0.107	0.150 0.600	0.018 0.1586	3.20	0.9734 0.9812	0.9677 0.1447

		20		0.128 0.113	0.050 0.590	0.0008 0.0875	5.50	0.9767 0.9695	0.8062 0.2814
			0.1	0.151 0.119	0.090 0.316	0.065 0.377	3.00	0.9533 0.9637	0.9051 0.1899
			0.2	0.096 0.078	0.100 0.235	0.180 0.582	2.50	0.9153 0.9508	0.8593 0.2267

Naphthalene; # Langmuir exponential-quadratic model

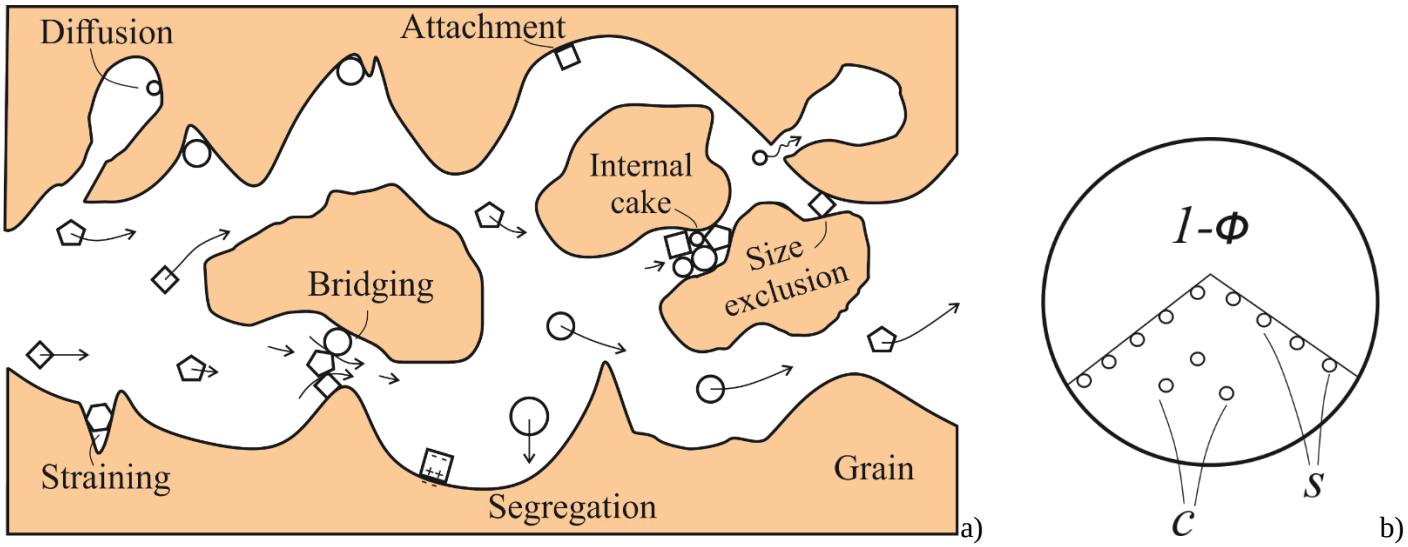


Fig. 1. Conceptual schematic for colloidal transport with particle capture in porous media: a) suspension and retention particles in pore space; b) various particle capture mechanisms.

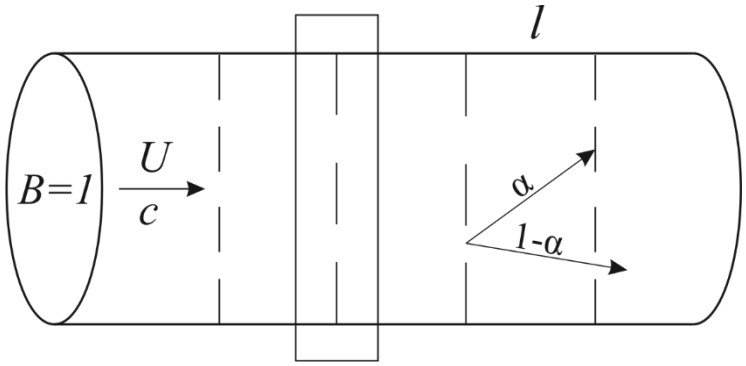


Fig. 2. Representation of multiple capture in porous media by the sequence of sieves.

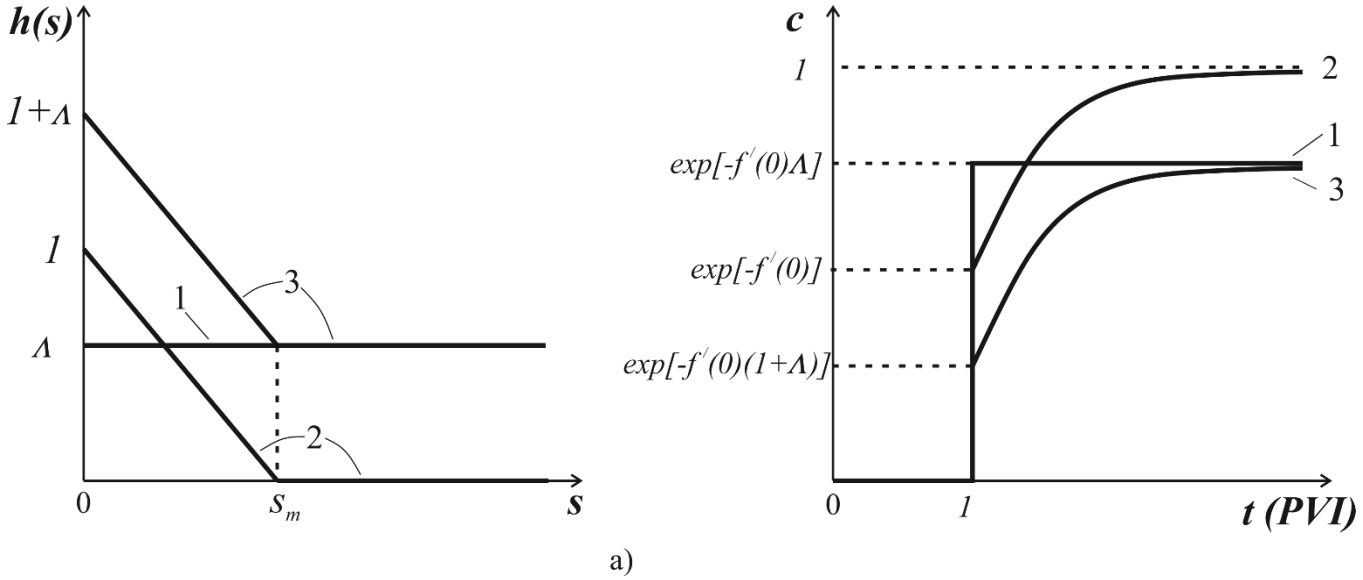


Fig. 3. Various forms of breakthrough curves for different forms of filtration function: a) filtration functions; b) breakthrough curves. Here 1 – constant filtration function, 2 – Langmuir (blocking) filtration function, and 3 is the binary filtration function.

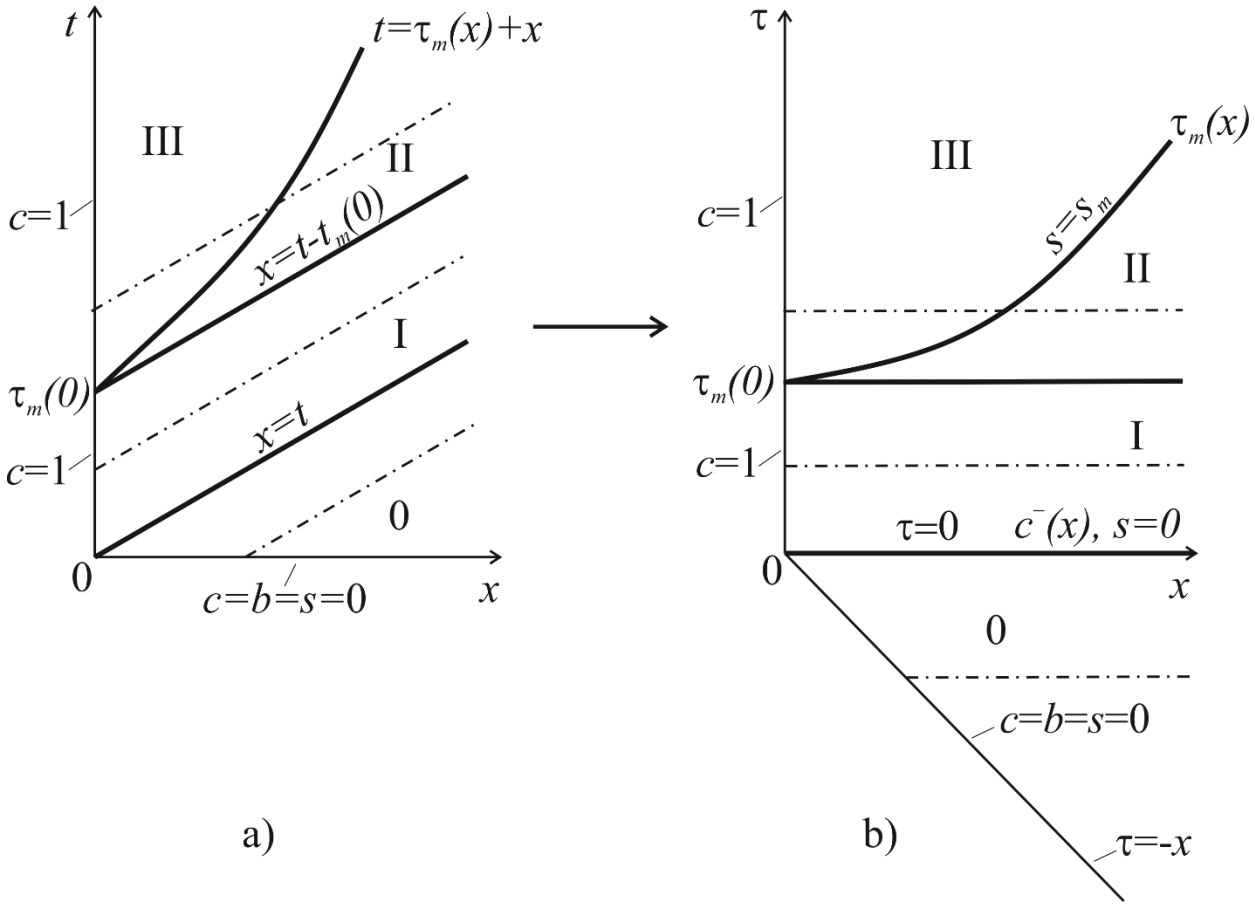


Fig 4. Mapping $(x,t)\rightarrow(x,\tau)$

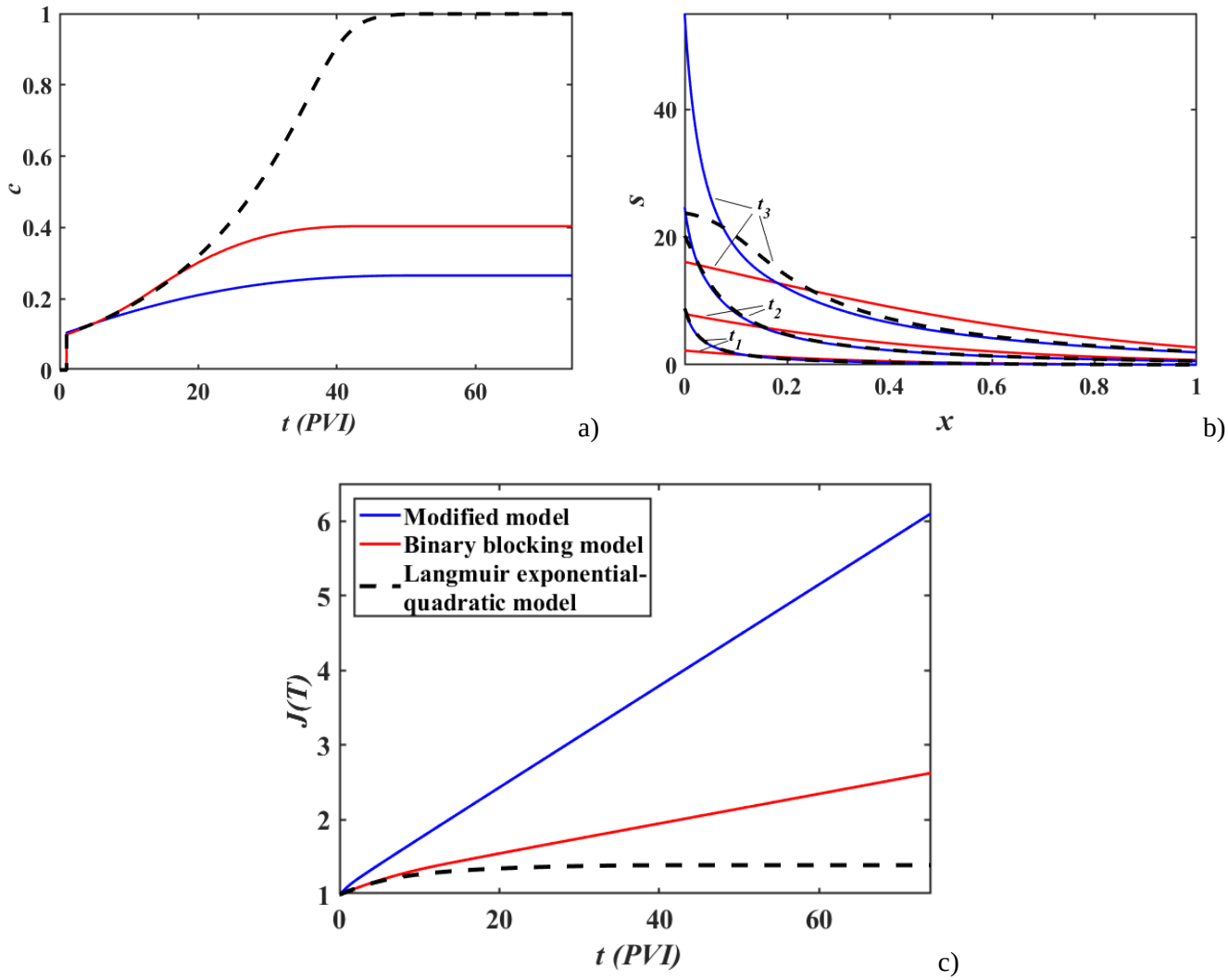


Fig. 5. BTCs, RPs, and impedance (dimensionless pressure drop across the core) for β=1000, other model constants are given in Table 1 in seventh row; t_1=1PVI, t_2=4 PVI; t_3=10 PVI.

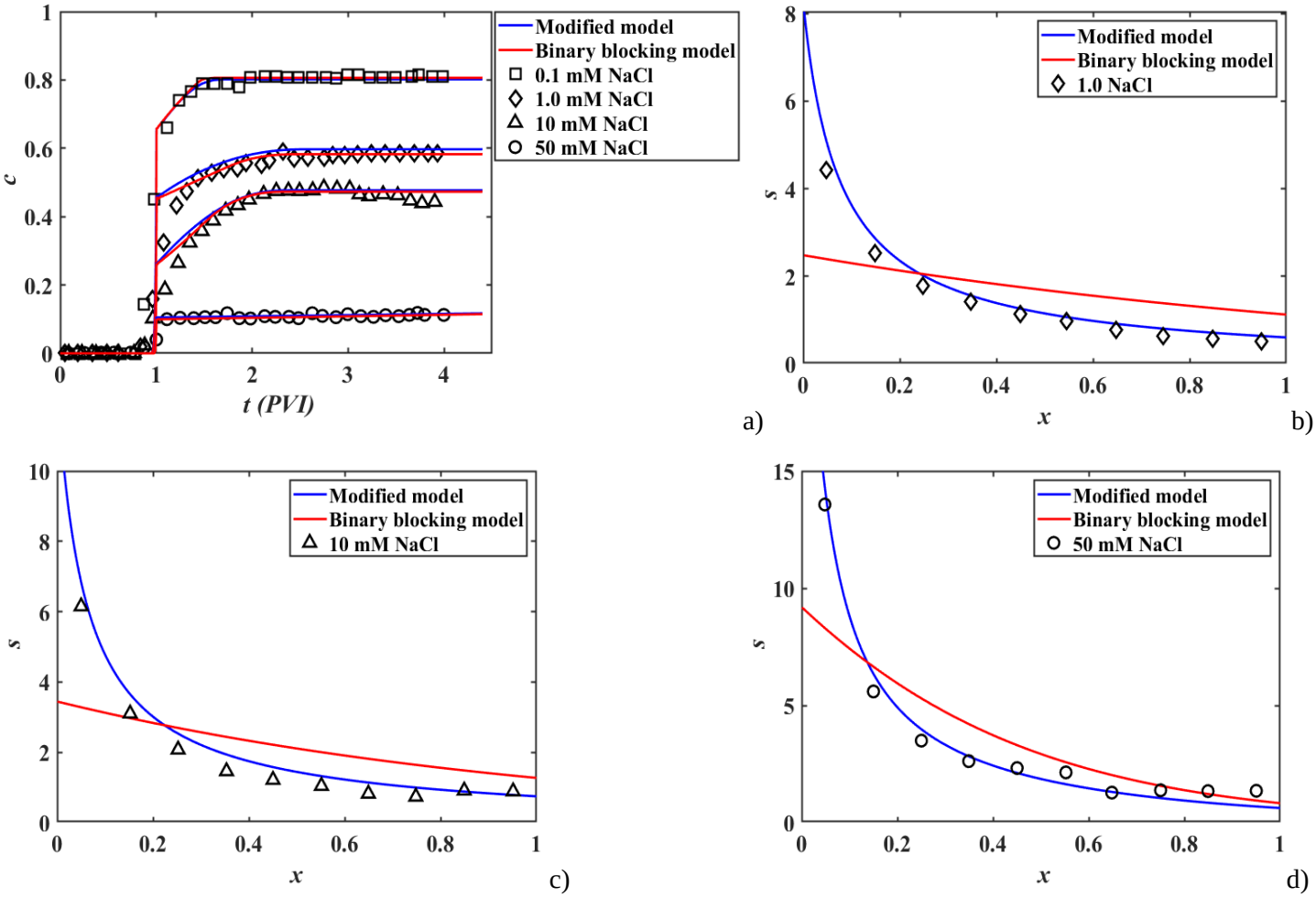


Fig. 5. Series of colloidal injection tests with diff salinity NaCl [*Wang et al.*, 2012a].

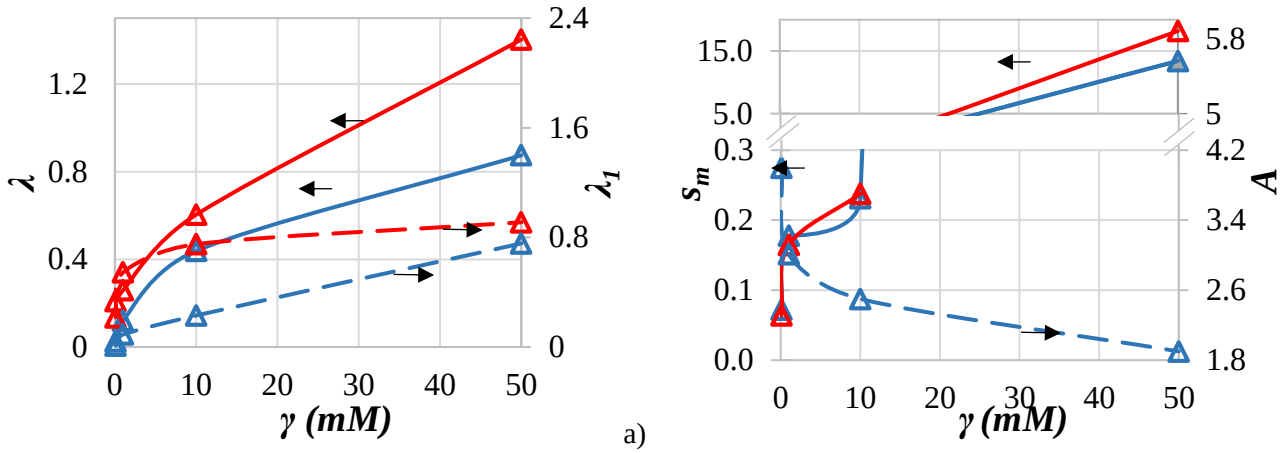


Fig. 6. Salinity dependencies of model coefficients [*Wang et al.*, 2012a].

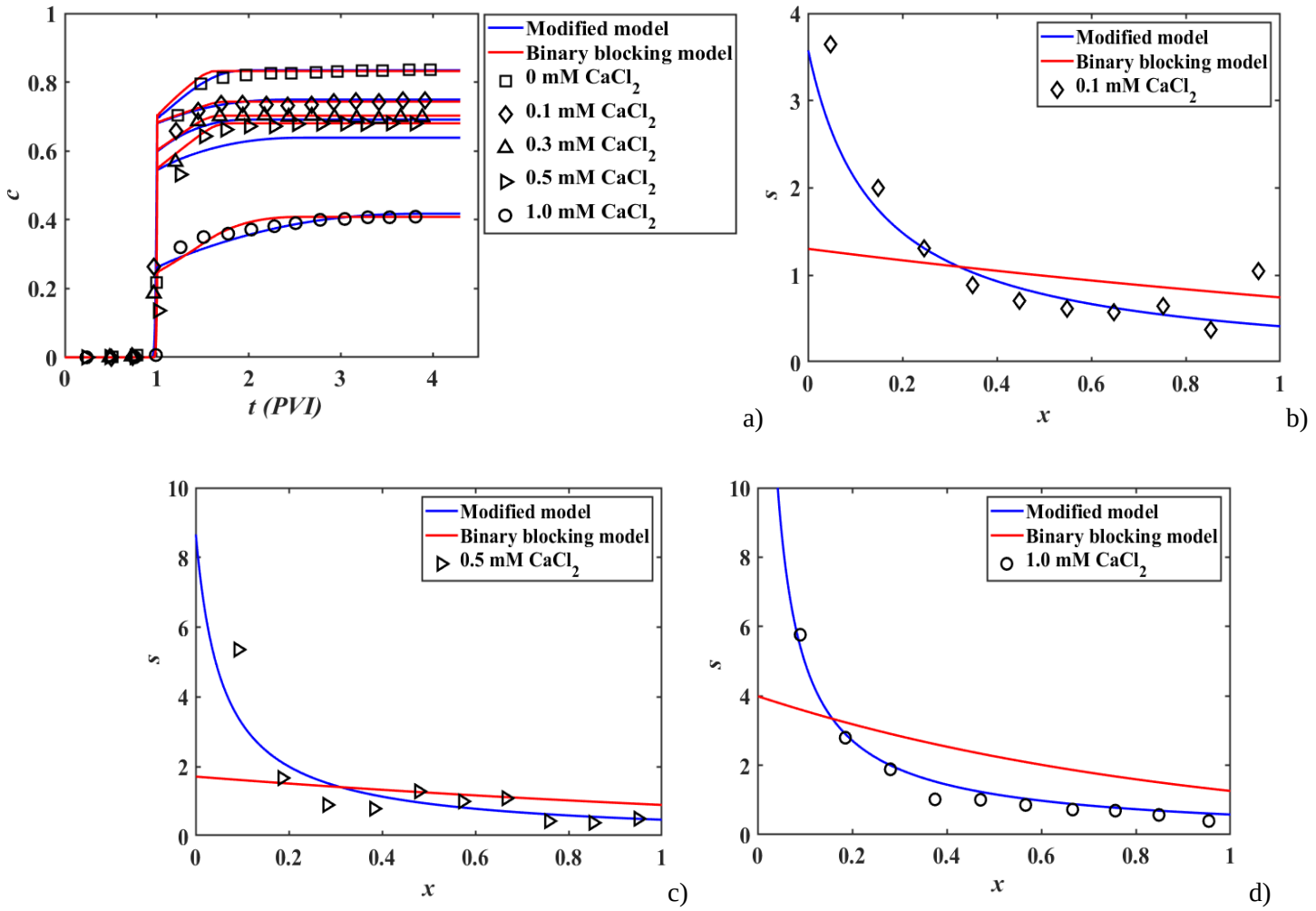


Fig. 7. Series of colloidal injection tests with different salinity $CaCl_2$ [*Wang et al.*, 2011].

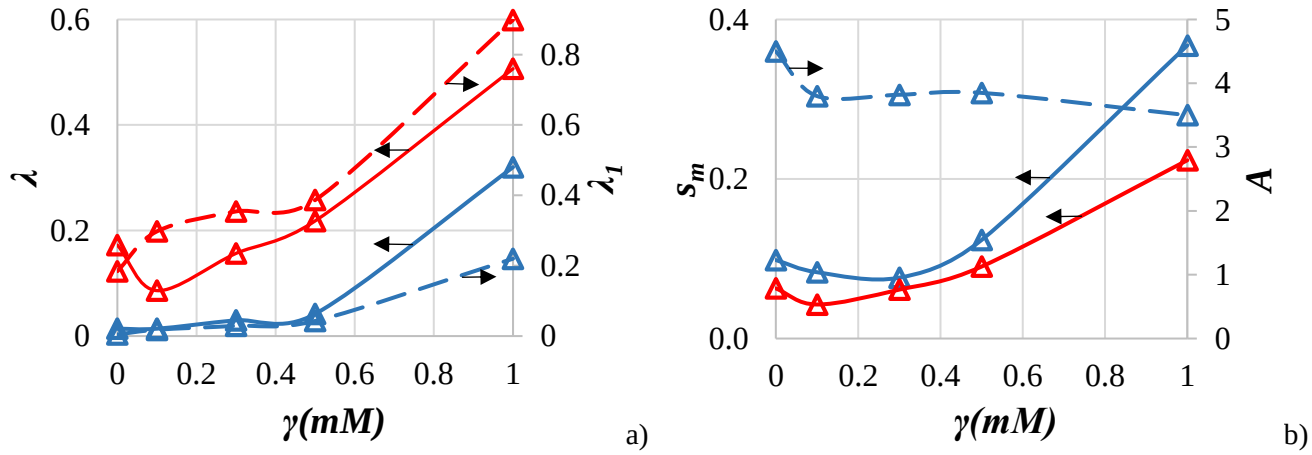


Fig. 8. $CaCl_2$ -salinity dependencies of model coefficients [*Wang et al.*, 2011].

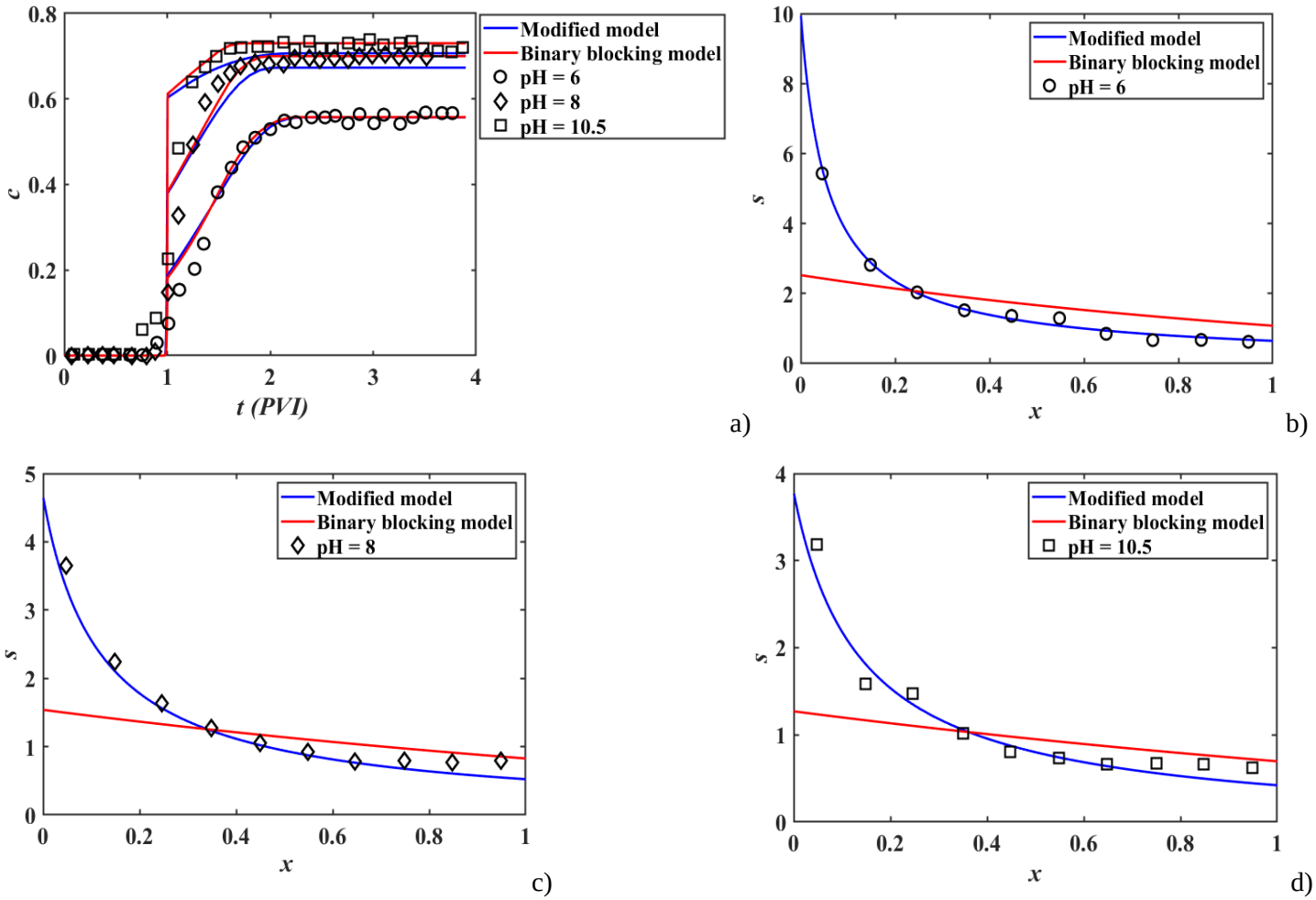


Fig. 9. Series of colloidal injection tests with different pH [*Wang et al.*, 2012b].

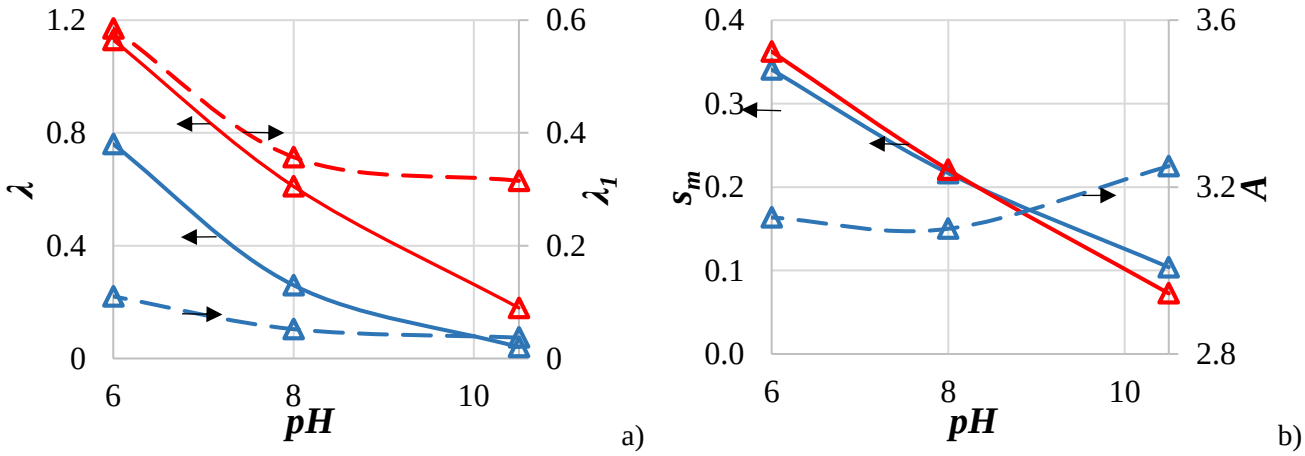


Fig. 10. pH dependencies of model coefficients [*Wang et al.*, 2012b].

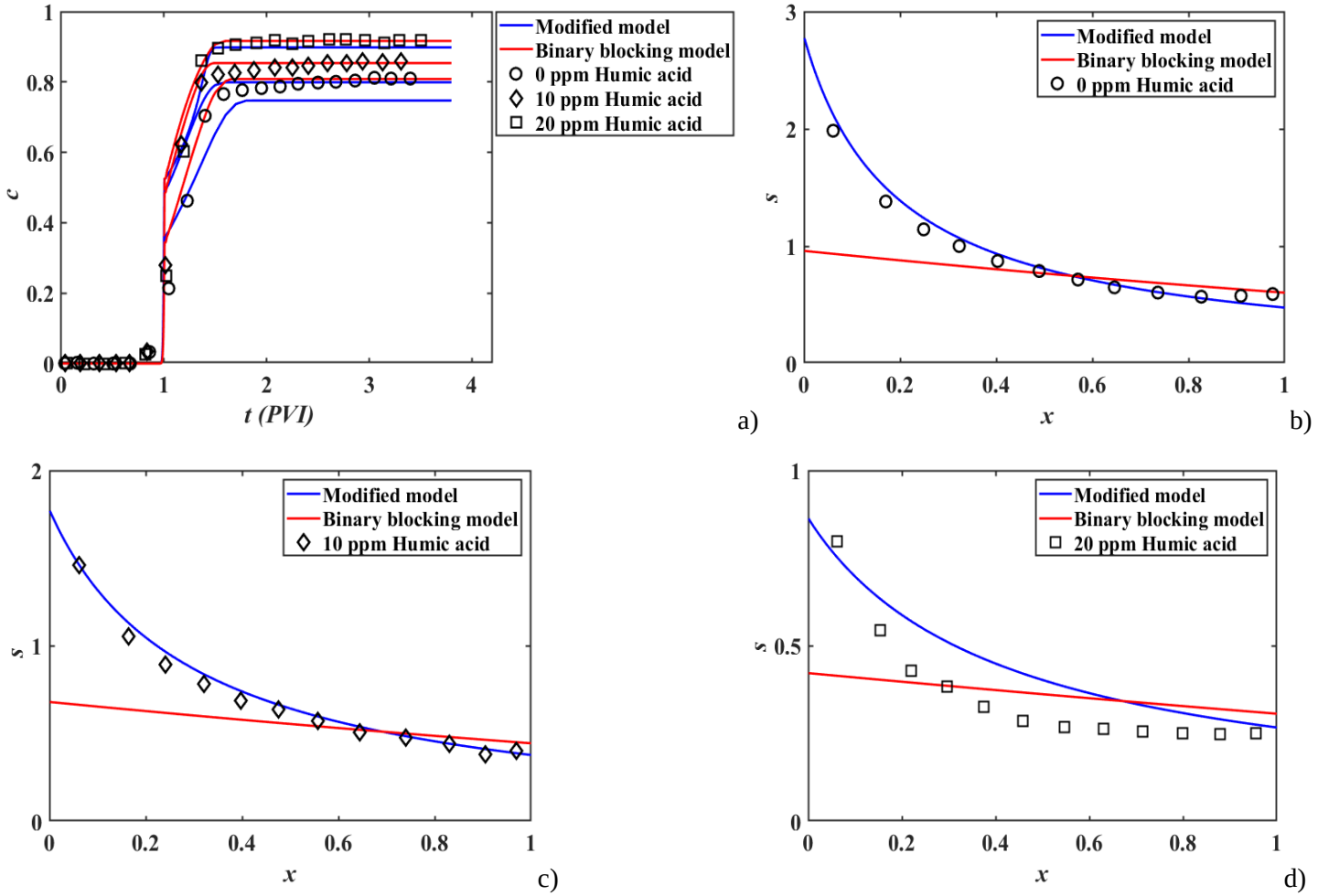


Fig. 11. Series of colloidal injection tests with different concentrations of HA [*Yang et al.*, 2017].

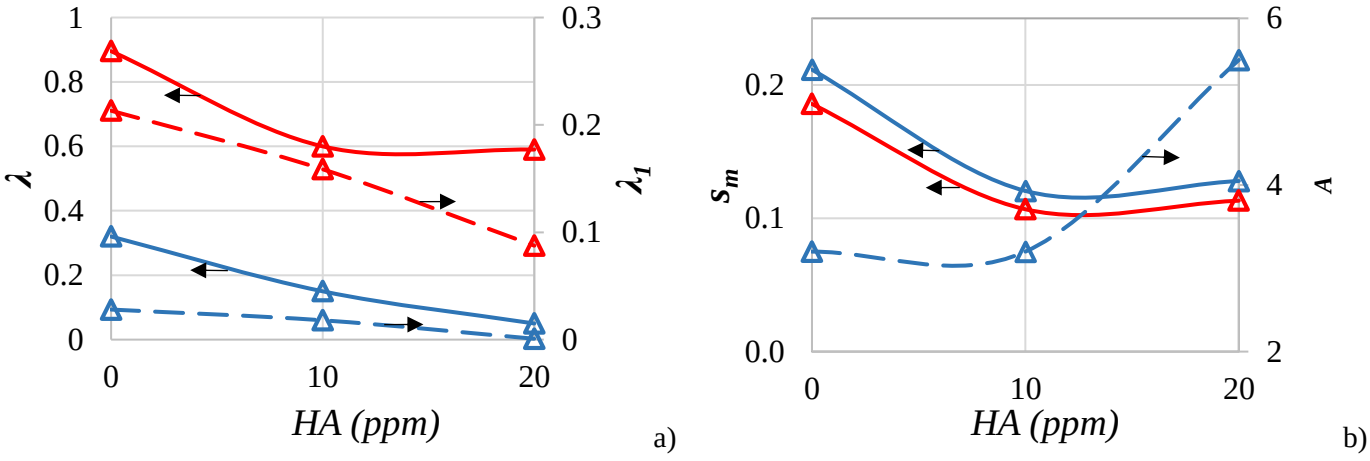


Fig. 12. Dependencies of model coefficients on HA concentration [*Yang et al.*, 2017].

Reference

Albinger, O., B. K. Biesemeyer, R. G. Arnold, and B. E. Logan (1994), Effect of bacterial heterogeneity on adhesion to uniform collectors by monoclonal populations, FEMS Microbiol. Lett., 124(3), 321-326.

Bai, H., L. Lassabatere, and E. Lamy (2018), Colloid Transport in Aggregated Porous Media with Intra-and Interaggregate Porosities, Industrial & Engineering Chemistry Research, 57(18), 6553-6567.

Bedrikovetsky, P. (2013), *Mathematical theory of oil and gas recovery: with applications to ex-USSR oil and gas fields*, Springer Science & Business Media.

Bedrikovetsky, P., Y. Osipov, L. Kuzmina, and G. Malgaresi (2019), Exact Upscaling for Transport of Size-Distributed Colloids, Water Resour. Res., 55(2), 1011-1039.

Bradford, S. A., and M. Bettahar (2006), Concentration dependent transport of colloids in saturated porous media, J. Contam. Hydrol., 82(1-2), 99-117.

Bradford, S. A., S. Torkzaban, and A. Wiegmann (2011), Pore-scale simulations to determine the applied hydrodynamic torque and colloid immobilization, Vadose Zone Journal, 10(1), 252-261.

Bradford, S. A., M. Bettahar, J. Simunek, and M. T. Van Genuchten (2004), Straining and attachment of colloids in physically heterogeneous porous media, Vadose Zone Journal, 3(2), 384-394.

Bradford, S. A., J. Simunek, M. Bettahar, M. T. van Genuchten, and S. R. Yates (2003), Modeling colloid attachment, straining, and exclusion in saturated porous media, Environ. Sci. Technol., 37(10), 2242-2250.

Chequer, L., P. Bedrikovetsky, T. Carageorgos, A. Badalyan, and V. Gitis (2019), Mobilization of Attached Clustered Colloids in Porous Media, Water Resour. Res., 55(7), 5696-5714.

Elimelech, M., J. Gregory, and X. Jia (2013), *Particle deposition and aggregation: measurement, modelling and simulation*, Butterworth-Heinemann.

Fogler, S. H. (2016), *Elements of chemical reaction engineering*, Prentice Hall.

Goldberg, E., M. Scheringer, T. D. Bucheli, and K. Hungerbühler (2014), Critical assessment of models for transport of engineered nanoparticles in saturated porous media, Environ. Sci. Technol., 48(21), 12732-12741.

Hilpert, M., and W. P. Johnson (2018), A binomial modeling approach for upscaling colloid transport under unfavorable attachment conditions: Emergent prediction of nonmonotonic retention profiles, Water Resour. Res., 54(1), 46-60.

Jiang, X., M. Tong, R. Lu, and H. Kim (2012), Transport and deposition of ZnO nanoparticles in saturated porous media, Colloids and Surfaces A: Physicochemical Eng. Aspects, 401, 29-37.

Kasel, D., S. A. Bradford, J. Šimůnek, M. Heggen, H. Vereecken, and E. Klumpp (2013), Transport and retention of multi-walled carbon nanotubes in saturated porous media: Effects of input concentration and grain size, Water Res., 47(2), 933-944.

Li, X., and W. P. Johnson (2005), Nonmonotonic Variations in Deposition Rate Coefficients of Microspheres in Porous Media under Unfavorable Deposition Conditions, Environ. Sci. Technol., 39(6), 1658-1665.

Li, X., T. D. Scheibe, and W. P. Johnson (2004), Apparent Decreases in Colloid Deposition Rate Coefficients with Distance of Transport under Unfavorable Deposition Conditions: A General Phenomenon, Environ. Sci. Technol., 38(21), 5616-5625.

Margules, M. (1904), *Über die Beziehung zwischen Barometerschwankungen und Konitinuitätsgleichung*, JA Barth.

Polyanin, A., and V. Zaitsev (2012), Handbook of nonlinear partial differential equations. Chapman & Hall/CRC Press, Boca Raton.

Polyanin, A. D., and A. V. Manzhirov (2006), *Handbook of mathematics for engineers and scientists*, CRC Press, Boca Raton.

Rabinovich, A., G. Dagan, and T. Miloh (2013), Dynamic effective properties of heterogeneous geological formations with spherical inclusions under periodic time variations, Geophysical Res. Lett., 40(7), 1345-1350.

Schijven, J. F., S. M. Hassanizadeh, and R. H. de Bruin (2002), Two-site kinetic modeling of bacteriophages transport through columns of saturated dune sand, J. Contam. Hydrol., 57(3-4), 259-279.
Shampine, L. (2005a), Solving hyperbolic PDEs in MATLAB, Appl. Num. Anal. Comp. Math., 2(3), 346-358.
Shampine, L. F. (2005b), Two-step Lax–Friedrichs method, Appl. Math. Lett., 18(10), 1134-1136.
Shapiro, A. A. (2007), Elliptic equation for random walks. Application to transport in microporous media, Physica A: Statistical Mech. its Applic., 375(1), 81-96.
Tartakovsky, A. M., M. Panzeri, G. D. Tartakovsky, and A. Guadagnini (2017), Uncertainty Quantification in Scale- Dependent Models of Flow in Porous Media, Water Resour. Res., 53(11), 9392-9401.
Tong, M., and W. P. Johnson (2007), Colloid Population Heterogeneity Drives Hyperexponential Deviation from Classic Filtration Theory, Environ. Sci. Technol., 41(2), 493-499.
Tufenkji, N., and M. Elimelech (2004), Deviation from the classical colloid filtration theory in the presence of repulsive DLVO interactions, Langmuir, 20(25), 10818-10828.
Tufenkji, N., and M. Elimelech (2005a), Breakdown of colloid filtration theory: Role of the secondary energy minimum and surface charge heterogeneities, Langmuir, 21(3), 841-852.
Tufenkji, N., and M. Elimelech (2005b), Spatial distributions of Cryptosporidium oocysts in porous media: Evidence for dual mode deposition, Environ. Sci. Technol., 39(10), 3620-3629.
Wang, D., W. Zhang, X. Hao, and D. Zhou (2013), Transport of biochar particles in saturated granular media: effects of pyrolysis temperature and particle size, Environ. Sci. Technol., 47(2), 821-828.
Wang, D., S. A. Bradford, R. W. Harvey, X. Hao, and D. Zhou (2012a), Transport of ARS-labeled hydroxyapatite nanoparticles in saturated granular media is influenced by surface charge variability even in the presence of humic acid, J. Hazard. Mater., 229, 170-176.
Wang, D., M. Paradelo, S. A. Bradford, W. J. Peijnenburg, L. Chu, and D. Zhou (2011), Facilitated transport of Cu with hydroxyapatite nanoparticles in saturated sand: effects of solution ionic strength and composition, Water Res., 45(18), 5905-5915.
Wang, D., S. A. Bradford, R. W. Harvey, B. Gao, L. Cang, and D. Zhou (2012b), Humic acid facilitates the transport of ARS-labeled hydroxyapatite nanoparticles in iron oxyhydroxide-coated sand, Environ. Sci. Technol., 46(5), 2738-2745.
Yang, W., Y. Wang, J. Shang, K. Liu, P. Sharma, J. Liu, and B. Li (2017), Antagonistic effect of humic acid and naphthalene on biochar colloid transport in saturated porous media, Chemosphere, 189, 556-564.
Yuan, H., and A. A. Shapiro (2010), Modeling non-Fickian transport and hyperexponential deposition for deep bed filtration, Chem. Eng. J., 162(3), 974-988.
Yuan, H., and G. Sin (2011), Uncertainty and sensitivity analysis of filtration models for non-Fickian transport and hyperexponential deposition, Chem. Eng. J., 168(2), 635-648.
Zhang, H., G. Malgaresi, and P. Bedrikovetsky (2018), Exact solutions for suspension-colloidal transport with multiple capture mechanisms, Int J. Non-linear Mech., 105, 27-42.

6 Explaining non-monotonic retention profiles during flow of size-distributed colloids

Gabriel Malgaresi, Ben Collins, Paul Alvaro, Pavel Bedrikovetsky

Chemical Engineering Journal

Statement of Authorship

Title of Paper	Explaining non-monotonic retention profiles during flow of size-distributed colloids
Publication Status	☑ Published ☐ Accepted for Publication ☐ Submitted for Publication ☐ Unpublished and Unsubmitted w ork w ritten in manuscript style
Publication Details	Malgaresi, G., Collins, B., Alvaro, P. and Bedrikovetsky, P., 2019. Explaining non-monotonic retention profiles during flow of size-distributed colloids. Chemical Engineering Journal, p.121984.

Principal Author

Name of Principal Author (Candidate)	Gabriel Malgaresi
Contribution to the Paper	Derivation of the mathematical model for non-monotonic retention profile. Sensitivity analysis of the mathematical model. Tuned the laboratory data. Developed the explanation for the non-monotonic retention profiles.
Overall percentage (%)	70%
Certification:	This paper reports on original research I conducted during the period of my Higher Degree by Research candidature and is not subject to any obligations or contractual agreements with a third party that would constrain its inclusion in this thesis. I am the primary author of this paper.
Signature	Date 25/10/2019

Co-Author Contributions

By signing the Statement of Authorship, each author certifies that:

i. the candidate's stated contribution to the publication is accurate (as detailed above);

ii. permission is granted for the candidate in include the publication in the thesis; and

iii. the sum of all co-author contributions is equal to 100% less the candidate's stated contribution.

Name of Co-Author	Ben Collins
Contribution to the Paper	Helped to develop the explanation for the non-monotonic retention profiles. Helped with the derivation of mathematical model and with the tuning of the laboratory data.
Signature	Date 25/10/2019

Name of Co-Author	Paul Alvaro
Contribution to the Paper	Helped to develop the explanation for the non-monotonic retention profiles. Helped with the derivation of mathematical model and with the tuning of the laboratory data.
Signature	Date 25/10/2019

Name of Co-Author	Pavel Bedrikovetsky
Contribution to the Paper	Problem formulation and supervision of the development of the whole work.
Signature	Date 23/10/2019

Chemical Engineering Journal 375 (2019) 121984

Contents lists available at ScienceDirect

Chemical Engineering Journal

journal homepage: www.elsevier.com/locate/cej

Explaining non-monotonic retention profiles during flow of size-distributed colloids

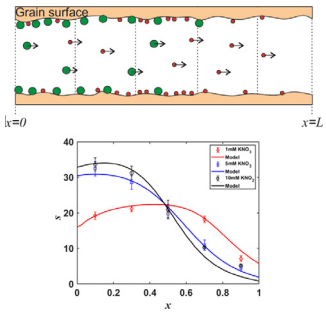
Gabriel Malgaresi, Ben Collins, Paul Alvaro, Pavel Bedrikovetsky*

Australian School of Petroleum, University of Adelaide, Australia

HIGHLIGHTS

- Non-monotonic retention profiles during colloidal flows are due to colloid heterogeneity.
- Exact upscaling of colloidal flow with fines adsorption, flux accessibility and reduction.
- Analytical model for 1D flow with colloid sorption, accessibility, and flux reduction.
- The analytical model exhibits non-monotonic retention profiles.
- Five-parametric model closely marches 7-dimensional lab-data array, validating the model.

GRAPHICAL ABSTRACT



ARTICLE INFO

Keywords:
Colloid
Attachment
Retention
Deep bed filtration
Particle size distribution
Non-monotonic

ABSTRACT

Non-monotonic retention profiles (NRP) have been observed in numerous studies of colloidal-nano flows in porous media. For the first time, we explain the phenomenon by distributed particle properties (size, shape, surface charge). We discuss colloidal-nano transport with fines attachment considering stochastically distributed filtration coefficient (particle attachment probability) and the area occupied by particle on the rock surface. The distributed dynamic system allows for exact averaging (upscaling) yielding a novel 3 × 3 system of equations for total concentrations. Besides the traditional equations of particle mass balance and capture-rate, the novel system contains a third independent equation for kinetics of site occupation during particle attachment. Ten laboratory tests exhibiting NRP have been successfully matched by the upscaled system for binary colloids. These laboratory tests with 7-parametric data arrays have been successfully matched by the 5-parameter model, which validates the model. The tuned parameter values belong to their common intervals. The laboratory data tuning was significantly simplified by deriving the exact solution of upscaled equations. These results provide valuable insights for understanding the transport mechanisms and environmental impact in colloidal-nano flows exhibiting NRP. Besides, the upscaled system and the analytical model for 1D transport facilitate interpretation of the laboratory coreflood data and allows for the laboratory-based predictions for 3D colloidal-nano transport at the field scale.

1. Introduction

Colloidal-nano transport in porous media occurs in numerous chemical engineering and environmental technologies. The examples include but are not limited to industrial filtering, storage of fresh water in underground reservoirs, propagation of viruses and bacteria in

* Corresponding author.
E-mail address: pavel.bedrikovetski@adelaide.edu.au (P. Bedrikovetsky).

https://doi.org/10.1016/j.cej.2019.121984
Received 1 May 2019; Received in revised form 13 June 2019; Accepted 15 June 2019
Available online 15 June 2019
1385-8947/ © 2019 Elsevier B.V. All rights reserved.

Nomenclature

$\tilde{B}$	surface area fraction occupied by a single particle with radius r, L^4
b	overall concentration of occupied sites on the rock surface
$\tilde{C}$	suspended concentration distribution, L^{-4}
c	total suspended particle concentration, L^{-3}
d	site occupation function,
F	individual suspension function for particles with size r, L^{-5}
f	upscaled suspension function, L^{-4}
h	filtration function
$\tilde{S}$	attached concentration distribution, L^{-4}
s	total attached particle concentration, L^{-3}
t	time, T
x	Cartesian coordinate, L
n	ratio between the filtration coefficients for small and large particles

Greek letters

α	fraction of the overall flux
β	accessibility factor
Γ	Henry's sorption coefficient
ε	ratio of areas occupied by large and small particles
λ	filtration coefficient, L^{-1}
μ	viscosity, $ML^{-1}T^{-1}$
ϕ	porosity

Abbreviations

BTC	breakthrough curve
NP	nanoparticle
NRP	non-monotonic retention profile
PVI	pore volumes injected
RP	retention profile

subterranean waters, disposal of industrial wastes in aquifers, transport of engineered nanoparticles (NPs), size-exclusion chromatography, and disposal of water produced during oilfield exploitation in aquifers [1–12]. Laboratory-based predictive mathematical modelling determines decision-making in these technologies.

During colloidal, suspension and NP transport in natural porous reservoirs (so-called deep bed filtration), the particles are captured by the rock. The capture mechanisms are size exclusion, attachment, straining, gravitational segregation, bridging, and diffusion into dead-end pores [1–3,5,13].

The mathematical model for deep bed filtration adopted in this study consists of mass balance of suspended, captured and adsorbed particles, and capture kinetics [14–17]

$$\frac{\partial}{\partial t}(\phi\beta c + s + \Gamma c) + U\frac{\partial(\alpha c)}{\partial x} = 0, \tag{1}$$

$$\frac{\partial s}{\partial t} = h(s)f(c)\alpha U. \tag{2}$$

Here c and s are suspended and attached concentrations, respectively, ϕ is the porosity, β is the accessibility factor, α is the fraction of the overall flux moving the accessible pores, Γ is Henry's adsorption coefficient, U is the fluid velocity, $h(s)$ is the filtration function, and $f(c)$ is the suspension function. Concentration c is defined as a number of suspended particles per unit of the liquid volume, while s is a number of retained particles per unit of the rock volume. For small c, the retention rate is proportional to suspended concentration

$$f(c) = \lambda c, \tag{3}$$

where the filtration coefficient λ (probability of particle capture per unit length of the trajectory) is equal to $\lambda = k_d\phi/U$, where k_d is the deposition rate coefficient [14,18,19].

Particle capture by a pore is analogous to chemical reaction "pore + particle". Therefore, the capture kinetics (2) is analogous to the active mass law that contains the product of the filtration function that depends on the retained concentration, and the suspension function that depends on the suspended concentration. Like in the active mass law, the functions are proportional to the corresponding concentrations for small values of these concentrations. Different forms of suspension function $f(c)$ are used to match the experimental data [20,21].

The initial-boundary value conditions for constant-concentration colloid injection into a clean bed are:

$$t = 0:\ c = s = 0,\quad x = 0:\ c = c^0 \tag{4}$$

where c^0 is particle concentration in the injected suspension.

Eq. (2) suggests gradual retention accumulation with time. During injection of one pore volume into a core with length L, $1/\omega$ pore volumes are injected into the first core section with length ωL ($\omega < 1$). So, for each $\omega < 1$, the total retained concentration in the first section of the core is higher than that in the overall core. Therefore, the retention profiles (RPs) given by solutions of system (1, 2) monotonically decrease. All available analytical models for deep bed filtration exhibit monotonic RPs [13,22–29]. In contrast to this expected behaviour, numerous experimental studies of particle flows through porous media exhibit NRP. NRPs have been observed for pathogens [30–33], engineered NPs [2,34,35], and glass microspheres [32,36].

NRP can be reproduced by the mathematical model that accounts for depth dependency of the filtration function $h(x,s)$, introduced by Bradford, et al. [37]. This dependency is considered to have power-law type; tuning the power yields high agreement between the laboratory and modelling data. Close match has been obtained for breakthrough curves (BTCs) and RPs. Presently, this model is widely used for interpretation of the laboratory data on colloidal transport [17,38]. Yet, Goldberg et al. [38] suggested that more physics justification for x-dependency of the filtration function is required.

The two-speed mathematical model to explain the NRP for monodispersed flow was developed by Yuan and Shapiro [39]. The slow particles are assumed to move along the grain surfaces into the stagnant zones, while the fast particles move in the bulk of the carrier fluid. Both fines attachment and detachment are considered. Seven empirical model parameters are tuned from the laboratory data. An excellent match of BTCs and RPs was achieved. Besides, the paper shows that two models with essentially non-equivalent physical assumptions may describe the same set of coreflood data. Knowledge of the micro-level filtration mechanisms is necessary to discriminate between the models.

Another two-velocity model to explain the NRPs was proposed by Bradford, et al. [40]. Neglecting retained-fines detachment into the bulk flux reduces the number of model coefficients to six. The authors highlight non-uniqueness of the tuning problem, where the same laboratory data can be reproduced by different sets of the model parameters. The model successfully matches numerous laboratory tests.

Hilpert and Johnson [41] developed a random-walk model in a one-dimensional (1D) network of Happel cells for colloid transfer between bulk pore fluid, the near-surface fluid domain, and irreversible attachment. The particles move in the bulk of the fluid and in the near-surface fluid domain with different speeds. The particle detachment to the bulk pore fluid occurs via diffusion and the expulsion at rear flow stagnation zones. The non-monotonic retention profiles emerge from the upscaled modelling.

Two-speed effects are pronounced in heterogeneous media with large size of micro-heterogeneity, like layer-cake laminated or

fractured-porous formations [21]. For low-dispersed heterogeneity, where distances between the high- and low-conductivity channels have an order of magnitude of the pore length, the Peclet's number has an order of magnitude of 10^{-3}–10^{-5}, suggesting "instant" equalising of the suspension concentrations in the populations [42]. This yields effective single-population transport with the average "low" velocity [43,44].

Wang et al. [45] and Becker et al. [46] experimentally observed non-monotonic particle retention during commingled injection of colloid with surfactant. Numerical modelling of colloidal-surfactant transport with competitive attachment/adsorption exhibits experimentally observed non-monotonic retention profiles. The model matches the experimental data with high accuracy.

Currently, NRP is an important topic of significant and frequent debates [2,4,5,35,36,39,47–52]. There is no consensus on the physics phenomena yielding NRPs.

The current paper explains non-monotonic retention behaviour by the colloid heterogeneity, where the attached particles with different properties (size, surface charge, form) occupy different areas on the rock surface. We discuss multicomponent colloidal flow in porous media without detachment accounting for pore accessibility and consequent flux reduction, slow particle motion and adsorption. The retention rate is a function of the vacant area for attachment to the rock (Langmuir's blocking) [53]. The micro-scale population-balance equations have first integrals along the characteristic lines; this allows for exact upscaling procedure, yielding the mass balance and kinetics equations for averaged concentrations. The upscaled 1D problem allows for exact solution. The analytical model exhibits NRP. The upscaled binary-colloid model successfully matches ten laboratory tests. Moreover, the dimension of the measured data array exceeds the number of tuned parameters, which validates the model. Tuning the model coefficients and using first integrals along the characteristic lines yield downscaling, i.e., determining the individual properties for each particle population. These results provide valuable insights for understanding the colloidal-nano transport phenomena exhibiting NRP.

The structure of the paper is as follows. Section 1 introduces the mathematical model for transport of uniform colloids and presents the physics explanations of NRPs. Section 2 provides a qualitative analysis of binary colloidal transport with attachment and predicts NRPs. Section 3 develops the exact upscaling procedure for multicomponent colloidal flows and derives the exact solution for upscaled model. Section 4 discusses the results, including type curves for BTC and RP and matching the experimental data. Section 5 concludes the paper.

2. Qualitative explanation of non-monotonic retention profiles

In this section we explain the occurrence of non-monotonic RP during colloidal injection with two distinct particle sizes. The large particles have a higher filtration coefficient (probability of particle capture per unit length of the trajectory) and occupy a higher proportion of area on the rock surface when attached.

Consider an early time (t_1) when the total area occupied by the retained particles is significantly lower than the initial vacant area on the rock surface. The particles do not compete for vacancies, so the two populations filter independently. The retention rate of large particles is higher than that of small particles at the inlet, as capture probability is higher for large particles. Consequently, the suspended and retained concentrations of large particles decline faster along the core. At some distance Δ from the core inlet, the suspended concentration of large particles is significantly lower than that of small particles. Therefore, as

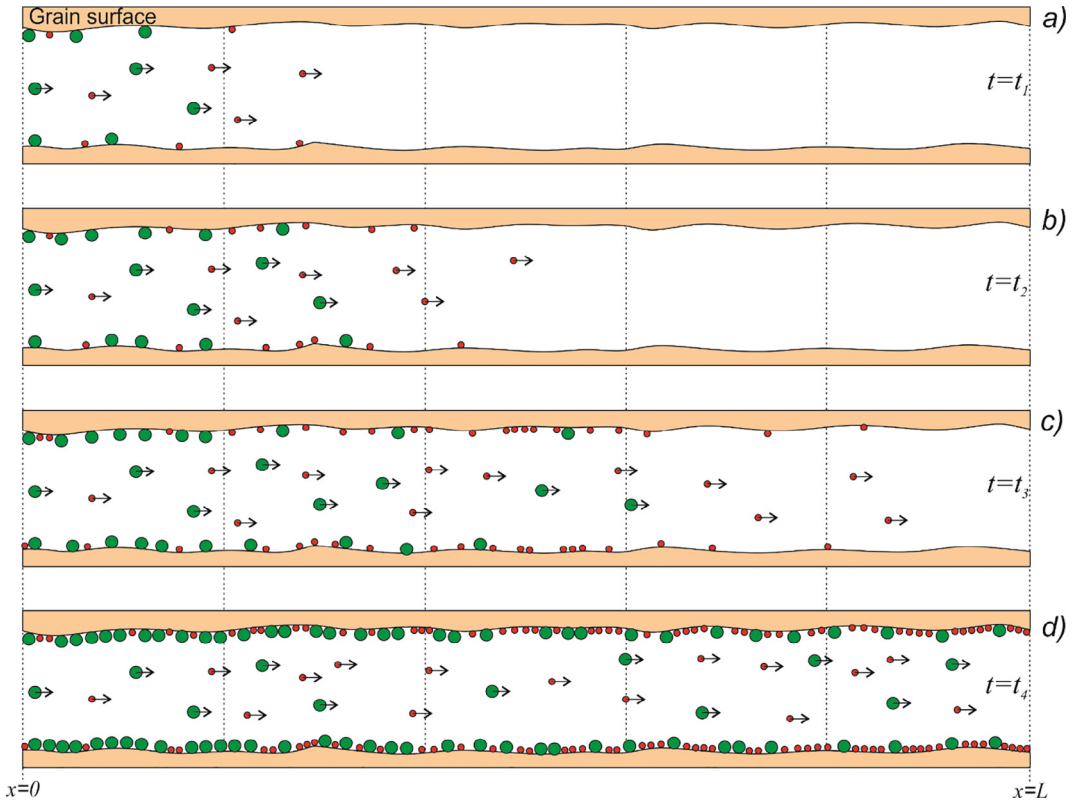


Fig. 1. Schematic showing retained particle distribution for four-stage evolution of retention profiles during simultaneous transport of two colloid size populations: a) large (green) and small (red) particles do not compete for vacancies, yielding declining profiles for both populations at an early stage of injection (moment t_1); b) at intermediate moment (t_2), large particles accumulate in the beginning of the core, while small particles travel further to accumulate within the core, resulting in non-monotonic profile for small particles; c) at the next intermediate moment (t_3), the total retention profile also becomes non-monotonic; d) at moment (t_4) all vacancies are occupied, with large and small particle quantities decreasing and increasing, respectively, with distance.(For interpretation of the references to colour in this figure legend, the reader is referred to the web version of this article.)

shown in Figs. 1a and 2a, near to the core inlet large-particle retention exceeds that for small particles, while small particle retention is predominant further in the core. Individual and total retention and suspension profiles monotonically decline across the core.

At later time (t_2), the area occupied by attached particles near the inlet reaches the order of magnitude of the initial vacant area (Fig. 1b). The particles are now competing for vacancies. As large particles that occupy higher area are retained predominantly near the inlet, vacant surface area increases rapidly along the core. Therefore, the retention rates of both populations is higher at positions further in the core than at the inlet, as there is higher vacant area.

At distance Δ from the core inlet, the suspended concentration of small particles is not significantly lower than its injected concentration; however, the amount of vacant surface area is significantly higher than at the inlet. So the retention rate of small particles at this point exceeds that at the inlet, and at some moment the retained concentration of small particles at the distance Δ exceeds that at the inlet. The small-particle retained concentration is zero at the suspended concentration front and increases from the inlet. Therefore, the small-particle RP has transitioned to non-monotonic (red curve in Fig. 2b). In Fig. 2b, its maximum is reached in the second core section.

As shown above, the suspended large-particle concentration always declines rapidly near to the inlet. As retention occurs in positions with low vacant area, the negative gradient of the large particle RP increases with time near to the inlet but the profile always monotonically decreases (green curve in Fig. 2c). The total RP monotonically decreases at initial stages but at some time (t_3) becomes non-monotonic (black curve). The maximum of total RP is reached in the third section of the core (Fig. 1c).

Further we refer to the maximum points as the positions where the retained concentrations are maximum. So far we have discussed the maximum points for small particle and total retained concentrations. Consider any point of the core ahead of the maximum point for small particles after the moment t_3. The vacant area at the maximum point is lower than at positions further into the core; whereas, the suspended concentration is not significantly lower. So the retention rate for small particles is higher at positions ahead of the maximum point. Hence, the maximum point for small particles transitions through the core; i.e., the small particle RP monotonically increases over the core once the maximum point reaches the end of the core at the moment t_4 (Fig. 2d). By the same reasoning, the total RP also monotonically increases. As shown above, large particle retention never exceeds that at the inlet and monotonically decreases over the core. The three RPs asymptotically tend to their stabilised shapes as time tends to infinity, remaining monotonic.

3. Mathematical modelling

This section presents the model assumptions and system of governing equations (Sections 3.1 and 3.2), develops an exact upscaling procedure (Sections 3.3 and 3.4), develops the downscaling procedure (Section 3.5), and verifies the analytical model (Appendix A) by comparison with the numerical solution (Section 3.6).

3.1. Model assumptions for multi-size colloidal transport

We consider a single-phase carrier fluid transporting colloidal suspension with multiple-size particles. The fluid and particles are incompressible. The volume of suspension is equal to the total of volumes of liquid and particles (Amagat's law) [54]. Those assumptions yield

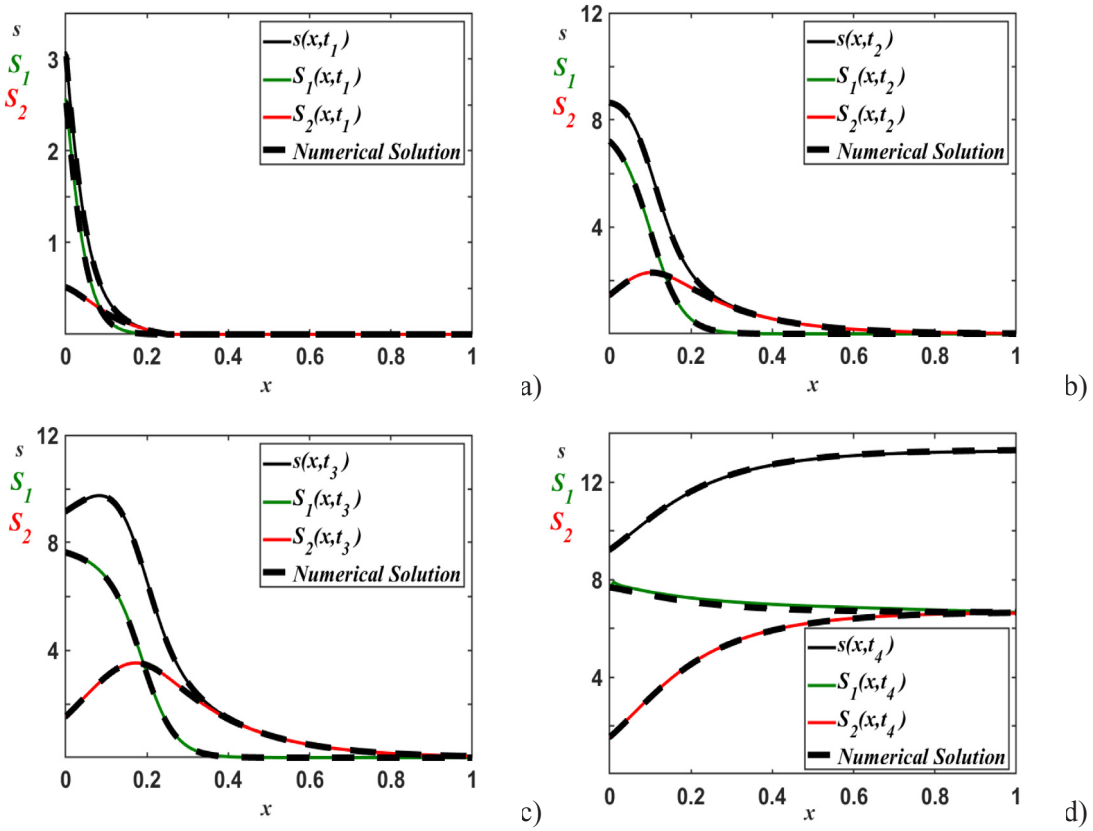


Fig. 2. Large-particle, small-particle, and total retention profiles (green, red and black curves, respectively) corresponding to moments $t_1 = 1$, $t_2 = 1.7$, $t_3 = 3$, and $t_4 = 50$ PVI: a) all profiles monotonically decrease; b) the small-particle profile becomes non-monotonic; c) the total profile becomes non-monotonic; d) stabilised large-particle profile monotonically decreases and stabilised small-particle and total profiles monotonically increase. Indexes 1 and 2 correspond to small and large particles, respectively.

conservation of the overall suspension flux.

The particles can adsorb on the rock surface; the equilibrium adsorption with Henry's isotherm takes place [55]. The finite-size particles occupy β-th fraction of the porous space, called the accessibility factor [15,37,56–58]. The flux that carries particles through the accessible pore space is equal to α-th fraction of the overall flux of carrier fluid. The model (1, 2) accounts for low particle speed if compared with the carrier water, because the flux reduction factor α contains the drift-delay factor [43,44]. We assume that Henry's constant, accessibility and flux reduction factors are the same for all particles.

The filtration function is the same for all populations, while the suspension function depends on particle radius [21,59]. So, different particle populations compete for the same attachment vacancies. We assume the conditions of large-scale approximation, where the reference time τ of the sorption kinetics is significantly smaller than the time of the pore volume injection $\phi L/U << 1$ (the assumption of long cores). In this case, the deviation between the current and equilibrium adsorption concentrations is negligible [54]. Adsorption is also assumed to be reversible, while the attachment is fully irreversible, i.e., no particle detachment occurs. Diffusion and dispersion fluxes large-scale approximation are assumed to be negligibly small if compared with the advective fluxes [60,61]. We assume the competitive blocking of the populations, where the filtration function h depends on the total concentration of attached particles, representing the influence of the attached particles on the availability of the vacancies. In the particular case of the Langmuir's attachment, the filtration function is equal to vacancy concentration [46,62–65].

3.2. Governing equations for multiple populations

Basic equations for single-phase multi-component suspension-nano transport in porous media include mass balance of suspended, attached and adsorbed particles, and capture rate, for all populations [57,59]:

$$\frac{\partial}{\partial t}(\phi\beta\tilde{C}_k + \tilde{S}_k + \tilde{\Gamma}\tilde{C}_k) + U\frac{\partial}{\partial x}(\alpha\tilde{C}_k) = 0 \tag{5}$$

$$\frac{\partial\tilde{S}_k}{\partial t} = h\left(\sum_{i=1}^{m}\tilde{B}_i\tilde{S}_i\right)F_k(\tilde{C}_k)\alpha U, \quad k = 1, 2. ..N \tag{6}$$

where all parameters with tilde are dimensional, $\tilde{C}_k$ and $\tilde{S}_k$ are suspended and attached concentrations of k-th particle population, respectively, ϕ is the porosity, λ_k is the filtration coefficient of each population, $\tilde{B}_k$ is the ratio between the area occupied by a single attached particle and the overall rock surface, and Γ is Henry's sorption coefficient.

We use the following dimensionless parameters and variables:

$$x = \frac{\tilde{x}}{L};\ t = \frac{U\tilde{t}}{\phi L};\ c^0 = \sum_{i=1}^{m} C_i^0;\ C_k = \frac{\tilde{C}_k}{c^0};\ S_k = \frac{\tilde{S}_k}{\phi c^0};\ \lambda_k = \tilde{\lambda}_k L;$$
$$B_k = \phi c^0\tilde{B}_k;\ A = \frac{\tilde{A}}{\phi c^0};\ \Gamma = \frac{\tilde{\Gamma}}{\phi};\quad k = 1, 2, ...,N \tag{7}$$

where all parameters without tilde are dimensionless, and L is the core length.

Substituting parameters (7) into system (5) and (6) we obtain the dimensionless governing system

$$\frac{\partial}{\partial t}(\beta C_k + S_k + \Gamma C_k) + \frac{\partial}{\partial x}(\alpha C_k) = 0 \tag{8}$$

$$\frac{\partial S_k}{\partial t} = h\left(\sum_{i=1}^{m} B_i S_i\right)F_k(C_k)\alpha, \quad k = 1, 2. ..N \tag{9}$$

where $F_k(C_k)$ is the suspension function of k-th population.

The initial conditions and boundary conditions correspond to injection of colloids with constant composition into a clean bed:

$$t = 0{:}\ C_k = S_k = 0;\ x = 0{:}\ C_k = C_k^0 \tag{10}$$

System of Eqs. (8)–(10) determines $2N$ unknowns C_k and S_k.

3.3. Upscaling and system for total concentrations

In this section we derive the upscaled system for total suspended, retained and adsorbed concentrations. Substituting Eq. (9) into Eq. (8) yields

$$(\beta + \Gamma)\frac{\partial C_k}{\partial t} + \alpha\frac{\partial C_k}{\partial x} = -h\left(\sum_{i=1}^{m} B_i S_i\right)F_k(C_k)\alpha \tag{11}$$

Characteristic form of first order partial differential equations (PDE) is a system of ordinary differential equations along characteristic lines in domain $\alpha(\beta + \Gamma)^{-1}t > x$ [60,61]

$$\frac{dt}{dx} = \frac{\beta + \Gamma}{\alpha},\ \frac{dC_k}{dx} = -h\left(\sum_{i=1}^{m} B_i S_i\right)F_k(C_k) \tag{12}$$

Dividing variables in Eqs. (12) yields

$$\frac{dG_k(C_k)}{dx} = -h\left(\sum_{i=1}^{m} B_i S_i\right);\ \ G_k(C_k) = \int_{C_k^0}^{C_k}\frac{du}{F_k(u)},\ \ k = 1, 2. ..N \tag{13}$$

The right hand sides of Eqs. (13) coincide for all k = 1,2…N. Functions G_k are equal at $x = 0$. Therefore, values $G_k(C_k(x,t))$ are equal for all k. In particular,

$$G_k(C_k) = G_1(C_1) \tag{14}$$

The total concentrations for suspended and retained particles and occupied area are determined as

$$c = \sum_{k=1}^{N} C_k,\quad s = \sum_{k=1}^{N} S_k,\quad b = \sum_{k=1}^{N} B_k S_k \tag{15}$$

Expressing individual concentrations C_k from Eq. (14), accounting for monotonicity of functions G_k,

$$C_k = G_k^{-1}[G_1(C_1)], \tag{16}$$

substituting relationships (16) into Eq. (15) and expressing total concentration c via C_1 yield

$$c = \sum_{k=1}^{N} G_k^{-1}[G_1(C_1)],\ \ C_1 = g_1(c),\ \ g_1 = \left[\sum_{k=1}^{N} G_k^{-1}(G_1)\right]^{-1} \tag{17}$$

Here symbol $()^{-1}$ corresponds to inverse function.

Substituting Eqs. (17) into Eqs. (16) leads to expressing each individual component C_k versus total suspension concentration

$$C_k = G_k^{-1}[G_1(g_1(c))] = g_k(c) \tag{18}$$

So, all individual concentrations C_k are functions of the total concentration c.

Summing Eqs. (15) into Eq. (8) yields total mass balance for all particle populations

$$\frac{\partial}{\partial t}(\beta c + s + \Gamma c) + \frac{\partial(\alpha c)}{\partial x} = 0 \tag{19}$$

Multiplying each Eq. (9) by B_k, accounting for expressions (18), and summing the results lead to kinetics equation for site occupation:

$$\frac{\partial b}{\partial t} = h(b)d(c)\alpha,\quad d(c) = \sum_{k=1}^{N} B_k F_k(g_k(c)) \tag{20}$$

where $d(c)$ is the occupation function.

Adding Eqs. (9) for k = 1,2…N yields the kinetics equation for retention rate

$$\frac{\partial s}{\partial t} = h(b) f(c)\alpha, \quad f(c) = \sum_{k=1}^{N} F_k(g_k(c)) \tag{21}$$

For $x < \alpha(\beta + \Gamma)^{-1}t$, the solution is zero at both scales. System (19)–(21) describes 1D multicomponent colloidal-suspension transport. Initial condition $b = 0$ adds to conditions (10) for injection into a clean bed.

3.4. System for binary colloid transport

Consider small injected concentrations where the suspension functions are linear, like in Eq. (3):

$$F_k(C_k) = \lambda_k C_k, \quad k = 1, 2 \tag{22}$$

Formulae (13), (16), (17) for $N = 2$ become:

$$G_k(C_k) = \ln\left[\frac{C_k}{C_k^0}\right]^{1/\lambda_k}, \quad C_2 = C_2^0\left[\frac{C_1}{C_1^0}\right]^{\lambda_2/\lambda_1}, \quad c = C_1 + C_2^0\left[\frac{C_1}{C_1^0}\right]^{\lambda_2/\lambda_1},$$
$$n = \frac{\lambda_1}{\lambda_2}; \quad k = 1, 2 \tag{23}$$

yielding explicit expressions for suspension and occupation functions

$$f(c) = \lambda_1 g_1(c) + \lambda_2 C_2^0\left[\frac{g_1(c)}{C_1^0}\right]^{\lambda_2/\lambda_1} \tag{24}$$

$$d(c) = B_1\left\{\lambda_1 g_1(c) + \varepsilon\lambda_2 C_2^0\left[\frac{g_1(c)}{C_1^0}\right]^{\lambda_2/\lambda_1}\right\}, \quad \varepsilon = \frac{B_2}{B_1} \tag{25}$$

3.5. Downscaling: determining individual population properties from total-concentration data

Expressing individual concentrations via total concentration in Eqs. (9) facilitates downscaling:

$$C_k(x, t) = C_k^0\left[\frac{g_1(c(x, t))}{C_1^0}\right]^{\lambda_k/\lambda_1}, \quad S_k(x, t)$$
$$= \alpha\int_0^t (1 - b(x, y))F_k(C_k(x, y))dy, \tag{26}$$

i.e. the individual concentrations can be obtained from matching the large-scale model using the laboratory data on both BTCs and RPs.

3.6. Comparison between the analytical and numerical models

One-dimensional problem of colloidal injection into clean bed (10), (19), (20), (21) allows for exact analytical solution derived in Appendix A. Here we validate this analytical model (A.1–A.5) by comparison with the numerical solution using the Shampine [66,67]. The two-step Lax–Friedrichs finite-difference method [66,67] is inbuilt into MATLAB computer software (http://faculty.smu.edu/shampine/current.html). The speed of characteristics in Eq. (8) is equal to $\alpha(\beta + \Gamma)^{-1}$. Consequently, the Courant–Friedrichs–Lewy (CFL) stability condition is expressed by inequality $\alpha\Delta x[(\beta + \Gamma)\Delta t]^{-1} > 1$. We divide the spatial domain [0,1] into 1000 evenly spaced intervals, with the time step selected to satisfy the CFL condition, $\Delta t = 0.9\,\alpha(\beta + \Gamma)^{-1}\Delta x$.

Fig. 2 presents the comparison-study results for the following parameters: $B_2 = 0.025$, $B_1 = 0.125$ ($\varepsilon = 0.2$), $C_2{}^0 = 0.5$, $\lambda_2 = 5$, and $\lambda_1 = 25$ ($n = 5$). Close agreement between the exact and numerical

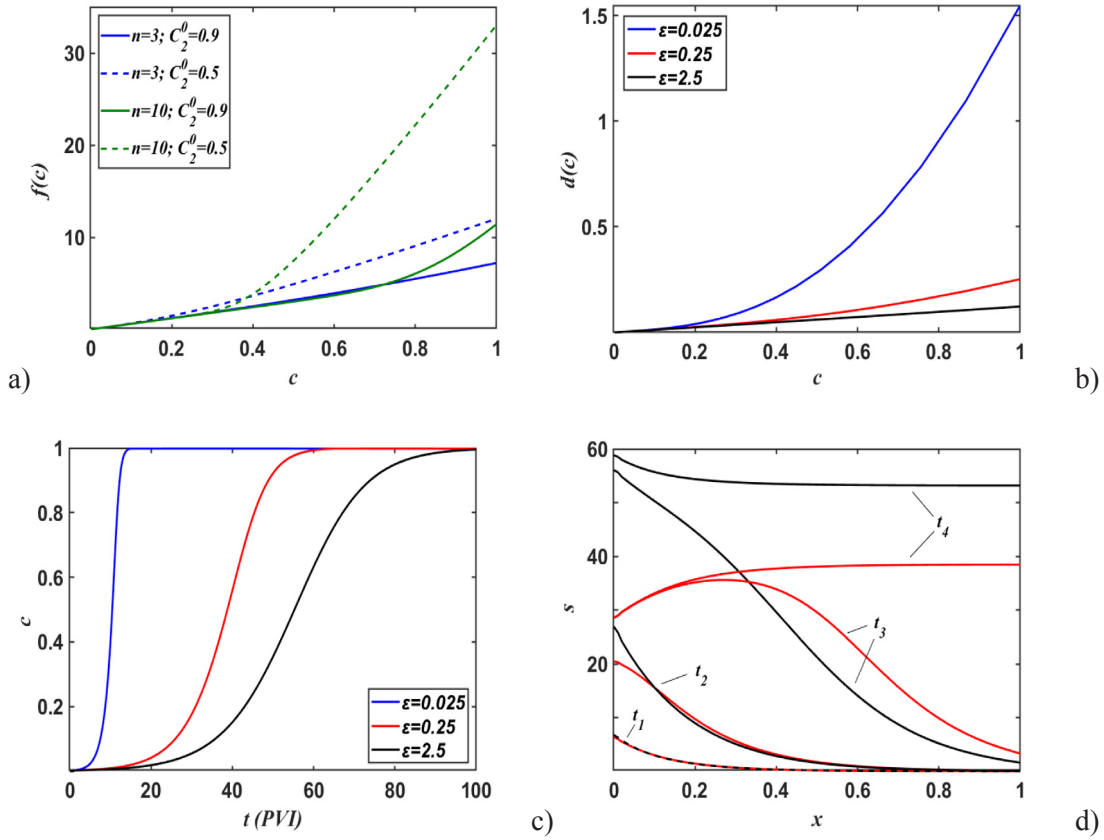


Fig. 3. Type curves for the model functions and solutions: a) suspension function for different ratios between filtration coefficients λ_2 and λ_1, $n = 3$ and 10, and injection concentrations $C_2{}^0 = 0.5$ and 0.9; b) occupation function for different ratios of occupied areas B_2 and B_1 ($\varepsilon = 0.025$, 0.25, and 2.5); c) effect of ε on the breakthrough concentration profile; d) retention profiles for $\varepsilon = 0.25$ (red curves) and $\varepsilon = 2.5$ (black curves) at the moments $t_1 = 1$, $t_2 = 5$, $t_3 = 25$ and $t_4 = 100$ PVI. Fixed parameters used in the modelling for b, c and d) are $B_2 = 0.02$, $C_2{}^0 = 0.9$, $\lambda_2 = 6$; $n = 3$.

solutions is observed for RP at four typical moments.

4. Results and discussion

In this section we present the type curves for suspended and occupation functions, based on the upscaling procedure, and investigate the forms of BTCs and RPs, based on the analytical model (Section 4.1). Section 4.2 presents matching of the laboratory data and tuning the model coefficients. Sensitivity study of BTCs and RPs with respect to flux reduction coefficient and adsorption constant are given in Section 4.3. Section 4.4 presents the summary of upscaling and exact integration and discusses their extension to more complex flow systems.

4.1. Analysis of 1D analytical modelling

Analytical modelling presented in Fig. 2 exhibits monotonically decreasing RP at the initial stage of injection, appearance of a peak in the RP for small-particles during the second stage, occurrence of non-monotonic total RP at the third stage, and monotonically increasing profiles at stabilisation. So, the analytical modelling fully reproduces the qualitative behaviour of binary-colloid flow predicted by the qualitative analysis (Fig. 1).

Fig. 3 shows the effects of the ratios $n = \lambda_1/\lambda_2$ and $\varepsilon = B_2/B_1$ on suspension and occupation functions, BTCs and RPs.

Increase of ratio n under fixed filtration coefficient for small particles yield an increase in λ_1, so the suspension function increases. Green curves in Fig. 3a are located above the corresponding blue curves. Increase in injected concentration of small particles ${C_2}^0$ and consequent decrease in ${C_1}^0$ causes the suspension function to decrease. Dashed curves in Fig. 3a are located above the corresponding continuous curves. For small total concentration ($c \to 0$), suspension function degenerates into linear function (3).

Fig. 3b shows that if the ratio of occupied areas ε increases under fixed occupied area by small particles B_2, the area B_1 decreases, area b is occupied at lower rate, filtration function h increases; as it follows from kinetics (21) the occupation function $d(c)$ decreases. Total suspended concentration also decreases, i.e. the BTC moves down (Fig. 3c).

For $\varepsilon = n$ the occupation function $d(c)$ becomes linear. This corresponds to the same area being occupied by each population per unit of time. For all cases where $\varepsilon \neq n$, $d(c)$ is nonlinear. The larger the difference between B_1 and B_2, the larger the curvature of the occupation function. The $d(c)$-curves are convex for $\varepsilon < n$ and concave for $\varepsilon > n$ (Fig. 3b).

The red curves in Fig. 3d are RPs corresponding to the case where large particles attach with higher intensity and occupy larger area than small particles ($\lambda_1 > \lambda_2$ and $B_1 > B_2$). The profile is monotonic and convex at the beginning of injection (t_1). It remains monotonic but at the moment t_2 the profile becomes concave near to the inlet. The profile then becomes non-monotonic at the moment t_3 and stabilises with concave monotonically increasing shape at the moment t_4.

Black curves in Fig. 3d correspond to the case where large particles attach with lower intensity ($\lambda_1 < \lambda_2$) and occupy higher area than small particles ($B_1 > B_2$). The RPs always keep the monotonically decreasing form.

The effect of the filtration coefficient ratio $n = \lambda_1/\lambda_2$ on the RP are shown in Fig. 4. The first three stages shown in Fig. 1 are reproduced. The higher the filtration ratio n, the faster that non-monotonicity appears and the more pronounced is the non-monotonic behaviour. For fixed filtration ratio, increase in the filtration coefficient for small particles yields increase in the retained concentration.

4.2. Matching the experimental data

Fig. 5 shows the laboratory data on injection of silver NPs into soil specimen with length 10 cm, diameter 1.1 cm and with three salinities 1, 5, and 10 mM for KNO_3 (Fig. 5a and b) and 0.1, 0.5 and 1 mM for Ca $(NO_3)_2$ (Fig. 5c and d) [35]. Here six tests correspond to mean particle sizes of 40, 79, 92, 109, 147, and 161 nm; the particle diameters in each population vary from 5 nm to doubled mean diameter. The model parameters - filtrations coefficients and occupied areas for both populations and the injected concentration – are estimated by least-square minimisation of the deviation between the laboratory and modelling breakthrough curves and retention profiles (RPs). The matching is performed by the nonlinear least squares method [68] implemented as an internal optimisation procedure within Matlab. Simultaneous matching of BTCs and RPs is performed by tuning five model coefficients λ_2, n, ${C_2}^0$, B_2 and ε. We consider no adsorption mechanism ($\Gamma = 0$), no flux reduction $\alpha = 1$, and an accessibility factor of $\beta = 1$. The values of five tuned model coefficients are presented in Table 1. The BTCs have at least three free parameters and the number of degrees of freedom for RPs is at least four. All matched curves are located insides the areas bounded by the error bars. The tenth and eleventh columns in Table 1 reveal coefficient-of-determination values close to one for the bulk of the data. Close match of seven-parametric array of experimental data by five model parameters validates the model.

Matching of silver NPs injection into quartz sand column also exhibit close agreement between the experimental and analytical modelling data (rows 8 and 9 of Table 1) [47]; here the particle diameters vary from 40 to 75 nm. Rows 10 and 11 correspond to the tests on deionised water injection with TiO_2 NPs into white sand column, where the hydrodynamic particle diameters vary from 6 to 70 nm [2].

The model parameters determined from 20 PVI's history (red curves in Fig. 5a and b) allow revealing long-term total and individual breakthrough histories until stabilisation (50 PVI) as shown in Fig. 6a. The corresponding total and individual RPs near stabilisation are revealed in Fig. 6b and c at moment t_4. Moment t_3 in Fig. 6c reveals the individual RPs at termination of the experiment. Individual and total retention profiles at earlier moments t_1 and t_2 are also shown in Fig. 6b and c. The behaviour of the individual and total retention profiles match that qualitatively predicted in Fig. 1.

The breakthrough and retained concentrations in Fig. 5 are measured as a particle number per unit of volume, as defined in the comments after Eqs. (1) and (2). However, the original experimental publications [2,35,47] are using volumetric concentrations. Using given particle sizes, we re-calculated the volumetric concentrations into c and s used in the present paper. The non-monotonic profiles are less pronounced in the original publications. This phenomenon is explained by lower contribution of small particles into the overall concentration than that by the large particles. The total NRP is the result of NRPs of small

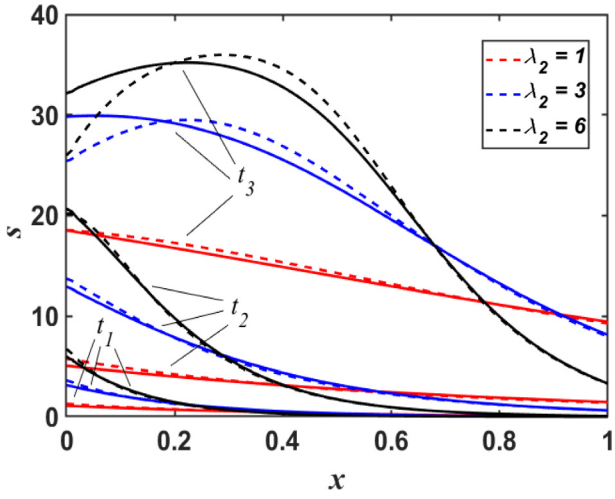


Fig. 4. Effect of $n = \lambda_1/\lambda_2$ on the retention profile: $n = 2$ (continuous curves) and $n = 4$ (dashed curves) for $\lambda_2 = 1$, 3, and 6; at 3 moments $t_1 = 1$, $t_2 = 5$, and $t_3 = 25$. Fixed parameters used in the modelling are $B_2 = 0.02$, ${C_2}^0 = 0.9$, $\varepsilon = 0.25$.

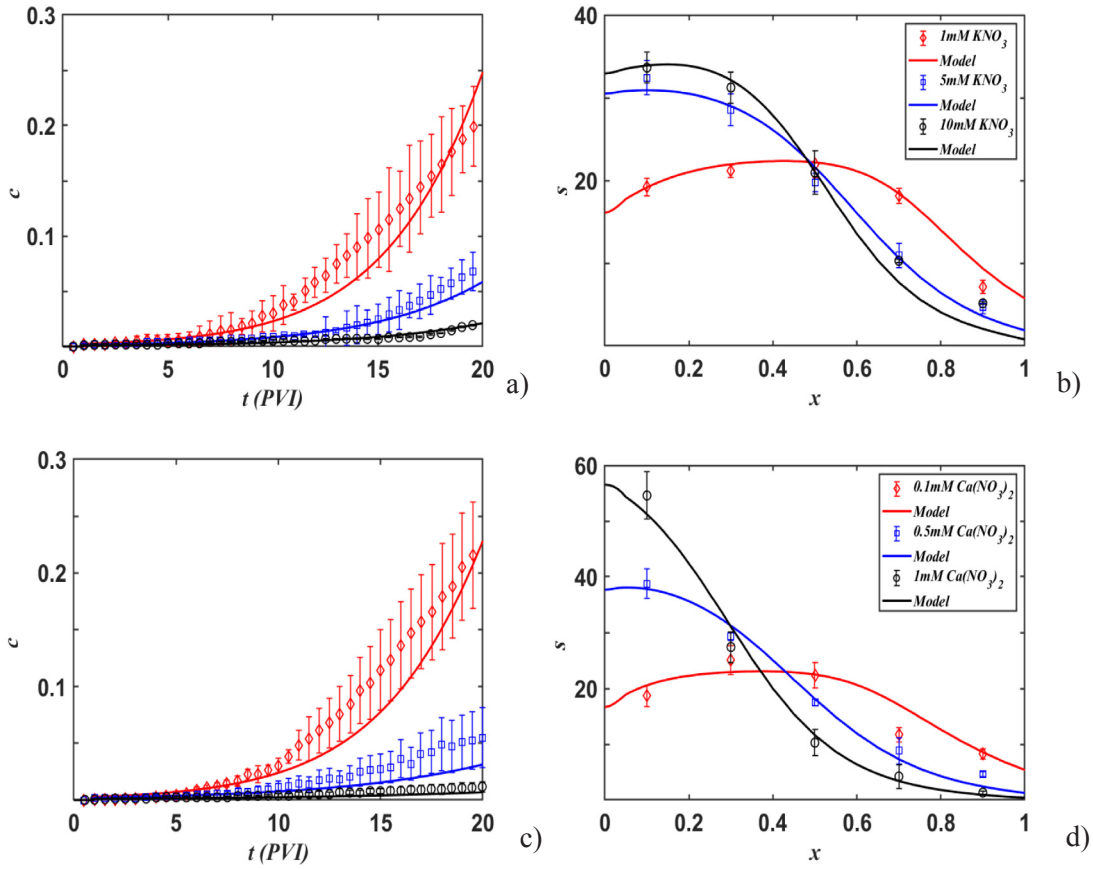


Fig. 5. Matching of the laboratory data by the model for different salts and salinities: a) and c) breakthrough concentration profiles for KNO_3 and $Ca(NO_3)_2$, respectively; and the corresponding retention profiles b) and d) at t = 20 PVI.

Table 1
Tuned model coefficients as obtained from laboratory data.

Ref.	KNO_3 (mM)	$Ca(NO_3)_2$ (mM)	Velocity (cm/min)	ϕ	λ_2	λ_1	C_2^0	B_2	B_1	R_c^2	R_s^2
[35]	1.0	–	0.26	0.4	5.90	19.18	0.860	0.0305	0.122	0.9493	0.9625
	5.0	–	0.26	0.4	6.30	11.53	0.930	0.0242	0.103	0.9438	0.9933
	10.0	–	0.26	0.4	7.15	11.44	0.940	0.0200	0.118	0.8669	0.9641
	–	0.1	0.26	0.4	5.80	29	0.895	0.0350	0.103	0.9456	0.8175
	–	0.5	0.26	0.4	6.15	18.45	0.980	0.0225	0.075	0.6326	0.9848
	–	1.0	0.26	0.4	7.00	9.8	0.990	0.0140	0.14	0.4710	0.9860
[47]	2.5	–	0.70	0.4	1.50	15	0.670	0.1000	0.345	0.8494	0.9378
	5.0	–	0.70	0.4	2.90	23.2	0.580	0.0300	0.25	0.8411	0.9964
[2]	–	–	3.00	0.38	7.00	63	0.975	0.0035	0.041	–	0.9010
	–	–	6.80	0.38	6.00	33	0.975	0.0045	0.075	–	0.8653

particles, so the maxima for volumetric retention concentrations are not so contrast as those for s in Fig. 5b, d, and $S2$ in Fig. 6c.

4.3. Sensitivity study

Let us discuss how the flux reduction factor α and the adsorption constant Γ affect the BTCs and RPs during the corefloods.

Fig. 7 shows BTCs and RPs for both populations and the total. The injected concentrations for both populations are the same, so the suspended concentrations stabilise at the same value (Fig. 7a). For the case modelled, stabilisation occurs at t = 20 PVI. The total RP and individual RPs are shown at the moments t_1 = 1, t_2 = 5, t_3 = 10 and t_4 = 20 PVI at Fig. 7b and c, respectively. Those four moments represent four typical stages for the deep bed filtration of binary colloid (Fig. 1).

Fig. 7d, e, and f correspond to slow particle filtration α = 0.01 [43]. Change of time variable $t \rightarrow \alpha t$ transforms system (19)–(21) to the same system but with α = 1. If compared with the case, the evolution in system (19)–(21) is delayed $1/\alpha$ times. BTCs in Fig. 7a and d coincide, if the time axis in Fig. 7d is expanded $1/\alpha$ times. RPs in Fig. 7b and e coincide if the four PRs in the case α = 0.01 are taken at the instances t_k/α, k = 1…4. The same corresponds to individual RPs in Fig. 7c and f.

The effects of Henry's adsorption constant on the colloidal-nano transport is shown in Fig. 8. Fig. 8a, b, and c compare the adsorption-free case with the case Γ = 1. BTCs with sorption repeat the forms of the sorption-free case with delay 1 PVI (Fig. 8a). Pink, green, and blue curves in Fig. 8b correspond to retained, adsorbed and total concentrations, respectively. The total concentration repeats type curves for retained concentrations as obtained in the four typical moments. This result is important, because there is no way to distinguish between adsorbed and retained particles in porous media during laboratory corefloods, they cannot be measured separately, and what profile is

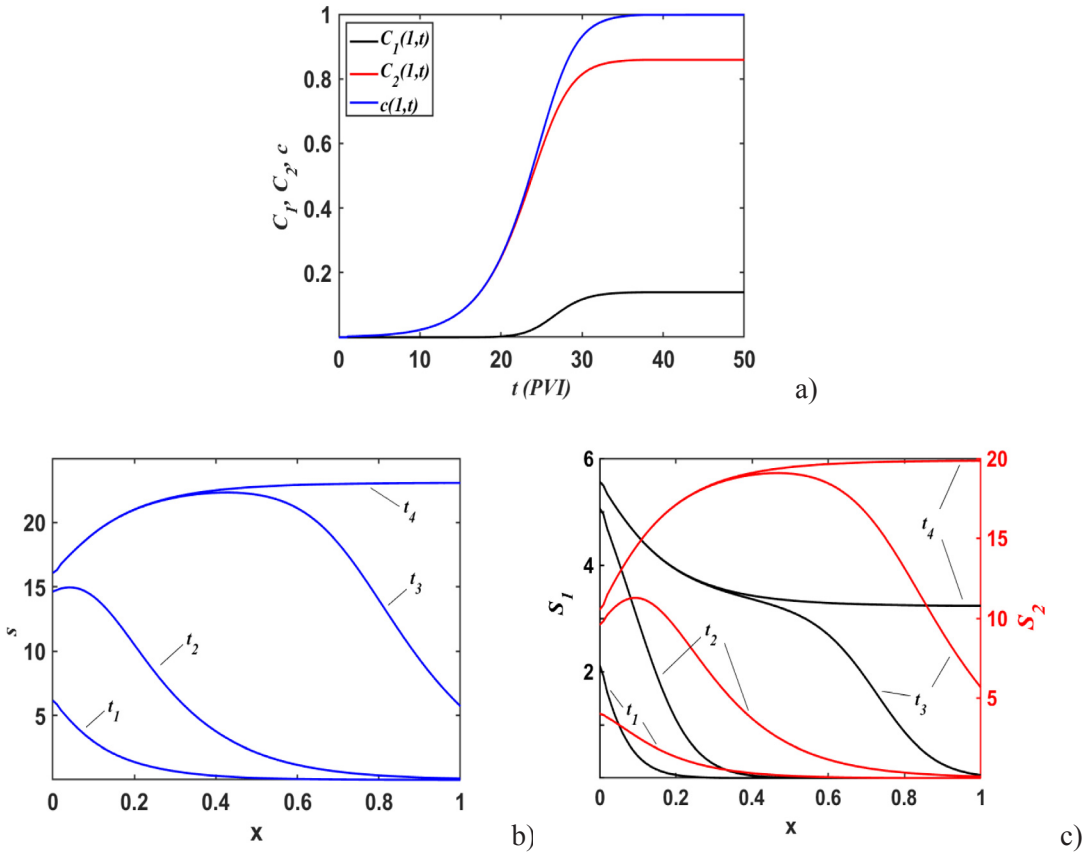


Fig. 6. Revealing micro- and macro-scale behaviour from the matched laboratory data: a) breakthrough concentration profiles for each component and the total colloid; b) revealed earlier and later retention profiles from limited-time matching; c) retention profiles for each component at moments $t_1 = 1$, $t_2 = 5$, $t_3 = 20$, and $t_4 = 50$ PVI for 1 mM KNO_3 (Fig. 5b).

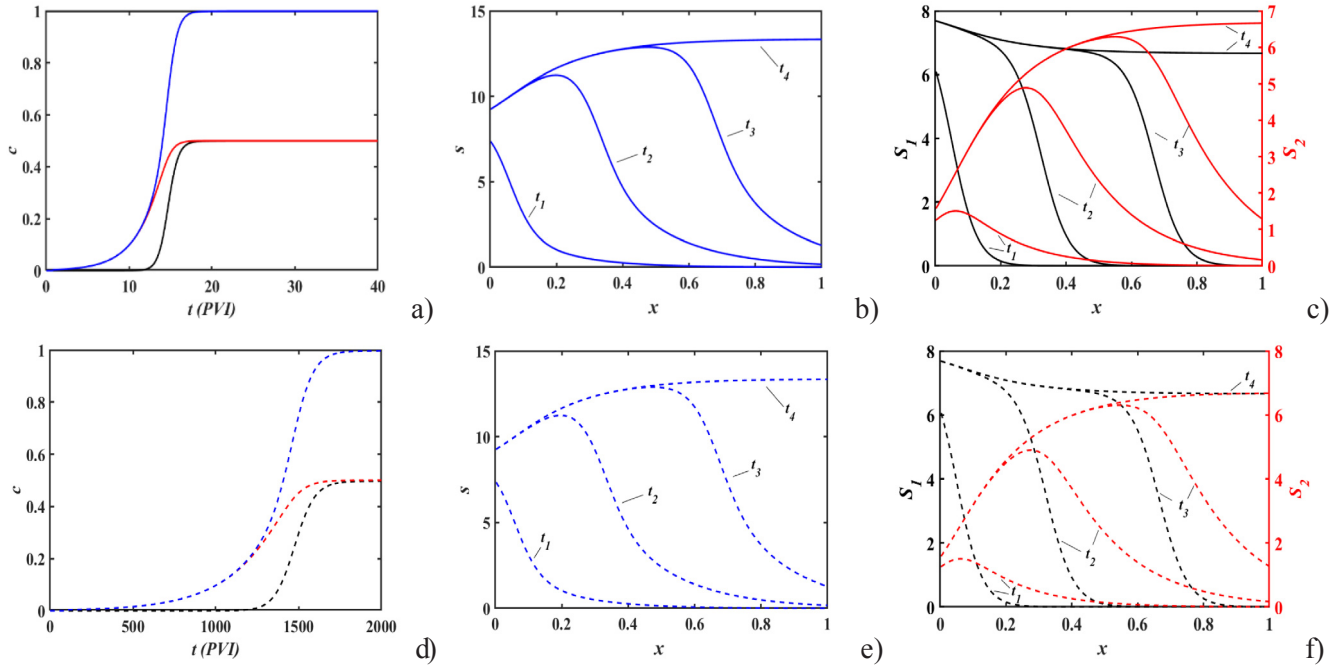


Fig. 7. Comparison between BTCs and RPs for small-particle population (red), large-particle population (black) and total colloid (blue) for different f_0. For a), b) and c) $f_0 = 1$ at the moments $t_1 = 1$, $t_2 = 5$, $t_3 = 10$ and $t_4 = 20$ PVI; for d), e) and f) $f_0 = 0.01$ at the moments $t_1 = 100$, $t_2 = 500$, $t_3 = 1000$ and $t_4 = 2000$ PVI. Parameters used for analytical model: $B_2 = 0.025$; $\varepsilon = 0.2$; $C_2^0 = 0.5$; $\lambda_2 = 5$; n = 5; $\Gamma = 0$; $s_0 = 0.8$.

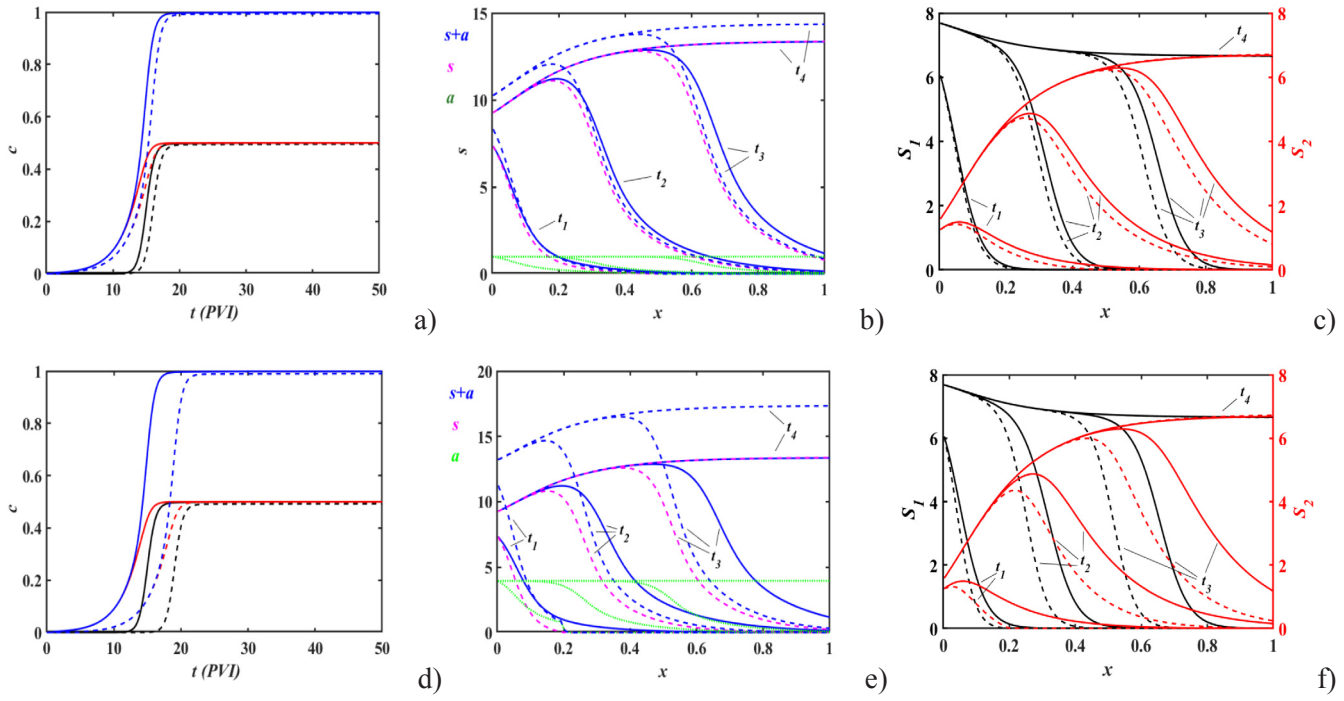


Fig. 8. Comparison of BTCs for macro- and micro-scale and RPs for macro- and micro-scale for different Henry's adsorption coefficient Γ. For a), b) and c) $\Gamma = 0$ (continuous curves) and $\Gamma = 1$ (dashed curves); for d), e) and f) $\Gamma = 0$ (continuous curves) and $\Gamma = 4$ (dashed curves). Parameters used for the analytical modelling are $B_2 = 0.025$; $\varepsilon = 0.2$; $C_2^0 = 0.5$; $\lambda_2 = 5$; n = 5; $s_0 = 1$; $f_0 = 1$ at the moments $t_1 = 1$, $t_2 = 5$, $t_3 = 10$ and $t_4 = 20$ PVI.

measured by CT is the total RP [14,20,39].

Red and black curves in Fig. 8c correspond to small and large retained particles, respectively. At the presence of adsorption, the individual RPs also follow the four-stage scenarios of sorption-free case. At the case of sorption, the RPs of each population repeat the sorption-free profiles with delay. So, equilibrium sorption results in delay in colloidal transport.

Fig. 8d, e, and f compare the cases $\Gamma = 0$ and $\Gamma = 4$. The effects are the same as in the previous case, but the delay is larger (4 PVI).

The filtration coefficient λ in Eq. (3) for colloidal retention rate is proportional to the deposition rate coefficient k_d. Tufenkji and Elimelech [18] present empirical formulae for k_d versus particle size, density, grain size, and velocity. As it follows from these formulae, the higher is the particle size and the smaller are the grains, the higher is the filtration coefficient. Particle density increases the particle capture and filtration coefficient by sedimentation. The higher is the flow velocity, the lower is the attachment filtration coefficient; the filtration coefficient for size exclusion is independent of velocity. Eq. (24) shows that the filtration function $f(c)$ is monotonic with respect to all individual filtration coefficients, so the above-mentioned qualitative dependencies are extended for $f(c)$ and the retention rate.

4.4. Upscaling of more complex systems. Applications

Non-monotonic variation of the attached particle concentration along the core has been observed in numerous laboratory studies, where the mathematical models describing the NRP phenomenon have been developed [37,39–41,45,46]. The above mentioned models account for both attachment and detachment of the mono-sized particles. Besides, the model developed by Bradford, et al. [37] assumes depth dependency of the filtration function $h(x,s)$; the models by Yuan and Shapiro [39] and by Bradford, et al. [40] assume two-speed structure of the particle flux. The above-mentioned models tune 6, 7, and 6 model coefficients, respectively.

We suggest that NRP phenomenon can be reproduced by the simpler model that accounts for single-speed flux of the size-distributed particles and ignores the detachment. Besides, the binary version of the proposed model, which matches the laboratory tests, tunes 4 model coefficients only.

This is the upscaled (averaged) model for colloidal transport of size-distributed particles, where each particle population flow fulfils the traditional deep-bed filtration equations. We discuss colloids with stochastically distributed particle properties that affect attachment (size, shape, surface charge) and account for attachment, adsorption, accessibility, and slow particle motion. The resulting upper-scale model, along with mass-balance and attachment-rate kinetics, contains an equation for site-occupation kinetics. Despite the upscaled 3 × 3 hyperbolic system is non-linear, 1D transport problem allows for exact solution. The upscaled analytical model facilitates tuning the model coefficients from the laboratory coreflood data and allows for the laboratory-based predictions for 3D field-scale behaviour using streamline modelling. This determines the impact of the upscaling technique and the analytical model.

The upscaling procedure (11)–(21) permits for several extensions. Consider travelling waves in system of PDEs (19)–(21), where the solutions depend on one variable x-Dt, where D is travelling-wav velocity. It results in system of ordinary differential equations (ODE), coinciding with Eqs. (A.3)–(A.5). The following derivations (A.6)–(A.9) are valid for the system of ODE yielding the upscaled model.

Consider suspension injection with varying concentrations $C_k^0(t)$. It yields time-dependency of the lower limit in integral (13). Consequently, in right hand sides of dependencies (14)–(16) appear variable t, resulting in time-dependencies of suspension and occupation functions in the upscaling system (19)–(21).

Zero boundary conditions and non-zero initial conditions (10) correspond to migration of natural suspended reservoir fines [20,59]. The upscaling procedure (11–21) also yields the averaged system (19)–(21). For non-uniform initial fines distribution $C_k^0(x)$, suspension and occupation functions in the upscaling system (19)–(21) are x-dependent.

Eqs. (5) and (6) for colloidal-nano transport in porous media are

similar to the reactive flow models, which often do not allow for upscaling [69]. In this case, the upper scale system depends on the micro-scale behaviour, and the hybrid models with simultaneous simulations at different scales are applied [70].

In the case of two-phase flow, the capillary forces highly exceed drag and electrostatic forces. So, the particles are captured and held on the interface by capillary forces. The corresponding mathematical model uses the force-balance equations defining the interface dynamics [71,72].

5. Conclusions

Analysis of NRPs using the exact upscaling the multi-component colloidal flow system that accounts for adsorption and pore accessibility and the analytical 1D model yield the following conclusions.

Under the assumption that the particles that occupy larger area on the rock surface are attached with larger probability, the analytical model of macro-scale equations exhibits NRPs. This assumption is more realistic than the opposite one, so the non-monotonic behaviour is a rule rather than exception.

Qualitative analysis allows distinguishing four typical periods for colloidal transport of a binary mixture: a) initial stage with monotonically declining RPs; b) appearance of the concentration "hill" of small particles at the inlet and its movement along the flux in the core; c) appearance of the "hill" for overall particle concentration at the inlet and its movement along the flux; d) occupation of the core by ascending sides of both hills and monotonically increasing stabilised profiles for small-particle and overall concentrations.

This scenario is fully supported by the concentration-wave behaviour exhibited by the analytical model.

The model for colloidal transport of binary mixture exhibits close simultaneous match of the laboratory data for BTCs and RPs. Moreover, the data array with 7 degrees of freedom was matched by the 5-parametric model, which validates the model.

If the smaller particles are captured faster ($B_1 < B_2, \lambda_1 > \lambda_2$), retention profiles remain monotonically decreasing during the overall injection period.

The exact upscaling includes expressing each individual suspended concentration versus the averaged value. It allows for complete downscaling, i.e. determining the individual population concentrations $C_k(x,t)$ and $S_k(x,t)$ from their upscaled values $c(x,t)$ and $s(x,t)$.

The stabilised profiles correspond to trivial steady-state solution of the upscaled system: $b = 1$, and $c = 1$. However, stabilised retention profile $s(x,t)$ with $t \to \infty$ cannot be found from the upscaled system. It is found using the Riemann invariants.

Acknowledgements

The authors are grateful to Profs. A. Shapiro (Technical University of Denmark) , Y. Osipov (Moscow State University of Civil Engineering) and A. Roberts (University of Adelaide) for fruitful discussions.

Appendix A. Analytical model for multi-component colloidal transport

Let us discuss the initial-boundary vale problem (10) fort 3 × 3 system (19)–(21) for the particular case of Langmuir's filtration blocking function [46,62–65]

$$h(b) = 1 - b \tag{A.1}$$

We obtain the solution by method of characteristics [60,61], similarly to the solution of simplified colloidal transport [56,59]. Introduce Lagrangian coordinate τ:

$$\tau = t - \left(\frac{\beta + \Gamma}{\alpha}\right)x \tag{A.2}$$

which is the time of arrival of the concentration front to any arbitrary point x of the core, $0 < x < 1$.

System (19)–(21) in coordinates (x, τ) becomes

$$\frac{\partial c}{\partial x} = -(1 - b)f(c) \tag{A.3}$$

$$\frac{\partial s}{\partial \tau} = (1 - b)f(c)\alpha \tag{A.4}$$

$$\frac{\partial b}{\partial \tau} = (1 - b)d(c)\alpha \tag{A.5}$$

Ahead of the concentration front that moves with velocity $\alpha(\beta + \Gamma)^{-1}$, i.e. for $\tau < 0$, the initial conditions hold. Axes $\tau = 0$, which is the concentration front trajectory, is the characteristic line for system (A.3-A.5), i.e. Eq. (A.3) is an ordinary differential equation with respect to variable x. Along this line, $b = 0$. It allows determining suspension concentration behind the front c^-, by separating variables in ordinary differential equation Eqs. (A.3):

$$\int_{c^-\left(x,-\frac{\beta+\Gamma}{\alpha}x\right)}^{1} \frac{dy}{f(y)} = x \tag{A.6}$$

Now, express occupied vacancy concentration $b(x,\tau)$ from Eqs. (A.3) and substitute the obtained expression into Eq. (A.5). Integrating the obtained equation in x yields the expression for suspended concentration $c(x,\tau)$ given by the transcendental equation:

$$\int_{c^-\left(x,-\frac{\beta+\Gamma}{\alpha}x\right)}^{c} \frac{\alpha^{-1}dy}{f(y)w(y)} = \tau; \quad w(c) = \int_{c}^{1} \frac{d(y)}{f(y)}dy \tag{A.7}$$

Taking x-derivative of both sides of Eq. (A.7), expressing gradient of suspended concentration and substituting the result into Eq. (A.3), we express occupied concentration $b(x,\tau)$ via suspended concentration:

$$b(x, \tau) = 1 - \frac{w(c)}{w(c^-)} \tag{A.8}$$

The retained concentration $s(x,\tau)$ is also expressed via suspended concentration:

$$s(x,\tau) = \frac{c(x,\tau) - c^{-}(x)}{w(c^{-})} \tag{A.9}$$

The stabilised RP under the injected colloid flow in the rock with fully occupied vacancies for $\tau \to \infty$ is obtained as a limit of solution (A.9):

$$s(x,\infty) = \frac{1 - c^{-}(x)}{w(c^{-}(x))} \tag{A.10}$$

Exact solution (A.6)–(A.9) is used in Section 4.2 for matching the experimental data.

References

[1] R. Anders, C.V. Chrysikopoulos, Evaluation of the Factors Controlling the Time-Dependent Inactivation Rate Coefficients of Bacteriophage MS2 and PRD1, Environ. Sci. Technol. 40 (2006) 3237–3242.
[2] C.C. Choy, M. Wazne, X. Meng, Application of an empirical transport model to simulate retention of nanocrystalline titanium dioxide in sand columns, Chemosphere 71 (2008) 1794–1801.
[3] C.V. Chrysikopoulos, N.P. Sotirelis, N.G. Kallithrakas-Kontos, Cotransport of graphene oxide nanoparticles and kaolinite colloids in porous media, Transp. Porous Med. 119 (2017) 181–204.
[4] W.P. Johnson, X. Li, G. Yal, Colloid retention in porous media: mechanistic confirmation of wedging and retention in zones of flow stagnation, Environ. Sci. Technol. 41 (2007) 1279–1287.
[5] W.P. Johnson, A. Rasmuson, E. Pazmiño, M. Hilpert, Why variant colloid transport behaviors emerge among identical individuals in porous media when colloid-surface repulsion exists, Environ. Sci. Technol. 52 (2018) 7230–7239.
[6] E.F. Pazmino, H. Ma, W.P. Johnson, Applicability of colloid filtration theory in size-distributed, reduced porosity, granular media in the absence of energy barriers, Environ. Sci. Technol. 45 (2011) 10401–10407.
[7] D. Wang, S.A. Bradford, R.W. Harvey, B. Gao, L. Cang, D. Zhou, Humic acid facilitates the transport of ARS-labeled hydroxyapatite nanoparticles in iron oxyhydroxide-coated sand, Environ. Sci. Technol. 46 (2012) 2738–2745.
[8] M. Zhang, S.A. Bradford, J. Šimůnek, H. Vereecken, E. Klumpp, Do goethite surfaces really control the transport and retention of multi-walled carbon nanotubes in chemically heterogeneous porous media? Environ. Sci. Technol. 50 (2016) 12713–12721.
[9] V. Gitis, C. Dlugy, G. Ziskind, S. Sladkevich, O. Lev, Fluorescent clays—similar transfer with sensitive detection, Chem. Eng. J. 174 (2011) 482–488.
[10] E. Timchak, V. Gitis, A combined degradation of dyes and inactivation of viruses by UV and UV/H2O2, Chem. Eng. J. 192 (2012) 164–170.
[11] M. Asraf-Snir, V. Gitis, Tracer studies with fluorescent-dyed microorganisms—A new method for determination of residence time in chlorination reactors, Chem. Eng. J. 166 (2011) 579–585.
[12] V. Sygouni, C.V. Chrysikopoulos, Characterization of TiO2 nanoparticle suspensions in aqueous solutions and TiO2 nanoparticle retention in water-saturated columns packed with glass beads, Chem. Eng. J. 262 (2015) 823–830.
[13] V. Gitis, I. Rubinstein, M. Livshits, G. Ziskind, Deep-bed filtration model with multistage deposition kinetics, Chem. Eng. J. 163 (2010) 78–85.
[14] M. Elimelech, J. Gregory, X. Jia, Particle Deposition and Aggregation: Measurement, Modelling and Simulation, Butterworth-Heinemann, 2013.
[15] A. Santos, P. Bedrikovetsky, A stochastic model for particulate suspension flow in porous media, Transp. Porous Med. 62 (2006) 23–53.
[16] E.D. Vecchia, M. Luna, R. Sethi, Transport in porous media of highly concentrated iron micro- and nanoparticles in the presence of xanthan gum, Environ. Sci. Technol. 43 (2009) 8942–8947.
[17] C. Bianco, T. Tosco, R. Sethi, A 3-dimensional micro-and nanoparticle transport and filtration model (MNM3D) applied to the migration of carbon-based nanomaterials in porous media, J. Contam. Hydrol. 193 (2016) 10–20.
[18] N. Tufenkji, M. Elimelech, Correlation equation for predicting single-collector efficiency in physicochemical filtration in saturated porous media, Environ. Sci. Technol. 38 (2004) 529–536.
[19] H. Yuan, A. Shapiro, Z. You, A. Badalyan, Estimating filtration coefficients for straining from percolation and random walk theories, Chem. Eng. J. 210 (2012) 63–73.
[20] F. Civan, Reservoir Formation Damage, Gulf, Professional Publishing, 2015.
[21] L.I. Kuzmina, Y.V. Osipov, Y.P. Galaguz, A model of two-velocity particles transport in a porous medium, Int J. Non-linear Mech. 93 (2017) 1–6.
[22] G. Ziskind, H. Shmueli, V. Gitis, An analytical solution of the convection–dispersion–reaction equation for a finite region with a pulse boundary condition, Chem. Eng. J. 167 (2011) 403–408.
[23] A.A. Shapiro, Elliptic equation for random walks. Application to transport in microporous media, Physica A: Statistical Mech. its Applic. 375 (2007) 81–96.
[24] H. Yuan, A.A. Shapiro, Modeling non-Fickian transport and hyperexponential deposition for deep bed filtration, Chem. Eng. J. 162 (2010) 974–988.
[25] A. Shapiro, H. Yuan, Application of stochastic approaches to modelling suspension flow in porous media, Statistical Mechanics and Random Walks: Principles, Processes and Applications, Nova Science Publishers, Incorporated, 2012, pp. 1–36.
[26] Z. You, Y. Osipov, P. Bedrikovetsky, L. Kuzmina, Asymptotic model for deep bed filtration, Chem. Eng. J. 258 (2014).
[27] J. Pérez Guerrero, L. Pimentel, T. Skaggs, M.T. Van, Genuchten, Analytical solution of the advection–diffusion transport equation using a change-of-variable and integral transform technique, Int. J. Heat Mass Transfer 52 (2009) 3297.
[28] J.P. Guerrero, E. Pontedeiro, M.T. van Genuchten, T. Skaggs, Analytical solutions of the one-dimensional advection–dispersion solute transport equation subject to time-dependent boundary conditions, Chem. Eng. J. 221 (2013) 487–491.
[29] A.D. Polyanin, S.A. Lychev, Decomposition methods for coupled 3D equations of applied mathematics and continuum mechanics: Partial survey, classification, new results, and generalizations, Appl. Math. Modell. 40 (2016) 3298–3324.
[30] C.H. Bolster, A.L. Mills, G.M. Hornberger, J.S. Herman, Spatial distribution of deposited bacteria following Miscible Displacement Experiments in intact cores, Water Resour. Res. 35 (1999) 1797–1807.
[31] T. Harter, S. Wagner, E.R. Atwill, Colloid transport and filtration of cryptosporidium parvum in sandy soils and aquifer sediments, Environ. Sci. Technol. 34 (2000) 62–70.
[32] M. Tong, W.P. Johnson, Colloid population heterogeneity drives hyperexponential deviation from classic filtration theory, Environ. Sci. Technol. 41 (2007) 493–499.
[33] X. Li, C.-L. Lin, J.D. Miller, W.P. Johnson, Role of grain-to-grain contacts on profiles of retained colloids in porous media in the presence of an energy barrier to deposition, Environ. Sci. Technol. 40 (2006) 3769–3774.
[34] Y. Liang, S.A. Bradford, J. Simunek, M. Heggen, H. Vereecken, E. Klumpp, Retention and remobilization of stabilized silver nanoparticles in an undisturbed loamy sand soil, Environ. Sci. Technol. 47 (2013) 12229–12237.
[35] D. Wang, L. Ge, J. He, W. Zhang, D.P. Jaisi, D. Zhou, Hyperexponential and non-monotonic retention of polyvinylpyrrolidone-coated silver nanoparticles in an Ultisol, J. Contam. Hydrol. 164 (2014) 35–48.
[36] X. Li, W.P. Johnson, Nonmonotonic variations in deposition rate coefficients of microspheres in porous media under unfavorable deposition conditions, Environ. Sci. Technol. 39 (2005) 1658–1665.
[37] S.A. Bradford, J. Simunek, S.L. Walker, Transport and straining of E. coli O157:H7 in saturated porous media, Water Resour. Res. 42 (2006).
[38] E. Goldberg, M. Scheringer, T.D. Bucheli, K. Hungerbühler, Critical assessment of models for transport of engineered nanoparticles in saturated porous media, Environ. Sci. Technol. 48 (2014) 12732–12741.
[39] H. Yuan, A.A. Shapiro, A mathematical model for non-monotonic deposition profiles in deep bed filtration systems, Chem. Eng. J. 166 (2011) 105–115.
[40] S.A. Bradford, S. Torkzaban, J. Simunek, Modeling colloid transport and retention in saturated porous media under unfavorable attachment conditions, Water Resour. Res. 47 (2011).
[41] M. Hilpert, W.P. Johnson, A binomial modeling approach for upscaling colloid transport under unfavorable attachment conditions: Emergent prediction of non-monotonic retention profiles, Water Resour. Res. 54 (2018) 46–60.
[42] A. Polyanin, V.V. Dil'man, Methods of Modeling Equations and Analogies in Chemical Engineering, CRC Press, Boca Raton, 1994.
[43] M.A. Oliveira, A.S. Vaz, F.D. Siqueira, Y. Yang, Z. You, P. Bedrikovetsky, Slow migration of mobilised fines during flow in reservoir rocks: laboratory study, J. Pet. Sci. Eng. 122 (2014) 534–541.
[44] Y. Yang, F.D. Siqueira, A.S. Vaz, Z. You, P. Bedrikovetsky, Slow migration of detached fine particles over rock surface in porous media, J. Natural Gas Sci. Eng. 34 (2016) 1159–1173.
[45] Y. Wang, M.D. Becker, V.L. Colvin, L.M. Abriola, K.D. Pennell, Influence of residual polymer on nanoparticle deposition in porous media, Environ. Sci. Technol. 48 (2014) 10664–10671.
[46] M.D. Becker, Y. Wang, K.D. Pennell, L.M. Abriola, A multi-constituent site blocking model for nanoparticle and stabilizing agent transport in porous media, Environ. Sci.: Nano 2 (2015) 155–166.
[47] Y. Liang, S.A. Bradford, J. Simunek, H. Vereecken, E. Klumpp, Sensitivity of the transport and retention of stabilized silver nanoparticles to physicochemical factors, Water Res. 47 (2013) 2572–2582.
[48] M. Tong, X. Li, C.N. Brow, W.P. Johnson, Detachment-influenced transport of an adhesion-deficient bacterial strain within water-reactive porous media, Environ. Sci. Technol. 39 (2005) 2500–2508.
[49] J.A. Redman, S.B. Grant, T.M. Olson, M.K. Estes, Pathogen filtration, heterogeneity, and the potable reuse of wastewater, Environ. Sci. Technol. 35 (2001) 1798–1805.
[50] Y. Liu, C.-H. Yang, J. Li, Influence of extracellular polymeric substances on pseudomonas Aeruginosa transport and deposition profiles in porous media, Environ. Sci. Technol. 41 (2007) 198–205.
[51] Y. Li, Y. Wang, K.D. Pennell, L.M. Abriola, Investigation of the transport and deposition of fullerene (C60) nanoparticles in quartz sands under varying flow conditions, Environ. Sci. Technol. 42 (2008) 7174–7180.
[52] Y. Wang, Y. Li, H. Kim, S.L. Walker, L.M. Abriola, K.D. Pennell, Transport and retention of fullerene nanoparticles in natural soils, J. Environ. Qual. 39 (2010)

1925–1933.
[53] H. Fogler, Elements of Chemical Reaction Engineering. International Series in the Physical and Chemical Engineering Sciences, Prentice Hall, New Jersey, USA, 2006.
[54] P. Bedrikovetsky, Mathematical Theory of Oil and Gas Recovery: with Applications to ex-USSR Oil and Gas Fields, Springer Science & Business Media, 2013.
[55] A. Shapiro, J. Wesselingh, Gas transport in tight porous media: gas kinetic approach, Chem. Eng. J. 142 (2008) 14–22.
[56] P. Bedrikovetsky, Z. You, A. Badalyan, Y. Osipov, L. Kuzmina, Analytical model for straining-dominant large-retention depth filtration, Chem. Eng. J. 330 (2017) 1148–1159.
[57] P. Bedrikovetsky, Upscaling of stochastic micro model for suspension transport in porous media, Transp. Porous Med. 75 (2008) 335–369.
[58] S.A. Bradford, H.N. Kim, B.Z. Haznedaroglu, S. Torkzaban, S.L. Walker, Coupled factors influencing concentration-dependent colloid transport and retention in saturated porous media, Environ. Sci. Technol. 43 (2009) 6996–7002.
[59] P. Bedrikovetsky, Y. Osipov, L. Kuzmina, G. Malgaresi, Exact upscaling for transport of size-distributed colloids, Water Resour. Res. (2019).
[60] A.D. Polyanin, A.V. Manzhirov, Handbook of Mathematics for Engineers and Scientists, CRC Press, Boca Raton, 2006.
[61] A. Polyanin, V. Zaitsev, Handbook of Nonlinear Partial Differential Equations, Chapman & Hall/CRC Press, Boca Raton, 2012.
[62] H.E. Reynel-Avila, A. Bonilla-Petriciolet, G. de la Rosa, Analysis and modeling of multicomponent sorption of heavy metals on chicken feathers using Taguchi's experimental designs and artificial neural networks, Desalin. Water Treat. 55 (2015) 1885–1899.
[63] H.-K. Rhee, R. Aris, N. Amundson, Multicomponent adsorption in continuous countercurrent exchangers, Philosophical Transactions of the Royal Society of London, Series A, Math. Phys. Sci. 269 (1971) 187–215.
[64] H.-K. Rhee, R. Aris, N.R. Amundson, First-order Partial Differential Equations, Courier Corporation, 2014.
[65] F.G. Helfferich, G. Klein, Multicomponent chromatography, (1970).
[66] L. Shampine, Solving hyperbolic PDEs in MATLAB, Appl. Num. Anal. Comp. Math. 2 (2005) 346–358.
[67] L.F. Shampine, Two-step Lax-Friedrichs method, Appl. Math. Lett. 18 (2005) 1134–1136.
[68] T.F. Coleman, Y. Li, An interior trust region approach for nonlinear minimization subject to bounds, SIAM J. Optim. 6 (1996) 418–445.
[69] I. Battiato, D.M. Tartakovsky, Applicability regimes for macroscopic models of reactive transport in porous media, J. Contam. Hydrol. 120–121 (2011) 18–26.
[70] I. Battiato, D.M. Tartakovsky, A.M. Tartakovsky, T.D. Scheibe, Hybrid models of reactive transport in porous and fractured media, Adv. Water Resour. 34 (2011) 1140–1150.
[71] A.A. Shapiro, Two-phase immiscible flows in porous media: The Mesocopic Maxwell-Stefan approach, Transp. Porous Med. 107 (2015) 335–363.
[72] A.A. Shapiro, Mechanics of the separating surface for a two-phase co-current flow in a porous medium, Transp. Porous Med. 112 (2016) 489–517.

7 Non-monotonic retention profiles during axi-symmetric colloidal flows

Gabriel Malgaresi, Nastaran Khazali, and Pavel Bedrikovetsky.

Hydrology Journal

Statement of Authorship

Title of Paper	Non-monotonic retention profiles during axi-symmetric colloidal flows
Publication Status	☑ Published ☐ Accepted for Publication ☐ Submitted for Publication ☐ Unpublished and Unsubmitted w ork w ritten in manuscript style
Publication Details	Malgaresi, G., Khazali, N., and Bedrikovetsky, P., 2019. Non-monotonic retention profiles during axi-symmetric colloidal flows. Journal of Hydrology, Manuscript Number: HYDROL32942.

Principal Author

Name of Principal Author (Candidate)	Gabriel Malgaresi
Contribution to the Paper	Developed an analytical model to predict non-monotonic retention profiles. Validated the model by tuning the laboratory data for linear flow. Predicted the behaviour of the retention profiles in axisymmetric coordinates. Performed sensitivity analyses for the linear and axisymmetric models.
Overall percentage (%)	80%
Certification:	This paper reports on original research I conducted during the period of my Higher Degree by Research candidature and is not subject to any obligations or contractual agreements with a third party that would constrain its inclusion in this thesis. I am the primary author of this paper.
Signature	Date 25/10/2019

Co-Author Contributions

By signing the Statement of Authorship, each author certifies that:

i. the candidate's stated contribution to the publication is accurate (as detailed above);

ii. permission is granted for the candidate in include the publication in the thesis; and

iii. the sum of all co-author contributions is equal to 100% less the candidate's stated contribution.

Name of Co-Author	Nastaran Khazali
Contribution to the Paper	Helped to predict the behaviour of the retention profiles in axisymmetric coordinates.
Signature	Date 26/10/2019

Name of Co-Author	Pavel Bedrikovetsky
Contribution to the Paper	Problem formulation and supervision of the development of the whole work.
Signature	Date 23/10/2019

Journal of Hydrology 580 (2020) 124235

Contents lists available at ScienceDirect

Journal of Hydrology

journal homepage: www.elsevier.com/locate/jhydrol

Research papers

Non-monotonic retention profiles during axi-symmetric colloidal flows

Gabriel Malgaresi, Nastaran Khazali, Pavel Bedrikovetsky*

Australian School of Petroleum, University of Adelaide, Australia

ARTICLE INFO

This manuscript was handled by Huaming Guo, Editor-in-Chief

Keywords:
Porous media
Groundwater flow
Colloid
Suspension
Upscaling
Analytical model

ABSTRACT

The article studies axi-symmetric suspension and nano-colloidal transport with size-distributed fines in subterranean reservoirs and presents non-monotonic behaviour of the particle retention profiles (RPs). First, we introduce the averaging (upscaling) of the governing system for groundwater with fines over the probabilistic particle-size distribution, and use the analytical model for linear one-dimensional flows to match the laboratory experiments. One set of four tests provides breakthrough curves and post-mortem retention profiles; the results are closely matched. Another test gives retention profiles in three moments; high match was achieved for two moments. In all tests, the number of degrees of freedom of the experimental data array is higher than the number of tuned model parameters; therefore, the close match validates the mathematical model. Subsequently, we develop an upscaling procedure for axisymmetric flow, providing the transport equations for "averaged" particle population. Next, we solve the upscaled equations for suspension injection into a vertical well numerically. It was found out that the radial flows exhibit non-monotonic retention profiles (NRPs). The upscaled equations for axi-symmetric flow allow calculating well injectivity decline during suspension injection and the size of damaged zone, which is important for well stimulation design.

1. Introduction

Rock permeability decline and well injectivity impairment are widely reported in water resource and environmental processes and projects (Civan, 2015; Nunes et al., 2010). This phenomenon is frequently occurring at industrial waste disposal in sub-terrain water reservoirs, water based management, fresh water storage in aquifers, exploitation of geothermal fields, enhanced geothermal project, waterflooding of oilfields, well hydraulic fracturing, and water resources management in aquifers (Bradford et al., 2013; Bradford et al., 2011; Cheng et al., 2019; Chrysikopoulos et al., 2017; Farajzadeh, 2019; Farajzadeh et al., 2019; Hilpert and Johnson, 2018; Hilpert et al., 2017; Rabinovich, 2019; Rosenbrand et al., 2014; Sahai and Moghanloo, 2019; Yakirevich et al., 2013; Yu et al., 2012; Yuan and Moghanloo, 2017; Yuan and Moghanloo, 2018; Zhang et al., 2015; Zhang et al., 2016). Particle retention from the groundwater by the rock with the consequent permeability decline occurs in those processes. The decision-making on injected water treatment, particularly on filtering or chemical treatment, stems from the laboratory-based mathematical modelling. The well behaviour prediction includes laboratory corefloods, matching the experimental data by the adequate mathematical model for linear (x,t)-flow, and using the tuned model coefficients in axi-symmetric (r,t) modelling (Chequer et al., 2017; Civan, 2015; Zhang et al., 2015; Zhang et al., 2016).

The traditional mathematical models for one-dimensional (1D) suspension-colloidal transport in porous media contains mass balance for suspended and attached particles, kinetics equation for particle attachment rate, and Darcy's law that accounts for permeability damage due to retained fines (Bedrikovetsky, 2008; Bradford et al., 2003; Bradford et al., 2006; Chrysikopoulos and Katzourakis, 2015; Chrysikopoulos and Sim, 1996; Zheng et al., 2014):

$$\frac{\partial}{\partial t}(\phi\eta(s)c + s) + U\frac{\partial[\alpha(s)c]}{\partial x} = 0 \tag{1}$$

$$\frac{\partial s}{\partial t} = \lambda h(s)cU \tag{2}$$

$$U = -\frac{k}{\mu(1+\beta s)}\frac{\partial p}{\partial x} \tag{3}$$

where c and s are suspended and attached concentrations, respectively, ϕ is the porosity, U is the fluid velocity, $\eta(s)$ is the accessibility factor, $\alpha(s)$ is the flux reduction factor, $h(s)$ is the filtration function, k is the permeability, μ is the viscosity, λ is the filtration coefficient, and β is the formation damage coefficient. The suspended concentration c is defined as the number of particles per unit water volume, while the attached concentration s is calculated as the number of particles per unit of the

* Corresponding author.
E-mail address: pavel@asp.adelaide.edu.au (P. Bedrikovetsky).

https://doi.org/10.1016/j.jhydrol.2019.124235
Received 22 August 2019; Received in revised form 5 October 2019; Accepted 12 October 2019
Available online 18 October 2019
0022-1694/ © 2019 Elsevier B.V. All rights reserved.

Nomenclature

B	surface area fraction occupied by a single particle with radius r, L^4
b	overall concentration of occupied sites on the rock surface
C	suspended concentration distribution, L^{-4}
c	total suspended particle concentration, L^{-3}
d	site occupation function,
F	individual suspension function for particles with size r, L^{-5}
f	upscaled suspension function, L^{-4}
h	filtration function
k_0	initial permeability, L^2
n	ratio between the filtration coefficients for small and large particles
p	fluid pressure, $MT^{-2}L$
P	dimensionless fluid pressure
q	volumetric injection rate per unit formation thickness, L^2T^{-1}
r	radial distance, L
r_d	damage zone radius, L
r_e	drainage radius, L
r_s	solid (particle) radius, L
r_p	pore radius, L
r_w	wellbore radius, L
S	attached concentration distribution, L^{-4}
s	total attached particle concentration, L^{-3}
t	elapsed time, T
T	pore Volumes Injected
U	Darcy fluid velocity, LT^{-1}
x	cartesian coordinate, L
X	dimensionless radial distance
y	cartesian coordinate, L

Greek letters

A	fraction of the overall flux
B	formation damage coefficient
Γ	Henry's sorption coefficient
δ	proportion of skin to remain
ε	ratio of areas occupied by small and large particles
η	accessibility factor
λ	filtration coefficient, L^{-1}
μ	viscosity, $ML^{-1}T^{-1}$
ϕ	porosity

Abbreviations

BTC	breakthrough curve
NRP	non-monotonic retention profile
PVI	pore volumes injected
RP	retention profile.

rock volume. The accessibility factor is the fraction of porosity that is accessible to the particles with finite (non-zero) size (Bedrikovetsky, 2008). The flux reduction factor is the fraction of the overall flux that passes through the accessible porous space.

The initial-boundary conditions for the constant-concentration colloid injection into a clean bed are:

$$t = 0:\ c = s = 0, \quad x = 0:\ c = c^0 \tag{4}$$

where c^0 is particle concentration in the injected suspension.

The mathematical models for suspension-colloidal transport in porous media, including the one given by Eqs. (1)–(3), exhibit monotonically decreasing retention profiles during colloidal-suspension injection into clean bed (Bradford et al., 2006; Bradford et al., 2011; Polyanin and Zaitsev, 2012; Polyanin and Manzhirov, 2006). However, non-monotonic profiles of retained fine particles have been widely reported in the literature (Bradford et al., 2006; Bradford et al., 2011; Goldberg et al., 2014; Li et al., 2008; Wang et al., 2010; Yuan and Shapiro, 2011).

Bradford et al. (2006) introduced depth dependency of the filtration function $h(x,s)$ in Eq. (2). The model reproduces non-monotonic retention profiles (NRPs). Yet, more physics justification for the x-dependency of the filtration function $h(x,s)$ is required (Goldberg et al., 2014).

The two-particle-speed approach to model NRPs was undertaken by Bradford et al. (2011), and Yuan and Shapiro (2011), where the particle velocity is high in the pore centres and low near the grain walls. The dispersivity α_L for such systems has the same order of magnitude as the pore length. Consequently, the Peclet's number L/α_L has an order of magnitude of 10^3-10^5, i.e. the suspension concentrations of slow and fast particles become equal during the period that is negligibly smaller than the time of one pore volume injected (PVI) (Polyanin and Dil'man, 1994). Therefore, two-speed equations almost instantly tend to the single-population transport model with the average "low" velocity, which exhibits only monotonic RPs (Oliveira et al., 2014; Yang et al., 2016).

Recently, non-monotonic retention profiles (NRPs) have been successfully matched by the upscaled multi-component suspension-colloidal transport model (Malgaresi et al., 2019). Here, post-mortem RPs (taken at the moment when the test is finished) along with the breakthrough histories have been matched. Yet, a model validation requires more than just a successful match; a reliable prediction is essential. Moreover, the timely evolution of retention profiles measured during suspension-colloidal flow is available in the literature (Wang et al., 2010). However, the model was validated only by matching of non-monotonic retention profiles, where the multi-dimension experimental data array is tuned using just few model constants; the following predictions have not been performed.

Usually, the injected suspensions and colloids causing injectivity decline have wide particle-size distributions. Wide particle-size distributions have been reported in numerous water management and injection projects, including low-salinity water storage in aquifers, enhanced geothermal developments, and waterflooding in oilfields (Civan, 2015; Rabinovich et al., 2015; Rabinovich et al., 2013; Rosenbrand et al., 2014). The mobilised fines causing well productivity and injectivity impairment also have sizes distributed in wide ranges. However, the upscaled model for axi-symmetric flow of size-distributed colloids is not available.

In the current paper, using analytical model for 1D linear (x,t)-flows, we provide a close matching of six laboratory tests on colloidal-suspension-nano transport. The number of degrees of freedom of the experimental data array is higher than the number of tuned model parameters for all tests, which validates the model. We derive upscaled governing equations for radial flows. The corresponding numerical model exhibits NRPs around the vertical well during the injection. The upscaled governing equations allow predicting the well injectivity decline using the tuned laboratory-based model parameters. For binary two-sized suspension, stabilised RP monotonically increases from the wellbore toward the reservoir, while it stabilises uniformly during the injection of mono-size suspension. The upscaled model provides the formula to predict the damaged-zone size, which is a valuable information for well stimulation.

The structure of the text is as follows. Section 1 introduces the traditional model for deep bed filtration of mono-sized colloids and briefly overviews the corresponding research on mathematical

modelling. Section 2 presents governing equations for three-dimensional (3D) suspension-colloid-nano transport of particles with continuous size-distribution. Section 3 introduces the upscaled model for multi-component deep-bed filtration and the analytical model for 1D transport. Section 4 presents the matching of the laboratory data with time-evolution of retention profiles, using the analytical 1D linear model. Section 5 develops the upscaled axi-symmetric equations for injection of binary particulate mixture and their numerical solution. Section 6 derives expressions for impedance and radius of the damaged zone during water injection, based on the upscaled model. Section 7 discusses the model validation and applicability. Section 8 concludes the paper.

2. Governing equations for suspension-colloidal transport of size-distributed particles

This section presents the main assumptions of the mathematical model for colloidal-suspension-nano transport of size-distributed particles (section 2.1) and introduces the governing equations for 3D flows (section 2.2).

2.1. Assumptions of the model

Fig. 1 shows the schematic for colloidal-suspension flow of large and small particles with particle capture by the rock. The particles are suspended in the carrier groundwater, attached to the rock, and adsorbed on the rock surface. The attachment kinetics depends on the suspended and attached concentrations, like in Eq. (2). The particles are suspended in the carrier groundwater, attached to the rock, and adsorbed on the rock surface. The attachment kinetics depends on the suspended and attached concentrations, like in Eq. (2), and on the flow velocity U. Under thermodynamic equilibrium, the adsorbed concentration is determined by the suspended concentration via the sorption isotherm; here we assume that the relaxation time of the adsorption kinetics is significantly smaller that the time of one pore volume injection. For small time t, the rate of non-equilibrium adsorption is independent of velocity, which is not the thermodynamic variable. So, the retention rate cannot be expressed via a thermodynamic potential. Therefore, Yerramilli et al. (2014) and Farajzadeh et al. (2016) consider attachment and sorption as independent particle-capture processes. The fines attach and adsorb on different rock-surface sites, so there is no competition between the suspended particles for attachment and adsorption.

The model considers final particle sizes and a fraction of the pore volume inaccessible to the particles. Consequently, the particles are transported only via η-th fraction of the porous space, and the carrier water flux through the accessible space is fraction α of the overall flux through the porous medium. Particle-free water fills the inaccessible pores and flows through them. We assume that η, α, and Γ are constant.

It is assumed that the overall volume of suspended, attached, and adsorbed particles does not change during attachment and sorption. This assumption includes incompressibility of the particles and water, and the Amagat's law for volume additivity (Bedrikovetsky, 2013). If volumetric particle concentrations are negligibly small compared with the rock porosity, the same equations are valid even if Amagat's law is not fulfilled for the water–rock-particles system.

Here we discuss large-scale approximation, where the advective flux of particles significantly exceeds the dispersive-diffusive flux, i.e. the model is diffusion-free (Barenblatt et al., 1989; Polyanin and Dil'man, 1994). The relaxation time of non-equilibrium sorption is significantly lower than the time of one pore volume injection, so equilibrium sorption is assumed. We consider Henry's sorption isotherm, where the proportionality coefficient between the adsorbed and suspended concentrations is independent of the particle size.

2.2. 2.2. Governing equations for 3D multi-component suspension-colloidal flows

Consider 3D transport of the fine particles that can be attached to the rock surface and adsorb on this surface. The suspended and attached fines are distributed by size (radius)

$$c(x_1, x_2, x_3, t) = \int_0^\infty C(r_s, x_1, x_2, x_3, t)dr_s,$$
$$s(x_1, x_2, x_3, t) = \int_0^\infty S(r_s, x_1, x_2, x_3, t)dr_s \quad (5)$$

where x_1, x_2, and x_3 are the Euler coordinates, C and S are the concentration distributions over particle radius.

The ratio between the individual surface occupied by the attached particle $B(r_s)$ and the overall rock surface, available for attachment, depends on the particle size, so the expression for the overall occupied surface is

$$b(x_1, x_2, x_3, t) = \int_0^\infty B(r_s)S(r_s, x_1, x_2, x_3, t)dr_s \quad (6)$$

Consequently, b is the ratio between the overall surface occupied by the attached particles and the rock surface, available for attachment.

Mass balance for suspended, attached and adsorbed fines is

$$\frac{\partial}{\partial t}[\phi\eta C(r_s, x_1, x_2, x_3, t) + S(r_s, x_1, x_2, x_3, t) + \Gamma C(r_s, x_1, x_2, x_3, t)]$$
$$+ U_{xi}\frac{\partial}{\partial x_i}[\alpha C(r_s, x_1, x_2, x_3, t)] = 0 \quad (7)$$

where the sum is performed by the repeating index $i = 1,2,3$. Here Γ is the Henry's constant for particle adsorption.

The attachment rate is defined by analogy to active mass law, where an attached particle is the product of the reaction between the suspended particles of the same size and the rock-surface vacancies (Bedrikovetsky, 2008)

$$\frac{\partial S(r_s, x_1, x_2, x_3, t)}{\partial t} =$$
$$h\left(\int_0^\infty B(r_s)S(r_s, x_1, x_2, x_3, t)dr_s\right)F(C(r_s, x_1, x_2, x_3, t), r_s)\alpha\,|U| \quad (8)$$

Here $|U|$ is module of 3D velocity vector (U_{x1},U_{x2},U_{x3})

$$|U|^2 = \sum_i U_{xi}^2 \quad (9)$$

Incompressibility of the suspension flux is expressed as

$$\frac{\partial U_{xi}}{\partial x_i} = 0 \quad (10)$$

Darcy's law for the suspension flux accounts for permeability decline due to particle attachment and adsorption (Bedrikovetsky, 2008)

$$U = -\frac{k[S(r_s, x_1, x_2, x_3, t), C(r_s, x_1, x_2, x_3, t)]}{\mu}\nabla p \quad (11)$$

Here sign [] corresponds to scalar-permeability dependency of functions $S(r_s, x_1, x_2, x_3,t)$ and $C(r_s, x_1, x_2, x_3, t)$.

Substitution of Eqs. (11) into Eq. (10) yields system of 3 equations (7, 8, 10), which determines three unknowns C, S, and p, i.e. the

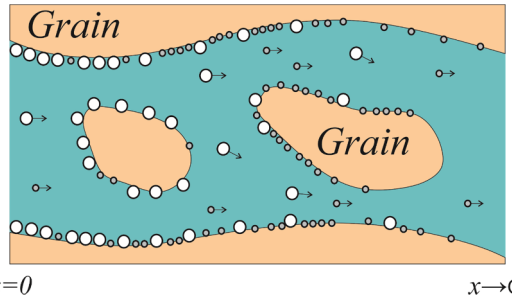


Fig. 1. Schematic for transport of binary colloid with particle attachment to rock surface.

governing system is closed.

3. Upscaling and analytical modelling for 1D linear (*x,t*)-flows

This section presents governing equations for 1D linear flows of multi-component suspension (Section 3.1), introduces the upscaled system of equations for averaged population (Section 3.2), and shows the exact solution for injection of multi-component suspension into a core (Section 3.3).

3.1. Governing equations for 1D linear multi-component flows

Consider the linear flow model, which will be used further in the text for tuning the coreflood data. We discuss colloidal-suspension transport where the particles have *N* distinct sizes. Substituting sums of delta-functions for suspended and attached concentrations into Eq. (7) yield

$$\frac{\partial}{\partial t}[\phi\eta C_k + S_k + \Gamma C_k] + U\frac{\partial}{\partial x}[\alpha C_k] = 0, \quad k = 1. ..N \tag{12}$$

where index k corresponds to population with distinct particle radius r_{sk}.

Eq. (8) for retention rate of each population becomes

$$\frac{\partial S_k}{\partial t} = h\left(\sum_{i=1}^{N} B_i S_i\right) F_k(C_k)\alpha U \tag{13}$$

Initial and boundary conditions correspond to injection of mixture with given composition into a clean bed

$$t = 0\text{: } C_k = S_k = 0;\ x = 0\text{: } C_k = C_k^0 \tag{14}$$

Appendix A presents dimensionless form of system (12, 13) subject to initial and boundary conditions (14).

3.2. Upscaled system for linear flow of multi-component colloid

Substituting sums of delta-functions for suspended and attached concentrations of the suspension with *N* distinct sizes in Eqs. (5) yields

$$c = \sum_{k=1}^{N} C_k, \quad s = \sum_{k=1}^{N} S_k, \quad b = \sum_{k=1}^{N} B_k S_k \tag{15}$$

Appendix A derives the upscaled system for *N*-component suspension-colloidal transport, given by Eqs. (12), (13). The upscaled 3 × 3 system has total concentrations *c*, *s*, and *b* as unknowns. The upscaled system consists of mass balance equation for the overall suspended flux and two kinetics equations for attachment and site occupation rates

$$\frac{\partial}{\partial t}(\eta c + s + \Gamma c) + \frac{\partial(\alpha c)}{\partial x} = 0 \tag{16}$$

$$\frac{\partial b}{\partial t} = h(b)d(c)\alpha, \quad d(c) = \sum_{k=1}^{N} B_k F_k(g_k(c)) \tag{17}$$

$$\frac{\partial s}{\partial t} = h(b)f(c)\alpha, \quad f(c) = \sum_{k=1}^{N} F_k(g_k(c)) \tag{18}$$

The site-occupation and suspension functions, *d(c)* and *f(c)*, depend on overall suspension concentration *c*. However, Eq. (B.2) shows that those functions are dependent of the boundary conditions for injected concentrations of each population, i.e. the phenomenological functions in the upscaled model (16)–(18) are process-dependent. In particular, Eqs. (C.3-C.5) exhibit the dependency of site-occupation and suspension functions of injected concentrations for both components in the binary colloid.

Appendix C presents the forms for suspension and occupation functions for the particular case of binary suspension-colloid. The particular expressions for functions *d(c)* and *f(c)* are given by Eqs. (C.4) and (C.5).

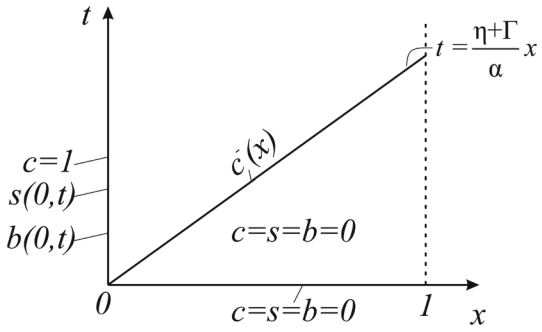


Fig. 2. Flow pattern structure for 1D linear flow pattern from well up to the drainage volume boundary for $0 < x < 1$. For radial flow, the inlet boundary condition is set at $X = X_w$, and $X_w < X < 1$.

The initial and boundary conditions that correspond to injection of suspension with constant fines concentration into clean bed are:

$$t = 0\text{: } c = s = b = 0;\ x = 0\text{: } c = c^0 \tag{19}$$

System (16)–(18) differs from the traditional system (1, 2) by site-occupation kinetics equation (17), which is independent of attachment kinetics (18). Besides, suspended concentration *c* in attachment kinetics equation (2) is substituted by the suspension function *f(c)* in Eq. (18).

3.3. Analytical model for 1D transport of upscaled colloidal system with size-distributed particles

Fig. 2 presents the structure of the flow pattern for 1D linear flow. Expressions (19) present initial and boundary conditions shown in Fig. 2 on abscissa and ordinate axis. The concentration front propagates with constant speed $\alpha/(\eta + \Gamma)$. The initial state of the system holds ahead of the concentration front.

Appendix D presents exact solution for 1D transport of multi-component colloid for the case of Langmuir's blocking function $h(b) = 1\text{-}b$. The solution is presented by implicit expressions (D.5, D.8, D.10, D.13). Formula (D.5) defines suspension concentration behind the concentration front $c^-(x)$. Eq. (D.7) defines function $w(c)$, which determines solution for suspended concentration in the overall domain (x,t). Attached and site-occupation concentrations are expressed via function $w = w(c)$ by formulae (D.13) and (D.10).

Exact solution (D.5, D.8, D.10, D.13) is implemented in MatLab (http://faculty.smu.edu/shampine/current.html) and is used for matching the laboratory coreflood data in the next section.

4. Matching of coreflood data by analytical 1D model for linear flow

Fig. 3 presents the laboratory data by Li et al. (2008). The experiments were performed in a glass column with diameter 2.5 cm and length 15 cm packed with Ottawa Sand. Two artificial porous media with different sand sizes had pore radii r_p = 9.6 and 12.7 μm. Five PVIs of 3 ppm suspension of fullerene (nC_{60}) nanoparticles, with a mean diameter of 120 nm, were injected into a porous column containing an aqueous solution of 1 mM $CaCl_2$ and 0.065 mM $NaHCO_3$. Particle size varied from 92 nm to 124 nm. In each porous media, the injection was carried out with two velocities: $u = 9.27 \times 10^{-5}$ m/s and $u = 1.20 \times 10^{-5}$ m/s. So, altogether four tests have been performed. Fig. 3a shows breakthrough curves (BTCs). Fig. 3b presents four RPs, and NRPs are observed in four tests. Li et al. (2008) used the mathematical model for single-size particles (1, 2) with Langmuir blocking formation damage function (30) for matching. Therefore, all four matched RPs were monotonically decreasing.

Fig. 3a shows the match of four BTCs by the upscaled model (16–18) for binary colloidal flow. The tuning of five model coefficients λ_1, λ_2,

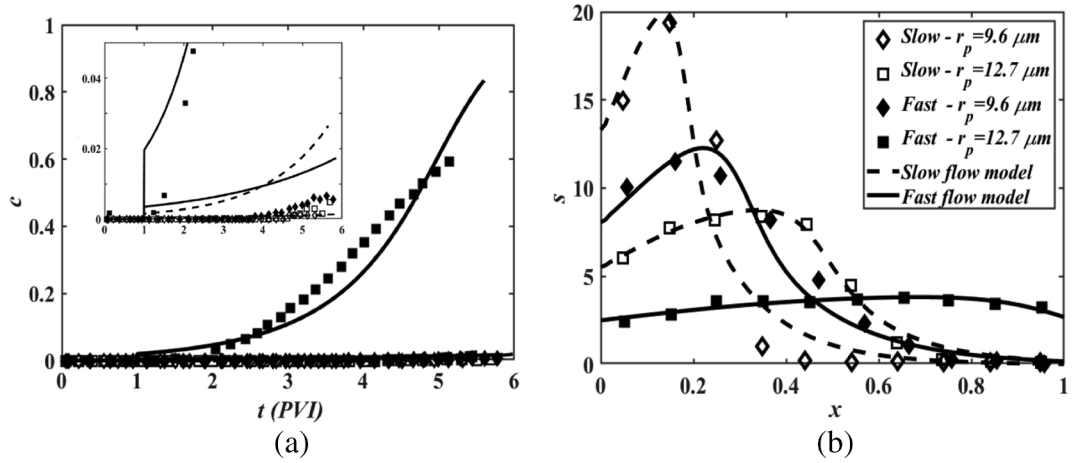


Fig. 3. Effects of pore size r_p on the binary colloidal transport: a) and b): BTCs and RPs, respectively, for flows in two media with two velocities $u = 9.27 \times 10^{-5}$ m/s (fast flow) and $u = 1.20 \times 10^{-5}$ m/s) (slow flow). (Li et al., 2008)).

B_1, B_2, and $C_2{}^0$ has been performed. No adsorption is assumed, $\Gamma = 0$. Accessibility and flux reduction due to finite particle sizes are ignored: $\eta = \alpha = 1$. Non-linear minimisation algorithm in Matlab was used for least square deviation between the laboratory and modelling data (Coleman and Li, 1996; Zhou et al., 2017).

The tuned values of individual occupation areas B_1 and B_2, presented in the second line of Table 1, provide relatively fast retention and occupation, the filtration function $h(s)$ decreases fast, so the breakthrough concentration already at $t = 2$–3 PVI becomes significantly higher than the breakthrough concentration $c(1,1)$ that corresponds to initial value of the filtration function $h(0)$. Therefore, the concentration $c(1,1)$ at the moment of front arrival cannot be distinguished in the graph in Fig. 3a. However, zoom in Fig. 3a exhibits concentration jumps at the moment of front arrival. Fig. 3b presents the match of four RPs by the upscaled model. For all four tests, the model (16–18) reproduces NRPs.

Table 1 presents the tuning results in lines two to five. All four tests have been matched with high accuracy. However, the coefficient of determination for RPs $R_s{}^2$ is closer to one rather than that for BTCs $R_c{}^2$ (columns eleven and twelve in Table 1). Alvarez et al. (2007) show that small variation of filtration function $h(s)$ yields small variation of RP, while the BTC's variation can be quite substantial. It explains significantly more precise match of the RPs than that for BTCs.

For flow in two identical sand-packs with two different velocities, the values of filtration coefficient for large fines are higher than those for small fines (the values in sixth column in lines 3–6 are higher than those in fifth column). For the core length $L = 0.15$ m, the dimensional filtration coefficient λ/L varies from 56/0.15 to 3.5/0.15 1/m, which is inside the common interval for the filtration coefficient (Bianco et al., 2016; James et al., 2018; Mirabolghasemi et al., 2015; Yuan and Shapiro, 2010; Zheng et al., 2014). The tuned concentration of small particles in the injected colloid is almost the same for the four tests.

It is expected that the higher is the velocity the lower is the filtration coefficient for attachment. This is the case for small particles in both media (fifth column) and for large particles in the rock with 9.6 mm pores (sixth column). For large particles in the rock with 12.7 μm pores (sixth column), this is not the case; yet two values of filtration coefficient are almost the same. The expected independence of individual occupation areas of velocities has not been observed. The phenomenon could be explained by non-ideal packing procedure, or by low accuracy in the approximation of the injected suspension by binary mixture.

BTCs in Fig. 3a can be approximated by quadratic parabolas with three free constants. RPs in Fig. 3b can be approximated by cubic parabolas with four free constants. High match of seven-dimensional experimental data array by five constants allows claiming the validity of the mathematical model (16–18).

Fig. 4 presents the laboratory data by Wang et al. (2010). The experiments were performed in a glass column with diameter 2.5 cm and length 11 cm packed with Appling Soil. Mean pore radius was $r_p = 16.9$ μm. Three porous columns packed using the same procedure were claimed to be identical. Suspension with 4.3 ppm of fullerene (nC_{60}) nanoparticles with a mean diameter of 100 nm was injected into a porous column. The injected aqueous solution contained 1 mM $CaCl_2$ and 0.05 mM $NaHCO_3$. Particle size varied from 98 nm to 121 nm. Volumes of 5, 32, and 65 PVs were injected into three cores. The attempt to match the data by the traditional model (1,2) was unsuccessful.

BTCs have not been measured due to low particle concentrations in the effluent water. Fig. 4a shows only the threshold of effluent concentration determined by the accuracy of the particle counter used. Fig. 4b shows matching of three retention profiles by the upscaled model (16–18). RPs for $t = 5$ and $t = 32$ PVI have been matched using the same tuned model coefficients. The dimension of the data array for two curves is eight; five model parameters have been tuned. Close match allows claiming that the model (16–18) is valid (lines 6, 7 and 8 in Table 1). Then RP for $t = 65$ PVI has been predicted using the same values of tuned parameters. Close agreement was observed at the first part of the core for $0 < x < 0.35$; despite the model correctly

Table 1
Tuned model coefficients as obtained from laboratory data.

Ref.	Salinity	Velocity (m/s)	ϕ	λ_2	λ_1	$C_2{}^0$	B_2	B_1	Parameters	$R_c{}^2$	$R_s{}^2$
Li et al. (2008)	1 mM $CaCl_2$	9.27×10^{-5}	–	5.2	27.0	0.63	0.008	0.160	$r_p = 12.7$ μm	0.7305	0.9678
			–	3.5	9.8	0.65	0.029	0.644	$r_p = 9.6$ μm	0.9408	0.8937
		1.20×10^{-5}	–	6.0	24.0	0.60	0.011	0.244	$r_p = 12.7$ μm	0.7018	0.9846
			–	7.0	56.1	0.58	0.0035	0.088	$r_p = 9.6$ μm	0.9014	0.9234
Wang et al. (2010)	1 mM $CaCl_2$	9.23×10^{-5}	0.34	6.5	52.0	0.98	0.0065	0.112	$t = 5$ PVI	–	0.9246
									$t = 32$ PVI	–	0.9682
									$t = 65$ PVI	–	0.7540

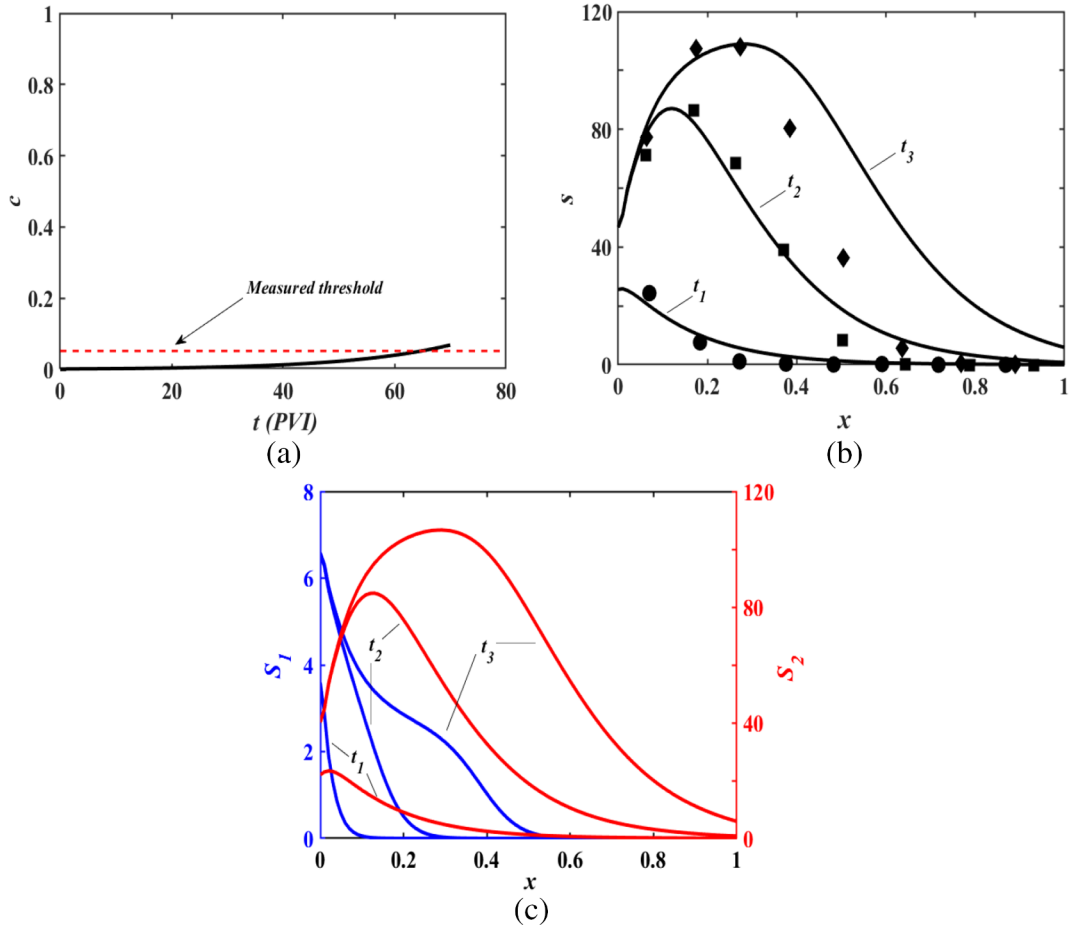


Fig. 4. Matching of experimental data on colloidal injection: a) BTC, b) RPs for the overall colloid; c) RPs for small and large particles at $t_1 = 5$, $t_2 = 32$, $t_3 = 65$ PVI. (Wang et al. 2010).

reproduces the declining tendency of RP at the second part of the core $0.35 < x < 1.0$, the deviation is significant. The BTCs predicted by the model with tuned coefficients (Fig. 4a) are below the threshold of concentration measurements, which also confirmed the laboratory observations.

Tuned model coefficients allow predicting RPs for small and large particles (Fig. 4c), i.e. to perform downscaling. Blue curves correspond to declining RPs of the large particles. Red curves for small particles show the transformation of declining RP at small times to later NRPs.

5. Upscaling of multi-component colloidal transport for 1D axi-symmetric transport (*r,t*)

This section presents governing equations for axi-symmetric flow that corresponds to injection of suspension with continuous size-distribution into vertical well (section 5.1), and that for injection of *N*-component suspension (section 5.2). Section 5.3 derives the upscaled equation for radial flow. Section 5.4 developed a numerical solution for flow with injection into vertical well.

5.1. Governing equations for 1D radial flows

In radial coordinates, Eqs. (7), (8) transform to the following form for axi-symmetric flow

$$\frac{\partial}{\partial t}[\phi\eta C(r_s, r, t) + S(r_s, r, t) + \Gamma C(r_s, r, t)] + \frac{q}{2\pi r}\frac{\partial}{\partial r}[\alpha C(r_s, r, t)] = 0 \tag{20}$$

$$\frac{\partial S(r_s, r, t)}{\partial t} = h\left(\int_0^\infty B(r_s)S(r_s, r, t)dr_s\right)F(C(r_s, r, t), r)\frac{\alpha q}{2\pi r} \tag{21}$$

$$\frac{q}{2\pi r} = -\frac{k_0}{(1 + \int_0^\infty \beta(r_s)S(r_s, X, t)dr_s)\mu}\frac{\partial p}{\partial r} \tag{22}$$

where r is the radius that counts from the well radius r_w and $q(t)$ is the injection rate. Here the formation damage coefficient depends on the particle radius. Introduction of dimensionless coordinates by expressions (E.1) allow getting rid of variable rate $q(t)$ in the governing system.

For incompressible flux, pressure does not enter in kinematic equations (20), (21), so the dynamic equation (22) separates from the kinematic equations. System (20), (21) can be solved separately, and then the pressure distribution $p(r,t)$ and the pressure drop across the reservoir can be found from direct integration in r from Eq. (22).

5.2. Radial flow of a discrete colloidal system

Substituting sum of N delta-functions for suspended, attached, occupied and adsorbed concentration into Eqs. (20)–(22) yields the system for 1D axi symmetric transport of N-component colloids:

$$\frac{\partial}{\partial t}[\phi\eta C_k + S_k + \Gamma C_k] + \frac{q}{2\pi r}\frac{\partial}{\partial r}[\alpha C_k] = 0, \quad k = 1. ..N \tag{23}$$

$$\frac{\partial S_k}{\partial t} = h\left(\sum_{i=1}^{N} B_i S_i\right)F_K(C_k)\frac{\alpha q}{2\pi r} \tag{24}$$

$$\frac{q}{2\pi r} = -\frac{k_0}{(1+\beta\sum_{k=1}^{N} S_k)\mu}\frac{\partial p}{\partial r} \tag{25}$$

In dimensionless form, this system is presented in Appendix E, and its upscaled form is given in the next section.

5.3. Upscaled radial flow model

The upscaled system for axi-symmetric colloidal *N*-component transport consists of mass balance for suspended, attached and adsorbed particles, and the kinetics equations for occupation and attachment rates:

$$\frac{\partial}{\partial T}(\eta c + s + \Gamma c) + \frac{\partial(\alpha c)}{\partial X} = 0 \tag{26}$$

$$\frac{\partial b}{\partial T} = h(b)d(c)\frac{\alpha}{2\sqrt{X_w}\sqrt{X}},$$
$$d(c) = \sum_{k=1}^{N} B_k F_k(g_k(c)) \tag{27}$$

$$\frac{\partial s}{\partial T} = h(b)f(c)\frac{\alpha}{2\sqrt{X_w}\sqrt{X}},$$
$$f(c) = \sum_{k=1}^{N} F_k(g_k(c)) \tag{28}$$

$$T = 0:\ c = s = b = 0, \quad X = X_w:\ c = 1 \tag{29}$$

The difference between axisymmetric-flow system (26–28) and linear-flow system (16)–(18) is the term $2(X_wX)^{1/2}$ appearing in denominators of the sink terms in kinetics equations (27), (28). This term corresponds to diverging flux with increasing cross section during radial flow.

Like in linear upscaled model (16–18), the site-occupation and suspension functions in Eqs. (26)–(28) depend not only on overall suspension concentration *c*, but also on the boundary conditions for injected concentrations of each population (Eq. (F.2)). Therefore, the phenomenological functions *d(c)* and *f(c)* are process-dependent.

5.4. Numerical modelling for axi-symmetric upscaled flow

The upscaled governing system (26–28) subject to initial and boundary conditions (29) is solved numerically. We use the numerical finite-difference model, developed by Shampine (2005a); Shampine (2005b). The two-step Lax–Friedrichs finite-difference method is inbuilt into MATLAB computer software (http://faculty.smu.edu/shampine/current.html). The speed of characteristics in Eq. (26) is equal to $\alpha(\eta+\Gamma)^{-1}$. Consequently, the Courant–Friedrichs–Lewy (CFL) stability condition is expressed by inequality $\alpha\Delta x[(\eta+\Gamma)\Delta t]^{-1} > 1$. We divide the spatial domain $[X_w,1]$ into 100,000 evenly spaced intervals, with the time step selected to satisfy the CFL condition, $\Delta T = 0.9\,\alpha(\eta+\Gamma)^{-1}\Delta X$.

In the next section, the numerical solution of the governing system (26–28) subject to initial and boundary conditions (29) is used to model well injectivity decline during injection of binary colloid.

6. Prediction of RPs and well injectivity during water injection

Here we discuss binary colloid injection into vertical well and its effects on groundwater flow. The numerical solution of the governing system (26–28) subject to initial and boundary conditions (29) uses as an input the parameters obtained by matching the laboratory data presented in Fig. 4. The tuned model parameters are presented in the sixth line of Table 1.

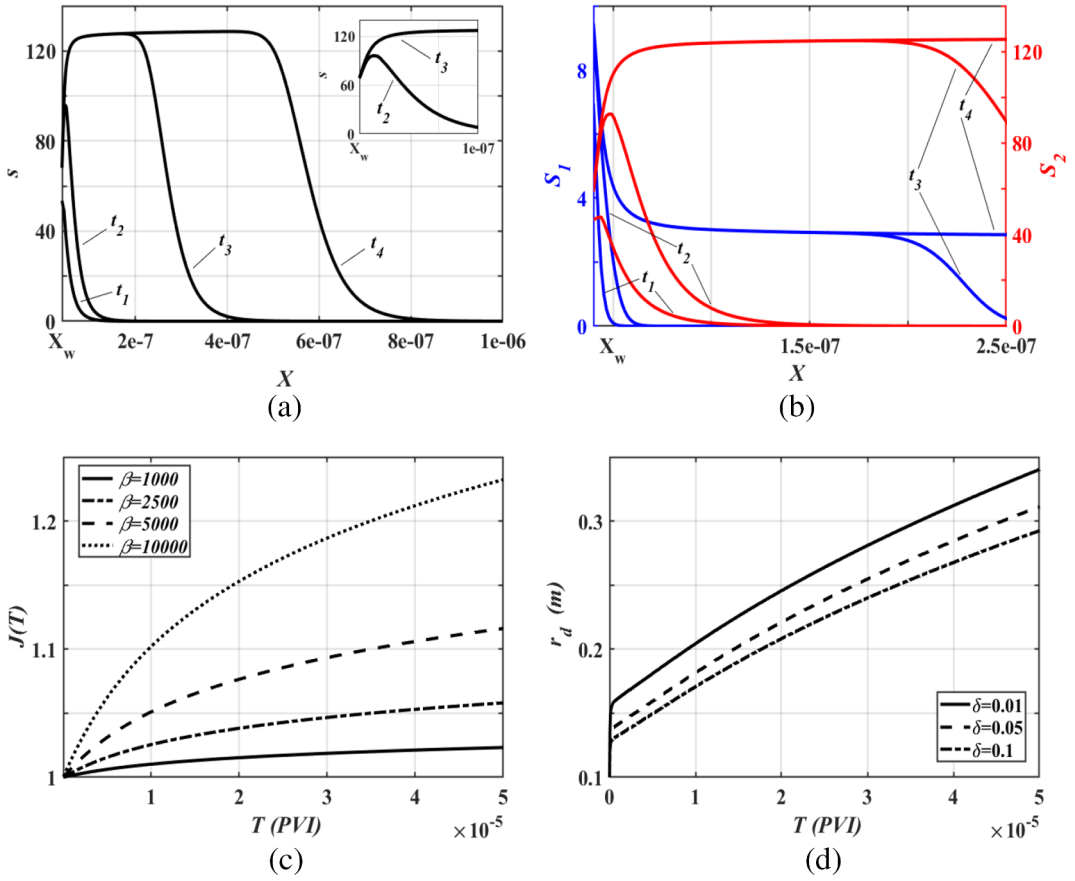


Fig. 5. Laboratory-based prediction of injectivity for vertical well: a) overall RP and c) RPs for large and small particles at four moments $t_1 = 1.0\times10^{-6}$, $t_2 = 3.0\times10^{-6}$, $t_3 = 3.0\times10^{-5}$ PVI, $t_4 = 7.0\times10^{-5}$ PVI, c) impedance for four values of formation damage coefficient β, d) damage zone radius vs pore volume injected for two values of accuracy δ.

Fig. 5a presents the RP dynamics for the overall binary suspension. RP monotonically decreases at the moment t_1. Non-monotonic wave appears near the wellbore at the moment t_2; zoom clearly shows this occurrence. Propagation of NRP into the reservoir continues at the moments t_3 and t_4. The RP asymptotically stabilises behind the pulse: the RPs at moments t_3 and t_4 behind the pulse almost coincide. When time tends to infinity, the stabilised RP monotonically increases. Fig. 5b shows the results of downscaling, i.e. the RPs for small and large particles (red and blue curves, respectively). Like in the linear flow, small particles exhibit non-monotonic behaviour of RPs. RPs for both populations monotonically decrease at the beginning of injection ($t = t_1$). The RP for large particles always remains monotonically decreasing. The small-particle RP becomes non-monotonic at the moment t_2 and asymptotically tends to increasing curve behind the pulse (moments t_3 and t_4).

Calculation of injectivity decline (impedance) is performed based on the numerical model using the RP values for the overall colloid, given a radial version of Eq. (3). Here we use the linearized expression for formation damage $k_0/k(s) = 1 + \beta s$, where β is called the formation damage coefficient. Pressure drop between the well and the drainage volume boundary is

$$\Delta P = \int_{X_w}^{1} \left(-\frac{\partial P}{\partial X}\right) dX = \int_{X_w}^{1} \frac{1 + \beta\phi c^0 s(X, T)}{2X} dX = -\frac{1}{2}\ln X_w + \frac{\beta\phi c^0}{2}\int_{X_w}^{1} \frac{s(X, T)}{X} dX \tag{30}$$

Consider injection with constant rate. The normalised reciprocal of the well injectivity index (impedance) becomes equal to dimensionless pressure drop (Nunes et al., 2010):

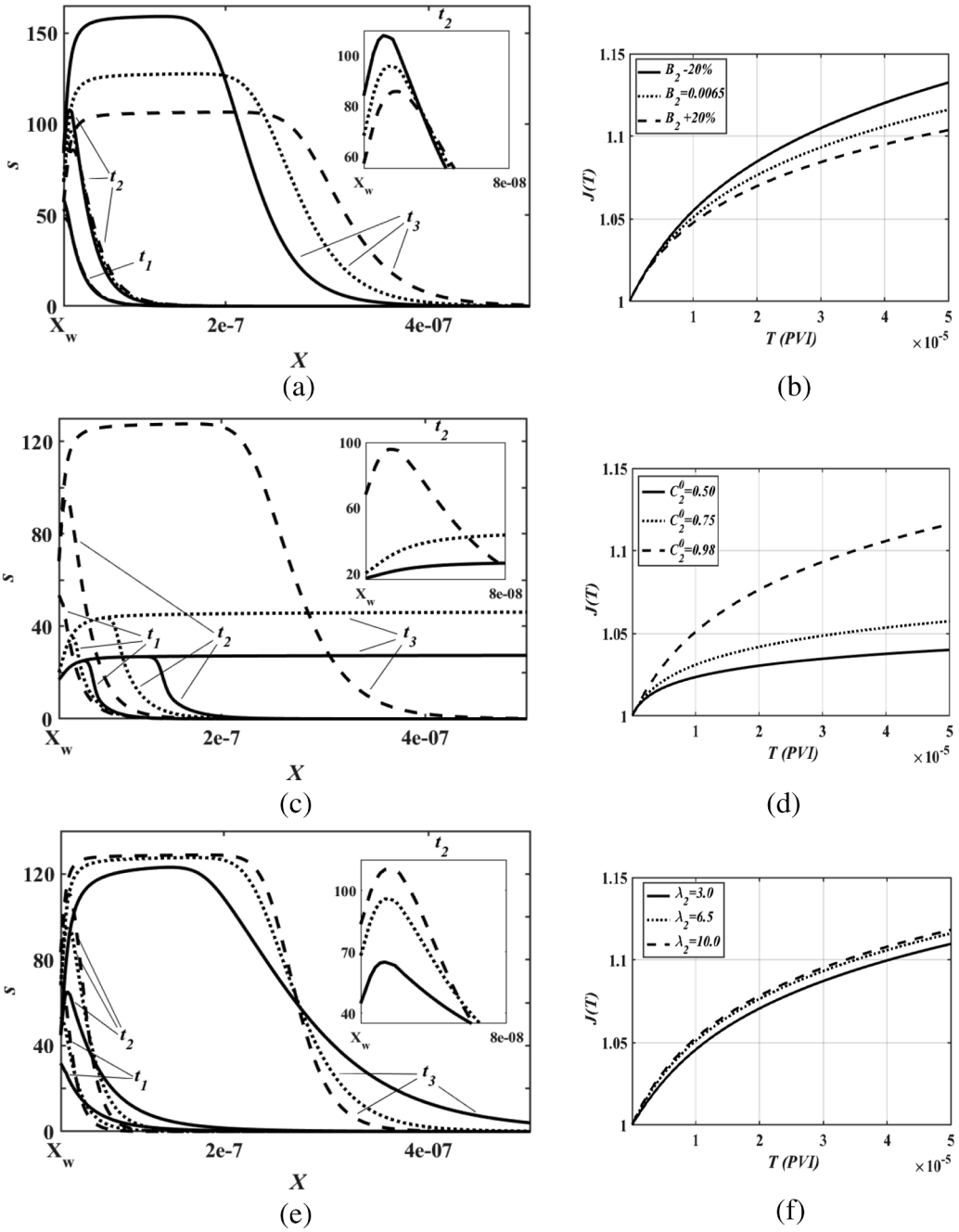


Fig. 6. Sensitivity analyses for total retention profile and impedance for a) and b) B_2 = 0.0052, 0.0065 and 0.0078 (C_2^0 = 0.98, λ_2 = 6.5); c) and d) C_2^0 = 0.5, 0.75 and 0.98 (B_2 = 0.0065, λ_2 = 6.5); e) and f) λ_2 = 3, 6.5 and 10 (B_2 = 0.0065, C_2^0 = 0.98); Fixed parameters used in the modelling are λ_1 = 52, B_1 = 0.112, β = 5000. $t_1 = 1.0 \times 10^{-6}$, $t_2 = 3.0 \times 10^{-6}$, $t_3 = 3.0 \times 10^{-5}$ PVI).

$$J(T) = \frac{\Delta P}{\Delta P_0} = 1 - \frac{\beta\phi c^0}{\ln X_w}\int_{X_w}^{1}\frac{s(X,T)}{X}dX \tag{31}$$

Fig. 5c shows the impedance growth for four values of formation damage coefficient β. The higher is the formation damage coefficient, the higher is the impedance. The most sensitive parameter for impedance is formation damage coefficient.

Let us define the size of formation damage zone X_d as a distance from the wellbore, ahead of which the retained particles almost do not affect the injectivity index, i.e. neglecting the retention concentration for $X > X_d$ decreases the normalised impedance no more than by $\delta \ll 1$:

$$\frac{\int_{X_w}^{X_w+\frac{\alpha}{\eta+\Gamma}T}\frac{s(X,T)}{X}dX - \int_{X_w}^{X_d}\frac{s(X,T)}{X}dX}{\int_{X_w}^{X_w+\frac{\alpha}{\eta+\Gamma}T}\frac{s(X,T)}{X}dX} \leqslant \delta, \tag{32}$$

yielding the inequality that determines X_d

$$\frac{\int_{X_d}^{X_w+\frac{\alpha}{\eta+\Gamma}T}\frac{s(X,T)}{X}dX}{\int_{X_w}^{X_w+\frac{\alpha}{\eta+\Gamma}T}\frac{s(X,T)}{X}dX} \leqslant \delta \tag{33}$$

Fig. 5d shows growth of the damaged zone during the injection for $\delta = 0.01$, $\delta = 0.05$, and $\delta = 0.1$. The higher is the fraction δ of the formation damage caused by the particle retention outside the damaged zone, the smaller is the zone, and the lower is the damaged zone size r_d. During re-perforation of the damaged injected well, the perforation holes must by-pass the zone of formation damage, so r_d is the lower bound for perforation length. The damage radius increases with time, so choice of the perforation length must account for r_d at the moment of the next planned re-perforation, allowing for injection into undamaged rock until the next well stimulation.

Well acidizing removes the formation damage by dissolution of the retained particles. The volume of injected acid V_a is determined by the damaged radius: $V_a = \pi r_d^2 h\phi$, where h is the formation thickness.

Fig. 6 shows sensitivity of RP and impedance with respect to area occupied by small particles B_2, fraction of small particles in the injected suspension concentration C_2^0, and filtration coefficient for small particles λ_2. The basic variant corresponds to experimental study by Wang et al. 2010; the sixth line of Table 1 presents the corresponding values of the model coefficients. The range of variation of parameters B_2, C_2^0, and λ_2 are presented in legends in Fig. 6b, 6d, and 6f, respectively. Other parameters and three moments t_1, t_2, and t_3 are specified in caption in Fig. 6.

Fig. 6a shows that the larger is the individual occupied area for small particles B_2, the less particles occupy the overall rock surface in the stabilised state, and the lower is located the stabilised RP. The figure shows that RP stabilisation occurs near to the injection well. With the fixed number of injected particles at the moment t_3, the lower stabilised attached concentration results in faster propagation of the pulse front. Fig. 6b shows that the higher is the B_2, the lower number of particles populate the surface under the stabilisation, and the lower is the impedance. Three retention profiles almost coincide during the monotonic stage for first two moments and significantly deviate from each other during non-monotonic period.

Fig. 6c shows that the higher is the fraction of small particles in the injected suspension, more particles populate the overall rock surface at the stabilised state, so the stabilisation value of RP is higher. The RPs stabilise near to the injection wellbore, so the pulse propagation speed is lower. Consequently, the impedance is higher (Fig. 6d).

Fig. 6e shows that the higher is the filtration coefficient for small particles λ_2, the faster they attach, the higher is the small particle fraction in the total retained concentration, the more particles populate the rock at the stabilised state. So, since more particles are attached as λ_2 increases, the impedance increases (Fig. 6f).

7. Discussion and summary

In the last two decades, spatial and probabilistic averaging − upscaling − of transport in micro-heterogeneous subterranean reservoirs has been highly developed, producing effective large-scale transport equations (Boso and Tartakovsky, 2016; Dagan et al., 2013; Fiori et al., 2015; Hilpert and Johnson, 2018; Rabinovich et al., 2013; Tartakovsky et al., 2017; Winter and Tartakovsky, 2002). We focus on an important particular case of uncorrelated stochastic properties, which corresponds to zero dispersivity of the micro-scale system (Dagan et al., 2013; Efendiev et al., 2016; Rabinovich, 2017). In this text, we use both terms upscaling and averaging.

Averaging (upscaling) of suspension transport with size-distributed particles The governing system for N-component suspension consists of $2N$ equations (23, 24), yielding extremely computer-time consuming calculations. The way around this problem is averaging over the particle size-distribution, resulting in single-population equations. This procedure was developed in Bedrikovetsky et al. (2019) for 1D linear flows (x,t). However, this paper focus on axi-symmetric flow for injection into vertical wells. Consequently, Appendix F derives the exact upscaling for radial N-component flows (r,t), yielding the large-scale 3×3 system (26–28). If compared with linear-flow upscaled model (16–18), the upscaled system for axi-symmetric flows (26–28) contains the cross-sectional area $2(X_w X)^{1/2}$ in denominators of kinetic rates given by Eqs. (27, 28). This corresponds to radial flow during the injection, where the area of cross-section is equal to $2\pi r$.

Non-monotonic retention profiles We derived an upscaled system for 1D axi-symmetric flows. The main feature of the solution are non-monotonic retention profiles. The solution allows exhibiting time-evolution of the RPs for the overall suspension and its small particles: all profiles are monotonically declining at the beginning of injection; then RPs for overall suspension and small particles translates into non-monotonic; asymptotically, both profiles stabilise at increasing curves; RPs for large particles remain monotonically declining.

Non-monotonic behaviour of RPs occurs for the following relationships between the filtration coefficients and individual occupation areas: $\lambda_1 > \lambda_2, B_1 > B_2$. It is typical that attachment of larger particles occurs faster. Therefore, non-monotonic RPs are rule rather than exception.

Quasi 3D flows In the damage-free case, where permeability is not affected by attached and adsorbed particles, Eqs. (11) separate from the rest of the governing system and yield Laplace equation for pressure p (x_1, x_2, x_3, t). Solution of Laplace equation and Eq. (10) determines flux U. So, flux in Eqs. (7, 8) and (12, 13) becomes a known vector-function, and system (7, 8) of $2N$ equations determine $2N$ unknowns C_k and S_k, $k = 1,2\ldots N$. Introduction of areal coordinate along streamlines and two transversal coordinates reduces 3D problem to 1D with one areal coordinate along the streamlines (Bedrikovetsky, 2013; Polyanin and Lychev, 2016).

The upscaling procedure presented in Appendix F for axi-symmetric flow and in Appendix B for linear flow, can be extended for 3D damage-free flows. Integration in characteristic form of the governing equations (F.1, F.2) uses coordinate x_1 along the streamlines. The resulting 3D system of three equations contains Jacobian of streamline transformation in denominator of expressions for attaching and site-occupation rates in Eqs. (28) and (27), respectively.

Validation of the upscaled model We validate the averaged equations (16–18) by comparison with two sets of laboratory data. The first set contains four tests exhibiting BTCs and *post-mortem* RPs. High match has been achieved for all tests. Dimension of the experimental data array for each test was at least seven, while five model parameters have been tuned. The high match allows claiming validity of the model (7, 8).

Yet, the model matches RPs with higher accuracy than it matches BTCs; the coefficient of determination in twelfth column of Table 1 is higher than R^2 in the eleventh column. Small perturbations of filtration

function *h(s)* yield significantly higher variations in BTC's than in RP's (Alvarez et al., 2005; Alvarez et al., 2007). Therefore, BT data are usually scattered significantly higher than the data on RPs. Consequently, the inverse problem for determination of *h(s)* from RP data is well posed, while treating BTCs yields ill-posed inverse problems and require regularization. The above speculations explain better matches of RPs than those of BTCs.

Another experimental set contains injection of NPs in three identical engineered porous media. The RPs are presented at three moments. The tests exhibit the same scenario that is predicted by the upscaled model: Fig. 4b shows monotonically declining RP at $t = 5$ PVI, non-monotonic pulse at $t = 32$ PVI, and stabilisation of monotonically-increasing RP behind the pulse at $t = 65$ PVI. The retention profiles provide at least eight-dimensional array of laboratory data, so successful match allows claiming the model validity. The deviation in the second section of the core at the third moment can be explained by inhomogeneous packing of sand in the artificial core; another explanation could be insufficient approximation of the injected colloid by a binary mixture; the ternary mixture model would be more precise. Three modelling-predicted BTCs for all cores are below the particle counter resolution, supporting the experimental observation that the particles do not appear in the effluent during the three tests.

The model limitations The kinetics of particle capture, given by Eq. (18) is a generalisation of Langmuir's blocking, which is typical for particle attachment by the rock from the groundwater flux. However, size exclusion of mono-sized particles in two-pore-sized media, where the particles plug small pores and pass through large pores, corresponds to linear Langmuir filtration function (Bedrikovetsky, 2008). For *N*-particle-sized suspension, the filtration function h monotonically increases with respect to individual retention concentrations S_k, as does function h in Eqs. (8) and (13). Approximation of size-exclusion filtration function by formula used in Eqs. (17, 18) and applying the upscaled model (16–18) for size exclusion and straining is a topic of forthcoming work.

We assume that inaccessible pore volume is comparable with the overall pore volume, and the flux through the inaccessible pore volume is comparable with the overall flux. However, we assume that the differences between the accessibility factors for different populations are negligibly small if compared with the average η-value. The same corresponds to flux reduction factor α and Henry's sorption coefficient Γ. Therefore, η, α, and Γ are assumed to be constant in the model given by Eq. (7), which are the limitations of the model.

Eqs. (16–18) are valid for particles distributed by other parameters rather than size, like surface charge, zeta-potential, density, shape, etc. Yet, so far, we found laboratory data on deep bed filtration of particles, distributed only by size.

8. Conclusions

Exact upscaling (averaging) of axi-symmetric suspension-colloidal-nano transport with size-distributed particles and analytical modelling of 1D flows allow concluding as follows.

Suspension-colloidal axi-symmetric transport of size-distributed particles corresponding to constant-composition injection allows for upscaling.

The upscaled 3×3 system consists of mass balance equation and two kinetics equations for particle attachment and site occupation, where the attachment and site occupation rates depend on radius.

Total RPs during injection of binary colloid or suspension, where larger particles occupy larger areas monotonically decrease at the beginning of injection, and with time translates to non-monotonic curves. By the time, RP asymptotically tends to monotonically increasing stabilised curve.

RP for small particles also monotonically decrease at the beginning of injection, with time the RP translates to non-monotonic curve, and then it tends to monotonically increasing profile as time tends to infinity. RPs for large particles remain monotonically decreasing during the overall injection period.

The numerical solution of the axi-symmetric binary-colloid flow problem corresponding to the injection of constant-composition suspension into a vertical well exhibits monotonically increasing stabilised RP, while for mono-size colloid the stabilised RP is uniform.

The numerical solution allows calculating well injectivity decline during the colloidal- suspension-nano injection, which permits for planning the well stimulation procedures. The solution also calculates the damaged zone size, which determines the volume of acid to be injected during well acidizing, and perforation length for well re-perforation.

Declaration of Competing Interest

The authors declare that they have no known competing financial interests or personal relationships that could have appeared to influence the work reported in this paper.

Acknowledgements

The authors are grateful to Dr Themis Carageorgos (The University of Adelaide) for useful discussions and conceptual improvement of the manuscript. G. Malgaresi thanks Brazilian Scientific Fund CNPq for generous support. Many thanks are due to David H. Levin (Murphy, NC, USA), who provided professional scientific and English-language editing of this article.

Appendix A

Dimensionless equations for 1D linear multi-component flows (x,t)

Let us introduce the following dimensionless parameters and variables

$$x \to \frac{x}{L};\ t \to \frac{Ut}{\phi L};\ c^0 = \sum_{i=1}^{N} C_i^0;\ C_k \to \frac{C_k}{c^0};\ S_k \to \frac{S_k}{\phi c^0};\ \lambda_k \to \lambda_k L;$$
$$B_k \to \phi c^0 B_k;\ \Gamma \to \frac{\Gamma}{\phi} \tag{A.1}$$

Here a transformation $A \to A/a$ corresponds to change of the dimensional parameter A' to dimensionless parameter $A = A'/a$. Eqs. (1)–(15) are dimensional. Eqs. (A.2), (A.3) and equations in Appendixes B-D contain only dimensionless variables and unknown functions.

Substituting the dimensionless parameters and variables (A.1) into Eqs. (12), (13) yield

$$\frac{\partial}{\partial t}[\eta C_k + S_k + \Gamma C_k] + \alpha \frac{\partial C_k}{\partial x} = 0 \tag{A.2}$$

$$\frac{\partial S_k}{\partial t} = h\left(\sum_{i=1}^{N} B_i S_i\right) F_k(C_k)\alpha \tag{A.3}$$

In dimensionless boundary conditions (14), the total of dimensionless injected concentrations is one.

Appendix B

Averaging of linear multi-component flow (x,t)

Following Bedrikovetsky et al. (2019), here we present the averaging procedure for system (A.2, A.3).

Substitute Eq. (A.3) into Eq. (A.2), expressing the capture rate in right hand side of the mass balance equation. Characteristic form of the obtained hyperbolic first-order partial differential equation is

$$\frac{dt}{dx} = \frac{\eta + \Gamma}{\alpha}, \quad \frac{dC_k}{dx} = -h\left(\sum_{i=1}^{N} B_i S_i\right) F_k(C_k) \tag{B.1}$$

Dividing variables in second equation (B.1) yields

$$\frac{dG_k(C_k)}{dx} = -h\left(\sum_{i=1}^{N} B_i S_i\right); \quad G_k(C_k) = \int_{C_k^0}^{C_k} \frac{du}{F_k(u)}, \quad k = 1,\ 2. ..N \tag{B.2}$$

As it follows from first Eqs. (B.2), the values of functions $G_k(C_k(x,t))$, $k = 1…N$ are equal for any $x > 0$, $t > 0$. It allows expressing each suspension concentration via overall suspension concentration:

$$C_k = G_k^{-1}[G_1(g_1(c))] = g_k(c) \tag{B.3}$$

Taking the total of Eqs. (A.2) from $k = 1$ to $k = N$ results in Eq. (16) for mass balance of the overall averaged mixture. Substituting expressions (B.3) into Eq. (A.3) and taking the total from $k = 1$ to $k = N$ leads to Eq. (18) for the overall capture rate. Taking the total of Eqs. (A.3) from $k = 1$ to $k = N$ with weighs B_k leads to Eq. (17) for the overall site-occupation kinetics.

Appendix C

Upscaling equations for flow of binary colloid

We consider simplified model with linear suspension functions (constant filtration coefficients)

$$F_k(C_k) = \lambda_k C_k, \quad k = 1,\ 2. ..N \tag{C.1}$$

and Langmuir's blocking for filtration function

$$h\left(\sum_{i=1}^{N} B_i S_i\right) = 1 - \sum_{i=1}^{N} B_i S_i \tag{C.2}$$

$$G_k(C_k) = \ln\left[\frac{C_k}{C_k^0}\right]^{1/\lambda_k}, \quad C_2 = C_2^0\left[\frac{C_1}{C_1^0}\right]^{\lambda_2/\lambda_1},$$

$$c = C_1 + C_2^0\left[\frac{C_1}{C_1^0}\right]^{\lambda_2/\lambda_1}, \quad n = \frac{\lambda_2}{\lambda_1}, \quad k = 1,\ 2 \tag{C.3}$$

$$f(c) = \lambda_1 g_1(c) + \lambda_2 C_2^0\left[\frac{g_1(c)}{C_1^0}\right]^n \tag{C.4}$$

$$d(c) = B_1\left\{\lambda_1 g_1(c) + \varepsilon\lambda_2 C_2^0\left[\frac{g_1(c)}{C_1^0}\right]^n\right\}, \quad \varepsilon = \frac{B_2}{B_1} \tag{C.5}$$

where function $g_1(c)$ is defined by Eq. (B.3).

Appendix D

Exact Solution for 1D flow of colloidal multi-component system

Introduce new variable τ that is equal to time since the concentration front reaches point x:

$$\tau = t - \left(\frac{\eta + \Gamma}{\alpha}\right)x \tag{D.1}$$

System (16–18) in coordinates (x,τ) becomes

$$\frac{\partial c}{\partial x} = -(1 - b)f(c) \tag{D.2}$$

$$\frac{\partial s}{\partial \tau} = (1 - b)f(c)\alpha \tag{D.3}$$

$$\frac{\partial b}{\partial \tau} = (1 - b)d(c)\alpha \tag{D.4}$$

Eqs. (D.3, D.4) imply that unknown functions s and b are continuous across the concentration front $\tau = 0$. Therefore, $b = 0$ at $\tau = 0$. It yields the expression for suspension concentration c^- behind the concentration front, which follows from Eq. (D.2):

$$\int_{c^-\left(x,-\frac{\eta+\Gamma}{\alpha}x\right)}^{1}\frac{dy}{f(y)}=x \tag{D.5}$$

Expression of b from Eq. (D.2) and its substitution into Eq. (D.3) results in

$$b=1+\frac{1}{f(c)}\frac{\partial c}{\partial x},\quad \frac{\partial}{\partial\tau}\left[\frac{1}{f(c)}\frac{\partial c}{\partial x}\right]=-\frac{d(c)\alpha}{f(c)}\frac{\partial c}{\partial x} \tag{D.6}$$

Changing the order of derivatives in left hand side of the second equation (D.6) and integrating it in × with respect to inlet boundary condition (19) yields

$$\frac{\alpha^{-1}}{f(c)}\frac{\partial c}{\partial\tau}=w(c);\quad w(c)=\int_c^1\frac{d(y)}{f(y)}dy \tag{D.7}$$

Separating variables in equation (D.7) yields implicit expression for suspended concentration $c(x,\tau)$ behind the concentration front, i.e. for $\tau > 0$

$$\int_{c^-\left(x,-\frac{\eta+\Gamma}{\alpha}x\right)}^{c}\frac{\alpha^{-1}dy}{f(y)w(y)}=\tau \tag{D.8}$$

Taking derivative in × from both sides of Eq. (D.8) results in the expression for Riemann invariant:

$$\frac{\alpha^{-1}}{f(c)w(c)}\frac{\partial c}{\partial x}=\frac{\alpha^{-1}}{f(c^-)w(c^-)}\frac{dc^-}{dx},\quad c^-=c^-\left(x,-\frac{\eta+\Gamma}{\alpha}x\right) \tag{D.9}$$

Expression for $b(x,\tau)$ follows from first Eq. (D.6) and Eq. (D.9) for known $c(x,\tau)$

$$b(x,\tau)=1-\frac{w(c)}{w(c^-)} \tag{D.10}$$

Since $b = 0$ at the concentration front, Eq. (D.10) can be also re-written as Riemann invariant

$$\frac{1-b}{1-b^-}=\frac{w(c)}{w(c^-)} \tag{D.11}$$

Expressing 1-b from Eq. (D.11), substituting it in Eq. (D.3), and expressing $w(c)$ from the obtained equation leads to

$$\frac{w(c^-)}{f(c)\alpha}\frac{\partial s}{\partial\tau}=w(c) \tag{D.12}$$

Substituting Eq. (D.12) into Eq. (D.7) and integrating in τ accounting for initial condition (19) yields solution for retained concentration

$$s(x,\tau)=\frac{c(x,\tau)-c^-(x)}{w(c^-)} \tag{D.13}$$

Appendix E

Dimensionless equations for radial flows of discrete colloids

Let us introduce the following dimensionless parameters and variables:

$$X=\left(\frac{r}{r_e}\right)^2;\quad T=\frac{1}{\pi\phi r_e^2}\int_0^t q(y)dy;\quad c^0=\sum_{i=1}^m C_i^0;$$
$$C_k\to\frac{C_k}{c^0};\quad S_k\to\frac{S_k}{\phi c^0};\quad F(C_k)\to\frac{F(C_k)r_w}{c^0};\quad B_k\to\phi c^0B_k;\quad P\to\frac{2\pi k_0}{q\mu}p;\quad k=1,2,\ldots,N \tag{E.1}$$

Like in Eq. (A.1), here a transformation $A\to A/a$ corresponds to change of the dimensional parameter A' to dimensionless parameter $A = A'/a$. Eqs. (20)–(25) are dimensional. Eqs. (26)–(33) and equations in Appendixes E and F contain only dimensionless variables and unknown functions.

System (20)–(22) takes the following dimensionless form:

$$(\eta+\Gamma)\frac{\partial C_k}{\partial T}+\alpha\frac{\partial C_k}{\partial X}=-\frac{\partial S_k}{\partial T} \tag{E.2}$$

$$\frac{\partial S_k}{\partial T}=h\left(\sum_{i=1}^N B_iS_i\right)F_k(C_k)\frac{\alpha}{2\sqrt{X_w}\sqrt{X}} \tag{E.3}$$

$$\frac{1}{X}=-\frac{2}{(1+\phi c^o\beta\sum_{k=1}^N S_k)}\frac{\partial P}{\partial X} \tag{E.4}$$

From Eqs. (E.1) follow the dimensionless initial conditions that correspond to injection into a clean bed

$$T=0:\ C_k=S_k=0 \tag{E.5}$$

and boundary condition for constant-concentration colloid injection into a vertical well:

$$X=X_w:\ C_k=C_k^0 \tag{E.6}$$

Appendix F

Upscaling procedure for axi-symmetric transport

The upscaling procedure for axi symmetric flow is similar to that for linear flow derived in Appendix B. However, the derivations for radial flow do not follow from those for linear flow. Therefore, here we present the exact upscaling for axi-symmetric multi-component flow in details.

Substitution of Eq. (E.3) into right hand side of Eq. (E.2) yields first order partial differential equation. Its characteristic form is:

$$\frac{dT}{dX} = \frac{\eta + \Gamma}{\alpha}, \quad \frac{dC_k}{dX} = -h\left(\sum_{i=1}^{N} B_i S_i\right) F_k(C_k) \frac{1}{2\sqrt{X_w}\sqrt{X}} \tag{F.1}$$

Separation of variables in second Eq. (F.1) yields

$$2\sqrt{X_w}\sqrt{X}\,\frac{dG_k}{dX} = -h\left(\sum_{i=1}^{N} B_i S_i\right); \; G_k(C_k) = \int_{C_k^0}^{C_k} \frac{du}{F_k(C_k)} \tag{F.2}$$

meaning that functions $G_k(C_k)$ for $k = 1,2\ldots N$ are equal at any $x > 0, \tau > 0$:

$$G_k(C_k) = G_1(C_1) \tag{F.3}$$

This allows expressing all concentrations for populations $k > 1$ versus C_1

$$C_k = G_k^{-1}[G_1(C_1)] \tag{F.4}$$

expressing total (mean) concentration versus concentration C_1 of the first population

$$c = \sum_{k=1}^{N} G_k^{-1}[G_1(C_1)], \;\; C_1 = g_1(c), \;\; g_1 = \left[\sum_{k=1}^{N} G_k^{-1}(G_1)\right]^{-1} \tag{F.5}$$

and, finally, expressing concentrations for all populations versus total concentration

$$C_k = G_k^{-1}[G_1(g_1(c))] = g_k(c) \tag{F.6}$$

Taking the total of Eqs. (E.2) from $k = 1$ to k = N results in Eq. (26). Substituting expressions (F.6) into Eq. (E.3) and taking the total from $k = 1$ to $k = N$ leads to Eq. (28). Taking the total of Eqs. (E.3) from $k = 1$ to $k = N$ with weighs B_k leads to Eq. (27). Closed upscaled 3 × 3 system is given by Eqs. (26, 27, 28) and determines unknowns $c(X,T)$, $s(X,T)$, and $b(X,T)$.

References

Alvarez, A., et al., 2005. A fast inverse solver for the filtration function for flow of water with particles in porous media. Inverse Probl. 22 (1), 69.

Alvarez, A.C., Hime, G., Marchesin, D., Bedrikovetsky, P.G., 2007. The inverse problem of determining the filtration function and permeability reduction in flow of water with particles in porous media. Transp. Porous Med. 70 (1), 43–62.

Barenblatt, G.I., Entov, V.M., Ryzhik, V.M., 1989. Theory of fluid flows through natural rocks.

Bedrikovetsky, P., 2008. Upscaling of stochastic micro model for suspension transport in porous media. Transp. Porous Med. 75 (3), 335–369.

Bedrikovetsky, P., 2013. Mathematical theory of oil and gas recovery: with applications to ex-USSR oil and gas fields, 4. Springer Science & Business Media.

Bedrikovetsky, P., Osipov, Y., Kuzmina, L., Malgaresi, G., 2019. Exact Upscaling for Transport of Size-Distributed Colloids. Water Resour. Res. 55 (2), 1011–1039. https://doi.org/10.1029/2018wr024261.

Bianco, C., Tosco, T., Sethi, R., 2016. A 3-dimensional micro-and nanoparticle transport and filtration model (MNM3D) applied to the migration of carbon-based nanomaterials in porous media. J. Contam. Hydrol. 193, 10–20.

Boso, F., Tartakovsky, D.M., 2016. The method of distributions for dispersive transport in porous media with uncertain hydraulic properties. Water Resour. Res. 52 (6), 4700–4712.

Bradford, S.A., Simunek, J., Bettahar, M., van Genuchten, M.T., Yates, S.R., 2003. Modeling colloid attachment, straining, and exclusion in saturated porous media. Environ. Sci. Technol. 37 (10), 2242–2250.

Bradford, S.A., Simunek, J., Walker, S.L., 2006. Transport and straining of E. coli O157:H7 in saturated porous media. Water Resour. Res. 42 (12). https://doi.org/10.1029/2005wr004805.

Bradford, S.A., Torkzaban, S., Shapiro, A., 2013. A theoretical analysis of colloid attachment and straining in chemically heterogeneous porous media. Langmuir 29 (23), 6944–6952.

Bradford, S.A., Torkzaban, S., Simunek, J., 2011. Modeling colloid transport and retention in saturated porous media under unfavorable attachment conditions. Water Resour. Res. 47 (10).

Cheng, K.B., Rabinovich, A., Dagan, G., 2019. Stochastic modeling of oscillatory pumping in heterogeneous aquifers with application to Boise aquifer test. J. Hydrol. 569, 278–290.

Chequer, L., et al., 2017. Non-monotonic permeability variation during colloidal transport: governing equations and analytical model. J. Hydrol.

Chrysikopoulos, C.V., Katzourakis, V.E., 2015. Colloid particle size-dependent dispersivity. Water Resour. Res. 51 (6), 4668–4683.

Chrysikopoulos, C.V., Sim, Y., 1996. One-dimensional virus transport in homogeneous porous media with time-dependent distribution coefficient. J. Hydrol. 185 (1–4), 199–219.

Chrysikopoulos, C.V., Sotirelis, N.P., Kallithrakas-Kontos, N.G., 2017. Cotransport of Graphene Oxide Nanoparticles and Kaolinite Colloids in Porous Media. Transp. Porous Med. 119 (1), 181–204.

Civan, F., 2015. Reservoir formation damage. Professional Publishing, Gulf.

Coleman, T.F., Li, Y., 1996. An interior trust region approach for nonlinear minimization subject to bounds. SIAM J. Optim. 6 (2), 418–445.

Dagan, G., Fiori, A., Jankovic, I., 2013. Upscaling of flow in heterogeneous porous formations: critical examination and issues of principle. Adv. Water Resour. 51, 67–85.

Efendiev, Y., Hou, T., Durlofsky, L., Tchelepi, H., 2016. Multiscale analysis and computation for flows in heterogeneous media, Texas A & M Univ., College Station, TX (United States).

Farajzadeh, R., 2019. Sustainable production of hydrocarbon fields guided by full-cycle exergy analysis. J. Petroleum Sci. Eng., 106204.

Farajzadeh, R., Bedrikovetsky, P., Lotfollahi, M., Lake, L., 2016. Simultaneous sorption and mechanical entrapment during polymer flow through porous media. Water Resour. Res. 52 (3), 2279–2298.

Farajzadeh, R., Zaal, C., van den Hoek, P., Bruining, J., 2019. Life-cycle assessment of water injection into hydrocarbon reservoirs using exergy concept. J. Cleaner Prod. 235, 812–821.

Fiori, A., Bellin, A., Cvetkovic, V., de Barros, F., Dagan, G., 2015. Stochastic modeling of solute transport in aquifers: from heterogeneity characterization to risk analysis. Water Resour. Res. 51 (8), 6622–6648.

Goldberg, E., Scheringer, M., Bucheli, T.D., Hungerbühler, K., 2014. Critical assessment of models for transport of engineered nanoparticles in saturated porous media. Environ. Sci. Technol. 48 (21), 12732–12741.

Hilpert, M., Johnson, W.P., 2018. A binomial modeling approach for upscaling colloid transport under unfavorable attachment conditions: emergent prediction of non-monotonic retention profiles. Water Resour. Res. 54 (1), 46–60.

Hilpert, M., Rasmuson, A., Johnson, W.P., 2017. A binomial modeling approach for upscaling colloid transport under unfavorable conditions: emergent prediction of extended tailing. Water Resour. Res. 53 (7), 5626–5644.

James, S.C., Wang, L., Chrysikopoulos, C.V., 2018. Modeling colloid transport in fractures with spatially variable aperture and surface attachment. J. Hydrology 566, 735–742.

Li, Y., Wang, Y., Pennell, K.D., Abriola, L.M., 2008. Investigation of the Transport and Deposition of Fullerene (C60) Nanoparticles in Quartz Sands under Varying Flow Conditions. Environ. Sci. Technol. 42 (19), 7174–7180. https://doi.org/10.1021/es801305y.

Malgaresi, G., Collins, B., Alvaro, P., Bedrikovetsky, P., 2019. Explaining non-monotonic retention profiles during flow of size-distributed colloids. Chem. Eng. J., 121984.

Mirabolghasemi, M., Prodanović, M., DiCarlo, D., Ji, H., 2015. Prediction of empirical properties using direct pore-scale simulation of straining through 3D

microtomography images of porous media. J. Hydrol. 529, 768–778.
Nunes, M., et al., 2010. Theoretical definition of formation damage zone with applications to well stimulation. J. Energy Resour. Technol. 132 (3), 033101.
Oliveira, M.A., et al., 2014. Slow migration of mobilised fines during flow in reservoir rocks: laboratory study. J. Petroleum Sci. Eng. 122, 534–541.
Polyanin, A., Dil'man, V.V., 1994. Methods of modeling equations and analogies in chemical engineering. CRC Press, Boca Raton.
Polyanin, A., Zaitsev, V., 2012. Handbook of nonlinear partial differential equations. Chapman & Hall/CRC Press, Boca Raton.
Polyanin, A.D., Lychev, S.A., 2016. Decomposition methods for coupled 3D equations of applied mathematics and continuum mechanics: partial survey, classification, new results, and generalizations. Appl. Math. Modell. 40 (4), 3298–3324.
Polyanin, A.D., Manzhirov, A.V., 2006. Handbook of mathematics for engineers and scientists. CRC Press, Boca Raton.
Rabinovich, A., 2017. Estimation of sub-core permeability statistical properties from coreflooding data. Adv. Water Resour. 108, 113–124.
Rabinovich, A., 2019. An analytical solution for cyclic flow of two immiscible phases. J. Hydrology 570, 682–691.
Rabinovich, A., et al., 2015. Frequency dependent hydraulic properties estimated from oscillatory pumping tests in an unconfined aquifer. J. Hydrol. 531, 2–16.
Rabinovich, A., Dagan, G., Miloh, T., 2013. Dynamic effective properties of heterogeneous geological formations with spherical inclusions under periodic time variations. Geophysical Res. Lett. 40 (7), 1345–1350.
Rosenbrand, E., Haugwitz, C., Jacobsen, P.S.M., Kjøller, C., Fabricius, I.L., 2014. The effect of hot water injection on sandstone permeability. Geothermics 50, 155–166.
Sahai, R., Moghanloo, R.G., 2019. Proppant transport in complex fracture networks – a review. J. Petroleum Sci. Eng. 182, 106199. https://doi.org/10.1016/j.petrol.2019.106199.
Shampine, L., 2005a. Solving hyperbolic PDEs in MATLAB. Appl. Num. Anal. Comp. Math. 2 (3), 346–358.
Shampine, L.F., 2005b. Two-step Lax-Friedrichs method. Appl. Math. Lett. 18 (10), 1134–1136.
Tartakovsky, A.M., Panzeri, M., Tartakovsky, G.D., Guadagnini, A., 2017. Uncertainty Quantification in Scale-Dependent Models of Flow in Porous Media. Water Resour. Res. 53 (11), 9392–9401.
Wang, Y., et al., 2010. Transport and retention of fullerene nanoparticles in natural soils. J. Environ. Quality 39 (6), 1925–1933.
Winter, C.L., Tartakovsky, D.M., 2002. Groundwater flow in heterogeneous composite aquifers. Water Resour. Res. 38 (8).
Yakirevich, A., et al., 2013. Modeling the impact of solute recycling on groundwater salinization under irrigated lands: A study of the Alto Piura aquifer. Peru. J. Hydrology 482, 25–39.
Yang, Y., Siqueira, F.D., Vaz, A.S., You, Z., Bedrikovetsky, P., 2016. Slow migration of detached fine particles over rock surface in porous media. J. Natural Gas Sci. Eng. 34, 1159–1173.
Yerramilli, R.C., Zitha, P.L., Yerramilli, S.S., Bedrikovetsky, P., 2014. A Novel Water-Injectivity Model and Experimental Validation With CT-Scanned Corefloods. SPE J. 20 (06), 1200–1211.
Yu, C., Gao, B., Muñoz-Carpena, R., 2012. Effect of dense vegetation on colloid transport and removal in surface runoff. J. Hydrology 434, 1–6.
Yuan, B., Moghanloo, R.G., 2017. Analytical model of well injectivity improvement using nanofluid preflush. Fuel 202, 380–394. https://doi.org/10.1016/j.fuel.2017.04.004.
Yuan, B., Moghanloo, R.G., 2018. Nanofluid pre-treatment, an effective strategy to improve the performance of low-salinity waterflooding. J. Petroleum Sci. Eng. 165, 978–991. https://doi.org/10.1016/j.petrol.2017.11.032.
Yuan, H., Shapiro, A.A., 2010. Modeling non-Fickian transport and hyperexponential deposition for deep bed filtration. Chem. Eng. J. 162 (3), 974–988.
Yuan, H., Shapiro, A.A., 2011. A mathematical model for non-monotonic deposition profiles in deep bed filtration systems. Chem. Eng. J. 166 (1), 105–115.
Zhang, W., Tang, X.-Y., Weisbrod, N., Zhao, P., Reid, B.J., 2015. A coupled field study of subsurface fracture flow and colloid transport. J. Hydrology 524, 476–488.
Zhang, W., et al., 2016. A field study of colloid transport in surface and subsurface flows. J. Hydrology 542, 101–114.
Zheng, X.-L., Shan, B.-B., Chen, L., Sun, Y.-W., Zhang, S.-H., 2014. Attachment–detachment dynamics of suspended particle in porous media: Experiment and modeling. J. Hydrology 511, 199–204.
Zhou, K., Hou, J., Fu, H., Wei, B., Liu, Y., 2017. Estimation of relative permeability curves using an improved Levenberg-Marquardt method with simultaneous perturbation Jacobian approximation. J. Hydrology 544, 604–612.

8 Conclusions

The new proposed mathematical models and the explanations for different phenomena during the transport of colloidal suspensions and nanoparticles in porous media allow drawing the following conclusions:

1. A new mathematical model based on two-capture mechanisms allows for an analytical solution. The solution reproduces breakthrough curves with monotonic growth during several PVIs, with further stabilisation at a concentration that is lower than the injected concentration. This phenomenon is well known and published in the literature, however, there was no mathematical model capable to reproduce this phenomenon. The new mathematical model proposed in this thesis treats several laboratory experiments with the mentioned behaviour;

2. The novelty of the new mathematical model based on two-capture mechanisms is based on the treatment of laboratory data, where the filtration coefficients for the attachment and straining/size-exclusion mechanisms are determined from the breakthrough concentration. The straining/size-exclusion filtration coefficient is determined after stabilisation, while the filtration coefficient for attachment is determined at the moment t=1 PVI. Therefore, the matching of laboratory data has only one tuning parameter, the maximum retention concentration (s_m);

3. The aggregation of multiple capture mechanisms shows that any system of n+1 PDEs for colloidal-suspension advective-diffusive transport of a single particle population flowing with n particle capture mechanisms is equivalent to a 2×2 system with a single capture mechanism and allows for the exact solution;

4. A new mathematical model for cotransport of colloids and nanoparticles where each particle population experiences two-capture mechanisms allows predicting the behaviour of binary-colloidal flow in porous media by tuning only two empirical constants;

5. The new mathematical model for cotransport uses properties of single-particle population transport to predict cotransport behaviour;

6. The population balance system for multi-sized colloidal-suspension transport with particle attachment allows for exact upscaling/averaging. The micro-scale system with distributed parameters contains two equations for each particle population. One equation describes particle conservation, while the other defines the attachment kinetics. In contrast, the derived upscaled system consists of three equations: particle conservation law, kinetics of particle attachment, and the kinetics of vacancy occupation. The averaging procedure contains implicit formulae for upscaled suspension and the occupied vacancy functions;

7. The analogy between particle capture and chemical reaction, expressed by the law of mass action considering the reactive species activities for high-concentration, allows introducing a nonlinear suspension function into the capture rate equation;

8. Introduction of one-parametric exponential-quadratic suspension function (analogous to Margules activity model) into the traditional deep bed filtration model allows successfully matching hyper-exponential retention profiles, simultaneously with the breakthrough curves. The modification of the traditional deep bed filtration model is due to high injected particle concentration and some phenomena that the traditional model is not able to capture;

9. A new physical explanation for non-monotonic retention profiles was developed based on the distribution of properties of particles (size, surface charge, form);

10. A novel mathematical model based on the new explanation for non-monotonic retention profiles was derived and allows for an exact analytical solution. The developed model allows distinguishing four typical periods for colloidal transport of a binary mixture: a) an initial stage with monotonically declining retention profiles; b) the appearance of the concentration "peak" of small particles at the inlet and its movement along the flux in the core; c) the appearance of the "peak" for overall particle concentration at the inlet and its movement in the direction of flow; d) the stabilisation of the core with a monotonically decreasing profile for large particles and a monotonically increasing profile for both the small particles and the overall particle concentration.

11. Suspension-colloidal axi-symmetric transport of size-distributed particles corresponding to injection of constant-composition allows for upscaling. The upscaled model allows calculating well injectivity decline during the suspension-colloidal injection, which improves the planning and designing of well stimulation procedures. The solution also allows calculating the damaged zone size, which determines the volume of injected acid during well acidizing and the perforation length for well re-perforation;

12. All the models presented in this thesis show a close match for the tests with pressure drop measurements, and also for the tests where the breakthrough curves and retention profiles have been measured. The proposed models are also used for prediction of well behaviour and formation damage zone;

13. All the tuned model coefficients vary in the common intervals available in the literature, and also present expected tendencies with different parameters, such as pH, salinity, velocity, and others, that agree with the traditional filtration theory;

14. The number of degree of freedom of all laboratory data utilized in this thesis exceeds the number of tuned model parameters for all proposed models, which validates the proposed models in the current thesis.